I. R. IRAN

ISSN: 2423-7167
e-ISSN: 1735-9244

International Journal of Engineering

Journal Homepage: www.ije.ir

MERC

TRANSACTIONS C: Aspects

Volume 34, Number 06, June 2021

Materials and Energy Research Center

In the Name of God

INTERNATIONAL JOURNAL OF ENGINEERING
Transactions A: Basics

International **J**ournal of **E**ngineering *Transactions A: Basics* (ISSN 1728-1431) (EISSN 1735-9244)
International **J**ournal of **E**ngineering *Transactions B: Applications* (ISSN 1728-144X) (EISSN 1735-9244)
International **J**ournal of **E**ngineering *Transactions C: Aspects* (ISSN 2423-7167) (EISSN 1735-9244)
Web Sites: www.ije.ir & www.ijeir.info E-mails: ije.editor8@gmail.com, Tel: (+9821) 88771578, Fax: (+9821) 88773352
Materials and Energy Research Center (MERC)

AIMS AND SCOPE

The objective of the International Journal of Engineering is to provide a forum for communication of information among the world's scientific and technological community and Iranian scientists and engineers. This journal intends to be of interest and utility to researchers and practitioners in the academic, industrial and governmental sectors. All original research contributions of significant value focused on basics, applications and aspects areas of engineering discipline are welcome.

This journal is published in three quarterly transactions: Transactions A (Basics) deal with the engineering fundamentals, Transactions B (Applications) are concerned with the application of the engineering knowledge in the daily life of the human being and Transactions C (Aspects) - starting from January 2012 - emphasize on the main engineering aspects whose elaboration can yield knowledge and expertise that can equally serve all branches of engineering discipline.

This journal will publish authoritative papers on theoretical and experimental researches and advanced applications embodying the results of extensive field, plant, laboratory or theoretical investigation or new interpretations of existing problems. It may also feature - when appropriate - research notes, technical notes, state-of-the-art survey type papers, short communications, letters to the editor, meeting schedules and conference announcements. The language of publication is English. Each paper should contain an abstract both in English and in Persian. However, for the authors who are not familiar with Persian, the publisher will prepare the latter. The abstracts should not exceed 250 words.

All manuscripts will be peer-reviewed by qualified reviewers. The material should be presented clearly and concisely:

- *Full papers* must be based on completed original works of significant novelty. The papers are not strictly limited in length. However, lengthy contributions may be delayed due to limited space. It is advised to keep papers limited to 7500 words.
- *Research* notes are considered as short items that include theoretical or experimental results of immediate current interest.
- *Technical notes* are also considered as short items of enough technical acceptability with more rapid publication appeal. The length of a research or technical note is recommended not to exceed 2500 words or 4 journal pages (including figures and tables).

Review papers are only considered from highly qualified well-known authors generally assigned by the editorial board or editor in chief. Short communications and letters to the editor should contain a text of about 1000 words and whatever figures and tables that may be required to support the text. They include discussion of full papers and short items and should contribute to the original article by providing confirmation or additional interpretation. Discussion of papers will be referred to author(s) for reply and will concurrently be published with reply of author(s).

INSTRUCTIONS FOR AUTHORS

Submission of a manuscript represents that it has neither been published nor submitted for publication elsewhere and is result of research carried out by author(s). Presentation in a conference and appearance in a symposium proceeding is not considered prior publication.

Authors are required to include a list describing all the symbols and abbreviations in the paper. Use of the international system of measurement units is mandatory.

- On-line submission of manuscripts results in faster publication process and is recommended. Instructions are given in the IJE web sites: www.ije.ir-www.ijeir.info
- Hardcopy submissions must include MS Word and jpg files.
- Manuscripts should be typewritten on one side of A4 paper, double-spaced, with adequate margins.
- References should be numbered in brackets and appear in sequence through the text. List of references should be given at the end of the paper.
- Figure captions are to be indicated under the illustrations. They should sufficiently explain the figures.
- Illustrations should appear in their appropriate places in the text.
- Tables and diagrams should be submitted in a form suitable for reproduction.
- Photographs should be of high quality saved as jpg files.
- Tables, Illustrations, Figures and Diagrams will be normally printed in single column width (8cm). Exceptionally large ones may be printed across two columns (17cm).

PAGE CHARGES AND REPRINTS

The papers are strictly limited in length, maximum 6 journal pages (including figures and tables). For the additional to 6 journal pages, there will be page charges. It is advised to keep papers limited to 3500 words.

Page Charges for Papers More Than 6 Pages (Including Abstract)	
For International Author ***	**$55 / per page**
For Local Author	**100,000 Toman / per page**

AUTHOR CHECKLIST

- Author(s), bio-data including affiliation(s) and mail and e-mail addresses).
- Manuscript including abstracts, key words, illustrations, tables, figures with figure captions and list of references.
- MS Word files of the paper.

International **J**ournal of **E**ngineering, P.O. Box 13145-1659, Tehran, I.R. Iran
Materials and Energy Research Center, 5 Ahuramazda St., Alvand Ave., Argentina Sq., Tehran, Islamic Republic of Iran
www.merc.ac.ir - www.emerc.ac.ir

ISSN: 2423-7167, e-ISSN: 1735-9244

International Journal of Engineering, Volume 34, Number 6, June 2021

CONTENTS:

ISSN: 2423-7167, e-ISSN: 1735-9244

International Journal of Engineering, Volume 34, Number 6, June 2021

IJE TRANSACTIONS C: Aspects Vol. 34, No. 6, (June 2021) 1390-1397

International Journal of Engineering

Journal Homepage: www.ije.ir

Flexural Characteristics of Fibre Reinforced Concrete with an Optimised Spirally Deformed Steel Fibre

M. Hajsadeghi*[a,b], M. Jalali[b], C.Seong Chin[c], T. Zirakian[d], M. Bahrebar[e]

[a] *School of Engineering, University of Liverpool, The Quadrangle, Brownlow Hill L69 3GH, UK*
[b] *Faculty of Civil Engineering, Shahrood University of Technology, Shahrood, Iran*
[c] *Department of Civil Engineering, Xian Jiaotong-Liverpool University, Suzhou Industrial Park, Jiangsu Province, China*
[d] *Department of Civil Engineering and Management, California State University Northridge, USA*
[e] *Department of Civil Engineering and Management, The University of Auckland, Auckland, New Zealand*

PAPER INFO

Paper history:
Received 31 March 2021
Received in revised form 26 April 2021
Accepted 27 April 2021

Keywords:
Fibre Reinforced Concrete
Flexural Performance
Optimised Spirally Deformed Steel Fibre
Deflection-hardening Response

ABSTRACT

In this paper, the flexural performance of Fibre Reinforced Concrete (FRC) with an optimised spirally deformed steel fibre developed by the authors is evaluated experimentally. For comparison purposes, concrete specimens with commercially available steel fibres (hooked-end and crimped) are tested and included in the study. The research findings indicate that the optimised spirally deformed steel fibre considerably enhances flexural characteristics of concrete compared with existing fibres on the market. Moreover, the deflection-hardening response (even in the presence of wide cracks) can also be achieved even with low spiral fibre dosages common in practice. Therefore, such a composite, i.e. concrete reinforced with spirally deformed steel fibre, can be deemed as a structural material.

***doi**: 10.5829/ije.2021.34.06c.01*

NOMENCLATURE

f_{ck}	Characteristic cylinder strength of concrete, MPa	L	Clear span between the supports
$f_{ck,\,cube}$	Characteristic cube strength of concrete, MPa	Pe, p	Peak elastic load, kN
f_m	Target mean cylinder strength of concrete for concrete mix design, MPa	Pp, pc	Peak post-cracking load, kN
f_r	Modulus of rupture, MPa	$T\,DX$	Toughness (area under the load vs. net deflection curve from 0 to L/X
f_u	Ultimate stress of steel, MPa	Vf	Fibre volume content
f^D_X	Residual strength at net deflection of L/X		

1. INTRODUCTION

The employment of steel reinforcing bars makes concrete a suitable composite material for various structural and non-structural applications. Such bars, however, reinforce concrete against tension only locally where the cracks in reinforced concrete (RC) members can freely initiate and propagate until encountering rebar. The need for multi-directional and closely spaced reinforcements for concrete led to fibre reinforced concrete (FRC). FRC is a cement-based composite material reinforced with discrete and randomly distributed fibres [1]-[3]. There are various fibre materials such as steel, carbon, and polypropylene; however, steel is the most suitable for structural applications due to its high modulus of elasticity and ductility [3,4].

The fibres act as crack growth arrestors (crack bridging mechanism), leading to a delay in the formation and propagation of the crack, reduction in crack widths, and consequently enhancement of post-cracking characteristics and ductility of concrete [4]. However, the structural applications of FRC are limited mainly because of the poor performance of the fibres at the cracking levels expected at the ultimate loading. After the initial

*Corresponding Author Institutional Email:
hajsadeghi.mohammad@xjtlu.edu.cn (M. Hajsadeghi)

Please cite this article as: M. Hajsadeghi, M. Jalali, C. Seong Chin, T. Zirakian, M. Bahrebar, Flexural Characteristics of Fibre Reinforced Concrete with an Optimised Spirally Deformed Steel Fibre, International Journal of Engineering, Transactions C: Aspects Vol. 34, No. 6, (2021) 1390-1397

stage of the fibre pullout process (peak pullout load), as the fibres are pulled out from concrete, their resistance usually decreases with the continuous slippage known as slip-softening behaviour. The continuous decay of pullout load would not result in a major contribution of fibres to the ultimate load bearing capacity. In other words, the overall internal force transferred by the fibres across the cracked sections (bridging contribution of fibres) is generally less than the internal force transferred through the sections before cracking [5,6].

There are examples of steel fibres on the market such as brass-coated straight, and twisted fibres which are engineered in terms of surface coating and geometry (shape) for compatibility with certain high- and ultra-high-performance concretes (HPC and UHPC) to achieve higher rates of increase in the fibre-matrix interface friction which could result in a hardening pullout response [7,8]. These fibres are relatively expensive and demand restrictive requirements on the concrete composition; hence their applications as structural reinforcement are limited in the construction industry.

Hajsadeghi et al. [9-10] developed a new generation of steel fibres which possesses slip-hardening response in normal concrete (an optimised spirally deformed fibre) in order to advance the adoption of such discontinuous fibres in the structural design of RC members.

Optimised spirally steel fibres [9] are applicable in energy absorption applications such as earthquake resistant structures [11], impact loading [12] and shrinkage control of concrete structures [13]. Besides, the most important feature of this optimised fibre is providing deflection hardening behaviour even in low volume fraction of fibres as it is subject of current research.

This paper presents the flexural characteristics of normal concrete with the incorporation of spirally deformed steel fibre to evaluate its contribution to the load bearing capacity of the basic concrete matrices. To this end, a set of fibrous concrete prisms are tested under flexure, where specimens with commercially available steel fibres (hooked-end and crimped) are included in the testing programme as the reference.

2. EXPERIMENTAL PROGRAM

2. 1. Materials Two different concrete mix designs are used in the programme with the 28-day target mean strengths (f_m) of 35 MPa and 45 MPa [14]. To increase the consistency of fibrous concrete, superplasticizer (High Water Reducing Admixture-HWRA) with the amount of 1 percent of the cement content is added to all mixes [15]. The dry composition per cubic meter of matrices is presented in Table 1. To decrease the risk of fibre balling during the mixing process, coarse aggregate with 95 percent of particles finer than 10 mm is used for the mixes. The fine and coarse aggregates conform to the requirements given in BS EN 12620 [17].

The newly-designed steel fibre with spiral configuration developed by Hajsadeghi et al. [9-10] having material strength (f_u) of 1500 MPa is employed in the experimental programme. To compare the effectiveness of the new fibre in enhancing the flexural characteristics of concrete with its counterparts, two types of commercially available steel fibres (hooked-end and crimped) are incorporated into the study. The ultimate strength (f_u) of the hooked-end and crimped fibres material is 1000 MPa and 1500 MPa, respectively. The geometrical properties of the fibres are shown in Figure 1.

The concrete strength (f_m), fibre volume content (V_f), and fibre type are considered as the experiment parameters, which are listed in Table 2. The steel material is assumed to have a density of 7850 kg/m^3 for calculating the required amount of fibres for the various volume fractions.

The concrete workability is assessed using the slump cone test [13]. The slump of all concrete batches with their corresponding I.D. is listed in Table 3. The mixes are labelled such that the specifications of each mix can be identified from the mix I.D. For instance, the label "P-35" represents the plain concrete (non-fibrous concrete) with target mean cylinder strength of 35 MPa; also, the label "N-0.5-45" indicates that the mix is reinforced with the new fibre at the fibre content of 0.5% having a target mean strength of 45 MPa.

To ensure proper mixing, ACI PRC-544.3-08 [15] methodology was taken into account. Moreover, a particular centrifuge mixer type was utilized (Figure 2a) to guarantee a uniform and homogenous mixture. Some photos were taken during the mixing procedure, which revealed uniform mixing (Figure 2b).

ACI 544.4R-18 [19] recommendations was considered in the design and selection of fibre dosage.

TABLE 1. Concrete mix design

Target strength (MPa)	Cement [1] (kg)	Water (kg)	Super plasticizer [2] (kg)	Fine aggregate [3] (kg)	Coarse aggregate [3] (kg)
f_m = 35	350.0	188.3	3.5	880	988
f_m = 45	423.1	188.3	4.25	802	993

[1] 42.5 type Portland cement [16]

[2] Sika ViscoCrete® 1200 series

[3] Saturated Surface-Dry (SSD) condition

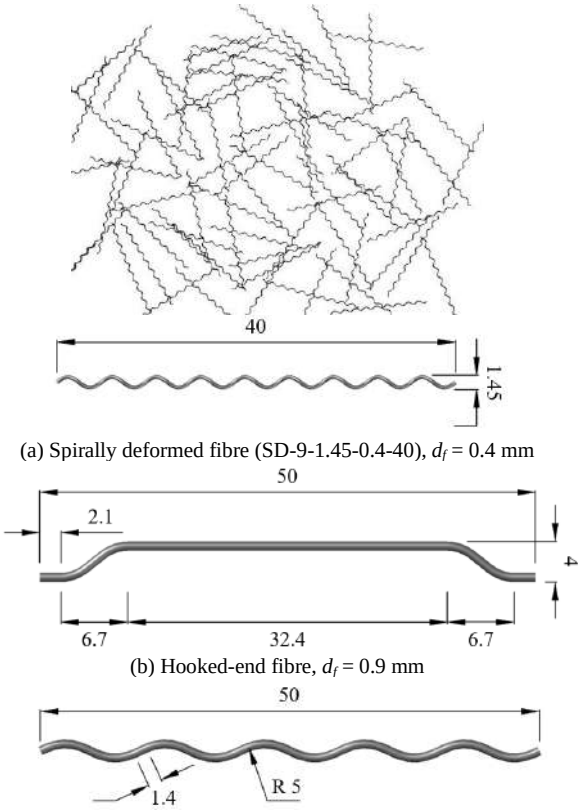

(a) Spirally deformed fibre (SD-9-1.45-0.4-40), d_f = 0.4 mm

(b) Hooked-end fibre, d_f = 0.9 mm

(c) Crimped fibre, d_f = 0.9 mm

Figure 1. Steel fibres (dimensions are in mm)

TABLE 2. Experimental parameters

f_m (MPa)	V_f (%)	Fibre type
35, 45	0, 0.2, 0.35, 0.5, 0.65	Spirally deformed
35	0.5	Hooked-end, Crimped

TABLE 3. Slump cone test results

Concrete Type		Mix ID	V_f (%)	f_m (MPa)	Slump (mm)
Plain		P-35	-	35	198
		P-45	-	45	136
Fibrous	Newly-designed	N-0.2-35	0.2	35	168
		N-0.2-45		45	112
		N-0.35-35	0.35	35	139
		N-0.35-45		45	91
		N-0.5-35	0.5	35	99
		N-0.5-45		45	63
		N-0.65-35	0.65	35	79
	Hooked-end	H-0.5-35	0.5	35	121
	Crimped	C-0.5-35	0.5	35	77

(a) Centrifuge mixer (inside view)

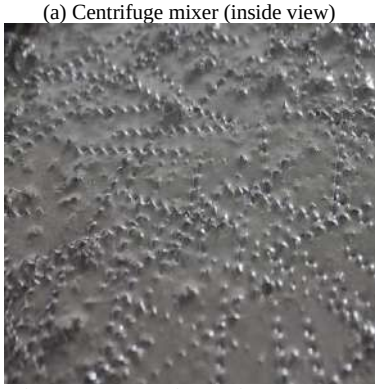

(b) Uniform distribution fibres after mixing procedure

Figure 2. Mixer and a sample of a mixed matrix

Furthermore, the optimised spiral fibre has been proposed recently by authors for the current paper and the design procedure is in progress by authors.

2. 2. Test Setup ASTM C1609/C1609M - 12 [20] is adopted to conduct the four-point loading flexure tests to characterize the flexural performance of FRC specimens modulus of rupture (f_r), residual flexural strengths, and toughness. The dimensions of the specimens, respectively width, height, and length, are 150 mm, 150 mm, 550 mm with a span length of 450 mm.

The test was performed using a 300 kN capacity closed-loop controlled universal testing machine (UTM). The loading arrangement and instrumentation setup of the flexure test are shown in Figure 3. As required in the standard [20], the clear span between the supports is 450 mm, and the distance between the four loading points is 150 mm (third-point loading). A rectangular jig that surrounds the specimen and is clamped to it at mid-depth directly over the supports, i.e. yoke, is employed to measure the net mid-span deflection (see Figure 3). Two linear variable differential transducers (LVDTs) with a total stroke of ±15 mm and precision of ±0.001 mm are mounted on the LVDT slots of the yoke to measure the mid-span deflections on each vertical face of the specimen. The average value is considered as the mid-span net deflection of the specimen.

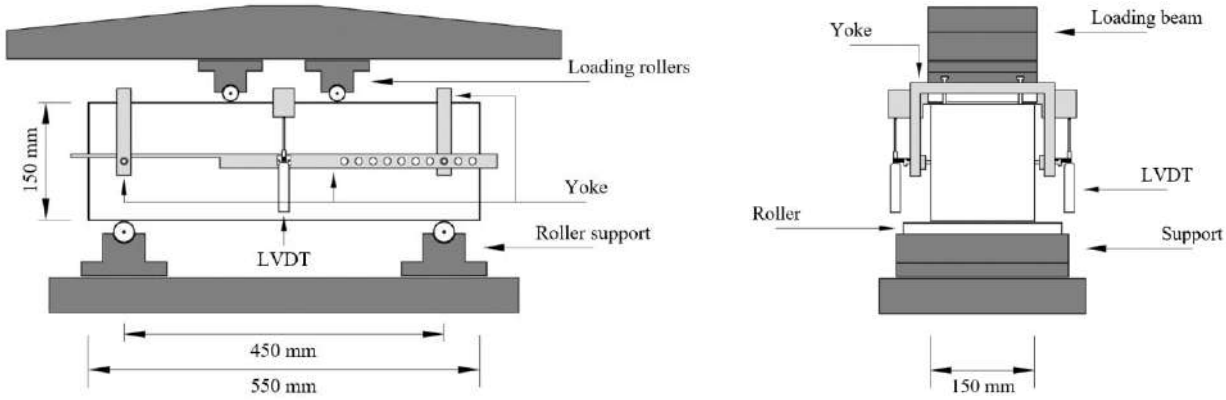

(a) Front view (b) Side view

Figure 3. Flexural test setup

The testing machine was set so that the net deflection of the specimens increases at the constant rate of 0.1 mm/min. For net deflection beyond 0.6 mm, the loading rate increases to 0.3 mm/min with an increment of 0.05 mm/min. During the test, the testing data, including load and displacement from the UTM and deflection from two LVDTs are collected with the frequency of 3 Hz. The test continues at least up to 12 mm net deflection for all the specimens. After completion, the specimens were removed from the machine, and the cross-sectional dimensions adjacent to the failure crack are measured [14].

2. 3. Experimental Results The average results of the compression tests of the cylinder and cube concrete specimens on the 28th day after casting are summarised in Table 4, in which the variation of each test set is also provided.

TABLE 4. Compression test results

Mix ID	f_{ck} * (MPa)	$f_{ck,\,cube}$ * (MPa)
P-35	35.9±1.9	45.9±1.8
P-45	46.0±2.2	55.9±2.4
N-0.2-35	35.3±2.1	45.8±2.3
N-0.2-45	46.5±1.6	55.6±2.5
N-0.35-35	35.4±0.7	44.7±0.3
N-0.35-45	46.0±1.7	55.2±3.4
N-0.5-35	36.7±0.8	47.5±1.6
N-0.5-45	47.3±0.6	58.2±1.0
N-0.65-35	34.2±1.1	44.5±0.6
H-0.5-35	35.7±0.5	43.9±0.5
C-0.5-35	35.1±1.0	44.6±0.4

* Average results based on three specimens

As evident from the table, the mix designs yield compressive strengths close to the corresponding target values. Besides, as anticipated, the inclusion of fibres does not influence the compressive strength. However, since the concrete batches are made separately, the variation in the peak strengths is reasonable due to slight differences in the moisture content of the aggregates and the mixing and casting process.

The flexure tests are conducted in accordance with ASTM C1609/C1609M - 12 [20]. In Figure 4, a concrete prism reinforced with new steel fibre under flexural testing is shown. For each batch of concrete, three specimens were prepared and tested on the 28th day after casting, where the average results are considered as the FRC behaviours.

The load-deflection curves of the FRC specimens with the new fibre and existing fibres on the market (hooked-end and crimped) under four-point bending are shown in Figures 5 and 6, respectively. The results of flexure tests are summarised in Table 5.

As shown in Figures 5 and 6, the flexure response of FRC specimens are characterized by a linear part up to the elastic limit load (pre-cracking stage before fibres

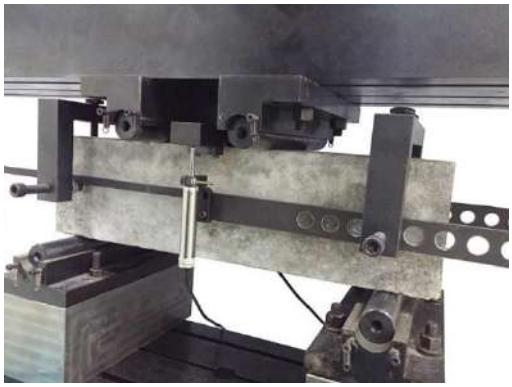

Figure 4. Fibrous concrete prism under flexural testing

contributions are activated), followed by a sudden load decay to a specific load which depending on the fibre type and volume content continues with a different trend (deflection-hardening or deflection-softening). The sudden load decay in the responses could be attributed to the low fibre volume contents used in this research so that wider cracks are needed to activate an adequate overall fibre bridging action. As evident from Figure 5 and Table 5, increasing the fibre content improves the flexure performance of FRC specimens with the new fibre by decreasing the severity of the sudden load drop as well as enhancing the post-cracking response.

Besides, the specimens with the new fibre (f_{ck} = 35 MPa / V_f = 0.5%) possess a relatively more severe sudden load decay compared with those containing hooked-end and crimped steel fibres (40.9% vs. 25.8% load decay, on average). This is likely attributable to the higher initial pullout stiffness of these commercially available fibres than the new steel fibre (spirally deformed fibre) [9-10].

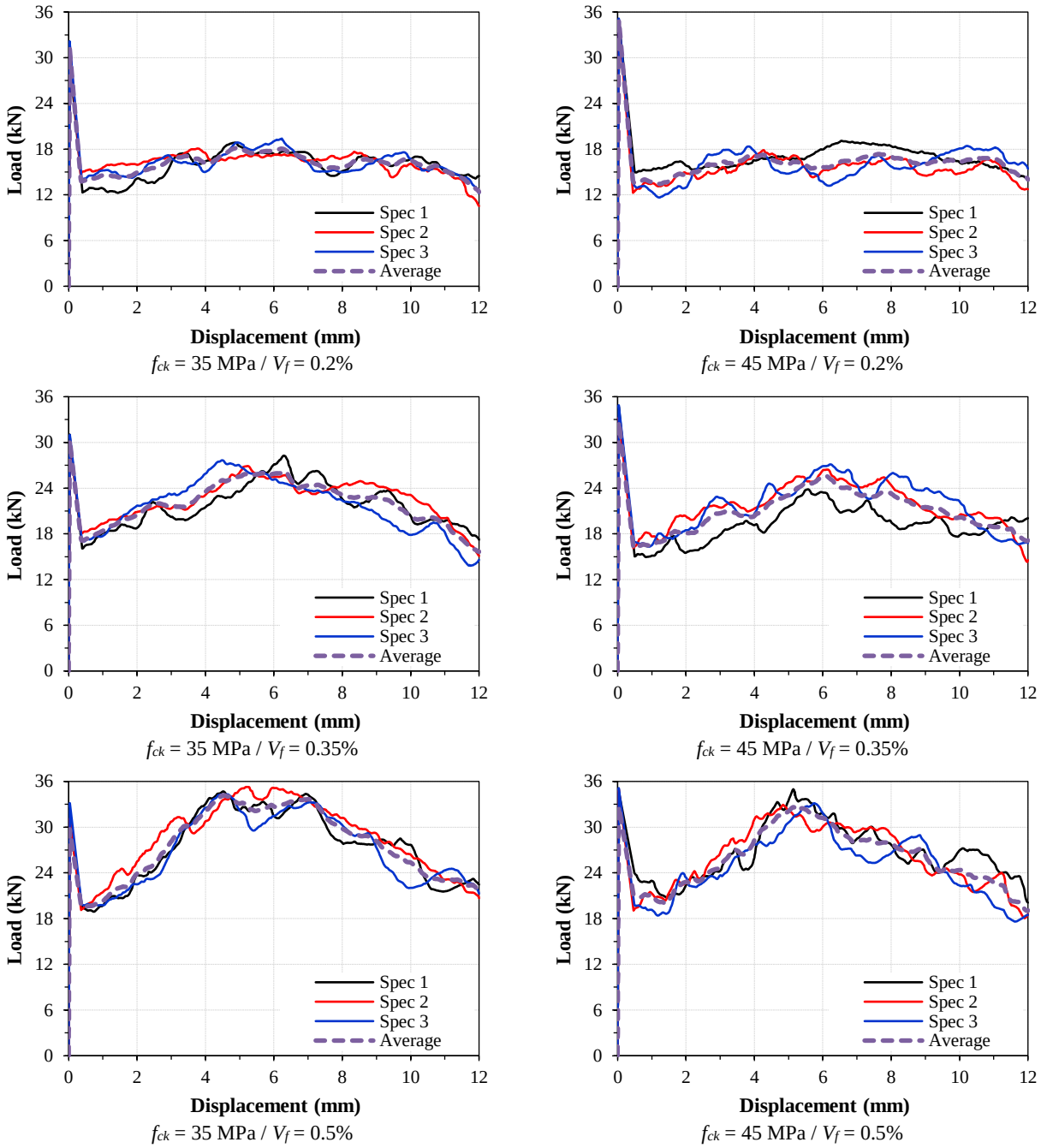

Figure 4. Individual and average flexural responses of FRC containing the new fibre. (Continued on the next page)

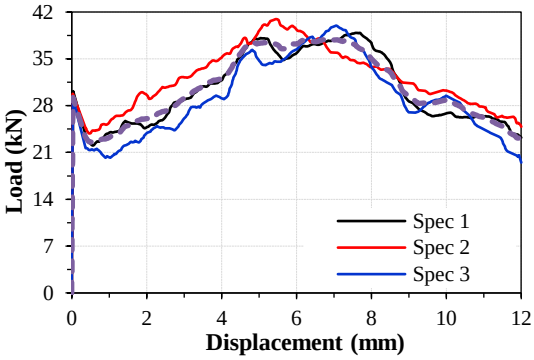

f_{ck} = 35 MPa / V_f = 0.65%

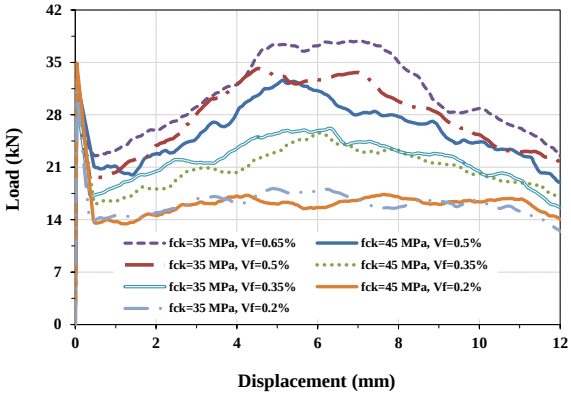

Comparison of average responses

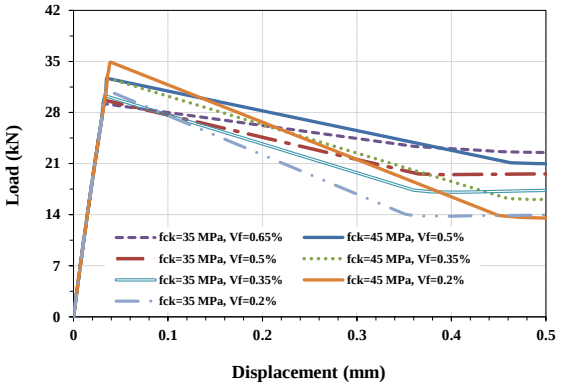

Comparison of average responses in primary displacement

Figure 5. Individual and average flexural responses of FRC containing the new fibre (Continue from previous page)

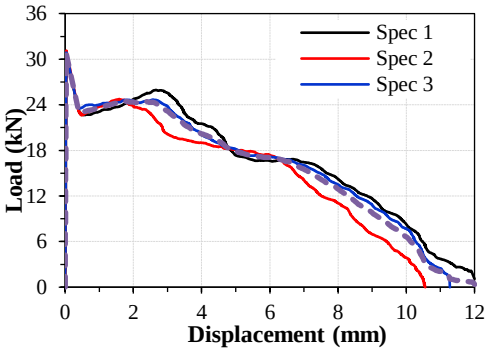

f_{ck} = 35 MPa / V_f = 0.5% / Hooked-end

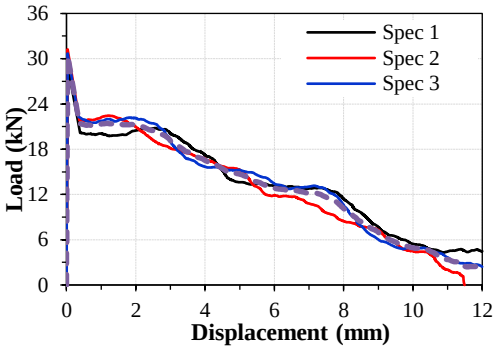

f_{ck} = 35 MPa / V_f = 0.5% / Crimped

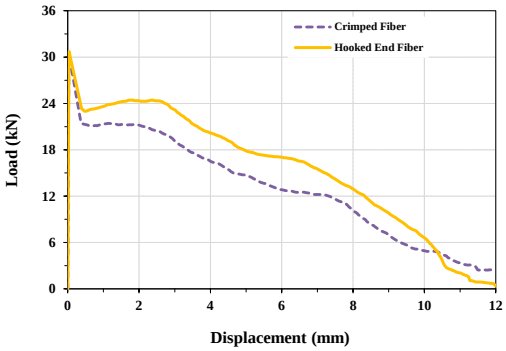

Comparison of average responses

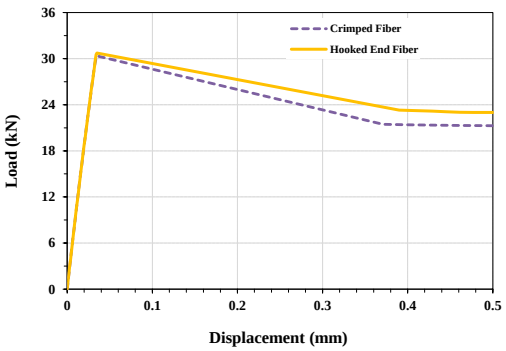

Comparison of average responses in primary displacement

Figure 6. Individual and average flexural responses of FRC containing commercially available fibres

TABLE 5. Flexural tests results

ID (Mix / Specimen)	f_r (MPa)	$P_{e,p}$ (kN)	$P_{p,pc}$ (kN)	$f_{45}^{D\ 1}$ (MPa)	$T_{45}^{D\ 2}$ (kN.mm)	Response
P-35	4.06±0.11	30.42	-	-	-	-
P-45	4.56±0.18	34.17	-	-	-	-
N-0.2-35	4.15±0.19	31.14	18.17	2.20	165.4	Softening
N-0.2-45	4.65±0.04	34.90	17.37	2.18	163.5	Softening
N-0.35-35	4.09±0.07	30.29	26.20	2.72	228.0	Softening
N-0.35-45	4.57±0.14	32.75	25.57	2.69	214.8	Softening
N-0.5-35	4.21±0.21	29.72	34.20	3.38	286.0	**Hardening**
N-0.5-45	4.65±0.05	32.69	32.63	3.25	267.5	Softening
N-0.65-35	3.95±0.08	29.21	37.88	3.85	315.6	**Hardening**
H-0.5-35	4.10±0.07	30.74	23.30	0.80	168.8	Softening
C-0.5-35	4.05±0.12	30.36	19.70	0.61	136.6	Softening

[1] Residual strength at net deflection of 10 mm (L/45)

[2] Toughness (area under the load vs. deflection curve from 0 to 10 mm

However, inclusion of 0.5% of the optimised spiral fibre results in the peak post-cracking load ($P_{p,pc}$) greater than the peak elastic load ($P_{e,p}$), i.e. deflection-hardening response [21], as well as superior post-cracking characteristics (higher toughness and residual strengths at various deflections) compared with hooked-end and crimped steel fibres. The results indicate that the new fibre greatly contributes to the load bearing capacity of the specimens which is more pronounced at large deflections e.g. 6 mm deflection.

To better understand differences between the load-deflection response of specimens, a comparative diagram using average responses is provided in Figures 5 and 6.

3 CONCLUSION

The contribution of the optimised spirally deformed steel fibre developed by the authors to the flexural performance of normal concrete specimens was investigated in this paper.

Findings of the experimental programme reveal that contrary to the existing fibres on the market, the newly-designed steel fibre has significantly improved the post-cracking characteristics of fibrous specimens, including the residual strength, especially at more considerable deflections, which is indicative of its effectiveness as structural reinforcement for concrete, contrary to those commercially available on the market. The authors perform another research project that aims to construct industrial facilities to produce a high volume of such fibre. In that way, the production of a high volume of optimised spiral fibres will be possible.

4. REFERENCES

1. Shaikh , F. U. A., Luhar, S., Arel, H. S., Luhar, I., "Performance evaluation of Ultrahigh performance fibre reinforced concrete – A review", ***Construction and Building Materials,*** Vol. 232, (2020), 117152. doi: https://doi.org/10.1016/j.conbuildmat.2019.117152.
2. Teja Prathipati, S. R. R., Rao, C. B. K., Dakshina Murthy, N. R., "Mechanical Behavior of Hybrid Fiber Reinforced High Strength Concrete with Graded Fibers", ***International Jornal of Engineering Transactions B: Applications***, Vol. 33, No. 8, (2020), 1465-1471.
3. Singh, H.,"Steel Fiber reinforced Concrete: Behavior, Modeling and Design", Springer Publication, ISSN 2363-7641, (2017), doi: 10.1007/978-981-10-2507-5.
4. ACI Committee 544, "Report on Fiber Reinforced Concrete (ACI 544.1R-09)", Farmington Hills, Mich., American Concrete Institute, (2009).
5. Aljazaeri, Z. R., Al-Jaberi, Z., "Numerical Study on Flexural Behavior of Concrete Beams Strengthened with Fiber Reinforced Cementitious Matrix Considering Different Concrete Compressive Strength and Steel Reinforcement Ratio", ***International Jornal of Engineering Transactions A: Basics***, Vol. 34, No. 04, (2021) 793-802.
6. Richardson, A. E., Coventry. K., Landless. S., "Synthetic and steel fibres in concrete with regard to equal toughness", ***Structural Survey***, Vol. 28, No. 5, (2010), 355-369, doi: https://doi.org/10.1108/02630801011089155.
7. Wille, K., Naaman, A. E., "Effect of Ultra-High-Performance Concrete on Pullout Behavior of High-Strength Brass-Coated Straight Steel Fibers", ***ACI Materials Journal***, Vol. 110, No. 4, (2013), 451-462.
8. Lin, W. J. V., Quek, S. T., "Tensile Behavior of Twisted Steel Fiber Reinforced Cementitious Composite", Proceedings of the 32nd Conference on Our World in Concrete & Structures. Singapore, (2007).
9. Hajsadeghi, M., Chin, C. S., "Geometrical and material optimisation of deformed steel fibres: Spirally deformed fibres", ***Engineering Structures***, Vol. 199, No. 15, (2019), 109636. doi:

https://doi.org/10.1016/j.engstruct.2019.109636.

10. Hajsadeghi, M., Chin, C. S., Jones, S., "Development of a Generic Three-Dimensional Finite Element Fibre Pullout Model", ***Construction and Building Materials***, Vol. 185, No. 10, (2018), 354-368, doi: https://doi.org/10.1016/j.conbuildmat.2018.07.069.
11. Zhang, J., Liu, J., Li, X., Cao, W., "Seismic behavior of steel fiber-reinforced high-strength concrete mid-rise shear walls with high-strength steel rebar", ***Journal of Building Engineering,*** Vol. 42, (2021), 102462. doi: https://doi.org/10.1016/j.jobe.2021.102462.
12. Yoo, D. Y., Banthia, N., "Impact resistance of fiber-reinforced concrete – A review", ***Cement and Concrete Composites*** , Vol. 104, (2019). doi: https://doi.org/10.1016/j.cemconcomp.2019.103389
13. Mashimo, H., Isago, N., Kitani, T., Endou, T., "Effect of fiber reinforced concrete on shrinkage crack of tunnel lining", ***Tunnelling and Underground Space Technology***, Vol. 21, No. 3-4, (2006). doi: https://doi.org/10.1016/j.tust.2005.12.194.
14. Mehta, P. K., Monteiro, P. J. M., "Concrete Microstructure, Properties, and Materials", McGraw-Hill Publication, 4th Ed., ISBN: 978-0-07-179788-7, (2014).
15. ACI Committee 544, "Guide for Specifying, Proportioning, and Production of Fiber-Reinforced Concrete (ACI 544.3R-08)", Farmington Hills, Mich., American Concrete Institute, (2008).
16. GB 175, "Common Portland Cement", Chinese Standard Publication, (2007).
17. BS EN 12620, "Aggregates for concrete", British Standards (BS) Publication, (2013).
18. ASTM C143/C143M - 15a, "Standard Test Method for Slump of Hydraulic-Cement Concrete", West Conshohocken, PA, American Society for Testing and Materials (ASTM) International, (2015).
19. ACI Committee 544, "Guide to Design with Fiber-Reinforced Concrete (ACI 544.4R-18)", Farmington Hills, Mich., American Concrete Institute, (2018).
20. ASTM C1609/C1609M – 12, "Standard Test Method for Flexural Performance of Fiber Reinforced Concrete (Using Beam with Third-Point Loading)", West Conshohocken, PA, American Society for Testing and Materials (ASTM) International, (2012).
21. Naaman, A.E., "Engineered Steel Fibers with Optimal Properties for Reinforcement of Cement Composites", ***Journal of Advanced Concrete Technology***, Vol. 1, No. 3, (2003), 241-252.

Persian Abstract

چکیده

این مقاله به مطالعه آزمایشگاهی رفتار خمشی بتن مسلح به الیاف مارپیچ فولادی پرداخته است. این الیاف توسط نویسندگان مقاله حاضر بهینه و معرفی شده است. با هدف مقایسه، نمونه های بتنی ساخته شده با الیاف فولادی متداول (الیاف قلاب دار و الیاف موجدار) نیز مورد آزمایش قرار گرفته است. نتایج تحقیق نشان می دهد الیاف فولادی مارپیچ به طور قابل ملاحظه ای نسبت به الیاف متداول فولادی، مشخصات خمشی را بهبود می دهد. پاسخ سخت شدگی کرنش حتی در بازشدگی های قابل ملاحظه ترک ها و با به کارگیری درصدهای نسبتا پایین الیاف حاصل شده است. در نتیجه کامپوزیت های سیمانی مسلح به الیاف مارپیچ به عنوان یک مصالح سازه ای با عملکرد بالا قابل معرفی می باشند.

IJE TRANSACTIONS C: Aspects Vol. 34, No. 6, (June 2021) 1398-1406

International Journal of Engineering

Journal Homepage: www.ije.ir

A Novel Lightweight Phase-changing Cooling Roof Tile

E. Arunraj[a], G. Hemalatha[a], E. Noroozinejad Farsangi*[b]

[a] *Karunya Institute of Technology and Sciences, India*
[b] *Faculty of Civil and Surveying Engineering, Graduate University of Advanced Technology, Kerman, Iran*

PAPER INFO

Paper history:
Received 19 March 2021
Received in revised form 16 April 2021
Accepted 17 April 2021

Keywords:
Cooling Roof Tile
Metakaolin
Phase Changing Material
Lightweight
Expanded Polystyrene Sheet

ABSTRACT

Roof tiles are the most common roof coverings in Indian buildings, especially in traditional residential buildings. Given the important role of roofing characteristics in building energy efficiency and indoor thermal comfort conditions, innovative solutions to improve the thermal energy performance of this diffused roofing element have become a key research issue. In this perspective, cool roofing applications represent an effective solution to this objective. The present work deals with the analysis of an innovative cooling roof tile manufactured using a combination of Metakaolin with different percentages, EPS, sodium silicate, and coating material. The experimental work was carried out during day and night. The thermal performance of cooling roof tiles was assessed in terms of the open-air temperature compared to the thermal performance of ordinary roofing tiles. The report discovered that using revolutionary cool roofs greatly increased thermal comfort during the daytime, and preserved thermal comfort during the night. The innovative cool roof tile is cheaper, easier to implement, and less expensive compared to other roofing technologies. The study revealed that the roof's exterior and interior surface temperature reduced about 8°C and 12°C, respectively during day time, while the roof's exterior and interior surface temperature maintain atmospheric temperature during nighttime. The compressive and transverse breaking strength was increasing about 9.1% and 39.6%.

***doi**: 10.5829/ije.2021.34.06c.02*

1. INTRODUCTION

The phenomenon of urban heat islands has caused architects, engineers, and contractors in the construction sector to employ passive design, construction, and building specification strategies. These passive design strategies involve making use of the environment in which the building is located to reduce heating or cooling. These strategies shall include; considerations of building orientation, shape, envelope; (the choice of materials), and landscape. Increasing the demand for shelter and an increase in population brought about (which is still growing), the architects, the builders, and the contractors have been forced to be more careful about the specification of the material selection of the elements used in the building roof. This is a passive design strategy for surface mitigation temperature of buildings in hot climates Various factors influence how much energy a building consumes, such as location, purpose, and the intended use. The thermal properties of the materials used for the exterior walls and roofs may have a major impact on the surface temperature and, in turn, on the amount of heat flowing through the surface of the building. A cool building surface (walls and/or roof) uses a coating with high thermal emissivity and solar reflectance properties to lower the temperature. Solar thermal load of a building reduces its energy requirements for cooling [1]. A number of experimental and modelling studies have been published which compare the energy-efficient building benefits of cooling roofing techniques [2-4]. Over the past decades, the advantages of cooling roof technologies have been thoroughly studied throughout the world [5-10]. A number of factors influence the thermal performance of materials, but the main determinants are solar reflectance and thermal emissivity. Other surface properties include the type of coating used on the surface of the material, the thickness and texture of the coating, the durability of the coating when exposed to weather elements [11].

*Corresponding Author Institutional Email: noroozinejad@kgut.ac.ir (E. Noroozinejad Farsangi)

Please cite this article as: E. Arunraj, G. Hemalatha, E. Noroozinejad Farsangi, A Novel Lightweight Phase-changing Cooling Roof Tile, International Journal of Engineering, Transactions C: Aspects Vol. 34, No. 6, (2021) 1398-1406

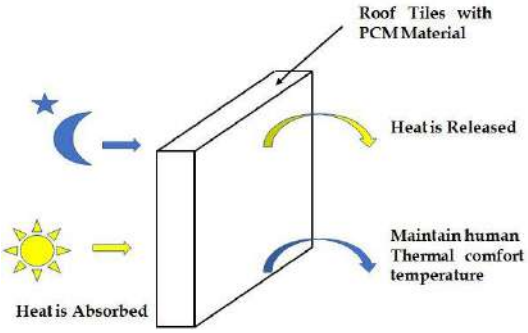

Figure 1. characteristic of PCM material

Cool roofs are a recognized passive cooling technology designed to reduce the energy consumption of buildings for cooling and to mitigate the effects of urban heat on islands [12]. High solar reflectivity and high thermal emissivity make up the cool roof. These roofs are typically light in colour and absorb less radiation, and effective at reducing the heat load on a building [13]. The temperature reached 50.6 degrees Celsius due to climate change in India, 2019 during daytime and average nighttime temperatures of 2–8 °C (36–46 °F). Low temperature can fall below freezing in the Punjab plains, falling to around −3 °C (27 °F) in Amritsar. So cool roof creates cooler the building it will affect the living people. To overcome this issue the phase change material (PCM) concept is introduced. Prior to 1980, PCMs were integrated into building materials for thermal energy storage applications and a great deal of attention was paid to the work concerned with the achievement and assessment of the application of PCMs in gypsum wallboards, plasterboards, textured finishes, etc. [10, 14-20]. The PCM has special characteristics it maintains the heating and cooling functions of the building and creates pleasant human comfort temperature [21]. The sodium silicate is used as the PCM material. Sodium Silicate is a colourless compound of oxides of sodium and silica. It has a phase-changing property [22]. Figure 1 shows the characteristic of PCM material.

In this research, a new innovative reflective roofing tile was developed using metakaolin, Expanded polystyrene sheet (EPS), and a PCM with a reflective coating material. The performance of roof tiles is measured in terms of thermal emissions, which are mainly determined by the cooling capacity of these materials. The thermal performance of the roof tile is measured during daytime and night-time at the top and bottom surface of the tile.

Metakaolin is widely used in mortar and concrete as pozzolanic material; it has a significant impact on improving the mechanical and durability properties of mortar and concrete [23-26]. Because of its highly amorphous structure, is known as the most reactive material for the geopolymerization process. It is obtained by heating kaolinite, a mineral of clay, at a high temperature and by rapid cooling afterward [27]. Metakaolin is white in colour as the heat absorption of construction material depends on the reflection of light on the surface, while whiter construction tends to remain cooler than darker materials, which provide a cooling property in concrete. Since the cost is higher in the materials than cement, the proportions are tested (15, 20 and 25%).

Expanded polystyrene sheet (EPS) is a versatile, low-weight substance with excellent energy absorption characteristics. EPS is a closed-cell polymer that does not readily retain vapor, and when exposed to sustained immersion of water, EPS can still maintain its form, scale, composition and physical appearance and maintain 80% of its thermal value. The production of EPS does not contain ozone-depleting gasses and does not use chlorofluorocarbons (CFCs). That, in addition, plays a constructive position in the elimination of carbon dioxide pollution and the impact in global warming. The EPS is a recycled plastic waste, that reduces the cost of cement mortar and saves the landfilling problem of plastic waste, which also acts as an insulation coating. This Expanded polystyrene type is fulfilling IPC Code: C04B26/02. Also using of EPS leads to a remarkable reduction in thermal conductivity [28, 29]. Hence using of EPS in tiles leads to reducing temperature.

Reflective coatings and light colour are used as an energy-saving measure for buildings, reducing the incoming solar radiation into the shell of the house [8, 22]. Light reflective paint for concrete is aimed at creating a retro-reflective impact on concrete and cement substrates that are heavily influenced by weather patterns. Reflective paint is immune to all sorts of natural environmental effects: heat, dust, wind, etc. Reflective material paint is scratch-resistant and will never crack. It also reduces the heat so, saves energy. It leads to a reduced requirement for air conditioning hence reduced electricity. It is highly reflective in the near infra-red (non-visible) portion of the solar spectrum, thus keeping interiors cool during hot summer months.

2. MATERIALS

All the materials meet up the Indian standard specification. The fine aggregate used in the mortar mix conforms to Zone-II as per IS 383-1970 [30] has a fineness modulus of 2.34. The cement utilized over the experiments is Portland Pozzolana Cement (PPC) conforming to IS (IS:269/ IS 12269: 2013) [31]. EPS sheets were obtained from the plastic waste factory, India. A type of commercially available rectangular EPS sheets which was ground in grinding machine to a maximum sieve size of 1.0 mm. The properties of various materials used in the experimental work are reported in Tables 1-3.

TABLE 1. Physical properties of Portland pozzolana cement

SI No	Characteristics	Test values	Value specified by IS:1489 (Part 1)-1991
1	Standard consistency (%)	32	-
2	Fineness of cement as retained on 90 lm sieve (%)	0.70	Maximum 10%
3	Setting times (minutes) Initial	40 minutes	Minimum 30 minutes
4	Setting times (minutes) Final	280 minutes	Maximum 600 minutes
5	7 days Compressive strength (MPa)	23.5	Minimum 22.0
6	28 days Compressive strength (MPa)	34.5	Minimum 33.0

TABLE 2. Physical properties of fine aggregate

SI No	Characteristics	Test Values
1	Specific gravity (oven-dry basis)	2.69
2	Bulk density loose (kg/l)	1.35
3	Fineness modulus	2.30
4	Water absorption (%)	2.39
5	Grading zone	II

TABLE 3. Physical and mechanical properties of EPS

SI No	Property	Average value
1	Compressive strength	0.09 MPa
2	Density	13 kg/m^3
3	Flexural strength	0.21 MPa
4	Water Vapor permeability	1.4 Perm-cm
5	Water Absorption	4 % by vol.

As cement provide heating to the tile, an alternate material metakaolin (Chinese clay) was used in different ratio, which was sieved through 2 μm sieve and weighed. The specific gravity of highly reactive metakaolin is 2.5. The white colour provides a cooling effect. To emphasis, a phase changing property to the tile an optimal 1% (of total cement) sodium silicate was added to the mix. The workability of fresh metakaolin aggregate cement mortar was determined at 20°C by the finger-touching method prescribed in Choi and Ohama.

Here metakaolin ratios, 15% (control sample), 20%, and 25% mix proportion by volume were prepared. EPS beads content for the mixtures were kept constant at 0.0001m^3. The interfacial zone between cement paste and fine aggregate plays a critical role in determining the mechanical properties of mortar. For this reason, EPS beads were wetted finally with a part of the mixing water after mixing the remaining materials. The pre-wetting of lightweight aggregate will critically affect the strength of its mortar. A technique similar to cement-wrapping was applied on the EPS beads. The concrete mixes were prepared in a laboratory counter current mixer for a total of 5 min. Precautions were taken to ensure homogeneity and full compaction. The fresh mortar was then poured into molds and compacted by hand and leveled using a vibration table.

3. DESCRIPTION OF THE TEST SPECIMENS

In this research work, three different types of tiles were casted using different percentages of metakaolin. The other materials like sodium silicate, EPS, crack shield coat and Flexi cool paint is constant in all the tiles. These three innovative cool roof tiles are compared with ordinary roof tiles. Different cool roof tile and ordinary tile is displayed in Figure 2. To cast the tile, a mold was designed and created from a welding yard. The mold consisted of a base plate for grip and it has two shoe levers that help the mold to open into two L-shaped brackets which enable to get crack-free edges of the tile. The base and the sidewalls of the mold were greased with waste oil for easy removal of hardened tile.

For each mixture, three sets of six samples of 70.6×70.6×70.6 mm cubes and three sets of four samples of 250×250×20 mm tiles were prepared. The specimens were cured two days under wet gunny bags initially and then removed from the molds and cured in lime saturated water up to the date of testing. Two days before testing the tiles and cubes were coated with two materials. Initially to fill the voids and to provide a well-finished surface, an apex Ultima Smart care crack shield was applied. To achieve a reflective surface 2 coating of excel flexicool coat paint was painted using a brush. The mix design was done for cement mortar 1:3, from the mix design different proportion of material was calculated. Table 4 displays the Quantity of material required for one tile with different percentages of metakaolin.

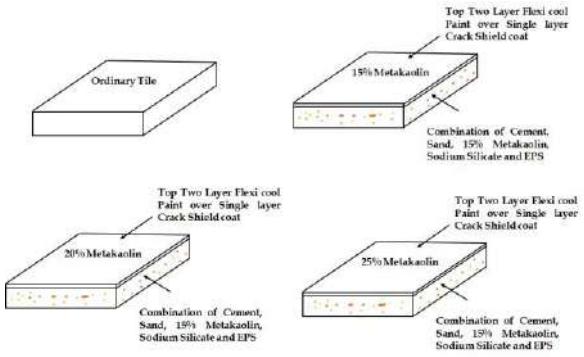

Figure 2. Cool roof tile specimens

TABLE 4. Quantity of material required for one tile with different percentage of metakaolin

S.No	Materials used	Quantity required for one Tile in kg (15%)	Quantity required for one Tile in kg (20%)	Quantity required for one Tile in kg (25%)
1	Cement	0.39	0.36	0.34
2	M sand	1.53	1.44	1.35
3	Metakaolin	0.34	0.45	0.57
4	Sodium silicate	3.8g	3.6g	3.4g
5	EPS	$0.0001m^3$	$0.0001m^3$	$0.0001m^3$
6	Crackshield	0.010	0.010	0.010
7	Flexicool paint	10ml	10ml	10ml

4. EXPERIMENTAL OBSERVATION

The experimental investigation was carried out for all four different tile specimens in the form of weight, temperature, strength, and durability.

4. 1. Weight Classification Test The weight classification of the tiles as per ASTM C1492 – 03 [33] is given in Table 5. It indicates the weight variation for the roof tiles to be classified as normal, medium, or lightweight.

4. 2. Temperature Test The temperature test was carried out on March 17, 2020 in Coimbatore, Tamilnadu, India. The rooftop surface temperature exceeds surrounding ambient air and indoor attic temperatures during hot summer days. To conduct a thermal performance study of white cement tiles four models of flat model rooftops were evaluated. The test models are shown in Figure 3.

Outdoor and indoor air temperatures near surfaces were measured using a digital thermocouple probe (model HTC IRX-64 K type range -50 to 1370˚C) and digital LCD display thermometer (model) 2040W as shown in Figure 4. The temperature was measured in two intervals as day and night for checking the phase changing property of roof tile.

Temperature probes were direct under sun and night when taking measurements. The temperatures measured

TABLE 5. Weight Classification (ASTM C1492-03)

Weight classification	Oven dry weight(lb/ft^3)
normal	greater than 125
medium	105 to 125
lightweight	less than 105

Figure 3. Test models

Figure 4. Thermometer k-type

outside and inside of the tile shown in Figure 5. At every hour from 9.00 A.M. to 7.00 P.M. Indoor and outdoor temperature during the daytime are displayed in Table 6.

During night time the temperatures were measured outside and inside of the tile at every hour from 12.00 A.M. to 4.00 A.M. Inside and outside temperature during night time are displayed in Table 7.

4. 3. Strength and Durability Test The compressive, transverse breaking strength was carried

Figure 5. Temperature testing inside and outside of tile

TABLE 6. Day time temperature comparison

Morning time	Side	15% MT (˚C)	20% MT (˚C)	25% MT (˚C)	Ordinary Tile (˚C)
09:0 0am	in	28.5	28.1	28.0	30.5
	out	27.6	27.0	27.0	37.0
10:00 am	in	32.0	31.2	31.0	34.0
	out	30.7	29.6	29.5	41.5
11:00 am	in	35.5	34.5	34.1	38.5
	out	33.7	32.7	32.5	45.2
12:00 pm	in	36.9	36.1	35.8	44.2
	out	35.1	34.8	34.7	46.6
01:00 pm	in	37.0	36.2	35.9	44.0
	out	35.3	34.8	34.8	46.2
02:00 pm	in	37.1	36.3	36.0	44.1
	out	35.6	35.0	34.9	46.3
03:00 pm	in	36.8	36.0	35.7	44.1
	out	35.0	34.7	34.5	46.4
04:00 pm	in	35.4	34.4	34.0	38.3
	out	33.6	32.6	32.4	43.0
05:00pm	in	35.2	34.0	33.8	38.0
	out	33.3	32.1	32.1	41.0
06:00pm	in	28.8	28.3	28.1	31.2
	out	27.6	27.2	27.3	35.0
07:00pm	in	27.9	27.6	27.5	30.0
	out	27.0	26.8	26.1	31.3

TABLE 7. Night time temperature comparison

Night time	Side	15% MT (°C)	20% MT (°C)	25% MT (°C)	Ordinary Tile (°C)
12:00 am	in	24.6	24.1	24.0	23.4
	out	24.2	23.9	23.7	26.1
01:00 am	in	24.4	24.0	23.9	23.2
	out	24.0	23.7	23.5	25.7
02:00 am	in	24.0	23.6	23.5	23.8
	out	23.8	23.4	23.2	25.2
03:00 am	in	23.6	23.1	23.1	22.9
	out	23.3	22.8	22.7	24.1
04:00 am	in	24.6	24.1	24.0	23.2
	out	24.1	23.7	23.5	25.1

out to find the strength of the specimen, and the impact strength test was carried out to find the durability of the specimen. The compressive test was conducted as per ASTM C270 – 14a [32], and the wet transverse breaking strength was carried out based on the standards 13801 [33] and ASTM 1167-11 [34]. From the experiment compressive strength and transverse breaking were recorded and it is summarized in Tables 8 and 9.

5. RESULT AND DISCUSSION

5. 1. Weight Calculation From the experimental investigation, it was observed that, all the tile specimen comes below the normal criteria. But an increase in the amount of metakaolin reduces the weight of the roof tile. The 20% metakaolin tile has more beneficial in terms of weight classification they are under lightweight. The EPS also contributes to lightweight. This is more clearly shown in Table 10.

5. 2. Temperature Test The temperature test was carried out on all the specimens and the temperature was taken inside and outside of the tiles during Day time and Nighttime. All the innovative tile specimens perform well in temperature compared to ordinary tile.

On March 17, 2020 the atmospheric temperatures recorded have been 37°C and 23°C during day and night, respectively. From Table 6 it was observed that the maximum temperature observed by the ordinary tile during the daytime outside of tile is 44.4°C, which is 18.9% higher compared to atmospheric temperature. However, another innovative tile (15% MT, 20% MT, 25% MT) is during the daytime outside temperature is less than one percent variation compared to atmospheric

TABLE 8. Compressive strength of the tile

Testing days	ordinary tile (N/mm^2)	15% MT (N/mm^2)	20% MT (N/mm^2)	25% MT (N/mm^2)
7 Days	10.48	11.09	12.32	11.93
14 Days	14.06	15.11	16.42	15.86
28 Days	22.27	23.1	24.3	23.61

TABLE 9. transverse breaking strength of the tile

Transverse breaking strengt	Ordinary tile (N)	15% MT (N)	20% MT (N)	25% MT (N)
Wet	901	1153	1258	1225

TABLE 10. Comparison of the weight of tiles

Test of tile	Ordinary tile	15% MT	20% MT	25% MT
Dry weight (kg)	2.89	2.68	2.1	2.23
(lb/ft3)	143.58	133.60	104.88	111.12
weight classification	normal	normal	light weight	medium

temperature. Figure 6 shows the temperature variation outside of tile compared with ordinary tile during day time it can be observed that compared to ordinary tile in all the innovative tile the temperature reduced nearly 8°C in Noon (between 12.00 P.M. to 3.00 P.M.). compared to atmospheric temperature, 20% MT and 25% MT specimen maintain the same atmospheric temperature during day time. The maximum temperature observed by the ordinary tile during daytime inside of tile is 46.6°C, which is 22.2% higher compared to atmospheric temperature. However, the tile 15% MT, 20% MT and 25% MT the average of 8°C temperature reduced compare to ordinary tile throughout the daytime from 9.00 A.M. to 5.00 P.M. The specimen 20% MT and 25% MT temperature variation is nearly 12°C compare to ordinary tile. The higher variation of 12.2°C in 20% MT and 12.3°C in 25% MT. Figure 7 shows the temperature variation inside of tile compared with ordinary tile during daytime.

Figure 8 shows the Day time temperature variation inside and outside tile. In the ordinary tile, the temperature increases inside compare to outside. The time between 9.00 A.M. to 11.00 A.M. the temperature increases average of 7°C. In noontime, the temperature variation is average of 2.5°C between 12.00 P.M. to 3.00 P.M. After this hour again the temperature variation becomes very large. however, in 15% MT, 20% MT and 25% MT the temperature is reduced inside compare to outside. Also, the temperature is less than the atmospheric temperature. From this, it is understood that, using metakaolin and reflective Flexi cool paint, the specimens were not absorbing the temperature because of the colour of the tile and reflective material.

To find the phase changing property of tile the temperature is measured during night time between 12.00 A.M. to 4.00 A.M. The atmospheric temperature during night time is on 17th March 2020 is 23°C. The average outside temperature of the ordinary tile during nighttime is 23.5°C. However, the average outside temperature of other tiles during nighttime is 24°C equal to atmospheric temperature. The temperature variation outside of tile for innovative tile compared with ordinary tile is an increased average of 0.5°C during night time. Also, it maintains the atmospheric temperature. Figure 9 shows the temperature variation outside of tile compared with ordinary tile during night time. Also, inside of the tile the average temperature reduced 2°C compared to ordinary tile, Figure 10 displays the temperature variation inside of tile compared with ordinary tile during night time.

The temperature variation of inside and outside tile for 15% MT, 20% MT and 25% MT is less than 0.5°C. Also, it maintains the atmospheric temperature. It shows the phase-changing property of the tile. However, the tile 20% MT is having very little temperature variation compared to inside and outside of the tile. Figure 11 shows the Nighttime temperature variation inside and outside tile. In ordinary tile, the temperature increases inside compare to outside this is due to the ordinary tile absorb the temperature during the day time.

5. 3. Strength And Durability Test From the experimental investigation, it is observed that the compressive strength and transverse breaking strength is

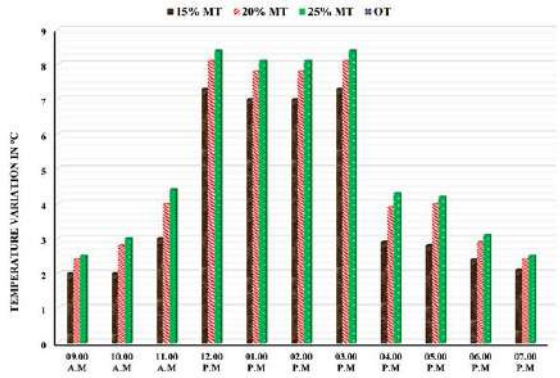

Figure 6. Temperature variation in outside of tile compared with ordinary tile- Day Time

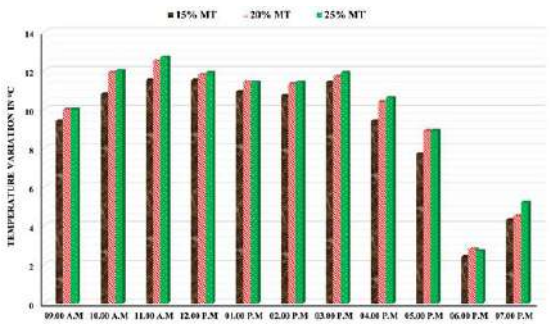

Figure 7. Temperature variation inside of tile compared with ordinary tile- Day Time

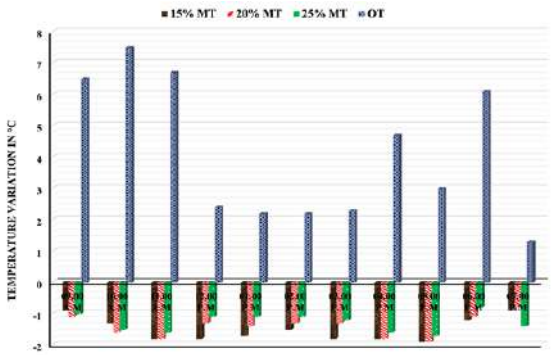

Figure 8. Day time temperature variation inside and outside tile

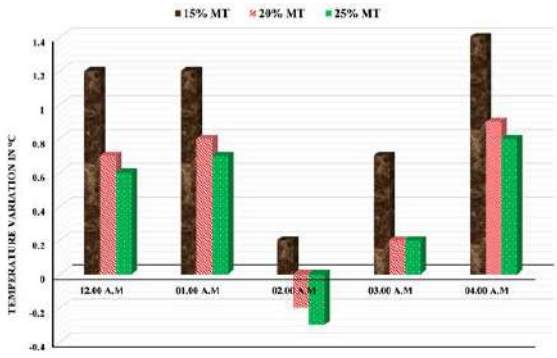

Figure 9. Temperature variation in outside of tile compared with ordinary tile- Nighttime

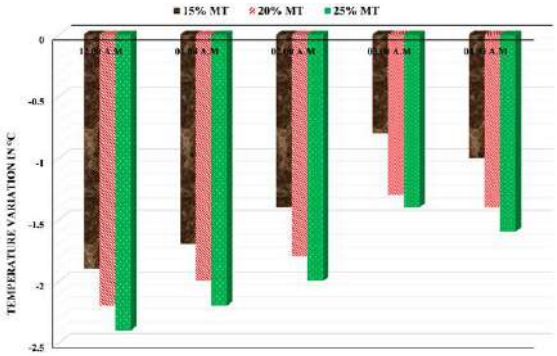

Figure 10. Temperature variation inside of tile compared with ordinary tile Nighttime

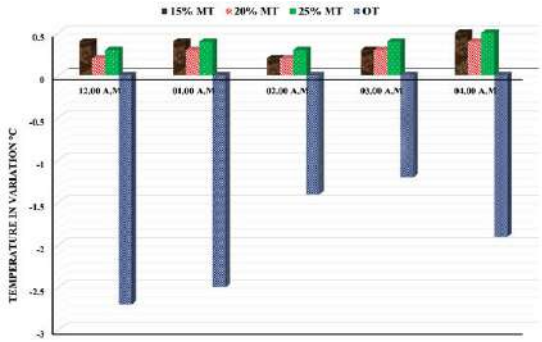

Figure 11. Nighttime temperature variation inside and outside tile

increasing in innovative tiles compared to ordinary tile. The 20% MT specimens were carrying higher compressive strength and transverse breaking strength. Compared to ordinary tile which is 9.1% higher in terms of compressive strength and 39.6% higher in transverse breaking strength. In terms of durability, after carrying out the tests, all the specimens were not breaking and free from defects such as cratering, blistering, superficial microcracking

6. CONCLUSION

In the present work, the cooling roof tile using metakaolin, sodium silicate, and Flexi cool paint has been investigated. four different specimens of tile were casted. In this three-specimen cast using cooling property and one as ordinary tile. Testing parameters considered for the study are temperature and weight. The analysis of the study led to the following conclusions:

- The proposed tile using metakaolin, sodium silicate, and Flexi cool paint specimens performed well in terms of temperature during and night time. According to the weight calculation, 20% MT is considered a lightweight tile.
- The maximum temperature observed by the ordinary tile during the daytime outside of the tile is 44.4°C, which is 18.9% higher compared to atmospheric temperature. However, another innovative tile (15% MT, 20% MT, 25% MT) is during the daytime outside temperature is less than one percent variation compared to atmospheric temperature.
- The temperature variation inside and outside during daytime, the temperature reduced nearly 8°C in Noon (between 12.00 P.M. to 3.00 P.M.) in all the innovative tile compared to ordinary tile. Compared to atmospheric temperature, 20% MT and 25% MT specimens maintain the same atmospheric temperature during day time.
- Maximum temperature observed by the ordinary tile during daytime inside of the tile is 46.6°C, which is 22.2% higher compared to atmospheric temperature. In the innovative tile, the temperature reduced the maximum of 12.2°C in 20% MT and 12.3°C in 25% MT.
- In the ordinary tile the temperature increases inside compare to outside during the daytime. The time between 9.00 A.M. to 11.00 A.M. the temperature increases average of 7°C. In noontime, the temperature variation is average of 2.5°C between 12.00 P.M. to 3.00 P.M. After this hour again the temperature variation becomes very large. however, in 15% MT, 20% MT and 25% MT the temperature is reduced inside compare to outside. Also, the temperature is less than the atmospheric temperature.
- Due to the phase changing property incorporated using sodium silicate. The temperature of the roof tile is higher than the ordinary tile. But cooling wise effective. This property helps in cold regions.
- Experimental measurements showed metakaolin type exhibit more indoor and outdoor temperature differences compared to ordinary roof tile types. The differences were lower in the forenoon, highest at noon, and between above in the afternoon.
- A comparative study was undertaken on three metakaolin type tiles to determine the relative thermal performance of specimen tiles over ordinary roof tiles. 20% and 25% type tiles gave more thermal insulation. Which will thereby lead to less usage of electricity in the buildings.

- The specimen 20% MT has higher strength compared to ordinary tile, which is 9.1% and 39.6% in terms of compressive strength and transverse breaking strength.
- Thus, by adopting the replacement method we can overcome problems such as the plastic waste disposal crisis. The utilization of EPS and its application for the sustainable development of the construction industry is the most efficient solution and also addresses the high-value application of such waste.

7. REFERENCES

1. Kolokotroni, M., Shittu, E., Santos, T., Ramowski, L., Mollard, A., Rowe, K., Wilson, E., de Brito Filho, J.P. and Novieto, D., "Cool roofs: High tech low cost solution for energy efficiency and thermal comfort in low rise low income houses in high solar radiation countries", ***Energy and Buildings***, Vol. 176, (2018), 58-70. doi: 10.1016/j.enbuild.2018.07.005.
2. Pisello, A.L., "State of the art on the development of cool coatings for buildings and cities", ***Solar Energy***, Vol. 144, (2017), 660-680. doi: 10.1016/j.solener.2017.01.068.
3. Akbari, H. and Kolokotsa, D., "Three decades of urban heat islands and mitigation technologies research", ***Energy and Buildings***, Vol. 133, (2016), 834-842. doi: 10.1016/j.enbuild.2016.09.067.
4. Santamouris, M., Synnefa, A. and Karlessi, T., "Using advanced cool materials in the urban built environment to mitigate heat islands and improve thermal comfort conditions", ***Solar Energy***, Vol. 85, No. 12, (2011), 3085-3102. doi: 10.1016/j.solener.2010.12.023.
5. Pisello, A.L., Cotana, F. and Brinchi, L., "On a cool coating for roof clay tiles: Development of the prototype and thermal-energy assessment", ***Energy procedia***, Vol. 45, (2014), 453-462. doi: 10.1016/j.egypro.2014.01.049.
6. Bellia, L., De Falco, F. and Minichiello, F., "Effects of solar shading devices on energy requirements of standalone office buildings for italian climates", ***Applied Thermal Engineering***, Vol. 54, No. 1, (2013), 190-201. doi: 10.1016/j.applthermaleng.2013.01.039.
7. Synnefa, A., Saliari, M. and Santamouris, M., "Experimental and numerical assessment of the impact of increased roof reflectance on a school building in athens", ***Energy and Buildings***, Vol. 55, (2012), 7-15. doi: 10.1016/j.enbuild.2012.01.044.
8. Androutsopoulos, A., Stavrakakis, G. and Damasiotis, M., "Cool roof impacts on a school-building thermal and energy performance in athens, greece", ***Procedia Environmental Sciences***, Vol. 38, (2017), 178-186. doi: 10.1016/j.proenv.2017.03.103.
9. Kolokotsa, D., Maravelaki-Kalaitzaki, P., Papantoniou, S., Vangeloglou, E., Saliari, M., Karlessi, T. and Santamouris, M., "Development and analysis of mineral based coatings for buildings and urban structures", ***Solar Energy***, Vol. 86, No. 5, (2012), 1648-1659. doi: 10.1016/j.solener.2012.02.032.
10. Bhatia, A., Mathur, J. and Garg, V., "Calibrated simulation for estimating energy savings by the use of cool roof in five indian climatic zones", ***Journal of Renewable and Sustainable Energy***, Vol. 3, No. 2, (2011), 023108. doi: 10.1063/1.3582768.
11. Jones, J., Roofing materials for thermal performance and environmental integration of buildings, in Materials for energy efficiency and thermal comfort in buildings. 2010, Elsevier.455-483. doi:10.1533/9781845699277.2.455
12. Pisello, A.L., Rossi, F. and Cotana, F., "Summer and winter effect of innovative cool roof tiles on the dynamic thermal behavior of buildings", ***Energies***, Vol. 7, No. 4, (2014), 2343-2361. doi: 10.3390/en7042343.
13. Akbari, H., "Measured energy savings from the application of reflective roofs in two small non-residential buildings", ***Energy***, Vol. 28, No. 9, (2003), 953-967. doi: 10.1016/s0360-5442(03)00032-x.
14. Faraj, K., Khaled, M., Faraj, J., Hachem, F. and Castelain, C., "A review on phase change materials for thermal energy storage in buildings: Heating and hybrid applications", ***Journal of Energy Storage***, Vol. 33, (2020), 101913. doi: 10.1016/j.est.2020.101913.
15. Wang, X., Zhang, Y., Xiao, W., Zeng, R., Zhang, Q. and Di, H., "Review on thermal performance of phase change energy storage building envelope", ***Chinese Science Bulletin***, Vol. 54, No. 6, (2009), 920-928. doi: 10.1007/s11434-009-0120-8.
16. Khudhair, A.M. and Farid, M.M., "A review on energy conservation in building applications with thermal storage by latent heat using phase change materials", ***Energy Conversion and Management***, Vol. 45, No. 2, (2004), 263-275. doi: 10.1016/s0196-8904(03)00131-6.
17. Pérez-Lombard, L., Ortiz, J. and Pout, C., "A review on buildings energy consumption information", ***Energy and Buildings***, Vol. 40, No. 3, (2008), 394-398. doi: 10.1016/j.enbuild.2007.03.007.
18. Ismail, K. and Castro, J., "Pcm thermal insulation in buildings", ***International Journal of Energy Research***, Vol. 21, No. 14, (1997), 1281-1296.
19. Parameshwaran, R., Kalaiselvam, S., Harikrishnan, S. and Elayaperumal, A., "Sustainable thermal energy storage technologies for buildings: A review", ***Renewable and Sustainable Energy Reviews***, Vol. 16, No. 5, (2012), 2394-2433. doi: 10.1016/j.rser.2012.01.058.
20. Kuznik, F., Virgone, J. and Noel, J., "Optimization of a phase change material wallboard for building use", ***Applied Thermal Engineering***, Vol. 28, No. 11-12, (2008), 1291-1298. doi: 10.1016/j.applthermaleng.2007.10.012.
21. Arunraj, E., Chacko, J., Mannaickal, A., Shaji, R. and Kumar, A.J., "A review on cooling roof tile materials", ***Journal of Critical Reviews***, Vol. 7, No. 13, (2020), 55-58. doi: 10.31838/jcr.07.13.08.
22. Sayadi, A.A., Tapia, J.V., Neitzert, T.R. and Clifton, G.C., "Effects of expanded polystyrene (EPS) particles on fire resistance, thermal conductivity and compressive strength of foamed concrete", ***Construction and Building Materials***, Vol. 112, (2016), 716-724. doi: 10.1016/j.conbuildmat.2016.02.218.
23. Pasupathy, A., Velraj, R. and Seeniraj, R., "Phase change material-based building architecture for thermal management in residential and commercial establishments", ***Renewable and Sustainable Energy Reviews***, Vol. 12, No. 1, (2008), 39-64. doi: 10.1016/j.rser.2006.05.010.
24. Siddique, R. and Klaus, J., "Influence of metakaolin on the properties of mortar and concrete: A review", ***Applied Clay Science***, Vol. 43, No. 3-4, (2009), 392-400. doi: 10.1016/j.clay.2008.11.007.
25. Al-dujaili, A., Disher Al-hydary, I. and Zayer Hassan, Z., "Optimizing the properties of metakaolin-based (na, k)-geopolymer using taguchi design method", ***International Journal of Engineering***, Vol. 33, No. 4, (2020), 631-638. doi" 10.5829/ije.2020.33.04a.14.
26. Jadidi, A. and Jadidi, M., "An algorithm based on predicting the interface in phase change materials", ***International Journal of Engineering***, Vol. 31, No. 5, (2018), 799-804. doi: 10.5829/ije.2018.31.05b.15.

27. Rao, D.V.P. and Mallikarjuna, C.S., "An experimental investigation on properties of concrete by partial replacement of cement with ggbs and fine aggregate with quarry dust", ***International Journal of Science and Research***, Vol. 6, No. 12 (2017), 706-710. doi: 10.21275/art20178797.
28. Ahmari, S. and Zhang, L., The properties and durability of alkali-activated masonry units, in Handbook of alkali-activated cements, mortars and concretes. 2015, Elsevier.643-660. doi:10.1533/9781782422884.4.643
29. Yajnik, S. and Roux, J., Spectral radiative properties and apparent thermal conductivity of expanded polystyrene foam insulation, in Insulation materials, testing and applications. 1990, ASTM International. doi:10.1520/stp23330s
30. 383, I., "Specification for coarse and fine aggregates from natural sources for concrete", Bureau of Indian Standards, (1970).
31. Specification, P.-P.C., "Is 1489 (part 1)-1991", Bureau of Indian Standards, New Delhi.
32. Astm c270-14a - standard specification for mortar unit for masonry.
33. Is 13801: Checkered cement concrete tiles", in, Bureau of Indian Standards, New Delhi.
34. Astm 1167-11 (2017) - standard specification for clay roof tiles.

Persian Abstract

چکیده

کاشی های سقفی رایج ترین پوشش سقف در ساختمان های هند، به ویژه در ساختمانهای مسکونی سنتی است. با توجه به نقش مهم خصوصیات سقف در بهره وری انرژی ساختمان و شرایط آسایش حرارتی داخلی، راه حل های نوآورانه برای بهبود عملکرد انرژی گرمایی این عنصر بام به یک موضوع تحقیقاتی اصلی تبدیل شده است. از این منظر، کاربردهای بام خنک نشان دهنده یک راه حل موثر برای این هدف است. کار حاضر به تجزیه و تحلیل یک نوع کاشی سقف خنک کننده ابتکاری ساخته شده با استفاده از ترکیبی از متاکائولین با درصدهای مختلف ، EPS ، سیلیکات سدیم و مواد پوشش دهنده می پردازد. مطالعات تجربی بر روی نمونه ها در طول شبانه روز انجام و عملکرد حرارتی کاشی های سقف خنک کننده از نظر دمای هوای آزاد در مقایسه با عملکرد حرارتی کاشی های بام معمولی ارزیابی شد. نتایج مطالعات آزمایشگاهی نشان داد که استفاده از سقف های خنک مطلوبیت حرارتی در طول روز و شب را افزایش می دهد. کاشی سقف خنک و نوآورانه در مقایسه با سایر فن آوری های مربوط به سقف ها، اجرای آسان تر و ارزان تری دارد. این مطالعه نشان داد که دمای سطح خارجی و داخلی سقف به ترتیب در طول روز حدود ۸ درجه سانتیگراد و ۱۲ درجه سانتیگراد کاهش می یابد، در حالی که سطح خارجی و داخلی سقف باعث حفظ دمای محیط در طول شب می شود. همچنین مقاومت گسیختگی فشاری و عرضی نمونه ها در مقایسه با نمونه ای مشابه حدود ۹.۱٪ و ۳۹.۶٪ افزایش داشت.

International Journal of Engineering

Journal Homepage: www.ije.ir

Supervised and Unsupervised Clustering Based Dimensionality Reduction of Hyperspectral Data

B. A. Beirami*, M. Mokhtarzade

Department of Photogrammetry and Remote Sensing, Faculty of Geodesy and Geomatics, K. N. Toosi University of Technology, Tehran, Iran

PAPER INFO

Paper history:
Received 22 September 2020
Received in revised form 17 April 2021
Accepted 12 May 2021

Keywords:
Hyperspectral Image
Principal Component Analysis
K-means Clustering
Classification
Feature Extraction
Weighted Mean

ABSTRACT

Nowadays, hyperspectral images (HIs) are widely used for land cover land use (LCLU) mapping. Hyperspectral sensors collect spectral data in numerous adjacent spectral bands, which are usually redundant. Hyperspectral data processing comes with important challenges such as huge processing time, difficulties in transfer, and storage. In this study, two supervised and unsupervised dimensionality reduction methods are proposed for hyperspectral feature extraction based on the band clustering technique. In the first method, the unsupervised method, after the unsupervised band clustering stage with some statistical attributes, the principal component transform is used in each cluster, and the first PC component is considered an extracted feature. In the second method, the supervised method, bands are clustered based on training samples mean vectors of each class, and the weighted mean operator is used for feature extraction in each cluster. The experiment is conducted on the classification of real famous HI named Indian Pines. Comparing the obtained results and some other state of art methods proved the proposed method's efficiency.

doi: *10.5829/ije.2021.34.06c.03*

1. INTRODUCTION

Hyperspectral sensors have high discrimination capabilities of ground surface materials due to recording hundreds of spectral portions of the electromagnetic wave. Classification is one of the most important methods for information extraction from HIs. Hughes phenomenon is the main problem in the supervised classification of HIs that degrades the classification accuracies. This phenomenon expresses that by increasing the number of features above some threshold, classification accuracy usually decreases [1, 2].

Dimensionality reduction is a common way to tackle this problem. Generally, feature selection and feature extraction are two main groups of dimensionality reduction methods. Feature selection methods try to find a lower-dimensional subset of the original feature so that essential discriminative information is preserved, while feature extraction methods try to find a transformation to map the features in lower-dimensional space. The main difference between these two methods lies in reduced features' physical meaning, which is only preserved in feature selection methods. In this study, we focus on feature extraction methods.

Numerous studies are available in the literature for feature extraction from HIs. Principal components analysis (PCA) and minimum noise fraction (MNF) are two widely used unsupervised methods that map the original features in lower dimensional space so that the first few reduced features contain the most information [3, 4]. Another version of PCA named segmented principal component analysis (SPCA) is proposed, which enhanced the original PCA version in the computational time aspect [5, 6]. Also, the nonlinear version of PCA named Kernel Principal Component (KPCA) is used in several studies dimensionality reduction of hyperspectral data [7, 8]. The wavelet-based dimensionality reduction method is another unsupervised method [9, 10]. In this method, high frequency and low-frequency components of the spectral signature curve (SSC) are separated, and the smoother version of SSC is used as the reduced features. The rational function curve fitting method is

*Corresponding Author Institutional Email: b_asghari@email.kntu.ac.ir (B. A. Beirami)

Please cite this article as: B. A. Beirami, M. Mokhtarzade, Supervised and Unsupervised Clustering Based Dimensionality Reduction of Hyperspectral Data, International Journal of Engineering, Transactions C: Aspects Vol. 34, No. 6, (2021) 1407-1412

recently used for hyperspectral feature extraction [11, 12]. In this method, a specific rational function approximation is developed to fit each pixel's SSC, and coefficients of the numerator and denominator are considered the newly extracted features.

Another widely used method that uses labeled samples of classes is linear discriminant analysis (LDA) [13, 14]. This method tries to maximize the within-class similarity and between-class separability. A generalized version of LDA that uses the kernel function is proposed by Baudat and Anouar [15]. LDA has three important drawbacks; first, this method works well only if the distributions of classes are normal-like. Second, this method can only extract (L-1) features (L is the number of classes), and third, the singularity of the within-class scatter matrix often occurs in the face with hyperspectral data [16]. Another supervised method named decision boundary feature extraction (DBFE) is a method that is extracted discriminately feature from the decision boundary between classes [17]. Nonparametric weighted feature extraction (NWFE) is another important feature extraction method for hyperspectral data [18]. The main idea of NWFE is to put different weights on every sample, compute the weighted means, and then define nonparametric between-class, and within-class scatter matrices. As a drawback, this method takes enormous time for the data reduction process. The kernel version of NWFE named kernel NWFE (KNWFE) is proposed to extend the NWFE for a nonlinear situation [16].

Recently, clustering-based methods are used for feature extraction [19, 20]. A supervised method named PSBS has been proposed based on k-means clustering of bands for band selection of HIs [21]. In a detailed paper, previous authors proposed the PSFE method based on fuzzy c-means clustering and feature weighting by class membership values [22]. Clustering-based feature extraction (CBFE) is proposed by Imani and Ghassemian [23]. This method considers a vector of mean values of training samples of all classes in each band and then a clustering algorithm such as k-means, groups these vectors in some clusters, and subsequently, the mean of bands whose associated vectors are located in a cluster is considered as an extracted feature. Usually, clustering-based methods work well even in small sample size situations (SSS situation) and do not have the other problems of some conventional supervised feature extraction methods such as enormous computation times, limitation of L-1 features (in LDA), and problems in estimating covariance matrix. An unsupervised version of band selection based on clustering of some bands statistics such as variance, mean absolute deviation (MAD), and standard deviation are for endmember extraction and classification of HIs [24-28].

This study introduced two unsupervised and supervised methods for dimensionality reduction of hyperspectral data based on bands clustering. As a result of the literature, when PCA transforms modified so that transformation is carried out by avoiding the low correlations between highly correlated blocks, PCA's efficiency improved [29]. This study's first proposed method is the unsupervised method named unsupervised clustering based principal components analysis (UCPCA). In this method, in the first stage, bands are clustered based on some statistical attributes. We expect adjacent and non-adjacent correlated bands to concentrate in the same cluster. In the second stage in each cluster, we carried out the PCA transform, and the first principal component (PC) is considered reduced features in each cluster. Unsupervised band clustering is the main novelty of this method, making UCPCA, like the original PCA, an unsupervised method. In the second proposed method, the supervised method named weighted mean clustering-based feature extraction (WMCFE), bands are clustered based on the mean values of training samples in each class, and the weighted mean of bands is based on MAD considered as an extracted feature in each cluster The major differences between UCPCA and WMCFE can be summarized as follows:

1. Each cluster of bands in the UCPCA is formed based on some statistical attributes of bands in an unsupervised manner without using any training samples, but bands clustering space in the WMCFE is formed based on the mean value of training samples in each class.
2. The UCPCA method used PCA transform for extracting the informative feature of each cluster of bands, but the WMCFE used a weighted mean for feature extraction in each cluster. Based on this explanation UCPCA method is grouped in the information-based feature extraction method, but WMCFE is the statistical feature extraction method.

In the next part, the methodology of the study that consists of two proposed methods is presented. In the second part, after introducing the data set results and related analysis of experiments are obtained. Finally, in the last part conclusion is presented.

2. METHODOLOGY

2. 1. UCPCA Unsupervised clustering-based principal components analysis (UCPCA) is an unsupervised method the same as PCA. This method has two stages. In the first stage, hyperspectral bands are grouped by K-means clustering based on some statistical attributes. Each band of HI can be represented by three statistical measures that are shown in Table 1.

In the above formulas, B_i is the value of i^{th} pixel, M, and N are image dimensions, $mean(b)$ is the mean of all pixel values in band b. In other words, each band can be shown as a point in 3-dimensional statistical space, and the K-means clustering algorithm tries to group each

TABLE 1. Statistical attributes

Statistical attribute	Formula
Variance (Var)	$SM1_b = \frac{1}{M.N}\sum_{i=1}^{M.N}(B_i - mean(b))^2$
Mean	$SM2_b = \frac{\sum_{i=1}^{M.N} B_i}{M.N}$
Kurtosis	$SM3_b = \frac{\frac{1}{M.N}\sum_{i=1}^{M.N}(B_i - mean(b))^4}{(\frac{1}{M.N}\sum_{i=1}^{M.N}(B_i - mean(b))^2)^2}$

band of HI so that the bands with similar information lie in the same cluster. K-means is one of the simplest unsupervised learning algorithms and consisted of four stages [30]:

1) Place K points into the attribute space represented by the statistics of bands. K is the number of desired reduced features.

2) Assign each band to the group that has the closest centroid based on some distance metrics such as square Euclidean

3) recalculate the positions of the K centroids by taking the mean of all bands assigned to that centroid's cluster

4) Repeat steps 2 and 3 until stopping criteria met (such as no centroid move, the sum of the distances is minimized, or user-defined maximum number of iterations)

Because of the algorithm's sensitivity to the initial randomly selected cluster centers and the probability of local optimum situation of results, the k-means algorithm may run multiple times.

In the second stage of the proposed algorithm, when the clusters formed, principal components analysis is applied in each cluster (for more information about the principal component analysis, referred to literature [31]), and the first PC of each cluster that contains the most information is considered as a new extracted feature.

2. 2. Weighted Mean Clustering-based Feature Extraction Weighted mean clustering-based feature extraction (WMCFE) is a supervised method based on the bands' K-means clustering and weighed mean operator. This method has three stages. In the first stage, based on training samples, we calculate the mean vector of training samples in each class for each band of HI. This vector is as follows:

$$b_i = [m_{i1} \quad m_{i2} \quad m_{i3} \quad \dots \quad m_{ic}]^T \tag{1}$$

In the above vector b_i is i^{th} band of HI and m_{ic} is mean of class c in i^{th} band. In other words, if we want to describe this method as the same as the UCPCA method, in the WMCFE method, the means of classes are attributes of each band. In the second stage, k-means clustering is introduced to group the bands the same as the UCPCA. The number of clusters in k-means clustering is user-defined and is equal to the desired numbers of reduced extracted features. In the last stage, the weighted mean of bands in each cluster is considered as extracted features. In this study, the weighted mean operator in each cluster is formulated as follows:

$$\text{weighted mean}(\boldsymbol{B}) = \frac{\sum_{i=1}^{k} w_i b_i}{\sum_{i=1}^{k} w_i} \tag{2}$$

In the above, b_i is the i^{th} band in a cluster, w_i is its corresponding weight and k is the number of bands in each cluster. Weighs in this study are defined by MAD statistical measure:

$$\frac{1}{M.N}\sum_{i=1}^{M.N}|B_i - mean(b)| \tag{3}$$

Bands with higher values of MAD get larger weights in each cluster because these bands contain more information, and so have more contribution to the extracted feature of each cluster [27].

3. EXPERIMENTAL RESULTS

3. 1. Data Set The airborn visible/ Infrared Imaging Spectrometer (AVIRIS) sensor acquired the Indian Pines scene from a mixed forest/agricultural from the Indian Pines Site in the USA. This data set consists of 145 × 145 pixels and 224 spectral bands. This data set's spatial resolution is 20 m, and band wavelengths are from 400 to 2500 nm with 10 nm resolution. After removing water absorption and noisy bands, the remaining 200 bands are used in this study. This scene contains 16 different land covers. Figure 1 illustrates the false-color composition of the original image and the ground-truth map .

After discarding four classes named alfalfa, grass-pasture-mowed, oats, and stone-steel-towers with a small number of samples in the ground truth map, the other 12 classes are used in this study.

3. 2. Results For evaluating proposed dimensionality reduction methods, a conventional maximum likelihood classifier is used to classify extracted features. The classification results for proposed methods are compared with four other dimensionality reduction methods named PCA, CBFE and NWFE. In this study, average and overall accuracies are two approaches used accuracy metrics [32].

Experiments are done in a few training-size situations with 60 training samples per class randomly chosen from the ground truth map. This training set is used for training classifiers and feature extraction. Half of these training samples are used in supervised feature extraction methods. The obtained overall and average accuracies values in the mentioned experiment for 60 training sample sizes are shown in Figures 2(a) and 2(b).

(a)

(b)

Figure 1. Indian pines data set - a) color composite image - b)ground-truth map

The highest ML achieved classification overall accuracies of extracted features from different methods

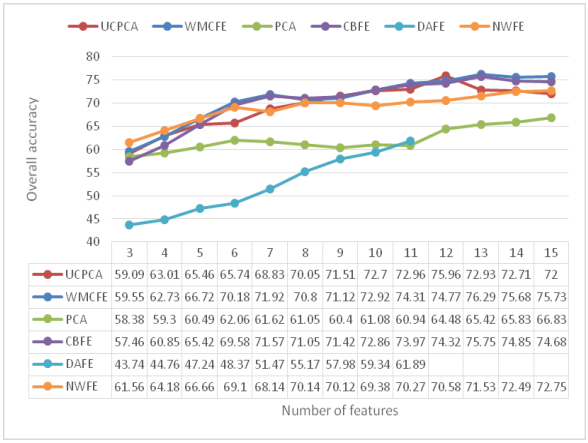

	3	4	5	6	7	8	9	10	11	12	13	14	15
UCPCA	59.09	63.01	65.46	65.74	68.83	70.05	71.51	72.7	72.96	75.96	72.93	72.71	72
WMCFE	59.55	62.73	66.72	70.18	71.92	70.8	71.12	72.92	74.31	74.77	76.29	75.68	75.73
PCA	58.38	59.3	60.49	62.06	61.62	61.05	60.4	61.08	60.94	64.48	65.42	65.83	66.83
CBFE	57.46	60.85	65.42	69.58	71.57	71.05	71.42	72.86	73.97	74.32	75.75	74.85	74.68
DAFE	43.74	44.76	47.24	48.37	51.47	55.17	57.98	59.34	61.89				
NWFE	61.56	64.18	66.66	69.1	68.14	70.14	70.12	69.38	70.27	70.58	71.53	72.49	72.75

(a)

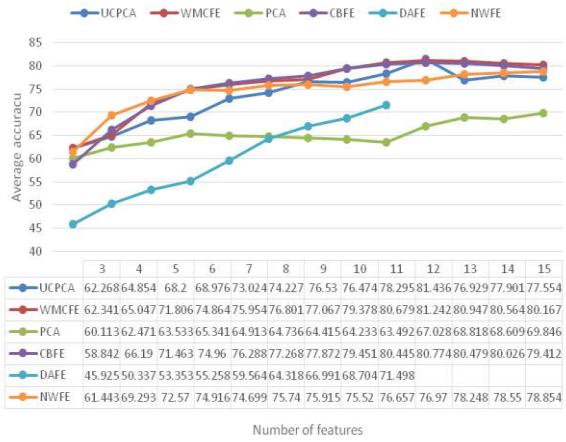

	3	4	5	6	7	8	9	10	11	12	13	14	15
UCPCA	62.268	64.854	68.2	68.976	73.024	74.227	76.53	76.474	78.295	81.436	76.929	77.901	77.554
WMCFE	62.341	65.047	71.806	74.864	75.954	76.801	77.067	79.378	80.679	81.242	80.947	80.564	80.167
PCA	60.113	62.471	63.533	65.341	64.913	64.736	64.415	64.233	63.492	67.028	68.818	68.609	69.846
CBFE	58.842	66.19	71.463	74.96	76.288	77.268	77.872	79.451	80.445	80.774	80.479	80.026	79.412
DAFE	45.925	50.337	53.353	55.258	59.564	64.318	66.991	68.704	71.498				
NWFE	61.443	69.293	72.57	74.916	74.699	75.74	75.915	75.52	76.657	76.97	78.248	78.55	78.854

(b)

Figure 2. Classification accuracies for different feature extraction methods in different number of features- a) overall accuracy - b) average accuracy

that are shown in Table 2 demonstrate that both proposed methods (UCPCA and WMCFE) perform better than the other feature extraction methods and at last WMCFE is superior. The main reason for the superiority of the UCPCA against the PCA is the bands clustering technique, which leads to the more homogenous band groups, and as a result, improves the performance of the PCA. In the comparison to CBFE, WMCFE uses the weighted mean operator that informative band has more contribution to the extracted feature of each cluster. Compared to some classical methods such as the DAFE and the NWFE, whose performance is dependent on a large number of the training samples (for accurate parameter estimation of models), the proposed method (UCPCA and WMCFE) works well even when few training samples are available.

The ground truth map of the Indian data set and the classified maps of different methods in the situation of Table 2 are shown in Figure 3. Based on Figure 3, one can understand that the proposed methods produced more smooth classification results.

TABLE 2. highest ML classification overall accuracies

	Methods					
	UCPCA	WMCFE	PCA	CBFE	DAFE	NWFE
OA	**75.96**	**76.29**	66.83	75.75	61.89	72.75
# of features	12	13	15	13	11	15

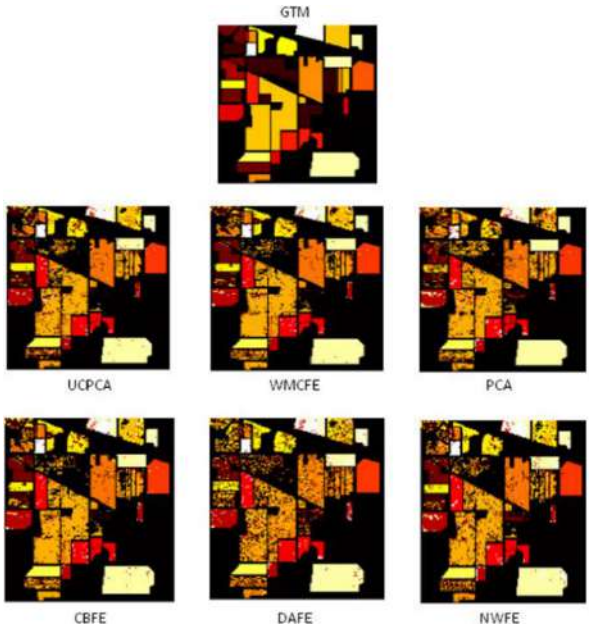

Figure 3. Ground truth map (GTM) and classified maps of different feature extraction methods

4. CONCLUSION

In this study, two unsupervised and supervised feature extraction methods based on bands clustering have been introduced for dimensionality reduction of hyperspectral data. The unsupervised method, named UCPCA, is based on unsupervised bands clustering and principal components analysis feature extraction. The supervised method, named WMCFE, is based on supervised bands clustering based on samples mean of classes and weighed mean operator based on the MAD measure. The experimental results showed better performance of proposed methods compared with some conventional feature extraction methods such as PCA, CBFE and NWFE.

5. REFERENCES

1. Hughes, G, "On the mean accuracy of statistical pattern recognizers", ***IEEE Transactions on Information Theory,*** Vol. 14, 1, (1968), 55-63. DOI: 10.1109/TIT.1968.1054102
2. Landgrebe, D., "Hyperspectral image data analysis", ***IEEE Signal Processing Magazine***, Vol. 19, 1, (2002), 17-28. DOI: 10.1109/79.974718
3. Lim, S., K.H. Sohn, and C. Lee. "Principal component analysis for compression of hyperspectral images", In IEEE International Geoscience and Remote Sensing Symposium,. IGARS S'01. (2001). DOI: 10.1109/IGARSS.2001.976068
4. Harris, J. R., Rogge, D., Hitchcock, R., Ijewliw, O., Wright, D. "Mapping lithology in Canada's Arctic: application of hyperspectral data using the minimum noise fraction transformation and matched filtering", ***Canadian Journal of Earth Sciences***, Vol. 42, 12, (2005), 2173-2193. DOI: 10.1139/e05-064
5. Jia, X. and J.A. Richards, "Segmented principal components transformation for efficient hyperspectral remote-sensing image display and classification", ***IEEE Transactions on Geoscience and Remote Sensing***, 1999. Vol. 37, 1, (1999), 538-542. DOI: 10.1109/36.739109
6. Bioucas-Dias, J. M., Plaza, A., Camps-Valls, G., Scheunders, P., Nasrabadi, N., & Chanussot, J., "Hyperspectral remote sensing data analysis and future challenges", ***IEEE Geoscience and Remote Sensing Magazine,*** Vol. 1, 2, (2013), 6-36. DOI: 10.1109/MGRS.2013.2244672
7. Datta, A., S. Ghosh, and A. Ghosh, "Unsupervised band extraction for hyperspectral images using clustering and kernel principal component analysis", ***International Journal of Remote Sensing,*** Vol 38, 3, (2017), 850-873. DOI: 10.1080/01431161.2016.1271470
8. Fauvel, M., J. Chanussot, and J.A. Benediktsson. "Kernel principal component analysis for feature reduction in hyperspectral images analysis". IEEE Proceedings of the 7th Nordic Signal Processing Symposium (2006). DOI: 10.1109/NORSIG.2006.275232
9. Kaewpijit, S., J. Le Moigne, and T. El-Ghazawi, "Automatic reduction of hyperspectral imagery using wavelet spectral analysis", ***IEEE Transactions on Geoscience and Remote Sensing,*** 2003. Vol 41, 4, (2003), 863-871. DOI: 10.1109/TGRS.2003.810712
10. Prabhu, N., M.K. Arora, and R. Balasubramanian, "Wavelet Based Feature Extraction Techniques of Hyperspectral Data", ***Journal of the Indian Society of Remote Sensing***, Vol. 44, 3, (2016), 373-384. DOI: 10.1007/s12524-015-0506-9
11. Hosseini, S.A. and H. Ghassemian. "A novel approach to hyperspectral data feature extraction using rational function curve fitting". IEEE International Conference on Signal and Image Processing Applications (ICSIPA), (2015). DOI: 10.1109/ICSIPA.2015.7412241
12. Hosseini, S.A. and H. Ghassemian, "Rational function approximation for feature reduction in hyperspectral data", ***Remote Sensing Letters***, Vol. 7, No. 2, (2016), 101-110. DOI: 10.1080/2150704X.2015.1101180
13. Fukunaga, K., Introduction to statistical pattern recognition. 2013: Academic Press. Hardcover ISBN: 9780122698514
14. David, L., "Hyperspectral image data analysis as a high dimensional signal processing problem", ***IEEE Signal Processing Magazin,*** Vol. 19, No. 1, (2002), 17-28. https://engineering.purdue.edu/~landgreb/SigProcPaper.pdf
15. Baudat, G. and F. Anouar, "Generalized discriminant analysis using a kernel approach", ***Neural Computation***, Vol. 12, No. 10, (2000) 2385-2404. DOI: 10.1162/089976600300014980
16. Kuo, B.-C., C.-H. Li, and J.-M. Yang, "Kernel nonparametric weighted feature extraction for hyperspectral image classification", ***IEEE Transactions on Geoscience and Remote Sensing***, Vol. 47, No. 4, (2009), 1139-1155. DOI: 10.1109/TGRS.2008.2008308
17. Lee, C. and D.A. Landgrebe, Feature extraction based on decision boundaries. ***IEEE Transactions on Pattern Analysis and Machine Intelligence***, Vol. 15, No. 4, (1993), 388-400. DOI: 10.1109/34.206958
18. Kuo, B.-C. and D.A. Landgrebe, "Nonparametric weighted feature extraction for classification", ***IEEE Transactions on Geoscience and Remote Sensing,*** Vol. 42, No. 5, (2004), 1096-1105. DOI: 10.1109/TGRS.2004.825578
19. Asghari Beirami, B., and M. Mokhtarzade. "Introducing an unsupervised method for feature extraction of hyperspectral images using bands clustering in the prototype space." ***Journal of Geomatics Science and Technology,*** Vol. 9, No. 2 (2019), 195-207. http://jgst.issge.ir/article-1-907-en.pdf

20. Esfandian, N., and K. Hosseinpourb. "A Clustering-Based Approach for Features Extraction in Spectro-Temporal Domain Using Artificial Neural Network." ***International Journal of Engineering, Transactions B: Applications***, Vol. 34, No. 2 (2021): 452-457. DOI: 10.5829/IJE.2021.34.02B.17
21. Mojaradi, B., Emami, H., Varshosaz, M., & Jamali, S. "A novel band selection method for hyperspectral data analysis", Int Arch Photogramm Remote Sens Spat Inf Sci, (2008).
22. Mojaradi, B., Abrishami-Moghaddam, H., Zoej, M. J. V., & Duin, R. P. "Dimensionality reduction of hyperspectral data via spectral feature extraction", ***IEEE Transactions on Geoscience and Remote Sensing***, Vol. 47, No. 7, (2009), 2091-2105. DOI: 10.1109/TGRS.2008.2010346
23. Imani, M. and H. Ghassemian, "Band clustering-based feature extraction for classification of hyperspectral images using limited training samples", ***IEEE Geoscience and Remote Sensing Letters***, Vol. 11, No. 8, (2014), 1325-1329. DOI: 10.1109/LGRS.2013.2292892
24. Ahmad, M., Haq, D. I. U., Mushtaq, Q., & Sohaib, M. "A new statistical approach for band clustering and band selection using K-means clustering", ***IACSIT International Journal of Engineering and Technology***, Vol. 3, No.6, (2011), 606-614.
25. Sohaib, M., Ihsan-Ul-Haq and Q. Mushtaq, "Dimensional Reduction of Hyperspectral Image DataUsing Band Clustering and Selection Based on Statistical Characteristics of Band Images", ***International Journal of Computer and Communication Engineering***, Vol. 2, No. 2, (2013), 101. http://www.ijcce.org/papers/148-B091.pdf
26. Datta, A., S. Ghosh, and A. Ghosh, "Combination of clustering and ranking techniques for unsupervised band selection of hyperspectral images", ***IEEE Journal of Selected Topics in Applied Earth Observations and Remote Sensing***, Vol. 8, No. 6, (2015), 2814-2823. DOI: 10.1109/JSTARS.2015.2428276
27. I ul Haq, I. and X. Xu. "A new approach to band clustering and selection for hyperspectral imagery". IEEE 9th International Conference on Signal Processing (ICSP), (2008). DOI: 10.1109/ICOSP.2008.4697345
28. Saqui, D., Saito, J. H., Campos, J. R., & Jorge, L. A. D. C. "Approach Based on Fuzzy C-Means for Band Selection in Hyperspectral Images", ***International Journal of Computer, Electrical, Automation, Control and Information Engineering,*** Vol. 10, No.5, (2016), 889-895.https://publications.waset.org/10004410/approach-based-on-fuzzy-c-means-for-band-selection-in-hyperspectral-images
29. Naik, G.R., Advances in Principal Component Analysis: Research and Development. 2017, Springer. Hardcover ISBN 978-981-10-6703-7. DOI:10.1007/978-981-10-6704-4
30. MacQueen, J. "Some methods for classification and analysis of multivariate observations". In Proceedings of the fifth Berkeley symposium on mathematical statistics and probability. (1967). Oakland, CA, USA.
31. Richards, J.A. and J. Richards, Remote sensing digital image analysis. Vol. 3. 1999: Springer. Hardcover ISBN 978-3-642-30061-5. DOI: 10.1007/978-3-642-30062-2
32. Beirami, B.A. and Mokhtarzade, M, "SVM classification of hyperspectral images using the combination of spectral bands and Moran's I features". IEEE 10th Iranian Conference on Machine Vision and Image Processing (MVIP), (2017). DOI: 10.1109/IranianMVIP.2017.8342334
33. Beirami, Behnam Asghari, and Mehdi Mokhtarzade. "Band Grouping SuperPCA for Feature Extraction and Extended Morphological Profile Production from Hyperspectral Images." ***IEEE Geoscience and Remote Sensing Letters,*** Vol. 17, No. 11, (2020), 1953-1957. DOI: 10.1109/LGRS.2019.2958833
34. Beirami, Behnam Asghari, and Mehdi Mokhtarzade. "Superpixel-Based Minimum Noise Fraction Feature Extraction for Classification of Hyperspectral Images." ***Traitement du Signal,*** Vol. 37, No. 5, (2020). DOI: https: //doi.org/10.18280/ts.370514

Persian Abstract

چکیده

در سال‌های اخیر از تصاویر ابرطیفی به طور گسترده‌ای برای تهیه تقشه از کاربری اراضی تحت پوشش زمین استفاده می‌شود. سنسورهای ابرطیفی باندهای طیفی را در نواحی مجاور متعددی که معمولاً اضافی هستند جمع‌آوری می‌کنند، از این رو پردازش داده‌های طیفی فوق با چالش‌های مهمی مانند زمان پردازش زیاد، مشکلات در انتقال و ذخیره‌سازی داده روبرو است. در این مطالعه، دو روش کاهش ابعاد تحت نظارت و بدون نظارت برای استخراج ویژگی‌های طیفی بر اساس روش خوشه‌بندی باند پیشنهاد شده است. در روش اول ، که روش بدون نظارت است، پس از مرحله خوشه‌بندی بدون نظارت باندها با استفاده از مشخصات آماری ، در هر خوشه، از تبدیل مولفه اصلی استفاده می‌شود و اولین مولفه آن در هر خوشه به عنوان ویژگی استخراج شده در نظر گرفته می‌شود. در روش دوم که روش نظارت شده است، باندها بر اساس میانگین بردارهای نمونه‌های آموزشی هر کلاس خوشه‌بندی شده و از عملگر میانگین وزندار برای استخراج ویژگی در هر خوشه استفاده می‌شود. آزمایش‌های این مقاله بر روی تصویر ابرطیفی مشهور واقعی ایندین پاین انجام شده است. مقایسه بین نتایج بدست آمده و برخی دیگر از روشهای مرسوم بیانگر کارآیی بیشتر روش پیشنهادی است.

International Journal of Engineering

Journal Homepage: www.ije.ir

A Signal Processing Method for Text Language Identification

H. Hassanpour[a], M. M. AlyanNezhadi*[b], M. Mohammadi[c]

[a] *Image Processing & Data Mining Lab, Shahrood University of Technology, Shahrood, Iran*
[b] *Department of Mathematics, University of Science and Technology of Mazandaran, Behshahr, Iran*
[c] *Department of Information Technology, College of Engineering and Computer Science, Lebanese French University, KR-Iraq*

PAPER INFO

Paper history:
Received 17 March 2021
Received in revised form 03 April 2021
Accepted 04 April 2021

Keywords:
Language Identification
Signal Processing
Wavelet Packet Transform
Artificial Neural Network

ABSTRACT

Language identification is a critical step prior to any natural language processing. In this paper, a signal processing method for Language Identification is proposed. Sequence of characters in a word and the order of words in stream identify the language. The sequence of characters in a stream provides a signature to recognize the language without understanding its meaning. The signature can be extracted using signal processing techniques via converting texts into time series. Although several research and commercial software have been developed to identify text language, they need a standard dictionary for each language. We proposed a dictionary independent method consisting of three main steps, I) pre-processing, II) clustering and finally III) classification .First, the texts are converted to time series using UTF-8 codes. Second, to group similar languages, the obtained series are clustered. Third, each cluster is decomposed into 32 sub-bands using a Wavelet packet, and 32 features are extracted from each sub-band. Also, a multilayer perceptron neural network is used to classify the extracted features. The proposed method was tested on our dataset with 31000 texts from 31 different languages. The proposed method achieved 72.20% accuracy for language identification.

***doi**: 10.5829/ije.2021.34.06c.04*

1. INTRODUCTION

Natural language processing (NLP) techniques play an important role in the classification and processing of huge digital documents on the Web [1, 2]. Determination of the language of a text's content is called Language Identification (LID classification). This is the initial step in many NLP pipelines such as tagging data stream from Twitter with relevant language, improving search results by searching in the relevant language, and automatically using machine translation [3]. Since most of the later steps are language-dependent, any errors in the first step is compounded by later steps. Although the determination of disjoint languages is not a tough task, distinguishing the languages originated from the same root (e.g., Persian and Arabic or Italian and English) is a difficult task.

The ability to identify the language of a document increases the accessibility of data. It has a vast range of applications, i.e., presenting information in a user's native language is critical in attracting website visitors [4]. Most of the text processing techniques presuppose that the document's language is known. However, in real-world data, automatic LID is required to identify the language of the document .

The rhythm of expression is different in languages. It is created by the sequence of letters. Therefore, in this study, we will use the sequence of letters to identify the language. Of course, due to cultural and political issues, words from languages such as English, Arabic and French have infiltrated other languages. This makes language identification a bit difficult.

In the proposed method's training phase, the text is converted into a time series using UTF-8 coding. The time series is clustered into different clusters then analyzed using the Wavelet packet. The statistical features are extracted from each sub-band and used as the inputs of a multilayer perceptron neural network.

The proposed method is examined with our collected dataset. The provided dataset covers similar languages.

*Corresponding Author Email: alyan.nezhadi@mazust.ac.ir (M. M. AlyanNezhadi)

Please cite this article as: H. Hassanpour, M.M. AlyanNezhadi, M. Mohammadi, A Signal Processing Method for Text Language Identification, International Journal of Engineering, Transactions C: Aspects Vol. 34, No. 6, (2021) 1413-1418

Designing a system to distinguish between similar languages such as Serbian and Croatian [5], language varieties like European Portuguese and Brazilian [6], or a set of Arabic dialects [7] is more challenging than designing systems to discriminate between, for example, Finnish and Japanese [8, 9]. The experimental results show the ability of the proposed method for LID with a similar languages dataset.

The rest of the paper is organized as follows. In the next section, we review several litterateurs dealing with LID, then the proposed method is described. In Section 3, our dataset is introduced, and applying the proposed method to the dataset is given. Finally, the study is concluded in section 4.

2. LITERATURE REVIEW

Some approaches have been proposed in literature for LID based on frequent word counting, unique tokens and n-gram [3] in which features such as the presence of particular characters, words or n-grams [10] are used as discriminators.

In the case of frequent words counting [11], the language is identified based on the frequencies of the words in the predefined dictionary constructed per each language. Another approach is based on n-gram. The n-gram is a contiguous sequence of items from a given text. There are some words with higher frequency for each human language than others, which can be used as discriminator feature. Ng and Selamat [12] studied three n-grams based identification method, i.e. , distance measurement, Boolean technique and optimum profile technique. In the first method, the profiles are produced and sorted based on n-gram frequencies. The minimum distance between testing and training profiles is selected as the winner. In the Boolean technique, the matching rate between testing and training profiles is computed. The language of the text is identified based on the highest matching rate. The first approach suffers from dimensionality problem and the latter fails in the case of the same n-gram frequency for multiple languages. The last approach applies both frequency and position features. The language with minimum converged point is known as the text language [12].

Common words such as conjunctions, determiners, and prepositions can be used to extract LID features. Dunning [13] used byte level n-grams of the entire string instead of the word's character level n-grams. Although n-gram based methods provide high accuracy in LID, but these methods suffer from high order of time complexity [14]

N-gram based methods are the most common LID methods in the literature. Several methods in combination with this approach have been developed, like SVM [15], Naive Bayes [16], prediction partial matching (PPM) [17], deep learning [18] and a combination of multiple classifier [19]. There are also benchmarking solutions to the LID. Google compact language detector (CLD) and TextCat employ n-gram based method[1], LogR [20] uses a discriminative strategy with regularized logistic regression [16]. Cavnar and Trenkle [14] provided outstanding results compared to the other state-of-the-art methods. They used rank order statistic as distance measure. The weakness of this method is that it relies to the tokenization while many languages have no boundaries.

The languages with the same origin are very similar in appearance and n-grams. For example, Arabic and Persian languages are of the same origin. As shown in Figure 1, they are very similar to each other. As can be seen in Equation (), 50% of 2-grams (bigrams) from the two example texts are joint. In addition, 59% and 76% of the two sample texts, the Persian and Arabic are existed in intersection of 2-grams sample texts (Equations () and ()). Therefore, the n-gram based approaches are unable to distinct between these languages.

$$\frac{bigram_{Persian} \cap bigram_{Arabic}}{bigram_{Persian} \cup bigram_{Arabic}} = \frac{29}{58} = 0.5 \quad (1)$$

$$\frac{bigram_{Persian} \cap bigram_{Arabic}}{bigram_{Persian}} = \frac{29}{49} = 0.59 \quad (2)$$

$$\frac{bigram_{Persian} \cap bigram_{Arabic}}{bigram_{Arabic}} = \frac{29}{38} = 0.76 \quad (3)$$

Various LID systems exist in literature for identifying text language but with a limited number of languages to identify. Shekhar et al. [21] and Gupta et al. [22] proposed an LID system to recognize Hindi and English languages.

After a rigorous search we found no prior study that employed signal processing techniques to identify the language of a text. In this paper, we address the problem of LID from a signal processing perspective. Different languages have different tones. Someone can recognize the language of a conversation if has previously heard such a conversation, even tough he/she does not understand the concept. Different languages show different frequency characteristics. This fact also can be observed from the text indicating correspondent phrases in a language. For each language, there is a dependency between components of a sentence as well as components that construct the word. These dependencies can be observed using both Fourier transform and Wavelet transform methods. The Fourier transform is not a good choice as it provides more diversity for the spectrum representation of the texts from the same language.

[1] https://github.com/google/cld3. [Last visited. 2021]

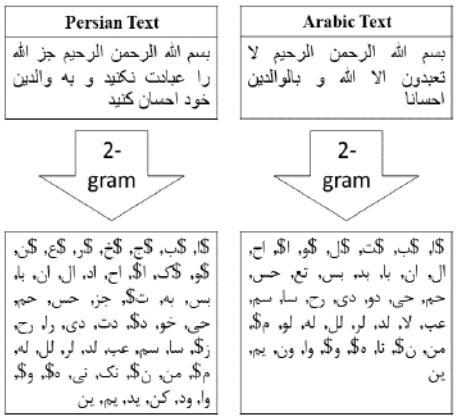

Figure 1. Samples of Persian and Arabic texts. As can be seen these languages are very similar to each other both in appearance and 2-grams

3. THE PROPOSED METHOD

Difference between languages is mainly due to their tunes. A language's tune depends on the succession of letters in a word and the pronunciation of successive words in a statement. Once we listen to a speech, we initially recognize the language and subsequently understand its meaning depending on the language's grammar. We may not fully understand a speech with a low volume level or low Signal to Noise (SNR) ratio, but we can still recognize the language spoken in if we know the language.

Once a French speaker talks English, the English speech is understandable even with a French accent. Indeed, speech in a language is a succession of letters that construct a tune. We propose a signal processing technique to convert text to time series and extract the tune for language identification. The flowchart of the algorithm is depicted in Figure 2.

In the proposed method, texts are converted to time series. The texts can be converted to time series using suitable coding. All texts in our dataset are coded with UTF-8.

Characters such as @,-,+ and # may exist in different texts. Therefore, they are removed from the time series . The obtained signal is clustered into several clusters using K-means method. The only feature for clustering is the mean of the signals UTF-8 codes. Some languages having unique UTF-8 codes are clustered in groups with only one language per group. However, the languages with similar UTF-8 codes appear in the same cluster. Thus, further processing is required to detect the language of texts in each cluster. To this aim, for each cluster, a model is trained and tested. The steps for the training are: I) feature extraction and II) classification.

Feature Extraction: The clustered signals are analyzed using the Wavelet packet transform, which is an extension of the Wavelet transform provided with more information regarding both high and low-frequency bands of the signal. By using the Wavelet packet transform, each signal is decomposed into 32 sub-bands.

The median of partial energy related to the sub-band coefficients is extracted from each sub-band as a feature.

$$F_x = log\left(\left|median\left((x^2)\right)\right|\right), \quad (4)$$

where, x is the sub-band coefficients. This feature is used for language identification introduced by AlyanNezhadi et al. [23].

Classification: Many techniques in literature employ neural networks in their classification [24-26]. In this paper, the extracted features are fed into multilayer perceptron neural network with one hidden layer and the network is trained to classify the languages. For testing a new text, first, the cluster of the text is determined. If the cluster contains only one language, that language will be assigned to the text. Otherwise, the correspondent model will be used to detect the language in the cluster.

4. DISCUSSION AND RESULTS

In the following first, we describe the dataset we have prepared, then the obtained results are discussed.

4. 1. Dataset We have selected 31 languages to assess the performance of the proposed method. For each language, 1000 texts were randomly extracted from Wikipedia. The minimum length for each text is 5000 characters. The languages include English (en), France

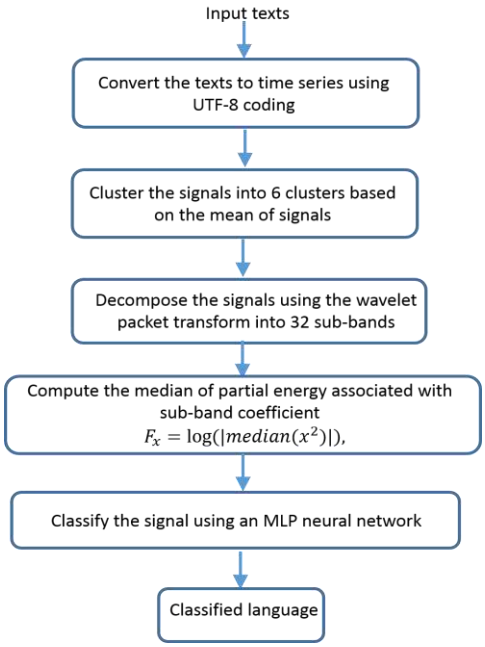

Figure 2. The flowchart of the proposed method

(fr), Italy (it), Arabic (ar), Russian (ru), arz (Egyptian Arabic), Azerbaijan (az), Byelorussian (be), Bulgarian (bg), Catalan (ca), ckb (Sorani, Central Kurdish), Czech (cs), Deutsch (de), Espernato (eo), Espanish (es), Persian (fa), Finnish (fi), Galician (gl), Hebrew (he), Hindi (hi), Croatian (hr), Indonesian (id), Dutch (nl), Polish (pl), Pashto (ps), Portoguese (pt), Romanian (ro), Tamil (ta) and Turkish (tr). Therefore, there is 310000 texts from 31 different languages.

4. 2. Evaluation To evaluate the performance of the proposed method, we used 31000 texts from our dataset. 80% of the texts are used for clustering, training and validation, and the remaining 20% of texts is used for testing randomly. The texts are converted to time series using UTF-8 coding and then the common characters are removed from them .

In the first stage, the K-means is used to cluster the whole data into six clusters based on only one simple feature (the average of the signals after elimination of common characters in the time domain). Table 1 shows the clustered languages in six groups with group centers and clustering precisions. As shown in Table 1, the texts with languages Tamil and Hindi are identified in this step with accuracy 90.50% and 95.50% for the testing dataset.

The average accuracy of 95.14% is achieved for six clusters with the centers: 1246.56, 878.73, 1370.18, 2820.96, 1874.38, 107.67 for testing data.

The obtained centers are used to cluster the test data. In the second stage, the texts from each cluster are separately classified. To this aim, the training texts (without elimination of common characters such as '?', '.', '!') are analyzed and decomposed using the Wavelet packet transform into 32 sub-bands. We have selected the Wavelet packet transform to analyze the texts. We employ a Wavelet packet transform with Daubachies kernel and five levels of decomposition. The Daubachies kernel is selected as it has valuable characteristics, i.e., vanishing moment and orthogonality conditions. We focussed on the sub-band energy to extract a feature as the classical multidimensional scaling (CMDS) representation of sub-band energy shows a separable cluster of different languages. This fact is shown in Figure 3 for seven languages from the dataset. The CMDS is a geometrical representation of data structure. Experimentally, we observed that the magnitude of the median provides more discrimination than the mean feature. We applied the logarithm to the median's magnitude to expand the distance between the languages with a close feature.

The multi-layer perceptron neural network with the parameters specified in Table 2; which is used to classify the languages based on the extracted features. The network has 32 input nodes as the length of the feature vector is 32. The number of neurons in the hidden layer is set equal to input layer. The network is trained 10 times and the results are averaged because the MLP may provide different results with different initial point. Table 3 shows the classification results for different states where 5, 7, and 12 spaces are inserted in-between two consecutive words of testing dataset. Finally, the accuracy of the system (clustering and classification) is given in Table 4. Figure 4 shows the structure of the experiment.

TABLE 1. Clustering the data into six clusters

Cluster members	Cluster centre	Accuracy (%)
ar, arz, ps	1246.56	87
ru, be, bg	878.73	94.83
fa, ckb	1370.18	77.50
ta	2820.96	90.50
hi	1874.38	95.50
en, fr, it, az, ca, cs, de, eo, es, fi, gl, he, hr, id, it, nl, pl, pt, ro, tr	107.67	98.55

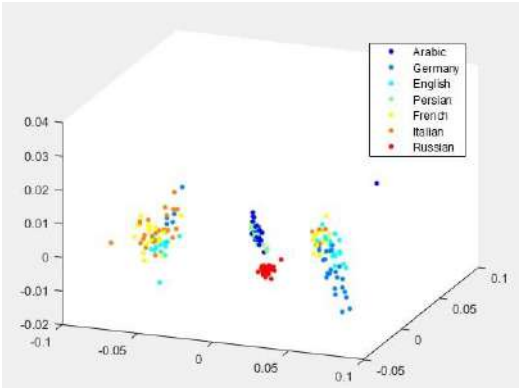

Figure 1. The CMDS representation of sub-band energy (with correlation distance) for seven languages

TABLE 2. The parameters of the neural network

Parameter	Value
Input layer neurons	The size of features
hidden layer neurons	The size of features
Output layer neurons	The number of languages
Hidden neurons activation function	Hyperbolic tangent sigmoid transfer function
Output neurons activation function	TSoft max transfer function
Data division	Random (80% train, and 20% validation data)
Maximum number of epochs	5000
Training method	Scaled conjugate gradient

TABLE 3. The accuracy of classification for testing data

Cluster members	1 space	5 spaces	7 spaces	12 spaces
ar, arz, ps	71.95	73.35	72.60	71.52
ru, be, bg	64.85	67.98	72.65	71.10
fa, ckb	75.65	76.88	76.77	77.12
en, fr, it, az, ca, cs, de, eo, es, fi, gl, he, hr, id, it, nl, pl, pt, ro, tr	62.72	67.72	69.38	69.50

TABLE 4. The accuracy of language identification

	1 space	5 spaces	7 spaces	12 spaces
Proposed method	66.88	70.70	72.20	72.02

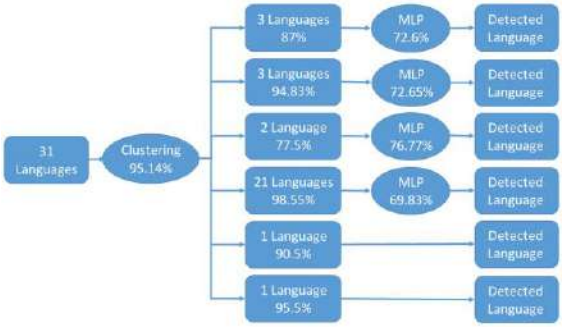

Figure 4. Structure of the designed system

5. CONCLUSION

LID plays an important role in most of the text processing applications. As this task is the first step to almost any text processing technique, the errors made in this task will propagate and deteriorate the results in the latter stages. In this paper, a new signal processing based technique was proposed to identify the text languages without any dictionary necessity. The proposed method includes the preprocessing, clustering, feature extraction, and classification stages. The proposed method was tested on our dataset with 31 different languages. Similar languages with the same origin exist in our dataset. The accuracy of 72.20% was achieved for text language identification.

6. REFERENCES

1. Cai, W., Cai, Z., Liu, W., Wang, X. and Li, M., "Insights in-to-end learning scheme for language identification", in 2018 IEEE International Conference on Acoustics, Speech and Signal Processing (ICASSP), IEEE, (2018), 5209-5213, DOI: 10.21437/Interspeech.2019-1386
2. Sharma, A.R. and Kaushik, P., "Literature survey of statistical, deep and reinforcement learning in natural language processing", in 2017 International Conference on Computing, Communication and Automation (ICCCA), IEEE, (2017), 350-354, DOI: 10.1109/CCAA.2017.8229841
3. Ambikairajah, E., Li, H., Wang, L., Yin, B. and Sethu, V., "Language identification: A tutorial", ***IEEE Circuits and Systems Magazine***, Vol. 11, No. 2, (2011), 82-108, DOI: 10.1109/MCAS.2011.941081
4. Kralisch, A. and Mandl, T., "Barriers to information access across languages on the internet: Network and language effects", in Proceedings of the 39th Annual Hawaii International Conference on System Sciences (HICSS'06), IEEE, (2006), 54b-54b, DOI: 10.1109/HICSS.2006.71
5. Radford, W. and Gallé, M., "Discriminating between similar languages in twitter using label propagation", ***arXiv preprint arXiv:1607.05408***, (2016), DOI: arXiv:1607.05408
6. Castro, D., Souza, E. and De Oliveira, A.L., "Discriminating between brazilian and european portuguese national varieties on twitter texts", in 2016 5th Brazilian Conference on Intelligent Systems (BRACIS), IEEE, (2016), 265-270, DOI: 10.1109/BRACIS.2016.056
7. Malmasi, S., Zampieri, M., Ljubešić, N., Nakov, P., Ali, A. and Tiedemann, J., "Discriminating between similar languages and arabic dialect identification: A report on the third dsl shared task", in Proceedings of the Third Workshop on NLP for Similar Languages, Varieties and Dialects (VarDial3), (2016), 1-14, DOI:
8. Zissman, M.A. and Berkling, K.M., "Automatic language identification", ***Speech Communication***, Vol. 35, No. 1-2, (2001), 115-124, DOI: 10.1016/S0167-6393(00)00099-6
9. Kosmajac, D. and Keselj, V., "Slavic language identification using cascade classifier approach", in 2018 17th International Symposium INFOTEH-JAHORINA (INFOTEH), IEEE, (2018), 1-6, DOI: 10.1109/INFOTEH.2018.8345541
10. Martins, B. and Silva, M.J., "Language identification in web pages", in Proceedings of the 2005 ACM symposium on Applied computing, (2005), 764-768, DOI: 10.1145/1066677.1066852
11. Bangalore, S. and Rambow, O., "Corpus-based lexical choice in natural language generation", in Proceedings of the 38th Annual Meeting of the Association for Computational Linguistics, (2000), 464-471,
12. Ng, C.-C. and Selamat, A., "Improving language identification of web page using optimum profile", in International Conference on Software Engineering and Computer Systems, Springer, (2011), 157-166, DOI: 10.1007/978-3-642-22191-0_14
13. Dunning, T., "Statistical identification of language": Computing Research Laboratory, New Mexico State University Las Cruces, NM, USA, (1994).
14. Cavnar, W.B. and Trenkle, J.M., "N-gram-based text categorization", in Proceedings of SDAIR-94, 3rd annual symposium on document analysis and information retrieval, Citeseer, (1994), DOI: 10.1.1.53.9367
15. Bhargava, A. and Kondrak, G., "Language identification of names with svms", in Human Language Technologies: The 2010 Annual Conference of the North American Chapter of the Association for Computational Linguistics, (2010), 693-696, DOI: 10.5555/1857999.1858101
16. Lui, M. and Baldwin, T., "Langid. Py: An off-the-shelf language identification tool", in Proceedings of the ACL 2012 system demonstrations, (2012), 25-30.
17. Bobicev, V., "Native language identification with ppm", in Proceedings of the Eighth Workshop on Innovative Use of NLP for Building Educational Applications, (2013), 180-187.
18. Duvenhage, B., "Short text language identification for under resourced languages", ***arXiv preprint arXiv:1911.07555***, (2019), DOI: https://arxiv.org/abs/1911.07555
19. Carter, S., Weerkamp, W. and Tsagkias, M., "Microblog language identification: Overcoming the limitations of short, unedited and

idiomatic text", ***Language Resources and Evaluation***, Vol. 47, No. 1, (2013), 195-215, DOI: 10.1007/s10579-012-9195-y

20. Bergsma, S., McNamee, P., Bagdouri, M., Fink, C. and Wilson, T., "Language identification for creating language-specific twitter collections", in Proceedings of the second workshop on language in social media, (2012), 65-74,
21. Shekhar, S., Sharma, D.K. and Beg, M.M.S., "Language identification framework in code-mixed social media text based on quantum lstm — the word belongs to which language?", ***Modern Physics Letters B***, Vol. 34, No. 06, (2020), 2050086, DOI: 10.1142/S0217984920500864
22. Gupta, Y., Raghuwanshi, G. and Tripathi, A., "A new methodology for language identification in social media code-mixed text", in International Conference on Advanced Machine Learning Technologies and Applications, Springer, (2020), 243-254, DOI: 10.1007/978-981-15-3383-9_22
23. AlyanNezhadi, M. M., Forghani, M. and Hassanpour, H., "Text language identification using signal processing techniques", in 2017 3rd Iranian Conference on Intelligent Systems and Signal Processing (ICSPIS), IEEE, (2017), 147-151, DOI: 10.1109/ICSPIS.2017.8311606
24. Pradeep, J., Srinivasan, E. and Himavathi, S., "Neural network based recognition system integrating feature extraction and classification for english handwritten", ***International Journal of Engineering, Transactions B: Applications***, Vol. 25, No. 2, (2012), 99-106, DOI: *10.5829/idosi.ije.2012.25.02b.03*
25. Akbari Foroud, A. and Hajian, M., "Discrimination of power quality distorted signals based on time-frequency analysis and probabilistic neural network", ***International Journal of Engineering***, ***Transactions C: Aspects***, Vol. 27, No. 6, (2014), 881-888, DOI: *10.5829/idosi.ije.2014.27.06c.06*
26. Hamidi, H. and Daraee, A., "Analysis of pre-processing and post-processing methods and using data mining to diagnose heart diseases", ***International Journal of Engineering, Transactions A: Basics***, Vol. 29, No. 7, (2016), 921-930, DOI: *10.5829/idosi.ije.2016.29.07a.06*

Persian Abstract

چکیده

چکیده: تشخیص زبان متن یک مرحله مهم قبل از هرگونه پردازش زبان طبیعی است. در این مقاله، یک روش مبتنی بر پردازش سیگنال برای تشخیص زبان متن پیشنهاد شده است. توالی کاراکترها در یک کلمه و ترتیب کلمات، زبان متن را مشخص می‌کند. توالی کاراکترها در متن می‌تواند یک امضا برای متن باشد که بتوان بدون فهمیدن معنای آن‌ها، زبان متن را تشخیص داد. این امضا می‌تواند به کمک روش‌های پردازش سیگنال از طریق تبدیل متن به سری زمانی استخراج شود. اگرچه پژوهش‌ها و نرم افزارهای تجاری متعددی برای تشخیص زبان متن وجود دارد، ولی آن‌ها به یک دیکشنری استاندارد برای هر زبان نیاز دارند. در این مقاله، یک روش بدون نیاز به دیکشنری با سه مرحله اصلی ۱) پیش پردازش، ۲) خوشه‌بندی و در نهایت ۳) دسته‌بندی پیشنهاد شده است. در اولین مرحله، متن به یک سری زمانی با کمک کدگذاری UTF-8 تبدیل شده است. در مرحله دوم، به منظور گروه‌بندی زبان‌های مشابه یکدیگر، خوشه بندی سری‌های زمانی انجام شده است. در مرحله سوم، سری‌های زمانی هر خوشه به ۳۲ زیرباند توسط تبدیل موجک تجزیه شده است و از زیرباندها ۳۲ ویژگی استخراج شده است. سپس از شبکه عصبی پرسپترونی چند لایه برای دسته‌بندی ویژگی‌های استخراج شده استفاده شده است. روش پیشنهادی بر روی پایگاه داده خودمان با ۳۱۰۰۰ متن از ۳۱ زبان مختلف آزمایش شده است. روش پیشنهادی دارای دقت ٪۷۲.۲ برای تشخیص زبان متن است.

IJE TRANSACTIONS C: Aspects Vol. 34, No. 6, (June 2021) 1419-1429

International Journal of Engineering

Journal Homepage: www.ije.ir

Improving the Load Balancing and Dynamic Placement of Virtual Machines in Cloud Computing using Particle Swarm Optimization Algorithm

A. Yousefipour[a], A. M. Rahmani*[a], M. Jahanshahi[b]

[a] *Department of Computer Engineering, Science and Research Branch, Islamic Azad University, Tehran, Iran*
[b] *Central Tehran Branch, Islamic Azad University, Tehran, Iran*

PAPER INFO

Paper history:
Received 20 August 2020
Received in revised form 16 November 2020
Accepted 19 January 2021

Keywords:
Cloud Computing
Placement
Dynamic Migration
Load Balancing
Particle Swarm

ABSTRACT

Nowadays, maximizing profits, decreasing operating cost and scheduling tasks are the most important issues of cloud computing with its growing usage. In this regard, one of the challenges in cloud computing is to provide an efficient method to deploy virtual machines on physical machines with the aim of optimizing energy consumption, fair load distribution and task scheduling. The purpose of present study is to provide a method for improving task scheduling through an improved particle swarm optimization algorithm. In the proposed method of present study, selection of a proper objective function has led to balanced workload of virtual machines, decreased time of all tasks as well as maximum utilization of all resources and increased productivity in addition to dynamic placement of virtual machine on physical machine. The results of simulation showed that the proposed method has provided an optimized solution for scheduling tasks, equal allocation of tasks in virtual machines and placement on the appropriate physical machine and less time with an improvement of 0.02 has been spent on the process of outsourcing virtual machines.

***doi**: 10.5829/ije.2021.34.06c.05*

1. INTRODUCTION

The third revolution in information technology after computer technology and the internet has been occurred with cloud computing [1]. This technology has led to a decreased in the cost of technology infrastructure due to its large data centers [2]. Nowadays, cloud computing has become a part of the market because many organizations and companies do not have the necessary resources due to the high cost of software and hardware. To overcome this problem, cloud computing practically provides the required software and hardware at an affordable rental cost [1]. These resources enjoy from the feature of remote access and users can access them from anywhere in the world. In the term of placement, cloud computing can be classified into four categories of public, private, hybrid and social [3]. In cloud computing, resources are provided to users as services [4]. These services can be categorized into three categories of software as a service, platform as a service, and infrastructure as a service [3, 2]. In infrastructure, this service is provided for client through hardware virtualization, which includes many suggestions such as virtual server space, network connections, bandwidth, IP addresses and load balancer [3]. In data centers, there are a significant number of physical and virtual machines with a large number of possible metrics [5], which resulting in a varied need for different resources. The efficient and dynamic use of shared resources through workloads varying from time to time [6]. Virtualization technology in a cloud data center eliminates server heterogeneity and provides server integration and enhances the efficiency of server usage [7]. Virtualization makes it possible to map several virtual machines on a physical machine with varying levels of access and performance quality [8]. However, one of the important challenges in cloud computing is to provide an efficient way for mapping of virtual machines on physical machines so that they can meet the quality of

*Corresponding Author Institutional Email: rahmani@srbiau.ac.ir (A. M. Rahmani)

Please cite this article as: A. Yousefipour, A. M. Rahmani, M. Jahanshahi, Improving the Load Balancing and Dynamic Placement of Virtual Machines in Cloud Computing using Particle Swarm Optimization Algorithm, International Journal of Engineering, Transactions C: Aspects Vol. 34, No. 6, (2021) 1419-1429

service requirements; may required by service providers in addition to maximum usage of physical machines [9, 6]. Virtual machine selection and mapping on any virtualized physical machine is known as virtual machine placement [9]. In this case, the virtual machine will migrate to the next most appropriate host when the host on which virtual machine is placed fails to provide the increasing demand-driven services [3]. Virtual machine migration in data centers helps to achieve goals such as balanced load distribution, fault tolerance (FT), energy management and decreasing service response time [10]. Once virtual machines are placed in a physical machine, the host of virtual machine provides different resources with different workloads at different times. This matter can lead to resource imbalances and a decline in the performance of cloud services. As a result, the virtual machine must migrate on the physical machine. To overcome such challenge, the overload of a virtual machine is removed and transferred to a machine with a lower-load in order to balance the load [11]. Load balancing is a technique for balanced distribution of load across resources [12]. Solving virtual machine placement and load balancing challenges is a type of nondeterministic polynomial time (NP)-Hard problem. Solving an NP-Hard problem through common methods such as Graph Theory is time-consuming and very costly in the term of computations. Therefore, it is better to solve such problems through other methods using meta-heuristic and heuristic techniques. meta- heuristic methods include particle swarm optimization (PSO) algorithm, ant colony optimization algorithm, genetic algorithm, neighborhood search algorithm and Tabu search algorithm [13]. Among the available meta-heuristic methods in this research, a method for optimization will be selected that has more optimal solutions and less computational cost than other algorithms.

Therefore, according to studies, PSO has been selected and the purpose of present study was to propose a method of virtual machines placement on physical machines to optimize energy consumption, balance of workload for fairly distribution of tasks, decreased time of completing all tasks and increase resource efficiency.

The proposed method and algorithm and its mathematical topics have been described in section three and the conclusion of present study has been provided in section five.

2. RELATED WORKS

Available solutions for virtual machines placements are utilizing from definitive algorithms include finite programming, linear programming, integer programming, and dynamic programming. Utilizing from heuristic algorithms for a large number of physical and virtual machines is impractical. Most of the heuristic-based articles on the algorithms such as case reduction algorithm, the best case algorithm, the first case algorithm, the heaviest case algorithm and the worst case algorithm have been conducted properly. Meta-heuristic algorithms are desirable to obtain good solutions at the right time. Among such algorithms, it can be referring to Memetic algorithm at an extension of the traditional genetic algorithm, particle swarm optimization (PSO) algorithm, ant colony optimization algorithm, genetic algorithm, neighborhood search algorithm and Tabu search algorithm [13]. Meta-heuristic, genetic, particle swarm optimization (PSO) and ant colony optimization algorithms have been also used to balance the load on virtual machines [14, 15]. In this section, the previous studies conducted on virtual machine placement as an important issue for cloud providers have been investigated.

Dong et al. [16] have suggested multi-resource constraint of physical machine for the problem of virtual machine placement. In this suggestion, the traffic model between virtual machines can be changed by minimizing all the traffic through placement of virtual machine in the data center and placing the high traffic virtual machine in the same physical machine.

Liu et al. [17] have proposed the multi-objective algorithm NS-GGA to solve the problem of virtual machine placement through a non-dominated sorting genetic algorithm. The proposed method attempts to achieve the optimal Pareto front based on non-dominated sorting and grouping of genetic operators. It is necessary for infrastructure providers to specify virtual machine places. The proposed algorithm utilizes from fuzzy logic system to combine multiple objectives into one function in order to solve the problem.

In fact, several resource allocation algorithms have been suggested for efficient energy management in the cloud environment [18]. The modified best fit decreasing (MBFD) algorithm focuses on locating virtual placment and deals with sending new virtual machine requests and assigning them to hosts. In this method, threshold, minimum and maximum utilizations of the hosts are used to optimize the current virtual machines.

Tordsson et al. [19] have been presented virtual infrastructures for placement optimization according to the criteria specified by users in different clouds. The proposed algorithm is on the basis of integer programming formula and cost reduction.

The main point in virtual machine placement is to consider the CPU and memory of the physical machine on which the virtual machine is placed. In previous studies, this important point has not been taken into account in virtual machine and unused physical machine kept in idle or stand-by mode. Several studies have ever been conducted on workload balancing. In general, load balancing algorithms are divided into two groups of static

and dynamic. In static method, allocation of tasks to virtual machines is based on the capabilities of virtual machine and initial state of each machine. In dynamic method, the distributer allocates the tasks to virtual machine based on its current state and its available workload in addition to the initial capabilities of each virtual machine [12]. For this reason, only the studies conducted on dynamic load balancing have been investigated in this section.

Song et al. [20] have been proposed an online packet classification-based algorithm called VISBP that dynamically allocates data center resources through live migration. The proposed algorithm is efficient in real resource allocation systems. The method has been designed implemented in CloudSim environment, which saves energy and decreases the number of active physical machines.

Alguliyev et al. [11] have considered the load balancing of virtual machines as a NP-Hard problem. In this article, a particle swarm-based algorithm called αPSO-TBLB has been proposed for load balancing.

Abdi et al. [21], have proposed a scheduling method using particle swarm optimization algorithm with the aim of decreasing the time of completing all tasks. In the proposed method, the particle swarm optimization algorithm has been improved through the algorithm of assigning the shortest task to the fastest CPU.

Finally, the proposed method has been comprised with genetic algorithm. Acharya et al. [12] Agnihotri, and Sharma [22] have been stated that load balancing is one of the important challenges of virtual machines in the cloud environment. In these references, live migration via a particle swarm-based algorithm has been performed to solve the problem of load balancing in virtual machines.

Here are some tasks related to multi-objective optimization:

Feng et al. [23] have introduced to diversify the needs of users in cloud computing, it is necessary to provide an efficient strategy in data centers. So virtualization is one of the most important aspects of cloud computing. Integrating resources for a single purpose and reducing energy consumption in cloud computing is possible. However, integrating resources using multi-objective optimization is challenging. In this research, a combined exploratory algorithm of PSO and ACO is presented in order to reduce costs and energy consumption. The PSO algorithm is used for the virtual machine positioning speed and the ACO is used for the virtual machine position. The simulation results showed that it has efficiently allocated dynamic resources.

Cloud computing enables users to use resources (hardware, software and operating system) through the network and virtualization technology as a major part of cloud computing [24]. The virtual machine in cloud computing is placed on the physical machine. But in a virtual machine, a few things like memory, processor, bandwidth are considered and energy consumption should be minimized. In a virtual machine, multi-objective algorithms are used when multiple goals are optimized. In this research, four algorithms NSGA-II, eMOEA, PAES and SPEA2 were used to locate and minimize energy consumption and the environment is clodsim simulation. The results showed that the NSGA-II algorithm performed better than the others.

Cloud computing offers a variety of services. Data centers in cloud computing have physical machines with millions of virtual machines on them [25]. Therefore, in this situation, load balance on any virtual machine is very important, which is a challenge for service providers in cloud computing. In this paper, two algorithms for load balancing are compared. The proposed algorithm is gray wolves (GWs) optimization and then the results of this algorithm are compared with the next multi-objective particle swarm optimization algorithm. The results showed that the proposed algorithm has shown good results in many experiments, but the multi-objective particle mass algorithm had better results than the proposed algorithm in some similar experiments.

In reference There are countless heterogeneous virtual machines in cloud computing data centers [26]. Therefore, the items that should be considered are energy consumption, resource usage, usage time and virtual machine location. Therefore, this paper presents a multi-objective optimization method for power consumption reduction (SLAV) called multiobjective combines salp swarm and sine-cosine algorithms (MOSSASCA). The results showed that the proposed method performed better than MOPSO, NSGA-II, MOEAD and MOSCA methods. In this paper, after the proposed algorithm, the MOPSO algorithm performed better than other algorithms.

Load balance is a very important task in scheduling tasks that directly affect cloud computing resources [27]. So this article is a nature-inspired method called Binary Load Balancing – Hybrid Particle Swarm Optimization and Gravitational Search Provides Algorithm (Bin-LB-PSOGSA). The results show that the BinLB-PSOGSA algorithm has a better result than Bin-LB-PSO.

Discussion:

As can be seen in the related articles, a variety of single-objective and multi-objective optimization algorithms have been used to optimize energy consumption, load balance, virtual machine placement, and so on.

This research includes single-objective and multi-objective optimization and particle swarm optimization algorithm has been used for optimization because this algorithm has more optimal solutions and less computational cost than other algorithms. Therefore, this article pursues several goals. The first goal is a method of virtual machines placement on physical machines to

optimize energy consumption; the second goal is balance of workload for fairly distribution of tasks and the third goal is to decrease time of completing all tasks and increase resource efficiency. To achieve these three goal, the proposed method is convergence and based on the improved particle swarm optimization, which avoids linearization by selecting appropriate objective functions and allocates the weights to indicate priority. In the proposed method, it has been prevented from linearization and premature convergence of objective function using particle swarm optimization algorithm and considering a variable called alpha with a value between 0 and 1. The better results can be obtained at the optimum time by assigning this weight to each of the objective criteria. Finally, the fourth goal is to optimize the previous three goals using the multi-objective particle swarm optimization (MOPSO) algorithm. The reason for this choice is that it can be seen in studies that this algorithm performed better than similar algorithms such as NSGA-II.

But A new and innovative aspect of the proposed method is the simultaneous optimization of target functions using a multi-objective particle swarm optimization and an improved particle swarm optimization, which has not been done in previous studies with this scope. Therefore, in this study, the objective is to optimize the response variables of the three functions and find the best combination of variable regulation using multi-objective PSO.

3. METHODOLOGY AND PROPOSED ALGORITHM

As it was mentioned in the introduction, the considered cloud coputing challenge in present study was proper placement of virtual machines on physical machines using CPU and memory; then, load balancing on virtual machines to prevent migration and completing all tasks of virtual machines in an appropriate scheduling. Therefore, the proposed method of present study has been aimed to right placement of virtual machine on the physical machine based on scheduling tasks to maximize profit as well as decreasing operating costs and preventing performance loss in service delivery. The procedure of the proposed method based on proposed algorithm is shown in Figure 1. In the first step for the first goal, virtual machine was placed on physical machine based on the amount of CPU and memory and the rest of unused physical machine was kept in idle or standby mode. In the second step for the second goal, the load balancing of virtual machines was created based on task scheduling and task execution time. In the third step for the third goal, the purpose was to complete all tasks on a virtual machine to increase efficiency by completing time of tasks. It should be noted that all three steps were finally for the fourth goal tested simultaneously using multi-objective particle swarm optimization algorithm.

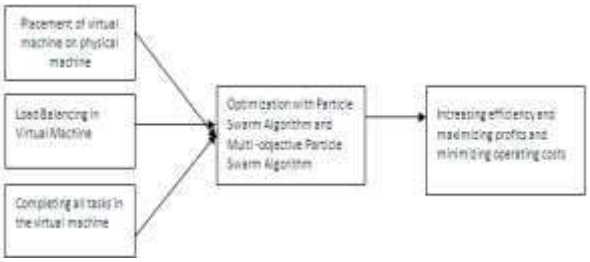

Figure 1. The proposed method of present study

3. 1. The Proposed Algorithm The particle swarm optimization algorithm was proposed by Kennedy and Eberhurt [28] whose idea was discovered by simulating a simple swarm model. The method of particle optimization is rooted in Reynold's work. The concept of Rooster was also added to this model in order to its further development, which was in the form of a memory of the best positions of each member and its neighbors. Each particle has a position indicating its coordinates in the multidimensional search space. The position of particle changes as it moves over time. ($X_i(t)$) indicates the position of particle ith at time tth. Also, each particle needs a velocity to move through space. ($V_i(t)$) indicates the velocity of particle ith at time tth. A new position can be created for each particle by increasing the velocity of its position. The way of updating particle position is presented in following equation (1):

$$X_i(t+1) = X_i(t) + V_i) \quad (1)$$

Whether a particle's position in the search space is a suitable position is evaluated using fitness function. Particles have the ability to memorize the best position they have been in their lifetimes. The best individual experience of a particle or the best visited position of particle is referred as y_i (y_i has been also named as $pbest$ in some algorithms). This position is referred as $\widehat{y_i}$ ($\widehat{y_i}$ has been also named as $gbest$ in some algorithms). The particle velocity vector in optimization process indicates the empirical knowledge of particle, particle information and particle society information. Each particle considers two components to move in search space including: 1) cognition component indicating the best solution a single particle can obtain ($pbest$) and 2) social component indicating the best solution recognized by the whole group ($gbest$), which were mentioned in the previous section. Considering $pbest$ and$gbest$, each particle utilize from following equations (2), (3) and (4) to determine its next position:

$$V_{ij}(t+1) = WV_{ij}(t) + c_1 r_1\left(p_{ij}(t) - X_{ij}(t)\right) + c_2 r_2\left(p_{ij}(t) - X_{ij}(t)\right) \quad (2)$$

$$X_{ij}(t+1) = X_{ij}(t) + V_{ij}(t+1) \quad (3)$$

$$\mathrm{W(t+1)} = w_{max} - (\frac{w_{max}-w_{min}}{t_{max}}).(t+1) \quad (4)$$

where, (i) is the particle index. The constants of (c_1) and (c_2) determine learning parameters (impact rate) for $pbest$ and$gbest$ are usually considered equal to 2. (r_1) and (r_2) are random numbers in the range of [0 and 1]. $(X_{ij}(t))$ represent the current position of particle. $(V_{ij}(t))$ represent the velocity of particle. The parameter W controls the velocity of particles which speeds up y at the beginning of algorithm implementation and slows down over time by approaching the response [28, 29]. The variables of algorithm have been presented in Table 1.

3. 2. Mathematical Model of Algorithm and Objective Function If m is the number of virtual machine in cloud environment, then we have $VM = \{VM_1.VM_2.\ldots.VM_m\}$ and if m virtual machines are available in p mechanical machine $PM = \{pm_1.pm_2.\ldots.pm_p\}$, then Equation (5):

$$where\ n_p = \begin{cases} 1 & If\ PM\ is\ active \\ 0 & Otherwise \end{cases} \quad (5)$$

where, (n_p) is a binary value indicating the active or inactive mode of PM. (n) The implementable tasks on virtual machine $Task = \{T_1.T_2.\ldots.T_n\}$

3. 2. 1. First Goal: Objective Function of Virtual Machine Placement The workloads of virtual and mechanical machines should be first considered for right virtual machine placement. In cloud computing, the amount of CPU and memory has a critical effect on the system. Therefore, it is necessary to define the workload in virtual and physical machines. By combining the load of CPU and memory of virtual machines or physical machines together, a new criterion is defined in Equation (6) called the volume which denoted by U [30] stated as follows:

$$\mathrm{U} = \frac{1}{1-cpu} * \frac{1}{1-mem} \quad (6)$$

TABLE 1. the variables of particle swarm optimization algorithm

Variables of algorithm	
W	Internal weight
c_1 ,c_2	Acceleration Coefficient
r_1, r_2	random numbers in the range of [0 and 1]
$X_{ij}(t)$	Current position of each particle
$V_{ij}(t)$	Current velocity of each particle
$pbest$	The best position that particle has ever received
$gbest$	The best position in all particles

In fact, the CPU and memory are resources used by virtual machine or physical server, which normalized through the number of CPUs and attributed memory size. The above equation indicates that the volume is increased with increase in the usage of a resource (CPU and memory). The ith CPU and ith memory are the CPU and consumed memory of virtual machine $V_i$and the pth CPU and pth memory are current CPU load and memory of physical machine p. If all of the k virtual machines are placed on the physical machine p, then the total load of p is obtained using below Equation (7):

$$\mathrm{U}_p = \frac{1}{1-(cpu_p+\sum_{i=1}^{k} cpu_i)} * \frac{1}{1-(mem_p+\sum_{i=1}^{k} mem_i)} \rightarrow$$
$$F_1 = \min\left(\frac{1}{1-(cpu_p+\sum_{i=1}^{k} cpu_i)} * \frac{1}{1-(mem_p+\sum_{i=1}^{k} mem_i)}\right) \quad (7)$$
$$\forall\ p = 1.\ldots.p \quad \forall\ i = 1.\ldots.k$$

$(\sum_{i=1}^{k} cpu_i)$ and $(\sum_{i=1}^{k} mem_i)$ are the total CPU and used memory of virtual machines, respectively. Also, better results can be obtained by assigning weight instead of one on the numerator of Equation (8) and generally the CPU and memory load of a physical machine is not more than 100%, so the following equation holds.

$$cpu_p + \sum_{i=1}^{k} cpu_i < 1 \qquad mem_p + \sum_{i=1}^{k} mem_i < 1 \quad (8)$$

3. 2. 2. Second Goal: Objective Function of Load Balancing The optimal value between the tasks and virtual machine should be determined based on the objective function in order to obtain scheduling and the best transfer time. Here, minimizing the task execution time (T_{exe}) and task transfer time (T_{trans}) have been considered as objective function [11]. It is calculated as Equation (9):

$$T_{exe} = \sum_{i=1}^{n}\sum_{k=1}^{m} x_{ik}\frac{DE_i}{VM_{m_k}} = \frac{number\ operations}{number\ operations/sec} \quad (9)$$
$$\forall\ i = 1.\ldots.n \qquad \forall\ k = 1.\ldots.m$$

Where, (DE_i) represent the work load of ith task (number of operations performed by task). (VM_{m_k}) represent is the speed of CPU (number of operations per second) in kth virtual machine. M is the number of virtual machine and n is the number of tasks. Also, (x_{ik}) is ith task on kth virtual machine with Equation (10):

$$T_{trans} = \sum_{i=1}^{n}\sum_{k=1}^{m}\sum_{z=1}^{m}(1 - x_{ik}x_{iz})\frac{DT_i}{B_{kz}} \quad (10)$$
$$\forall\ i = 1.\ldots.n \qquad \forall\ k = 1.\ldots.m$$

where, (DT_i) is the volume of data exchange between kth and zth virtual machines and (B_{kz}) is the bandwidth between kth and zth virtual machines. If ith task is on zth virtual machine, the value of x_{iz} is equal to 1 otherwise its value is 0. Better results can be obtained at the optimum time by weighting each criterion of objective function. Therefore, the following Equation (11) is obtained:

$$F_2 = \min(\alpha T_{exe} + (1-\alpha)T_{trans})) \quad \forall\ \alpha = 0. \ldots .1 \qquad (11)$$

3. 2. 3. Third Goal: Objective Function of Energy Efficiency In this step, the purpose of algorithm was to decrease the completing time of all tasks and increase the efficiency of resources. The completing time of all tasks I defined through following Equation (12) procedure [26].

$$Total\ time\ to\ complete\ all\ tasks = max \sum T_i VM_m * x_{im} \quad \forall\ i = 1. \ldots .n \qquad (12)$$

where, $(T_i VM_m)$ is the completing time of all ith tasks on mth virtual machine. (x_{im}) is equal to 1 when ith task is placed on mth virtual machine, otherwise its value is equal to 0. According to this equation, among a number of virtual machines between 1 to m, the value of machine with the highest total completing time of all assigned tasks is considered as the completing time of tasks. The value of efficiency from each resource is calculated using below Equations (13):

$$\text{Utilization}_j = \frac{\sum T_i VM_m * x_{im}}{Total\ time\ to\ complete\ all\ tasks} \quad \forall\ i = 1. \ldots .n \qquad (13)$$

where, the efficiency y of source j is equal to the sum of all tasks assigned to mth virtual machine by the processing ratio of machine with the highest total processing time. It is clear that the efficiency of each virtual machine is less than or equal to one stated in Equation (14).

$$Avg\text{Utilization} = \frac{\text{Utilization}_i}{m} \quad \forall\ i = 1. \ldots .n \qquad (14)$$

As a result, the objective function is obtained by decreased completing time of tasks and increased efficiency of resources with Equation (15):

$$f3 = \min\left(\frac{\sum T_i VM_m * x_{im}}{Avgtilization}\right) \quad \forall\ i = 1. \ldots .n \qquad (15)$$

3. 2. 4. Fourth Goal: Multi-objective Particle Swarm Optimization (MOPSO) At this stage, the simultaneous algorithm of the objective function of Equations (7), (11) and (15) is optimized.

The pseudo-code of particle swarm optimization algorithm is presented in Table 2.

TABLE 2. the pseudo-code of particle swarm optimization algorithm

Input: $VM = \{VM_1, VM_2, \ldots\ldots, VM_m\}, PM = \{pm_1, pm_2, \ldots\ldots, pm_p\}, Task = \{T_1, T_2, \ldots\ldots, T_n\}$

Output:

best position of Tasks on the VMs(Gbest) and best position of placement VMs on the PMs(Gbest) and best position of average utilization on the VMs(Gbest)

Start:

1: Set particle dimensionas equal to the size of ready tasks, placement and average utilization.
2: Initialize particles position randomly and velocity vi randomly.
3: for each particle run load balancing and placement algorithm for balance and placement particles position
4: For each particle, calculate its fitness value as in Equation(7,18 and 26) and set the alpha value
  If (fitness value < previousbestpbest)
    set the current fitness value as the newpbest
5: After Steps 4 for all particles, select the best particle as gbest
6: For all particles, calculate velocity using Equation (2)
    and update their positions using Equation (3)
7: If (stopping criteria or maximum iteration is not satisfied)
  repeat from Step 4.
 else
  Return gbest

Stop.

4. EVALUATION AND SIMULATION

In present study, the particle swarm optimization algorithm has been used to optimize the virtual machines. The simulation environment of MATLAB R2015a software was used for modeling and the computer with Intel i3-2350 series processor, 4GB of RAM and 500GB of hard drive used for simulation.

The simulations and steps of particle swarm optimization algorithm have been described below:

Step 1: Random selection of particles initial population: random generation of initial population includes random determination of particles initial place through a uniform distribution in the solution space (search space). The initial proposed range for particle velocity can be extracted through equation (16).

$$\frac{X_{min} - X_{max}}{2} \le V \le \frac{X_{max} - X_{min}}{2} \qquad (16)$$

Step 2: Select the number of initial particles: considering the problem, the initial population was determined equal to 50. Increasing number of initial particles leads to a decrease in the number of iterations required for algorithm convergence.

Step 3: Evaluation of particles objective function (calculation of the cost or fitness): in this step, each of the particles should be evaluated as a solution for problem. In present study, three objective functions have been considered including relations (7), (11) and (15). A variable called alpha has been defined for these functions in the range of 0 and 1 in order to prevent linearization and premature convergence. Better results can be obtained at the optimum time by allocating this weight to each of the objective criteria.

Step 4: Record the ($P_{i\ .best}$) and the ($P_{g\ .best}$) and update: in this step, two steps are possible based on the repetition number: (a) in the case of being in first repetition (t = 1), the current position of each particle is considered as the best specified place for it.

$$P_{i\ .best} = X_i(t) \quad .i = 1.2.3. \ldots .d$$
$$\text{cost}\ (P_{i\ .best}) = \text{cost}\ \left(X_j(t)\right) \qquad (17)$$

In other repetitions, the value obtained for particles in step 2 is comprised with value of the best cost value obtained for each particle. If this cost is less than the best recorded cost of this particle, then the place and cost of this particle is replaced with previous one. Otherwise no change is created in the recorded place and cost of this particle. It means that:

$$\begin{cases} \text{if cost}(X_i(t)) < cost\ (P_{i,best}) \Rightarrow \\ \quad \text{else Not change} \\ \text{cost}\ (P_{i,best}) = \text{cost}\ (X_j(t)) \\ \quad P_{i,best} = X_i(t) \end{cases} \quad (18)$$

$i = 1.2.3. \ldots . d$

The velocity vector update of all particles has been made according to the Equation (2) and the considered parameters have been based on literature [18].

Step 5: Algorithm stopping condition: a constant value has been considered for algorithm stopping condition. The simulation parameters and proposed algorithm have been presented in Table 3.

First Goal: According to Equation (7), all of virtual machines were placed on a physical machine and migrated to a physical machine in order to optimize the first objective function. The process of this optimization has been presented in Figure 2.

As it can be seen from Figure 4, the best objective function value was 3.9-e9381 and the objective function calling number for optimal response was approximately 4000 times and then, it has been converged. Finally, virtual machines were placed on the ninth physical machine in the last repetition. The number of these placements has been presented in Figure 3.

Second Goal: According to Equation (11), the second objective function was optimized for load balancing of virtual machines. The process of this optimization is shown in Figure 4.

TABLE 3. the simulation parameters

Simulation parameters and particle swarm optimization algorithm		
Particle swarm optimization algorithm	Size of initial population	50
	Number of repetitions	100
	Internal weight	0.7
	Acceleration coefficient	1.49445
	r_1 and r_2	Random numbers in the range of [0 and 1]
Physical machine	Number of physical machines	10
	CPU	Random numbers in the range of [1000 and 8000]
	Memory (Gig)	Random numbers in the range of [1and 8]
	Number of virtual machines	5
Virtual machine	CPU	Random numbers in the range of [1000 and 8000]
	Memory (Gig)	Random numbers in the range of [1and 8]
	Number of tasks	11
	Bandwidth (megabits per second)	Random numbers in the range of [1and 1024]
	Work load of task	Random numbers in the range of [1and 100]
	CPU speed (number of operations per second)	Random numbers in the range of [1000 and 10000]
	Alpha	Random numbers in the range of [0 and 1]

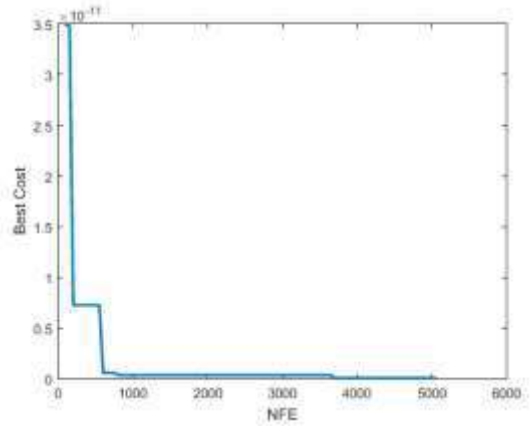

Figure 2. Optimization function of virtual machine placement

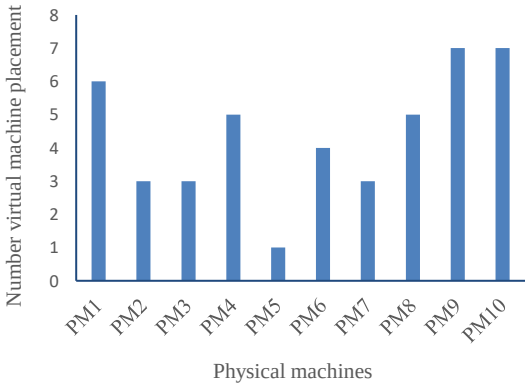

Figure 3. Number of virtual machines placements on physical machine

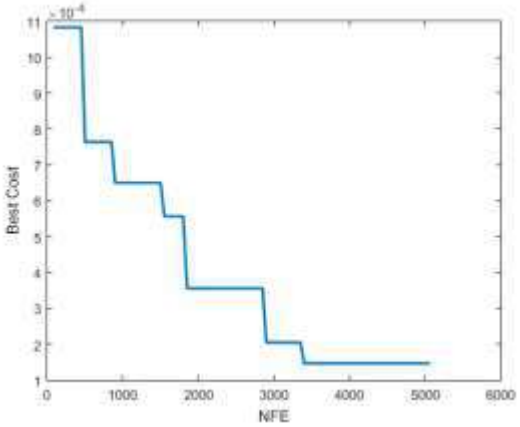

Figure 4. Optimization function of virtual machines' load balancing

As it can be seen from Figure 4, the best value of objective function was 0.00014644, the best time to transfer and execute tasks was close to 0.1 and the objective function calling number for optimal response was approximately 3500 times and then, it has been converged.

Third Goal: According to Equation (15), the third objective function was optimized for energy consumption optimization on virtual machines. The process of this optimization is presented in Figure 5. Whatever the value of this relation is lower, the utility is higher in the terms of decreased time of completing all tasks and increased efficiency of resources.

As it can be seen from Figure 5, the best objective function value was 72.122 and the objective function calling number for optimal response was approximately 3500 times and then, it has been converged.

Fourth Goal: Then, the multi-objective particle swarm optimization algorithm was used to simultaneously optimize all three objective functions.

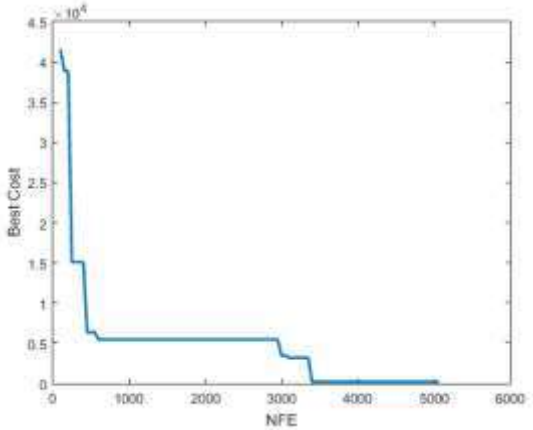

Figure 5. Optimization function of virtual machines efficiency

This algorithm is similar to the basic particle swarm optimization algorithm with the difference that objective function and particles are updated based on the best memory of each particle. In this algorithm, the non-dominated of initial population are separated after generation of initial population and stored in the Repository (Rep). Then, the discovered objective space is tabulated and each particle chooses a leader from Rep members and makes its move. Then the best personal memory of each particle is updated and non-dominated members of current population are added to Rep and remove the dominated members of Rep. If Rep members exceed the specified capacity, the extra members will be deleted and ultimately the algorithm is finished with specified repetitions of stopping condition. The optimized places of all three objective functions have been shown in Figure 6.

A comparison between the results of present study and the results of other studies conducted on this field has been presented as follows: Figure 7 represents a comparison between the results of present study and

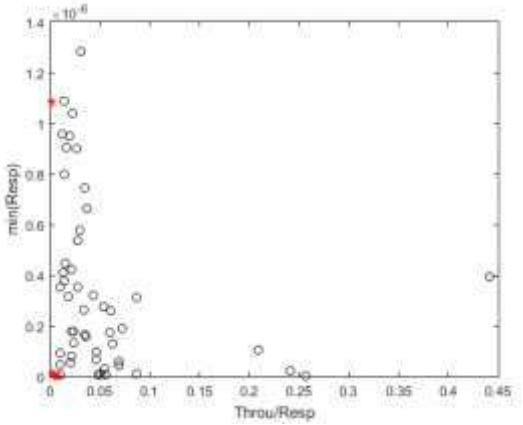

Figure 6. Simultaneous optimization of three objective functions

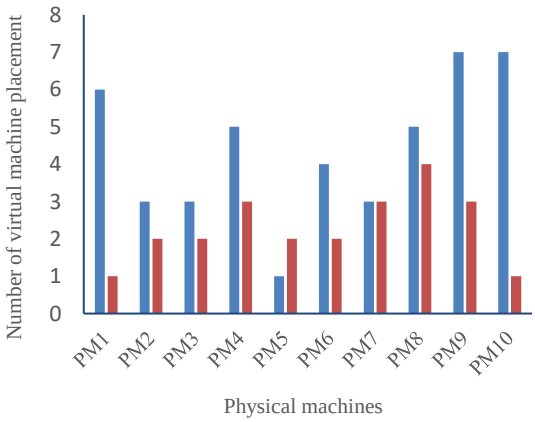

Figure 7. Comparison of virtual machines placement on physical machines

reported data in literature [30] in the term of virtual machine placement.

In this figure, the placement of virtual machine on physical machine is different in both studies. In both studies, the trend of number of virtual machine placements on physical machine has been well illustrated by particle swarm optimization algorithm. Figure (8) represents a comparison between the results of present study and literature [11] in the term of load balancing on virtual machines using task execution time and transfer time.

As it can be seen from Figure 8, the results of both studies are close to each other. In this study, the reason of obtaining better results with an improvement of 0.02 is proper calculation of alpha value. Figure 9 represents a comparison between the results of present study and literature [31] in the term of energy consumption optimization on virtual machines to decrease the completing time of all tasks and increase efficiency.

As it can be seen from Figure 9, the amount of efficiency with the same number of tasks is slightly better for present study compared to literature [31]. The reason is that the utility is higher in the terms of decreased time of completing all tasks and increased efficiency of resources whatever the value of this relation is lower and a lower and more optimized value was obtained in present study. Figure 10 represents the total completing time of all tasks.

As it can be seen form Figure 10, the total completing time of all tasks for present study and literature [31] is approximately equal because both studies have had a similar proposed model. However, a better result has been obtained in present study by determining a proper value of alpha. The significant difference between the results of present study and results of literature [21] is due to the fact that the reported data [21] and its coding and the way of its implementation can be different. It should be noted that the particle swarm optimization algorithm was comprised with genetic algorithm, which

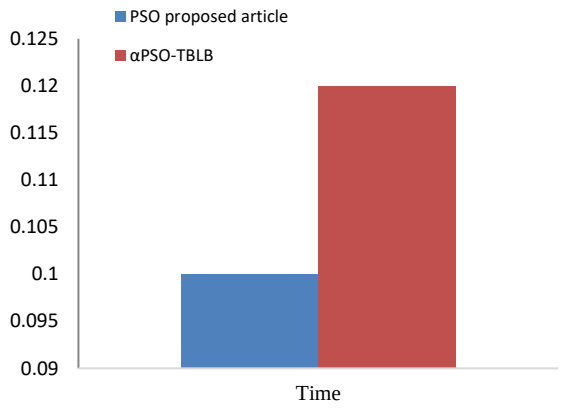

Figure 8. Comparison of load balancing in physical machine

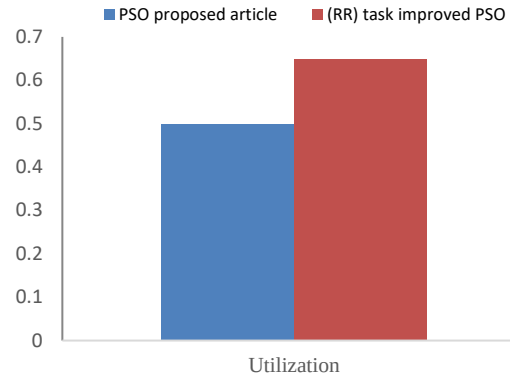

Figure 9. Comparison of physical machine efficiency

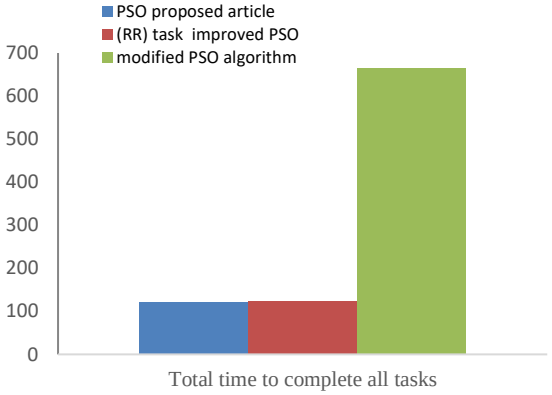

Figure 10. Comparison of total completing time of all tasks in physical machine

the comparison indicated the superiority of particle swarm optimization algorithm to genetic algorithm. In general, the difference point of present study compared to other conducted studies that can be also considered as a new and innovative aspect of present study is simultaneous optimization of objective functions using a multi-objective particle swarm optimization. For this reason, the MATLAB environment was more suitable for implementation of this algorithm.

5. CONCLUSION

The purpose of present study was to propose a method using a meta-heuristic approach as well as multi-objective particle swarm optimization and particle swarm optimization algorithms in order to increase profit and performance, decrease operating costs and optimize the utilization of resources in cloud computing. In this article, several goals have been pursued. The first goal a method of virtual machines placement on physical machines to optimize energy consumption is the second

goal balance of workload for fairly distribution of tasks aind the third goal decreased time of completing all tasks and increase resource efficiency. To achieve these three goal, the proposed method is convergence and based on the improved particle swarm optimization, which avoids linearization by selecting appropriate objective functions and allocates the weights to indicate priority. Finally, the fourth goal is to optimize the previous three goals using the multi-objective particle swarm optimization (MOPSO) algorithm. The better results can be obtained at the optimum time by assigning this weight to each of the objective criteria. The results of simulation showed that the proposed method has provided an optimized solution for scheduling tasks, equal allocation of tasks in virtual machines and placement on the appropriate physical machine and less time with an improvement of 0.02 has been spent on the process of outsourcing virtual machines. So the proposed methods can make it possible to obtain the most efficiency with minimum utilization of resources.

6. REFERENCES

1. Kaur, G. Sharma, S. "Optimized Utilization of Resources Using Improved Particle Swarm Optimization Based Task Scheduling Algorithms in Cloud Computing", ***International Journal of Emerging Technology and Advanced Engineering***, Vol. 4, No. 6, (2014), 110-115.
2. Askarizade H, M. Maeen, M. Haghparast, M. "An Energy-Effcient Dynamic Resource Management Approach Based on Clustering and Meta-Heuristic Algorithms in Cloud Computing IaaS Platforms", ***Wireless Personal Communications***, Vol. 104, No. 4, (2018), 1367-1391, doi: https://doi.org/10.1007/s11277-018-6089-3.
3. Kumar, A. Sathasivam, C. Periyasamy, P. "Virtual Machine Placement in Cloud Computing", ***Indian Journal of Science and Technology***, Vol. 9, No. 29, (2016), 1-5, doi: 10.17485/ijst/2016/v9i29/79768.
4. Goscinski, A. Brock, M. "Toward dynamic and attribute based publication", ***Future Generation Computer Systems***, Vol. 26, (2010), 947-970, doi: https://doi.org/10.1016/j.future.2010.03.009.
5. Pires, F. L. Baran, B. "A Virtual Machine Placement Taxonomy", 2015 15th IEEE/ACM International Symposium on Cluster, Cloud and Grid Computing, (2015), 159-168, doi: https://doi.org/ 10.1109/CCGrid.2015.15
6. L´opez-Pires, F. Bar´an, B. "Many-Objective Virtual Machine Placement", ***Journal of Grid Computing***, Vol. 15, No. 2, (2017), 161-176, doi: https://doi.org/10.1007/s10723-017-9399-x.
7. Vaquero, L M. Rodero-Merino, L. Caceres, J. Lindner, M. "A break in the clouds: Towards a cloud definition", ***ACM SIGCOMM Computer Communication Review***, Vol. 39, No. 1, (2009), 50-55, doi: https://doi.org/10.1145/1496091.1496100.
8. Gao, Y. Guan, H. Qi, Z. Hou, Y. Liu, L. "A multi-objective ant colony system algorithm for virtual machine placement in cloud computing", ***Journal of Computer and System Sciences***, Vol. 79, No. 8, (2013), 1230-1242, doi: https://doi.org/10.1016/j.jcss.2013.02.004.
9. Masdari, M. Nabavi, S. S. Ahmadi, V. "An Overview of Virtual Machine Placement Schemes In Cloud Computing", ***Journal of Network and Computer Applications,*** Vol; 66, (2016), 106-127, doi: https://doi.org/10.1016/j.jnca.2016.01.011.
10. Mishra, M. Das, A. Kulkarni, P. Sahoo, A. "Dynamic Resource Management Using Virtual Machine Migrations", ***IEEE Communications Magazine***, Vol. 50, No. 9, (2012), 34-40, doi: https://doi.org/10.1109/MCOM.2012.6295709.
11. Alguliyev, R. M. Imamverdiyev, Y. N. Abdullayeva, F. J. "PSO-based Load Balancing Method in Cloud Computing", ***Automatic Control and Computer Sciences***, Vol. 53, No. 1, (2019), 45–55, doi: https://doi.org/10.3103/S0146411619010024.
12. Acharya, J. Mehta, M. Saini, B. "Particle Swarm Optimization Based Load Balancing in Cloud Computing". IEEE. International Conference on Communication and Electronics Systems, (2017), 1-4, doi: https://doi.org/10.1109/CESYS.2016.7889943.
13. Xiao, Z. Jiang, J. Zhu, Y. Ming, Z. Zhong, S. Cai, S. "A solution of dynamic VMs placement problem for energy consumption optimization based on evolutionary game theory' ***Journal of Systems and Software***, Vol. 101, (2015), 260-272, doi: https://doi.org/10.1016/j.jss.2014.12.030.
14. Wang, L. Ai, L. "Task Scheduling Policy Based on Ant Colony Optimization in Cloud Computing Environment. in LISS".**,** Springer, Berlin, Heidelberg, (2013), 953-957, doi: https://doi.org/10.1007/978-3-642-32054-5-133.
15. Pacini, E. Mateos, C. Garino, Ca. G. "Balancing Throughput and Response Time in Online Scientific Clouds via Ant Colony Optimization", ***Advances in Engineering Software***, Vol. 84, (2015), 31-47, doi: https://doi.org/10.1016/j.advengsoft.2015.01.005.
16. Dong, J. k. Wang, H. LI, Y. Cheng, S. "Virtual machine placement optimizing to improve network performance in cloud data centers", ***The Journal of China Universities of Posts and Telecommunications***, Vol. 21, No. 3, (2014), 62-70, doi: https://doi.org/10.1016/S1005-8885(14)60302-2.
17. Liu, C. Shen, C. Li, S. Wang, S. "A new evolutionary multi-objective algorithm to virtual machine placement in virtualized data center", In 2014 IEEE 5th International Conference on Software Engineering and Service Science, (2014), 272-275, doi: https://doi.org/10.1109/ICSESS.2014.6933561.
18. Moges, F. F. Abebe, S. L. "Energy-aware VM placement algorithms for the OpenStack Neat consolidation framework", ***Journal of Cloud Computing***, Vol. 8, No. 1, (2019), 2-14, doi: https://doi.org/10.1186/s13677-019-0126-y.
19. Tordsson, J. Montero, R. Moreno-Vozmediano, R. Llorente, I. "Cloud brokering mechanisms for optimized placement of virtual machines across multiple providers". ***Future Generation Computer Systems***, Vol. 28, (2012), 358-367, doi: https://doi.org/10.1016/j.future.2011.07.003.
20. Song, W. Xiao, Z. Member, S. Chen, Q. Luo, H. "Adaptive Resource Provisioning for the Cloud Using Online Bin Packing". ***IEEE Transactions on Computers***, Vol. 63, No. 11, (2014), 2647-2660, doi: https://doi.org/10.1109/TC.2013.148.
21. Abdi, S. Sharifian. S. A. Sharifian, S. "Task Scheduling Using Modified PSO Algorithm in Cloud Computing Environment. Proc. International Conference on Machine Learning", Electrical and Mechanical Engineering, Dubai, (2014), 37-41, doi: http://dx.doi.org/10.15242/IIE.E0114078.
22. Agnihotri, M. Sharma, S. "Execution analysis of load balancing particle swarm optimization algorithm in cloud data center", IEEE. 2016 Fourth International Conference on Parallel, Distributed and Grid Computing, (2016), 668-672, doi: https://doi.org/10.1109/PDGC.2016.7913206.
23. Feng, D. Wu, Z. Zuo, D. Zhang, Z. "A multiobjective migration algorithm as a resource consolidation strategy in cloud computing", ***PLOS***, Vol. 14, No. 2, (2019), 1-25, doi: https://www.researchgate.net/deref/https%3A%2F%2Fdoi.org%2F10.1371%2Fjournal.pone.0211729.

24. Dörterler, S. Dörterler, M. Ozdemir, S. "Multi-Objective Virtual Machine Placement Optimization for Cloud Computing", IEEE, 2017 International Symposium on Networks, Computers and Communications, (2017), 1-6, doi: https://doi.org/10.1109/ISNCC.2017.8072013.

25. Fatima, F. Javaid, N. Butt, A.A. Sultana, T. Hussain, W. Bilal, M. Hashmi, R. m Akbar, M. Ilahi, Manzoor. "An Enhanced Multi-Objective Gray Wolf Optimization for Virtual Machine Placement in Cloud Data Centers", ***Electronics***, Vol. 8, No. 2, (2019), 218-250, doi: https://doi.org/10.3390/electronics8020218.

26. Alresheedi, S. Lu, S. Elaziz, M.A. Ewees, A.A. "Improved multiobjective salp swarm optimization for virtual machine placement in cloud computing", ***Human-centric Computing and Information Sciences***, Vol. 9, No. 15, (2019), 1-24, doi: https://doi.org/10.1186/s13673-019-0174-9.

27. Alnusairi, S. Shahin, A. Daadaa, Y. "Binary PSOGSA for Load Balancing Task Scheduling in Cloud Environment", ***International Journal of Advanced Computer Science and Applications***, Vol. 9, No. 5, (2018), 255-264, doi: https://dx.doi.org/ 10.14569/IJACSA.2018.090535.

28. Kennedy, J. Eberhart, R. "Particle Swarm Optimization". IEEE International Conference on Neural Networks, Proceedings, Vol. 4, (1995), 1942-1948, doi: https://doi.org/10.1109/ICNN.1995.488968.

29. Reynolds, Craig. W. "Flocks, herds and schools: a distributed behavioral model", ***Computer Graphics***, Vol. 21, No. 4, (1987), 25-34, doi: https://doi.org/10.1145/37402.37406.

30. Yan, J. Zhang, H. Xu, H. Zhang, Z. "Discrete PSO-based workload optimization in virtual machine placement", ***Personal and Ubiquitous Computing***, Vol. 22, (2018), 589-596, doi: https://doi.org/10.1007/s00779-018-1111-z.

31. Ebadifard, F. Babamir, S. M. "A PSO - based task scheduling algorithm improved using a load-balancing technique for the cloud computing environment", ***Concurrency and Computation: Practice and Experience***, (2017), 1-16, http://dx.doi.org/10.1002/cpe.4368.

Persian Abstract

چکیده

امروزه، با رشد استفاده از رایانش ابری، به حداکثر رساندن سود، کاهش هزینه عملیاتی و زمان‌بندی وظایف از مهمترین مسایل این حوزه هستند. در این راستا، یکی از چالش‌های رایانش ابری، ارائه روشی کارآمد برای جایابی ماشین‌های مجازی بر روی ماشین‌های فیزیکی به منظور بهبود مصرف انرژی، توزیع عادلانه‌ی بار و زمان‌بندی وظایف است. هدف از این مقاله ارائه روشی برای بهبود زمان‌بندی وظایف با استفاده از الگوریتم بهبود یافته توده ذرات می‌باشد. در این روش پیشنهادی با انتخاب تابع هدف مناسب علاوه بر جایابی پویا ماشین مجازی بر روی ماشین فیزیکی، سبب متعادل کردن بار کاری ماشین‌های مجازی، کاهش زمان تمامی وظایف و همچنین استفاده حداکثری از تمامی منابع و بالا بردن بهره‌وری شده است. نتایج شبیه سازی نشان می‌دهد یک راه حل بهینه برای زمان‌بندی کارها، تفکیک مساوی کارها در ماشینهای مجازی و قرارگیری در ماشین فیزیکی مناسب ارائه شده است و زمان کمتری با بهبود ۲۰ برای فرآیند واگذاری کارها به ماشینهای مجازی حاصل شده است.

IJE TRANSACTIONS C: Aspects Vol. 34, No. 6, (June 2021) 1430-1437

International Journal of Engineering

Journal Homepage: www.ije.ir

Fast Grid Voltage Synchronization using Modified Frequency-locked Loop in Single Phase Grid-connected Power Systems

H. Hassanpour*, M. Ehsanian

Faculty of Electrical Engineering, K. N. Toosi University of Technology, Tehran, Iran

PAPER INFO

Paper history:
Received 16 June 2020
Received in revised form 15 April 2021
Accepted 11 May 2021

Keywords:
Phase-locked Loop
Phase jump
Second-order Generalized Integrator
Frequency-locked Loop
DC Offset

ABSTRACT

One of the critical components for the efficient operation of single-phase grid-connected converters is the synchronization unit. This paper presents a fast and adaptive phase-locked loop (PLL) structure that ameliorates the dynamic response of the estimated frequency and amplitude for grid-connected single-phase power systems. The second-order generalized integrator (SOGI) with a novel frequency-locked loop (FLL) is utilized which contains a DC offset rejection loop. The proposed method not only eliminates the transient response of the estimated frequency which is produced by FLL in grid voltage phase angle jumps, but also improves the PLL dynamic characteristics. The whole system has been simulated in MATLAB Simulink environment where a very small settling time for the estimated frequency of the FLL has been achieved. Therefore, it will improve the whole dynamic parameters of the system. Based on the simulation results, the settling time for the estimated frequency and amplitude are 22 and 10 ms, respectively.

***doi**: 10.5829/ije.2021.34.06c.06*

1. INTRODUCTION

Single-phase grid-connected systems have gained substantial popularity in recent years. They are progressively utilized in numerous applications such as low power renewable energy resources [1-5]. One of the pivotal components for efficient operation of these systems is the synchronization unit. There is a multitude of synchronization methods in literature to monitor the grid voltage [6-8]. These units are responsible for the connection of the grid to the converter so that a unity power factor can be achieved. It is worth to note that phase, frequency, and amplitude are the other crucial information of the grid voltage for generating the reference current [9].

The most widespread technique of the synchronization is the Phase-Locked Loop (PLL) [10, 11]. The structures of PLLs that are presented in the literature, can generally be categorized into two classes: power-based PLLs (pPLLs) and quadrature signal generation PLLs (QSG-PLLs) [12]. In the pPLLs due to the presence of the multiplier, there are always second-order harmonic components [13, 14]. Therefore, the use of QSG-PLLs is more common than their pPLL counterparts [15-17]. The QSG-PLLs are a single-phase version of the synchronous reference frame (SRF), which are conventionally a three-phase PLL [18]. The predominant difference among the QSG-PLLs lies in their orthogonal signal generator (OSG) units which are responsible for generating a quadrature signal along with the PLL input signal [19]. There are various methods to generate the orthogonal signals, such as transport delay, Hilbert transformation, inverse park transformation, and filter base OSG [11]. All of these techniques have a suitable transient response, while they suffer from some weaknesses, such as frequency dependency, complexity, time-varying behavior, and inappropriate filtering.

The second-order generalized integrator (SOGI) method is another technique for generating quadrature signal which was introduced in literature [20] for the first time. The main issue of the SOGI is its frequency dependence, in which the estimated frequency is fed back to the SOGI blocks. Numerous techniques are presented in order to solve this problem. For instance, fixed

*Corresponding Author Institutional Email: h.hassanpour@email.kntu.ac.ir (H. Hassanpour)

Please cite this article as: H. Hassanpour, M. Ehsanian, Fast Grid Voltage Synchronization using Modified Frequency-locked Loop in Single Phase Grid-connected Power Systems, International Journal of Engineering, Transactions C: Aspects Vol. 34, No. 6, (2021) 1430-1437

frequency is one of the methods that is used to overcome this issue [21]. Rodríguez et al. [22], presented a novel structure which has employed frequency locked loop (FLL) to estimate the frequency instead of the utilization of the feedback loop [23-25]. Although in this method, the dynamics of PLL are improved [25-28], the estimated frequency is dependent on the phase jumps of the PLL input signal.

One of the critical problems in the frequency estimation of the PLLs is the low transient response in the presence of the phase angle error. A verity of reasons like system malfunctioning could be the important origin of this error. Since the FLL is settled in the PLL input section, it will increase the dependency of the estimated frequency to the PLL input signal variations. Therefore, if a phase jump occurs in the input signal, then it will directly be imported to the FLL.

The existence of DC offset in the input signal is another challenge which needs to be considered in the design of the PLL [11, 29]. Several factors might be the cause of the DC offset, such as DC offset of voltage sensors, data converters, and grid faults [9, 30]. One of the major deficiencies of the SOGI and the SOGI-FLL is the absence of a DC offset rejection loop in their structures. A multitude of techniques has been suggested in the literature to eliminate the DC offset [31, 32]. A common method which is used to such issue in SOGI structure is utilization of the modified SOGI [33, 34]. It is worth to mention that a comprehensive analysis of the DC offset rejection techniques in SOGI-PLLs has been discussed in literature [35].

In this paper, a novel adaptive method is presented which removes the effect of the phase angle error for the input signal in the estimation process of the frequency. It also eliminates the DC offset rejection of the input signal in a very suitable manner. The proposed method makes some changes in the structure of the SOGI-FLL so that it can enhance the transient response for the estimated frequency signal. With the minimization of the estimated signal error, the dynamic responses of the PLL are improved. Additionally, a DC offset rejection is utilized to cancel the offset of the input signal. The corresponding relations for the proposed structure are discussed completely, where the correctness of the relations was demonstrated by the simulations.

This paper is organized as follows: section 2 introduces the SOGI-PLL and its performance; and after that, the FLL block is described along with its problems. The DC offset rejection loop is also presented in this section. Section 3 proposes a solution to improve the FLL units which are used to enhance the PLL dynamic performance. This section formulates the proposed method. Simulation results and comparisons are presented in section 5. Section 6 contains the conclusions.

2. STRUCTURE OF SOGI-FLL WITH DC-OFFSET REJECTION

The general structure of the QSG-PLL is shown in Figure 1, where v_i is the input signal of the PLL. v_α and v_β demonstrate the quadrature signal and V represents the amplitude of the input voltage. Moreover, ω_n, $\hat{\theta}$, and $\hat{\omega}$ mark the nominal frequency, estimated phase angle, and the estimated frequency, respectively. As it can be observed, the QSG structure consists of an OSG block. In addition, the park transformation is utilized in their structure for converting $\alpha\beta$ to dq frame. The SOGI block will be used as an OSG block.

Figure 2 illustrates the whole structure of a SOGI in which the two orthogonal signals (v_α, v_β) have been produced in its output. v_α contains the same phase with the input signal, where its amplitude is equal to the input voltage amplitude. On the other hand, v_β has a 90° phase shift and the same amplitude with the input signal. The two closed-loop transfer functions of the SOGI will abide by Rodríguez et al. [22]:

$$H_\alpha(s) = \frac{v_\alpha(s)}{v_i(s)} = \frac{k\hat{\omega}s}{s^2+k\hat{\omega}s+\hat{\omega}^2} \quad (1)$$

$$H_\beta(s) = \frac{v_\beta(s)}{v_i(s)} = \frac{k\hat{\omega}^2}{s^2+k\hat{\omega}s+\hat{\omega}^2} \quad (2)$$

Where $\hat{\omega}$ is resonance frequency which is fed back from PLL output (before integrator in Figure 1), and k is the gain which affects the bandwidth of the closed-loop SOGI. It is equal to the damping ratio multiplied by two ($k = 2\xi$). The bode plot of $H_\alpha(s)$ and $H_\beta(s)$ for different values of $k = 0.1,\ 0.6,\ 2.2$ are shown in Figure 3. As it can be observed from the Figures 3(a) and 3(b), $H_\alpha(s)$ and $H_\beta(s)$ behave like a band-pass and a low-pass filter, respectively. For $H_\alpha(s)$, $\hat{\omega}$ is the central frequency, and because of the small bandwidth of the filter, the larger value of k provides better filtering capability. If the central frequency ($\hat{\omega}$) of the band-pass filter is considered equal to the nominal frequency ω_n ($\hat{\omega}$=ω_n), v_α will be identical to the input signal in steady-state ($v_\alpha = v_i$). Likewise, by the aforementioned assumption, v_β will be equal to v_i with a 90° phase shift. As a result, the SOGI structure can produce two orthogonal signals which then will be filtered.

In SOGI-PLL the estimated frequency is fed back to SOGI block, which causes the frequency dependency. Therefore, the transient response of the estimated frequency increases. In contrast, for SOGI-FLL the estimated frequency is prepared by the FLL block, and there is no need for a feedback loop, so the settling time of the estimated frequency is lower than the SOGI-PLL [23]. In order to solve this issue, the FLL block is added to the structure which provides the capability of generating the estimated frequency without using feedback loop. Figure 1(a) illustrates the SOGI-FLL

topology where e_v and e_f are the voltage and frequency errors, respectively, and γ represents the gain. The transfer function of e_v/v_i is as follows[20]:

$$\frac{e_v(s)}{v_i(s)} = \frac{s^2+\hat{\omega}^2}{s^2+k\hat{\omega}s+\hat{\omega}^2} \quad (3)$$

As the loop of SOGI-FLL demonstrates very nonlinear characteristics, we cannot perform linear analyses to determine the value of γ. Complete dynamic analysis along with the techniques of linearity enhancement for the SOGI-FLL are available in literature [22]. The linear loop of FLL is shown in Figure 4(b) where Γ is a constant coefficient, and can be obtained using following expression [22]:

$$\Gamma = \gamma \frac{V^2}{k\hat{\omega}} \quad (4)$$

The closed-loop transfer function of Figure 4(b) can be written as follows:

$$\frac{\hat{\omega}}{\omega} = \frac{\Gamma}{s+\Gamma} \quad (5)$$

It can be concluded from Equation (5) that the dynamic response of the FLL is only dependent to the value of Γ. Settling time for the FLL is approximately equal to:

$$t_s = \frac{5}{\Gamma} \quad (6)$$

By substituting the value of Γ from Equation (4) into Equation (6), the settling time will be:

$$t_s = \frac{5k\hat{\omega}}{\gamma V^2} \quad (7)$$

Offset DC rejection is also a critical issue in the design of the PLLs. As it was shown in the bode plot of Figure 3(b) , the ratio of $\frac{v_\beta}{v_i}(s)$ cannot filter the DC component. The value of $\frac{v_\beta}{v_i}(s)$ at $\omega = 0$ is equal to:

$$\frac{v_\beta}{v_i}(j0) = 1 \quad (8)$$

Equation (8) illustrates that if the input voltage v_i has a DC component, then it will deteriorate v_β. The modified SOGI is utilized to solve this problem, which is illustrated in Figure 5(a) where v_{DC} is the estimated DC component of the input signal, and k_{DC} is the gain of the DC offset rejection loop. This technique uses an integrator and a gain coefficient of $k_{DC}\hat{\omega}$ to estimate the DC component of the input signal. Afterwards, this estimated DC component is subtracted from the input signal to enhance the system capability in the DC offset rejection.

The corresponding transfer functions of SOGI with DC offset rejection loop are:

$$\frac{v_\alpha(s)}{v_i(s)} = \frac{k_{DC}\hat{\omega}s^2}{s^3+(k+k_{DC})\hat{\omega}s^2+\hat{\omega}^2 s+k_{DC}\hat{\omega}^3} \quad (9)$$

$$\frac{v_\beta(s)}{v_i(s)} = \frac{k_{DC}\hat{\omega}^2 s}{s^3+(k+k_{DC})\hat{\omega}s^2+\hat{\omega}^2 s+k_{DC}\hat{\omega}^3} \quad (10)$$

$$\frac{v_{DC}(s)}{v_i(s)} = \frac{k_{DC}\hat{\omega}(s^2+\hat{\omega}^2)}{s^3+(k+k_{DC})\hat{\omega}s^2+\hat{\omega}^2 s+k_{DC}\hat{\omega}^3} \quad (11)$$

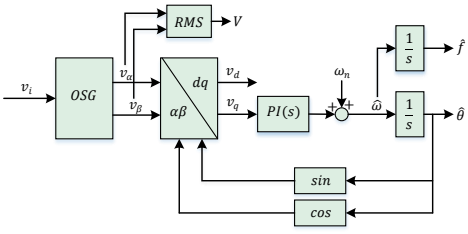

Figure 1. Diagram of a standard QSG-PLL

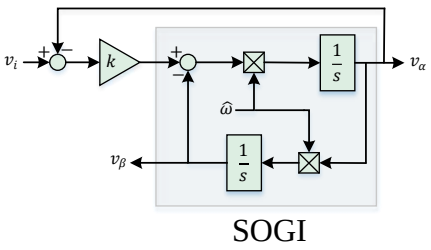

Figure 2. Structure of SOGI

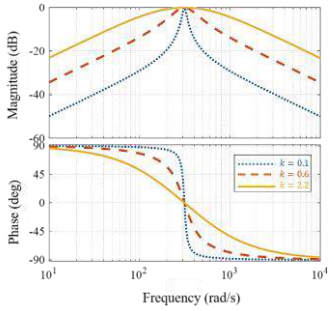

(a)

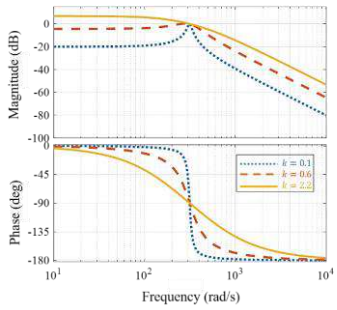

(b)

Figure 3. Bode diagram of SOGI closed-loop transfer function. a)$\boldsymbol{H_\alpha(s) = \frac{v_\alpha(s)}{v_i(s)}}$, b)$\boldsymbol{H_\beta(s) = \frac{v_\beta(s)}{v_i(s)}}$

The bode diagrams of the above transfer functions with the gains of $k = \sqrt{2}$ and $k_{DC} = 0 \cdot 4$ are demonstrated in Figure 5(b). As it is visible, the behavior of v_{DC}/v_i is similar to a low pass filter which makes the v_β/v_i characteristic behave like a band-pass filter. On the other hand, the ratio of v_α/v_i is a band-pass filter just as before.

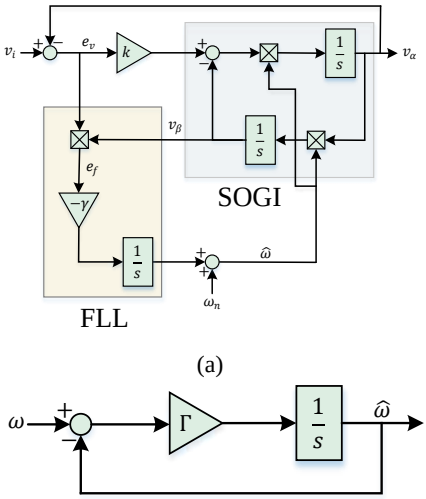

(a)

(b)

Figure 4. Structure of SOGI with FLL loop. a) Complete structure of SOGI-FLL, b) Simplified linear loop of FLL

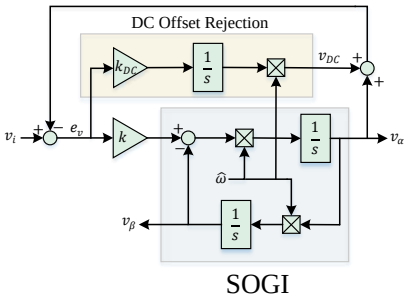

(a)

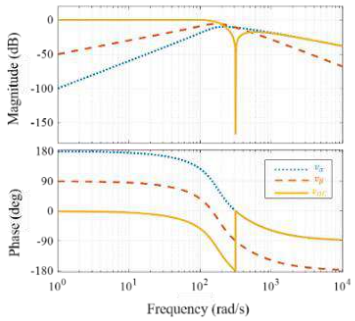

(b)

Figure 5. a) Structure of SOGI with DC offset rejection loop, b) Bode diagram of $\frac{v_\alpha}{v_i}, \frac{v_\beta}{v_i}, \frac{v_{DC}}{v_i}$

3. THE PROPOSED STRUCTURE

As it was mentioned before, utilization of an FLL results in a procedure for the estimation of the frequency. The virtue of this method is an independent estimation of the frequency which leads to a suitable transient response. Because the FLL is placed in the input of structure, changes of the input voltage can cause the unsatisfactory operation for the system. The phase jump of the input voltage is one of the changes that might happen. If a change occurs in the phase of the input signal, it will immediately be imported to the FLL unit. In other words, when the phase angle of the input voltage changes, the frequency error will no longer be equal to zero ($e_f \neq 0$). In order to illustrate this issue, a simulation for the SOGI-FLL structure is performed which is shown in Figure 6. In this test, a 45° phase jump in the time of $0 \cdot 1\ s$ is applied to the input voltage, and as a consequence, a considerable transient interval takes place in the estimated frequency response.

To solve the problem of frequency dependency, the structure of Figure 7 is proposed. In this structure, gain normalization is done in the first step. Then, the factor of Te^2 is added to the denominator of $\frac{1}{v_\alpha^2+v_\beta^2}$. When a phase

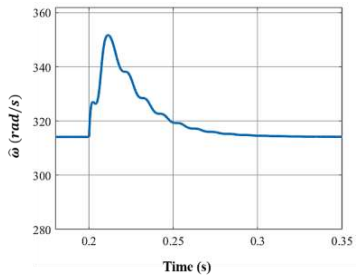

Figure 6. Transient response of FLL output signal

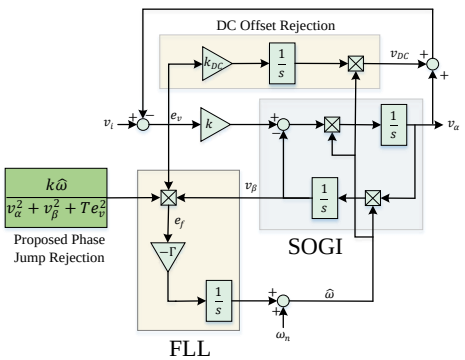

Figure 7. Proposed structure

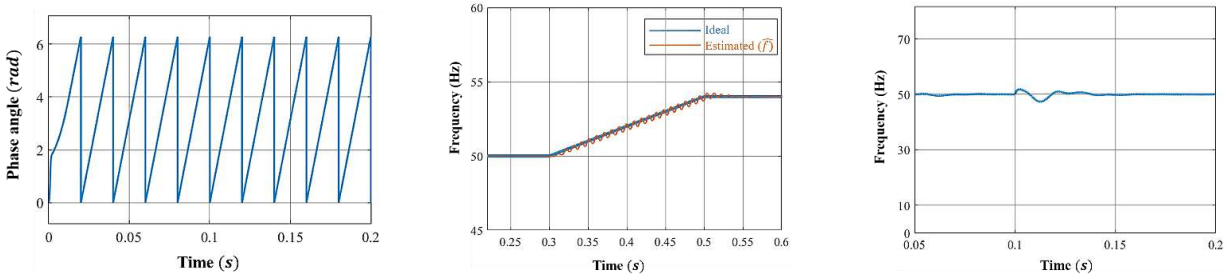

(a) (b) (c)

Figure 8. Performance of proposed structure. a) Phase angle of proposed structure, b) Estimated and ideal grid frequency, c) Estimated frequency with the presence of DC offset

jump occurs in the input signal, it leads to the voltage error (e_v). In the conventional SOGI-FLL structure e_v was multiplied by v_β to result the frequency error (e_f). However, in the proposed structure e_v is multiplied by a third term $\frac{k\hat{\omega}}{v_\alpha^2+v_\beta^2+Te_v^2}$. By taking into account that the term Te_v^2 is in the denominator, the effect of e_v on e_f will be suppressed, especially when a large value of T is chosen. By assuming that the input signal is as follow:

$$v_i(t) = V\cos(\omega t) \tag{12}$$

The two quadrature signals will be:

$$v_\alpha(t) = V\cos(\omega t) \tag{13}$$

$$v_\beta(t) = V\sin(\omega t) \tag{14}$$

Now, if a phase jump with the value of φ occurs in the input voltage, Equation (12) will change as:

$$v_i(t) = V\cos(\omega t + \varphi) \tag{15}$$

At the first moment, the phase change is not reflected in the quadrature signals, and Equation (13) as well as Equation (14) will remain unchanged. Hence, the frequency error can be written as follows:

$$e_f = v_\beta \times e_v = (V\sin(\omega t)) \times (v_i - v_\alpha) \tag{16}$$

By substituting Equations (13) and (14) into Equation (16), the frequency error will be calculated as follows:

$$e_f = (V\sin(\omega t)) \times (V\cos(\omega t + \varphi) - V\cos(\omega t)) \tag{17}$$

With the simplification of Equation (17), the average frequency error can be written as follows:

$$\bar{e_f} = -\frac{1}{2}\sin\varphi \tag{18}$$

The estimated frequency will be:

$$\hat{\omega} = \frac{1}{s}\left[\frac{k\hat{\omega}}{v_\alpha^2+v_\beta^2+Te_v^2} \times -\frac{1}{2}\sin(\varphi) \times -\Gamma\right] \tag{19}$$

As it can be observed in Equation (19), larger value of T will result in a corresponding smaller value for $\hat{\omega}$. Therefore, by considering Equation (7), the lower value of $\hat{\omega}$ will decrease the settling time to the desired amount.

4. SIMULATION RESULTS

4. 1. Performance of The Proposed Structure

The whole system is simulated in the MATLAB Simulink environment where the parameters of the systems are summarized in Table 1.

Figure 8(a) shows the estimated phase angle of the proposed PLL. It is obvious that the phase angle has periodic feature. Moreover, as the results indicate, the PLL works correctly. In Figure 8(b) the proposed structure is tested by means of a ramp change for the grid frequency where the grid frequency changes from $50\ Hz$ to $54\ Hz$ with a slope of $20\ Hz/s$. As it can be observed, the estimated frequency ($\hat{f}$) accurately follows the grid frequency where the grid frequency is shown with the blue plot, and the red plot represents the estimated frequency. Figure 8(c) shows the estimated frequency when the input grid voltage has a DC offset, which is a step change having the value equal to the 10 percent of the grid voltage amplitude.

TABLE 1. System parameters

Item	Parameter	Value
Grid voltage Amplitude	V	$220\ V$ (RMS)
Grid Frequency	f	$50\ Hz$
PLL Gain	k	$\sqrt{2}$
PI Proportional Gain	k_p	7878
PI Integral Gain	k_i	$137 \cdot 5$
FLL Gain	Γ	50
Proposed Phase Jump Rejection Parameter	T	300
Offset DC Rejection Gain	k_{DC}	$0 \cdot 4$

4. 2. Comparison In this section, SOGI, SOGI-FLL, and the proposed structures are compared. In the first test, the transient response of the estimated frequency between the conventional and the proposed FLL is compared. For this test, a step change with a value of 45° in $0.1\ s$ is applied to the phase of the input grid voltage. The transient response for the two structures is demonstrated in Figure 9 where the result shows that the estimated frequency of the conventional FLL has a considerable transient value. Also, its overshoot and settling time are $38\ Rad/s$ and $49\ ms$, respectively. On the other side, the estimated frequency of the proposed FLL, has $1\ Rad/s$ overshoot while the corresponding settling time is almost zero. The obtained characteristics of the conventional and proposed FLL are summarized in TABLE .

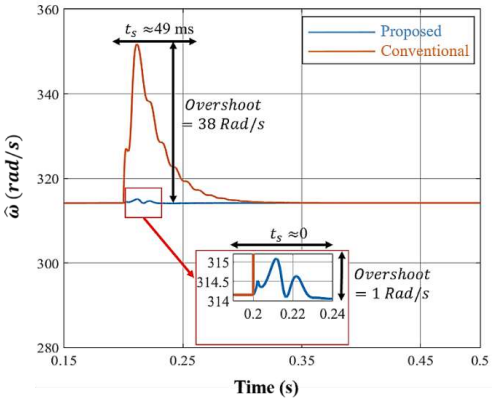

Figure 9. Output signal of FLL for conventional FLL and proposed FLL

TABLE 2. Comparison of conventional fll and proposed fll

Structure	Overshoot of $\hat{\omega}$	Settling Time of $\hat{\omega}$
Conventional FLL	$38\ Rad/s$	$49\ ms$
Proposed FLL	$1\ Rad/s$	zero

In another test, the estimated amplitude ($\hat{V}$) and frequency ($\hat{f}$) for the three structures are compared. All simulations have been performed in the same environment, where the corresponding parameters are shown in Table 1. Figure 10(a) shows the estimated frequency for SOGI which its settling time is equal to $157\ ms$. Also, Figure 10(b) shows the estimated amplitude for SOGI structure where its settling time is $140\ ms$. Figures 10 (c) and**Figure** 10(d) illustrate the estimated frequency and amplitude for the SOGI-FLL structure. They illustrate that the settling time is $50\ ms$ for the estimated frequency and $55\ ms$ for the estimated amplitude. The achieved results of the proposed system are demonstrated at Figures 10(e) and 10(f). Figure10(e) shows the estimated frequency in which the settling time is equal to $22\ ms$. Figure10(f) shows the estimated amplitude, where the settling time is $10\ ms$. Table 3 exhibits a comparison among the three structures from the viewpoint of settling time. It is apparently clear that the dynamic characteristics of the proposed method are better than the counterpart structures.

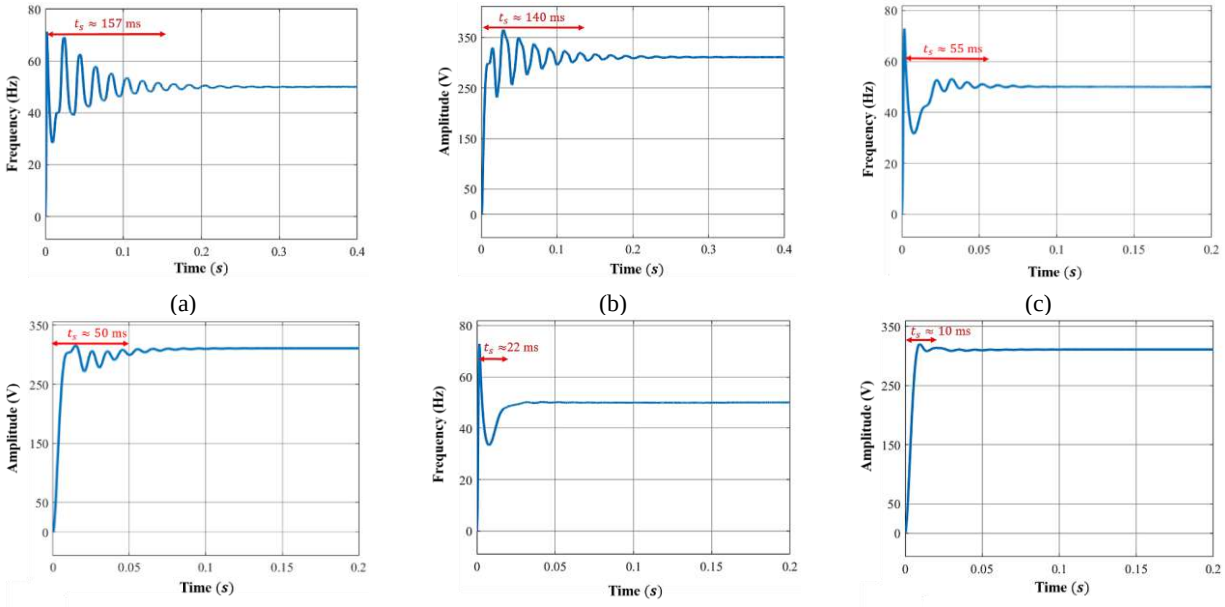

Figure 10. Dynamic performance of SOGI, SOGI-FLL, and proposed method. a) estimated frequency of SOGI, b) estimated amplitude of SOGI, c) estimated frequency of SOGI-FLL, d) estimated amplitude of SOGI-FLL, e) estimated frequency of proposed method, f) estimated amplitude of proposed method

TABLE 3. Comparison of sogi, sogi-fll, and proposed method

Structure	Settling Time of $\hat{V}$	Settling Time of $\hat{f}$
SOGI	140 ms	157 ms
SOGI-FLL	50 ms	55 ms
Proposed	10 ms	22 ms

5. CONCLUSION

The dynamic response of PLLs is a challenging issue in the design of the grid-connected single-phase power systems. A novel SOGI-FLL structure with DC offset rejection loop is introduced in this paper. The proposed mechanism solves the problem of the transient response produced by FLL in phase jumps of the grid voltage. From the viewpoint of the dynamic response, it completely removes the transient response. The simulations demonstrate the proper functionality of the system. Based on the results, the settling time for the estimated frequency along with the amplitude are $22ms$ and $10ms$, respectively.

6. REFERENCES

1. Golestan, S., Monfared, M., Freijedo, F.D. and Guerrero, J.M., "Design and tuning of a modified power-based pll for single-phase grid-connected power conditioning systems", ***IEEE Transactions on Power Electronics***, Vol. 27, No. 8, (2012), 3639-3650. doi: 10.1109/TPEL.2012.2183894.
2. Ming, W., Zhong, Q. and Zhang, X., "A single-phase four-switch rectifier with significantly reduced capacitance", ***IEEE Transactions on Power Electronics***, Vol. 31, No. 2, (2016), 1618-1632. doi: 10.1109/TPEL.2015.2414425.
3. Abeywardana, D.B.W., Hredzak, B. and Agelidis, V.G., "An input current feedback method to mitigate the dc-side low-frequency ripple current in a single-phase boost inverter", ***IEEE Transactions on Power Electronics***, Vol. 31, No. 6, (2016), 4594-4603. doi: 10.1109/TPEL.2015.2473170.
4. Karimi-Ghartemani, M., Khajehoddin, S.A., Jain, P. and Bakhshai, A., "A systematic approach to dc-bus control design in single-phase grid-connected renewable converters", ***IEEE Transactions on Power Electronics***, Vol. 28, No. 7, (2013), 3158-3166. doi: 10.1109/TPEL.2012.2222672.
5. Levron, Y., Canaday, S. and Erickson, R.W., "Bus voltage control with zero distortion and high bandwidth for single-phase solar inverters", ***IEEE Transactions on Power Electronics***, Vol. 31, No. 1, (2016), 258-269. doi: 10.1109/TPEL.2015.2399431.
6. Dean, R.N. and Rane, A.K., "A digital frequency-locked loop system for capacitance measurement", ***IEEE Transactions on Instrumentation and Measurement***, Vol. 62, No. 4, (2013), 777-784. doi: 10.1109/TIM.2013.2240092.
7. Lee, K., Lee, J., Shin, D., Yoo, D. and Kim, H., "A novel grid synchronization pll method based on adaptive low-pass notch filter for grid-connected pcs", ***IEEE Transactions on Industrial Electronics***, Vol. 61, No. 1, (2014), 292-301. doi: 10.1109/TIE.2013.2245622.
8. Reza, M.S., Ciobotaru, M. and Agelidis, V.G., "Tracking of time-varying grid voltage using dft based second order generalized integrator technique", in 2012 IEEE International Conference on Power System Technology (POWERCON). 1-6.
9. Golestan, S., Guerrero, J.M. and Vasquez, J.C., "Three-phase plls: A review of recent advances", ***IEEE Transactions on Power Electronics***, Vol. 32, No. 3, (2017), 1894-1907. doi: 10.1109/TPEL.2016.2565642.
10. Golestan, S. and Guerrero, J.M., "Conventional synchronous reference frame phase-locked loop is an adaptive complex filter", ***IEEE Transactions on Industrial Electronics***, Vol. 62, No. 3, (2015), 1679-1682. doi: 10.1109/TIE.2014.2341594.
11. Han, Y., Luo, M., Zhao, X., Guerrero, J.M. and Xu, L., "Comparative performance evaluation of orthogonal-signal-generators-based single-phase pll algorithms—a survey", ***IEEE Transactions on Power Electronics***, Vol. 31, No. 5, (2016), 3932-3944. doi: 10.1109/TPEL.2015.2466631.
12. Golestan, S., Guerrero, J.M. and Vasquez, J.C., "Single-phase plls: A review of recent advances", ***IEEE Transactions on Power Electronics***, Vol. 32, No. 12, (2017), 9013-9030. doi: 10.1109/TPEL.2017.2653861.
13. Golestan, S., Ramezani, M., Guerrero, J.M., Freijedo, F.D. and Monfared, M., "Moving average filter based phase-locked loops: Performance analysis and design guidelines", ***IEEE Transactions on Power Electronics***, Vol. 29, No. 6, (2014), 2750-2763. doi: 10.1109/TPEL.2013.2273461.
14. Elrayyah, A., Sozer, Y. and Elbuluk, M., "Robust phase locked-loop algorithm for single-phase utility-interactive inverters", ***IET Power Electronics***, Vol. 7, No. 5, (2014), 1064-1072. doi: 10.1049/iet-pel.2013.0351.
15. Lamo, P., López, F., Pigazo, A. and Azcondo, F.J., "An efficient fpga implementation of a quadrature signal-generation subsystem in srf plls in single-phase pfcs", ***IEEE Transactions on Power Electronics***, Vol. 32, No. 5, (2017), 3959-3969. doi: 10.1109/TPEL.2016.2582534.
16. Golestan, S., Guerrero, J.M., Vidal, A., Yepes, A.G., Doval-Gandoy, J. and Freijedo, F.D., "Small-signal modeling, stability analysis and design optimization of single-phase delay-based plls", ***IEEE Transactions on Power Electronics***, Vol. 31, No. 5, (2016), 3517-3527. doi: 10.1109/TPEL.2015.2462082.
17. Guan, Q., Zhang, Y., Kang, Y. and Guerrero, J.M., "Single-phase phase-locked loop based on derivative elements", ***IEEE Transactions on Power Electronics***, Vol. 32, No. 6, (2017), 4411-4420. doi: 10.1109/TPEL.2016.2602229.
18. Se-Kyo, C., "A phase tracking system for three phase utility interface inverters", ***IEEE Transactions on Power Electronics***, Vol. 15, No. 3, (2000), 431-438. doi: 10.1109/63.844502.
19. Stojić, D., Georgijević, N., Rivera, M. and Milić, S., "Novel orthogonal signal generator for single phase pll applications", ***IET Power Electronics***, Vol. 11, No. 3, (2018), 427-433. doi: 10.1049/iet-pel.2017.0458.
20. Ciobotaru, M., Teodorescu, R. and Blaabjerg, F., "A new single-phase pll structure based on second order generalized integrator", in 2006 37th IEEE Power Electronics Specialists Conference. 1-6.
21. Xiao, F., Dong, L., Li, L. and Liao, X., "A frequency-fixed sogi-based pll for single-phase grid-connected converters", ***IEEE***

Transactions on Power Electronics, Vol. 32, No. 3, (2017), 1713-1719. doi: 10.1109/TPEL.2016.2606623.

22. Rodríguez, P., Luna, A., Candela, I., Mujal, R., Teodorescu, R. and Blaabjerg, F., "Multiresonant frequency-locked loop for grid synchronization of power converters under distorted grid conditions", ***IEEE Transactions on Industrial Electronics***, Vol. 58, No. 1, (2011), 127-138. doi: 10.1109/TIE.2010.2042420.
23. Andromeda, T., Facta, M. and Setiawan, I., "Comparison of sogi-fll with sogi-pll for single-phase grid-connected inverters", in E3S Web of Conferences, EDP Sciences. Vol. 125, 14005.
24. Jackson, R., Zulkifli, S.A., Benbouzid, M., Salimin, S., Khan, M.H., Elhassan, G. and Pathan, E., "A comprehensive motivation of multilayer control levels for microgrids: Synchronization, voltage and frequency restoration perspective", ***Applied Sciences***, Vol. 10, No. 23, (2020), 8355.
25. Hackl, C.M. and Landerer, M., "Modified second-order generalized integrators with modified frequency locked loop for fast harmonics estimation of distorted single-phase signals", ***IEEE Transactions on Power Electronics***, Vol. 35, No. 3, (2020), 3298-3309. doi: 10.1109/TPEL.2019.2932790.
26. Karkevandi, A.E. and Daryani, M.J., "Frequency estimation with antiwindup to improve sogi filter transient response to voltage sags", in 2018 6th International Istanbul Smart Grids and Cities Congress and Fair (ICSG). 188-192.
27. Rodriguez, P., Luna, A., Ciobotaru, M., Teodorescu, R. and Blaabjerg, F., "Advanced grid synchronization system for power converters under unbalanced and distorted operating conditions", in IECON 2006 - 32nd Annual Conference on IEEE Industrial Electronics. 5173-5178.
28. Kherbachi, A., Bendib, A., Kara, K. and Chouder, A., "Arm based implementation of sogi-fll method for power calculation in single-phase power system", in 2017 5th International Conference on Electrical Engineering - Boumerdes (ICEE-B). 1-6.
29. Zheng, L., Geng, H. and Yang, G., "Fast and robust phase estimation algorithm for heavily distorted grid conditions", ***IEEE Transactions on Industrial Electronics***, Vol. 63, No. 11, (2016), 6845-6855. doi: 10.1109/TIE.2016.2585078.
30. Stringer, N.T., "The effect of dc offset on current-operated relays", ***IEEE Transactions on Industry Applications***, Vol. 34, No. 1, (1998), 30-34. doi: 10.1109/28.658712.
31. Xin, Z., Wang, X., Qin, Z., Lu, M., Loh, P.C. and Blaabjerg, F., "An improved second-order generalized integrator based quadrature signal generator", ***IEEE Transactions on Power Electronics***, Vol. 31, No. 12, (2016), 8068-8073. doi: 10.1109/TPEL.2016.2576644.
32. Matas, J., Castilla, M., Miret, J., Vicuña, L.G.d. and Guzman, R., "An adaptive prefiltering method to improve the speed/accuracy tradeoff of voltage sequence detection methods under adverse grid conditions", ***IEEE Transactions on Industrial Electronics***, Vol. 61, No. 5, (2014), 2139-2151. doi: 10.1109/TIE.2013.2274414.
33. Li, J., Zhao, J., Wu, J. and Xu, P., "Improved dual second-order generalized integrator pll for grid synchronization under non-ideal grid voltages including dc offset", in 2014 IEEE Energy Conversion Congress and Exposition (ECCE). 136-141.
34. Yu, J., Xu, Y., Cao, Y. and Yu, J., "An improved dual second-order generalized integrator pll under non-ideal grid conditions", in 2016 35th Chinese Control Conference (CCC)., 8644-8648.
35. Xie, M., Wen, H., Zhu, C. and Yang, Y., "Dc offset rejection improvement in single-phase sogi-pll algorithms: Methods review and experimental evaluation", ***IEEE Access***, Vol. 5, (2017), 12810-12819. doi: 10.1109/ACCESS.2017.2719721.

Persian Abstract

چکیده

یکی از اجزاء اصلی جهت عملکرد صحیح مبدل‌های تکفاز متصل به شبکه واحد همگام‌ساز است. این مقاله یک حلقه قفل فاز سریع و خود تطبیق ارائه می‌کند که پاسخ دینامیکی فرکانس و دامنه تخمین زده شده برای سیستم‌های قدرت تکفاز متصل به شبکه را بهبود می‌بخشد. انتگرال‌گیر تعمیم یافته مرتبه دوم (SOGI) به همراه حلقه قفل فرکانس مورد استفاده قرار گرفته است که شامل حلقه حذف‌کننده آفست DC نیز می‌باشد. روش ارائه شده نه تنها پاسخ گذرای فرکانس تخمین زده شده تولیدی توسط حلقه قفل فرکانس به ازای پرش‌های زاویه فاز ولتاژ شبکه را حذف می‌کند، بلکه ویژگی‌های دینامیکی حلقه قفل فاز را نیز بهبود می‌بخشد. تمامی سیستم در محیط متلب شبیه‌سازی شده، به طوری که زمان نشست بسیار کوچک برای حلقه قفل فرکانس بدست آمده است. لذا تمامی پارامترهای دینامیکی سیستم بهبود یافته است. بر اساس نتایج شبیه‌سازی، زمان نشست فرکانس و دامنه تخمین زده شده به ترتیب ۲۲ و ۱۰ میلی ثانیه بدست آمده‌اند.

IJE TRANSACTIONS C: Aspects Vol. 34, No. 6, (June 2021) 1438-1444

International Journal of Engineering

Journal Homepage: www.ije.ir

Dual Output Voltage Differencing Buffered Amplifier Based Active -C Multiphase Sinusoidal Oscillator

P. Gupta*, R. Pandey

Electronics and Communication Engineering Department, Delhi Technological University, Main Bawana Road, Delhi, India

P A P E R I N F O

Paper history:
Received 08 December 2020
Received in revised form 11 February 2021
Accepted 27 February 2021

Keywords:
Multiphase Sinusoidal Oscillator
Total Harmonic Distortion
Harmonic Distortion
All Pass Network
Non-idealities
Dual Output Voltage Differencing Buffered Amplifier

A B S T R A C T

A multiphase sinusoidal oscillator (MSO) using dual output voltage differencing buffered amplifier (DO-VDBA) is presented in this paper which provides n equally spaced phase sinusoids of equal magnitudes. The proposed MSO topology is realized using the first order all pass network (APN). In the proposed structure the output voltages are made available at low impedance nodes which makes the proposed MSO easy for cascadability. Making the proposed structure a resistorless structure is a major challenge. The main benefits of the structure are easy integration and less power losses. The formulation of frequency and condition of oscillation is derived mathematically. The oscillation frequency can be tuned electronically, is an added advantage of the proposed MSO. The effect of device non-idealities is also discussed in the study. To assess the proposed MSO performance further Monte Carlo analysis was carried out. The workability of the proposed structure is verified through SPICE simulations for a three (n=3) and four (n=4) phases MSO, and the obtained simulated results are in close agreement with the theoretical values. The total harmonic distortion (THD) is found to be quite low.

doi: *10.5829/ije.2021.34.06c.07*

NOMENCLATURE

C	Capacitance	**Greek Symbols**	
n	Nano	ε	Tracking Error
A	Ampere	α	$1-\varepsilon_{gm}$
V	Volt	β	1-ε
μ	Micro		

1. INTRODUCTION

The multiphase sinusoidal oscillators (MSO) generate multiple (≥3) sinusoidal signals of the same frequency which are equally spaced in phase. The widespread usage of MSO in telecommunication systems, power electronics, instrumentation, radar system and control systems is well known.

A large number of MSOs realization are available in the literature [1-22]. The available literature suggests that VDBA based MSO has not been realized so far; though a variety of MSOs has been designed using different active building blocks (ABB). These existing structures use n cascaded phase shifting networks such as first order low pass networks (LPNs) [1-4, 6-10, 12, 13, 17, 19], first order all pass networks (APNs) [5, 14-16, 18, 20] or first order high pass networks (HPNs) [11] in closed loop.

The available literature can be classified as voltage mode (VM) [1-9, 11, 12, 19, 20], or current mode (CM) [10, 11, 13-15, 18] configurations according to the output signal provided by MSO. The MSOs [1-5] realized using operational amplifiers (Op-Amp) have limited high frequency operation due to constant gain-bandwidth product and lower slew rate. To produce high frequency oscillations different current mode ABBs have been used such as second generation current conveyor (CCII) [6-11, 22] current differencing transconductance amplifier (CDTA) [14, 15], current differencing unit (CDU) [16], current feedback operational amplifier (CFOA) [17, 21], current controlled CDTA (CCCDTA) [18], and

*Corresponding Author Email: priyankagupta09@gmail.com (P. Gupta)

Please cite this article as: P. Gupta, R. Pandey, Dual Output Voltage Differencing Buffered Amplifier Based Active -C Multiphase Sinusoidal Oscillator, International Journal of Engineering, Transactions C: Aspects Vol. 34, No. 6, (2021) 1438-1444

operational transresistance amplifier (OTRA) [19, 20]. Moreover, these structures are capable of producing the high frequency oscillation. However, they suffer from few limitations including the number of active blocks per phase, the number of passive components, availability of output voltage at high impedance node. This paper presents a dual output voltage differencing buffered amplifier (DO-VDBA) based MSO consisting of n APN in a closed loop.

The DO-VDBA consists of an input voltage differencing stage and the output current is equal to transcoductance times the difference of voltages. Further, a voltage terminal at low impedance is also available, thus adding design flexibility. Thus it can be understood as a transconductance amplifier (TA) followed by a voltage buffer (inverting/non-inverting). Bias dependent transconductance adds the feature of electronic tunability of circuit parameters. Thus, the DO-VDBA has emerged as a promising choice for both VM and CM analog applications in the recent past. Since several structures of MSOs are available, a comparison Table 1 is drawn based on a) ABB, b) number of ABB required for per phase generation, c) mode of signal d) output impedance, e) design methodology f) no of passive components g) electronic tunability and h) the technology used.

It may be observed from Table 1 that, Opamp based structures have limited high-frequency operations [1-5]. MSOs provide voltage output at high impedance [6-9, 11, 12]. Structures presented in literature [1, 2, 8, 17] are not tunable as they make use of parasitic capacitance; MSOs provide current outputs so additional circuitry is required to convert it to voltage for driving voltage inputs circuits [10, 11, 13-15, 18], only limited structures provide electronic tenability [12-15, 18]. The MSO uses two

TABLE 1. Comparison with the previously available Multiphase sinusoidal oscillators

Ref.	ABB	No of ABB/ Phase	Mode of Output CM/VM operation Or mode of operation	Output Impedance	Design Technique	(R+C)/ Phase	Tunability/ Electronic control	Technology used
[1]	OpAmp	1	VM	Low	LPN	2+0	N/N	Op-Amp 741
[2]	OpAmp	1	VM	Low	LPN	2+0	N/N	Op-Amp 741
[3]	OpAmp	1	VM	Low	LPN	3+1	Y/N	LF351
[4]	OpAmp	1	VM	Low	LPN	2+1	Y/N	OPA 351 HA 2544
[5]	OpAmp	1	VM	Low	APN	3+1	Y/N	LF 351 HA 2533C Exp
[6]	CCII	1	VM	High	LPN	2+1	Y/N	AD844AN
[7]	CCII	1	VM	High	LPN	2+1	Y/N	AD844
[8]	CCII	1	VM	High	LPN	2+0	N/N	--
[9]	CCII	1	VM	High	LPN	2+1	Y/N	AD844Exp
[10]	CCII	1	CM	High	LPN	0+2	Y/N	Bipolar PR200N and R200N
[11]	CCII	1	VM	High	HPN	1+2	Y/N	CA 3096 E
[12]	OTA	1	VM	High	LPN	1+1	Y/N	CA3080
	OTA+buffer	1	VM	High	LPN	2+1	Y/N	
	OTA	2	VM	High	LPN	0+1	Y/Y	
	OTA+buffer	1	VM	High	LPN	0+3	Y/Y	
[13]	CDTA	1	CM	High	LPN	0+1	Y/Y	BipolarPR100N and NP100N
[14]	CDTA	2	CM	High	APN	0+1	Y/Y	BipolarPR100N and NP100N
[15]	CDTA	1	CM	High	APN	2+1	Y/Y	BipolarPR200N and NP200N
[16]	CDU	1	VM	High	APN	1+1	Y/N	CMOS 0.7 lm technology
[17]	CFOA	1	VM	Low	LPN	2+0	Y/N	AD844AN
[18]	CCCDTA	1	CM	High	APN	1+1	Y/Y	0.25µm CMOS technology
[19]	OTRA	1	VM	Low	LPN	2+1	Y/N	AD 844
[20]	OTRA	1	VM	Low	APN	3+1	Y/N	0.35µm TSMC CMOS technology
[21]	AOFC	٢	MV	woL	APN	5+1	N/N	AD 844
Proposed	DO-VDBA	1	VM	Low	APN	0+1	Y/Y	0.18 µm CMOS

ABBs per phase as against the rest of the structures [14, 21], only a few realizations are active C structures [10, 12-14].

Thus, this communication aims at presenting a new active – C MSO design using DO-VDBA based on APNs which overcomes all the limitations of existing structures and is the best suitable for voltage mode operations. Several applications have been used by many researchers in different fields including electronics [23-27] and others [28-32] using new advancements in technologies. The pros of the proposed MSO, when compared to the existing structures are that

- The proposed is resistorless giving the advantage of low power losses and better integration.
- The novelty of the current study is that MSO designed using DO-VDBA with zero resistors were explored very limited in previous researches.
- Moreover, a resistorless multiphase oscillator with DO-VDBA has not been studied in the past that makes the work new in the area.
- The proposed MSO provides a voltage output at a low impedance node. Therefore, no extra circuitry is required.
- The frequency of oscillation is electronically tunable.

2. PROPOSED DO-VDBA BASED ACTIVE -C MSO

The DO-VDBA is a five terminal element characterized by two high impedance voltage input terminals (p and n), one high output impedance terminal z and two low impedance inverted/non-inverted buffered output terminals (w-,w+), respectively; which makes it more flexible for circuit design applications as compared to other ABBs [22, 25-26].

The symbolic representation of DO-VDBA is given in Figure 1 and the port relationship is described by the matrix (1).

$$\begin{bmatrix} I_z \\ V_{w+} \\ V_{w-} \\ I_p \\ I_n \end{bmatrix} = \begin{bmatrix} 0 & 0 & 0 & g_m & -g_m \\ 1 & 0 & 0 & 0 & 0 \\ -1 & 0 & 0 & 0 & 0 \\ 0 & 0 & 0 & 0 & 0 \\ 0 & 0 & 0 & 0 & 0 \end{bmatrix} \begin{bmatrix} V_z \\ I_{w+} \\ I_{w-} \\ V_p \\ V_n \end{bmatrix} \quad (1)$$

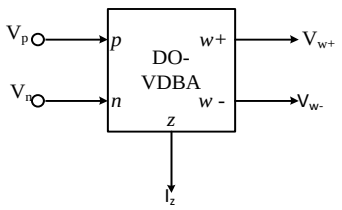

Figure 1. The circuit symbol of VDBA

where g_m represents the transconductance gain from input to z terminal of DO-VDBA. The DO-VDBA [24] based APN presented by Sotner et al. [23] and reproduced in Figure 2 is used for the proposed MSO realization.

The transfer function of the APN may be written as follows:

$$G(s) = \frac{V_o}{V_{in}} = \frac{g_m - sC}{g_m + sC} = \frac{1 - s\frac{C}{g_m}}{1 + s\frac{C}{g_m}} \quad (2)$$

The proposed MSO is shown in Figure 3 and its loop gain can be expressed as follows:

$$\mathbf{L(s)} = -\left(\frac{\mathbf{1} - \boldsymbol{s}\frac{\boldsymbol{C}}{\boldsymbol{g_m}}}{\mathbf{1} + \boldsymbol{s}\frac{\boldsymbol{C}}{\boldsymbol{g_m}}}\right)^{\mathbf{n}} \quad (3)$$

As per Barkhausen's criterion if the loop gain at a frequency ω_0, is unity the system results in sustained oscillation. Thus the proposed topology will provide sinusoidal oscillations if its loop gain is expressed as follows:

$$L(j\omega_o) = -A^n\left(\frac{1 - j\omega_o C/g_m}{1 + j\omega_o C/g_m}\right)^n = 1 \quad (4)$$

Thus the magnitude and phase response for Equation (4) can be found as Equations (5) and (6), respectively.

$$|L(j\omega_o)| = 1 \quad (5)$$

$$\angle L(j\omega_o) = 0 \quad (6)$$

As each APN provides an identical phase shift (ϕ), then the total phase shift of the loop (ϕ_t) to satisfy the Barkhausen Criteria for oscillations is given by the follow ing expressions:

$$\phi_t = n\phi + \pi = 2\pi \quad (7)$$

$$\phi = \frac{\pi}{n} \quad (8)$$

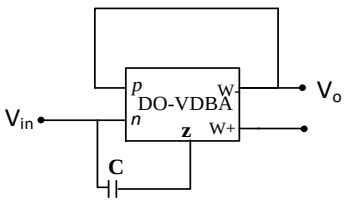

Figure 2. APN using DO-VDBA [25]

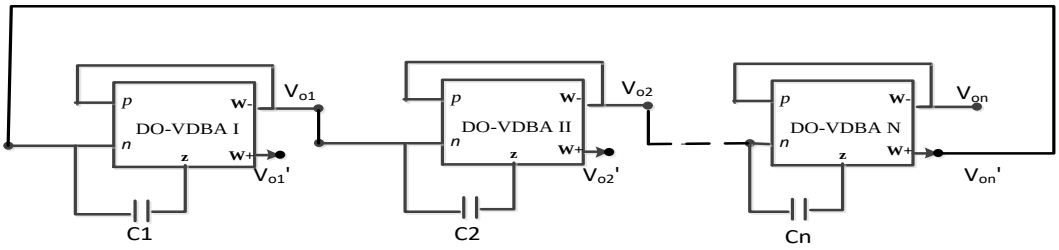

Figure 3. The proposed DO -VDBA based Active C MSO

Thus the condition of oscillation (CO) can be computed as CO: A=1 (9)

and the frequency of oscillation (FO) can be enumerated as follows:

$$f_o = \frac{g_m}{2\pi C}\tan\left(\frac{\pi}{2n}\right) \quad (10)$$

It may be observed from Equation (10) that the FO can be varied either by changing the value of C or can be electronically tuned through gm by varying the bias current.

3. NON-IDEALITY

The performance of the proposed MSO may deviate from the ideal one due to the deviation of the internal current and voltage transfer of VDBA from unity. These deviations amend the terminal characteristics as follow:

$$\begin{bmatrix} I_z \\ V_{w+} \\ V_{w-} \\ I_p \\ I_n \end{bmatrix} = \begin{bmatrix} 0 & 0 & 0 & \alpha g_m & -\alpha g_m \\ \beta_p & 0 & 0 & 0 & 0 \\ -\beta_p & 0 & 0 & 0 & 0 \\ 0 & 0 & 0 & 0 & 0 \\ 0 & 0 & 0 & 0 & 0 \end{bmatrix} \begin{bmatrix} V_z \\ I_{w+} \\ I_{w-} \\ V_p \\ V_n \end{bmatrix} \quad (11)$$

where $\alpha=1-\varepsilon_{gm}$.The ε_{gm} ($||\varepsilon_{gm}||<<1$) are transconductance tracking errors. The $\beta_p=1-\varepsilon_p$ where ε_p ($||\varepsilon_p||<<1$) represents the voltage tracking error from z terminal to w+. Similarly $\beta_n=1-\varepsilon_n$ with ε_n ($||\varepsilon_n||<<1$) being the voltage tracking error from z terminal to w- terminal. Considering these non-idealities into account the G(s) is modified as $G(s)_{\_n}$.

$$G(s)_{\_n} = \frac{1}{\beta_n}\frac{1-s\frac{C}{\alpha g_m}}{1+s\frac{C}{\alpha\beta_n g_m}} \quad (12)$$

$$L(s)_{\_n} = -\beta_p\left(\frac{1}{\beta_n}\right)^n\left(\frac{1-s\frac{C}{\alpha g_m}}{1+s\frac{C}{\alpha\beta_n g_m}}\right)^n \quad (13)$$

The non-ideal gains create some deviation in the transfer function. However, these small deviations can be compensated by properly adjusting the transconductance gains (g_m) of the VDBAs.

4. SIMULATION RESULTS

The proposed MSO has been validated through SPICE simulations using TSMC CMOS 0.18 µm technology. The CMOS DO-VDBA [23] which is reproduced in Figure 4 is used for simulation. Table 2 enlists the aspect ratios of the respective transistors. The supply voltages used are ± 1 V and the bias current I_b is set to 40µA. The g_m of the DO-VDBA is given by the following expression:

$$g_m = \sqrt{\mu_n C_{ox}\left(\frac{W}{L}\right)_{3,4} I_b} \quad (14)$$

The simulated value of g_m is observed to be 200µA/V against its theoretical value of 209 µA/V. The power consumption is observed to be 4 mW.

A simulation setup is arranged to get the output of the MSO of Figure 3 for n=3, for which values of all capacitors ($C_1=C_2=C_3$) are chosen as 5 pF. The steady-state output is shown in Figure 5(a) while the frequency spectrum is depicted in Figure 5(b). The simulated frequency of oscillations is observed to be 3.5 MHz against the theoretical value of 3.6 MHz. Total harmonic distortion (THD) was observed to be 0.78% which is a substantially low value.

Further, the proposed MSO was simulated for n = 4 and while capacitance values are still set as 5 pF. This results in a theoretically calculated FO of 2.6 MHz. The simulated steady-state output and corresponding frequency spectrum are depicted in Figures 6(a) and 6(b),

TABLE 2. Aspect Ratios

Transistor	(W/L)µm
M_1-M_4	7.2/1.8
M_5-M_8	27/0.54

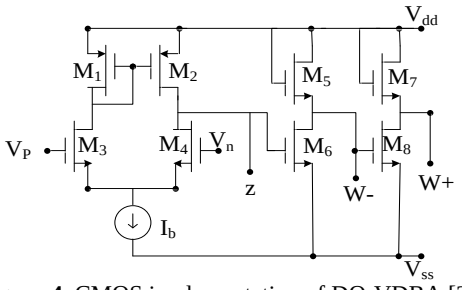

Figure 4. CMOS implementation of DO-VDBA [23]

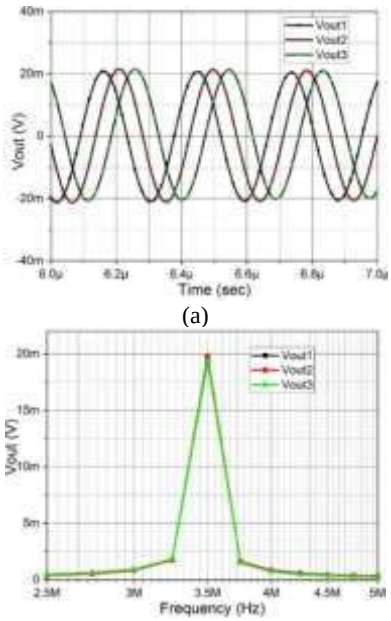

Figure 5. Simulated output for 3 phase MSO (a) Steady-state; (b) frequency spectrum

respectively. The simulated FO is observed to be 2.5 MHz and the THD as 1.19%.

Tuning of FO of 3 phase MSO with capacitance is depicted in Figure 7(a) and the variation of oscillating frequency with bias current I_{bias} is presented in Figure 7(b). It may be observed that the simulated frequencies closely follow the theoretical values.

To check the robustness and effect of parameter variations of the proposed MSO, the Monte-Carlo statistical analysis is done via simulation. Monte carlo analysis was carried out keeping n=4 and the resultant histogram obtained is shown in Figure 8. First, the 5% variation in the value of C is done and followed by considering 5% deviation in mobility, threshold voltage and oxide thickness to investigate the effect of mismatch on the frequency of oscillation. It is observed that the value of oscillation frequency remains close to its theoretical value of 2.6 MHz and hence almost unaffected by the parameter variations. Thus, it is worth mentioning that proposed structure is almost immune to parameteric variations.

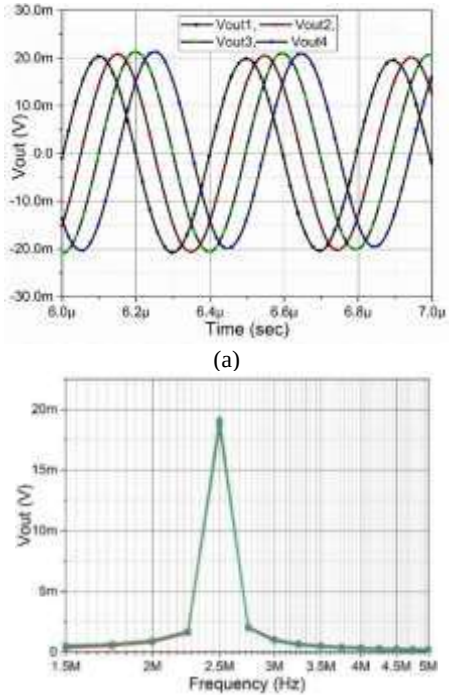

Figure 6. Simulated output for 4 phase MSO (a) Steady-state; (b) frequency spectrum

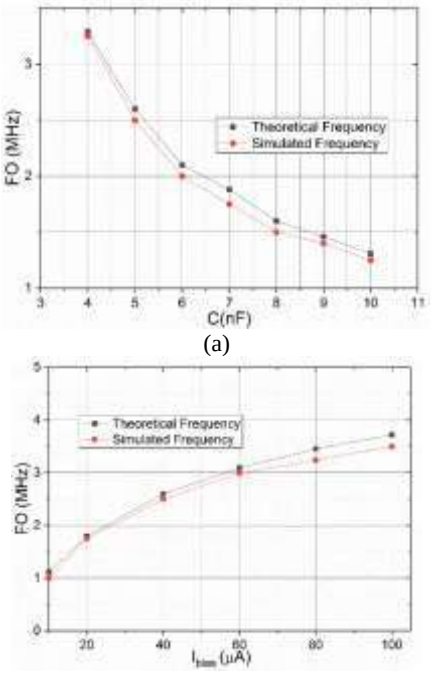

Figure 7. (a) FO vs C; (b) FO vs Ibias

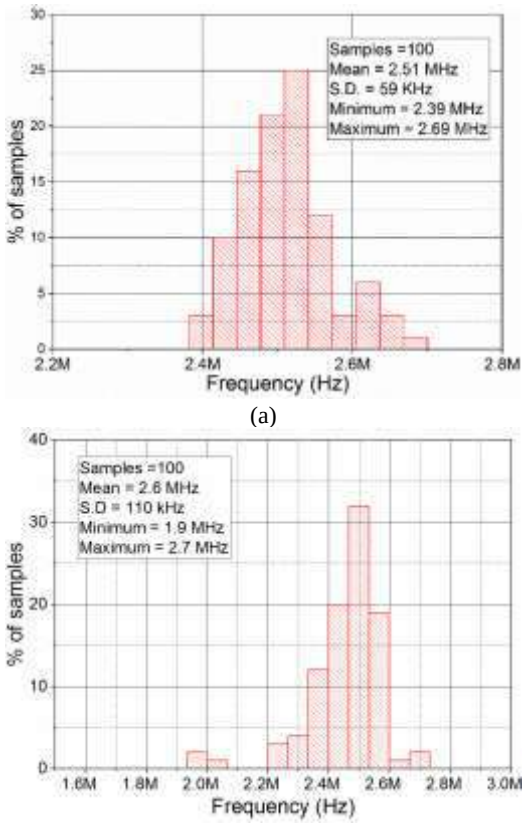

Figure 9. Monte Carlo simulation

5. CONCLUSION

An n phase Active-C MSO topology using DO-VDBAs was proposed in this paper. The proposed structure is a resistorless structure. The proposed structure provides n phase oscillations at low impedance nodes. As the proposed circuit provides output at low impedance nodes, so it can be readily used to drive voltage input circuits without needing any extra circuitry. Also, the frequency of oscillation can be tuned electronically. The effect of device non-idealities on the proposed MSO was analyzed. The functionality of the proposed MSO is verified through SPICE simulations for two instance cases (three and four-phase MSOs). The simulation results are found to be in close agreement with the theoretical values. Monte Carlo analyses have also been carried out to evaluate the robustness of the proposed structure. For future works, experimental analysis and validation of results shall be carried out using the off shelf ICs.

6. REFERENCES

1. Abuelma'atti M. T. and W. A. Almansoury, "Active-R multiphase oscillators," ***IEE Proceedings G-Electronic Circuits and Systems,*** Vol. 134, No. 6, (1987), 292-294. DOI: 10.1049/ip-g-1.1987.0046.
2. Stiurca, D. "On the multiphase symmetrical active-R oscillators," ***IEEE Transactions on Circuits and Systems II Analog Digital Signal Processing,*** Vol. 41, No. 2, (1994), 156-158. DOI: 10.1109/82.281848.
3. Gift, S. J. G. "Multiphase sinusoidal oscillator system using operational amplifiers," ***International Journal of Electronics,*** Vol. 83, No. 1, (1997), 61-68. DOI: 10.1080/002072197135652.
4. Gift, S. J. G. "Multiphase sinusoidal oscillator using inverting-mode operational amplifiers," ***IEEE Transactions on Instrumentation and Measurement,*** Vol. 47, No. 4, (1998), 986-991. DOI: 10.1109/19.744654.
5. Gift, S. J. G. "Application of all-pass filters in the design of multiphase sinusoidal systems," ***Microelectronics Journal,*** Vol. 31, No. 1, (2000), 9-13. DOI: 10.1016/S0026-2692(99)00084-1.
6. Wu, D. S., Liu, S.-I., Hwang, Y.-S. and Wu, Y.-P. "Multiphase sinusoidal oscillator using second-generation current conveyors," ***International Journal of Electronics,*** Vol. 78, No. 4, (1995), 645-651. DOI: 10.1080/00207219508926198.
7. Hou, C.-L. and Shen, B. "Second-generation current conveyor-based multiphase sinusoidal oscillators," ***International Journal of Electronics,*** Vol. 78, No. 2, (1995), 317-325. DOI: 10.1080/00207219508926165
8. Abuelma'atti, M. T. and Al-Qahtani, M. A. "A Grounded-Resistor Current Conveyor-Based Active-R Multiphase Sinusoidal Oscillator," ***Analog Integrated Circuits Signal Processing,*** Vol. 16, No. 1, (1998), 29-348. DOI: 10.1023/A:1008265817455
9. Skotis, G. D., and Psychalinos, C. "Multiphase sinusoidal oscillators using second generation current conveyors," ***AEU-International Journal of Electronics and Communications,*** Vol. 64, No. 12, (2010), 1178-1181. DOI: 10.1016/j.aeue.2009.11.013.
10. Abuelma'atti, M. T. and Al-Qahtani, M. A. "A new current-controlled multiphase sinusoidal oscillator using translinear current conveyors," ***IEEE Transactions on Circuits and Systems II Analog Digital Signal Processing,*** Vol. 45, No. 7, (1998), 881–885. DOI: 10.1109/82.
11. Abuelma'atti, M. T., Al-Qahtani and M. A. "Low component second-generation current conveyor-based multiphase sinusoidal oscillator," ***International Journal of Electronics,*** vol. 84, no. 1, (1998), 45–52. DOI: 10.1080/002072198134986
12. Khan, I. A., Ahmed, M. T. and Minhaj, N. "Tunable OTA-based multiphase sinusoidal oscillators," ***International Journal of Electronics,*** Vol. 72, No. 3, (1992), 443-450. DOI: 10.1080/00207219208925585
13. Tangsrirat, W. and Tanjaroen, W. "Current-Mode Multiphase Sinusoidal Oscillator Using Current Differencing Transconductance Amplifiers," ***Circuits, Systems & Signal Process.,*** Vol. 27, No. 1, (2008), 81-93. DOI: 10.1007/s00034-007-9010-y
14. Jaikla, W., Siripruchyanun, M., Biolek, D. and Biolkova, V. "High-output-impedance current-mode multiphase sinusoidal oscillator employing current differencing transconductance amplifier-based allpass filters," ***International Journal of Electronics,*** Vol. 97, No. 7, (2010), 811-826. DOI: 10.1080/00207211003733288.
15. Tangsrirat, W., Tanjaroen, W. and Pukkalanun, T. "Current-mode multiphase sinusoidal oscillator using CDTA-based allpass sections," ***International Journal of Electronics Communications,*** Vol. 63, No. 7, (2009), 616-622. DOI: 10.1016/j.aeue.2008.05.001.
16. Vavra, J. and Bajer, J. "Current-mode multiphase sinusoidal oscillator based on current differencing units," ***Analog Integrated Circuits Signal Processing,*** Vol. 74, No. 1, (2013), 121-128. DOI: 10.1007/s10470-012-9906-8.

17. Wu, D.-S., Liu, S.-I., Hwang, Y.-S. and Wu, Y.-P. "Multiphase sinusoidal oscillator using the CFOA pole," ***IEE Proceedings-Circuits, Devices and Systems,*** Vol. 142, No. I, (1995), 37. DOI: 10.1049/ip-cds:19951682.
18. Jaikla, V. and Prommee, P. "Electronically tunable current-mode multiphase sinusoidal oscillator employing CCDTA-based allpass filters with only grounded passive elements," ***Radioengineering***, Vol. 20, No. 3, (2011), 594-599.
19. Pandey, R., Pandey, N., Bothra, M. and Paul, S. K. "Operational transresistance amplifier-based multiphase sinusoidal oscillators," ***Journal of. Electrical Computer Engineering,*** Vol. 2011, (2011), 1-8. DOI: 10.1155/2011/586853
20. Pandey, R., Pandey, N., Mullick, R., Yadav, S. and Anurag, R. "All Pass Network Based MSO Using OTRA," ***Advances in Electronics,*** Vol. 2015, (2015), 1-7. DOI: 10.1155/2015/382360.
21. Yuce. E., Verma, R., Pandey, N. and Manaei, S. "New CFOA-based first-order all-pass filters and their applications," ***International Journal of Electronics and Communications (AEÜ),*** Vol. No. 103, (2019), 57-63. DOI : 10.1016/j.aeue.2019.02.017.
22. Kumar, A. and Paul, S.K. "Current mode First order Universal Filter and Multiphase Sinusoidal Oscillator" ***International Journal of Electronics and Communications,*** (2017). DOI: 10.1016/j.aeue.2017.07.004
23. Sotner, R., Jerabek, J. and Herencsar, N. "Voltage Differencing Buffered / Inverted Amplifiers and Their Applications for Signal Generation," ***Radioengineering,*** Vol. 22, No. 2, (2013), 490-504.
24. Gupta, P. and Pandey, R. "Voltage Differencing Buffered Amplifier based Voltage Mode Four Quadrant Analog Multiplier and its Applications," ***International Journal of Engineering, Transactions A: Basics,*** Vol. 32, No. 4, (2019), 528-535. DOI: 10.5829/IJE.2019.32.04A.10
25. Herencsar, N., Minaei, S., Koton, J., Yuce, E. and Vrba, K. "New resistorless and electronically tunable realization of dual-output VM all-pass filter using VDIBA," ***Analog Integrated Circuits and Signal Processing,*** Vol. 74, (2013), 141-154. DOI: 10.1007/s10470-012-9936-2
26. Singh, S. V., Tomar, R. S. and Chauhan D. S., "A New Trans-Admit tance-Mode Biquad Filter Suitable for Low Voltage Operation", ***International Journal of Engineering, Transactions B: Applications,*** Vol. 28, No. 12, (2015), 1738-1745. DOI: 10.5829/idosi.ije.2015.28.12c.06.
27. Farshidi, E. and Keramatzadeh, A., "A New Approach for low voltage CMOS based on current -controlled conveyors", ***International Journal of Engineering, Transactions B: Applications,*** Vol. 27, No. 5, (2014), 723-730. DOI: 10.5829/idosi.ije.2014.27.05b.07
28. Gharibshahian, E., "The Effect of Polyvinyl Alcohol Concentration on the Growth Kinetics of KTiOPO4 Nanoparticles Synthesized by the Co-precipitation Method", ***Hightech and Innovation Journal***, Vol. 1, No. 4, (2020), 187-193. DOI: 10.28991/HIJ-2020-01-04-06.
29. G. M. Elaragi. "Design and Operation of First Egyptian IEC Fusion Plasma Device", ***Emerging Science Jorrnal***, Vol. 3, No. 4, (2019), 241-248. DOI: 10.28991/esj-2019-01186.
30. Kibaara, S. K., Murage, D. K., Musau, P. and Saulo, M. J., "Comparative Analysis of Implementation of Solar PV Systems Using the Advanced SPECA Modelling Tool and HOMER Software: Kenyan Scenario", ***Hightech and Innovation Journal***, Vol. 1, No. 1, (2020), 8-20. DOI: 10.28991/HIJ-2020-01-01-02.
31. Sani, M. J., "Spin-Orbit Coupling Effect on the Electrophilicity Index, Chemical Potential, Hardness and Softness of Neutral Gold Clusters: A Relativistic Ab-initio Study, ***Hightech and Innovation Journal***, Vol. 2, No. 1, (2021), 38-50. DOI: 10.28991/HIJ-2021-02-01-05
32. Hosseini, S.M., "The Operation and Model of UPQC in Voltage Sag Mitigation Using EMTP by Direct Method", ***Emerging Science Jorrnal***, Vol. 2, No. 3, (2018), 148-156. DOI: 10.28991/esj-2018-01138.

Persian Abstract

چکیده

یک اسیلاتور سینوسی چند فازی (MSO)با استفاده از تقویت کننده بافر تفکیک کننده ولتاژ خروجی دوگانه (DO-VDBA)در این مقاله ارائه شده است که n سینوسیید فازی با اندازه مساوی با فاصله یکسان را ارائه می دهد. توپولوژی پیشنهادی MSO با استفاده از شبکه مرتب سازی برای اولین بار (APN)تحقق می یابد. در ساختار پیشنهادی ولتاژهای خروجی در گره های با امپدانس کم در دسترس قرار می گیرند که MSO پیشنهادی را برای انعطاف پذیری آسان می کند. ساخت ساختار پیشنهادی به عنوان سازه ای بدون مقاومت یک چالش اساسی است. مزایای اصلی سازه یکپارچه سازی آسان و اتلاف انرژی کمتر است. فرمول بندی فرکانس و شرایط نوسان از نظر ریاضی مشتق شده است. فرکانس نوسان را می توان به صورت الکترونیکی تنظیم کرد ، یک مزیت اضافی برای MSO پیشنهادی است. اثر غیر ایده آل بودن دستگاه نیز در این مطالعه مورد بحث قرار گرفته است. برای ارزیابی عملکرد پیشنهادی MSO تجزیه و تحلیل مونت کارلو بیشتر انجام شد. کارایی ساختار پیشنهادی از طریق شبیه سازی SPICE برای سه فاز MSO (n = 3) و چهار (n = 4)تأیید می شود و نتایج شبیه سازی شده به دست آمده با مقادیر نظری مطابقت نزدیک دارند. اعوجاج هارمونیک کل (THD)کاملا کم است.

International Journal of Engineering

Journal Homepage: www.ije.ir

Improved Object Matching in Multi-objects Tracking Based On Zernike Moments and Combination of Multiple Similarity Metrics

A. Dadgar, Y. Baleghi*, M. Ezoji

Department of Electrical & Computer Engineering, Babol Noshirvani University of Technology, Babol, Iran

PAPER INFO

Paper history:
Received 10 January 2021
Received in revised form 08 April 2019
Accepted 15 April 2021

Keywords:
Multi-objects Tracking
Zernike Moments
Gaussian Mixture Model
Hausdorff Distance
Earth Mover's Distance

ABSTRACT

In video surveillance, multiple objects tracking (MOT) is a challenging task due to object matching problem in consecutive frames. The present paper aims to propose an improved object matching approach in MOT based on Zernike moments and combination of multiple similarity distance metrics. In this work, the object is primarily detected using background subtraction method while the Gaussian Mixture Model (GMM) is applied for object extraction in the next frames. Subsequently, the color histogram and the magnitude of Zernike moments of the objects are calculated. In the next step, the objects are matched in the current and the previous frames based on the Hausdorff distance between objects, Earth Mover's distance (EMD) between their color histograms, and Chi-square distance between their Zernike moments. Then, a voting mechanism is designed to find the best consensus object matching from the aforementioned metrics. Eventually, the location of each object is predicted by the Kalman filter to continue tracking in subsequent frames. The results show that the object tracking and matching performance is improved using the proposed method in the video sequences of the multi-camera pedestrian "EPFL" video dataset. Specifically, errors caused by the merging of targets are reduced in the proposed tracking process.

doi: *10.5829/ije.2021.34.06c.08*

1. INTRODUCTION

Multi-Objects tracking (MOT) is an important task in computer vision and is often one of the first steps for video analysis in surveillance, sports, or industrial applications. In contrast to Single Object Tracking (SOT), the number of objects will vary in this approach and may merge, split, appear, or disappear in the scene over time. Due to challenges such as object shape deformations, brightness changes, and the issues of occlusion and distraction, the existing approaches still do not perform properly in all situations [1-4]. Increasing the number of objects creates a new and major difficulty in detection, data association and tracking. In MOT, special attention should be paid to determine the identity of each object at any time and to maintain the consistency of objects identities during tracking, and to solve multi identeties matching challenges [5-7]. Accordingly, validation criteria must be considered alongside each object to perform a proper object matching during the video sequence. In this regard, selecting suitable features that can separate the objects from the foreground or other scene objects, implementing and updating a robust model for the objects, and occlusion occurrence, are issues that will be addressed in the MOT process [8-9]. In the present study, the data association in the MOT process is based on extracting orthogonal Zernike moments [10-11] and also combination of three similarity metrics e.g., Hausdorff distance [12-13], Earth Mover's distance (EMD) [14] and Chi-square distance to improve object matching.

The present article is arranged as follows; a literature review will be carried out in the second section, and subsequently, the proposed method will be discussed in the third section. The results and evaluation will be presented in the fourth section. The fifth section will discuss the results, and the conclusion will be presented in the sixth section.

*Corresponding Author Institutional Email: y.baleghi@nit.ac.ir (Y. Baleghi)

Please cite this article as: A. Dadgar, Y. Baleghi, M. Ezoji, Improved Object Matching in Multi-objects Tracking Based On Zernike Moments and Combination of Multiple Similarity Metrics, International Journal of Engineering, Transactions C: Aspects Vol. 34, No. 6, (2021) 1445-1454

2. LITERATURE REVIEW

The MOT consists of two main parts; the first is object detection, and the second performs the association between the detected and tracked objects. Challenges such as the occlusion may yield undesirable results during the tracking process. In the following, the related investigations will be discussed regarding tracking and data association.

Object tracking utilizes two groups of non-predictive and predictive algorithms, depending on the situation. In the first group, the tracking is performed based on matching [15]. More specifically, by detecting the target area in each frame, the area of the next frame that most closely resembles the mentioned area is considered as the object area. In other words, no prediction is made about the target position in the next frame according to its current movement (e.g., Mean shift and CAM shfit) [16]. In the second group, the tracking is performed by algorithms that possess predictive features. The stated algorithms use the object position in frame k to predict the target position in frame $k + 1$ (e.g., Kalman filter and particle filter) [16-18]. The tracking problem can be considered as a posterior probability density function (PDF) estimation of the object's state variable [19]. In other words, the target's probability distribution is estimated in the current frame and desired in the next frame. The same framework is used as the basis of the tracker in the present paper.

In the MOT process, the objects are primarily detected, and subsequently, the association of the detected objects in the present frame must be established with the objects in the previous frames. The Nearest Neighbor (NN) and General Nearest Neighbor (GNN) methods are two common approaches of data association. The stated methods may also be inaccurate when the object areas are close to each other or when the number of incorrect measurements increases [20]. The Hungarian method is a combinatorial optimization algorithm that solves the assignment problem in polynomial time [21].

The Joint Probabilistic Data Association (JPDA) method has been proposed to renovate the GNN. Thus, each path is updated by the weighted sum of all measurements. The PDA method encounters several targets independently [22-23].The Multiple Hypothesis Tracking (MHT) method is a statistical association algorithm that may even postponed the data association to the next repetitions to eliminate the ambiguities. Generally, the MHT method is composed of the sections such as the generation of hypothesis matrix, generation of hypothesis, calculation of hypothesis probability, calculation of the Kalman filter associated with the target, and hypothesis management [24]. As a result, several hypotheses will be the output of one hypothesis in cases such as occlusion and noisy situation. However, the computational cost can be high, depending on the application complexity [25].

Although the majority of data association algorithms, such as JPDA and MHT, take the peer-to-peer measurements and objectives into account, the Markov Chain Monte Carlo data association method does not work based on such hypotheses. In general, the Monte Carlo method is an approximate solution that considers the problem as a hybrid optimization problem and examines it through random space exploration, rather than enumerating all association options [26]. However, issues like long occlusions, severe video blur, sudden movements of the camera, and disruption of the state of targets can cause tracking failure. MOT algorithm should be able to establish unique correspondences between objects in each frame of a video sequence.

A new trend is to use object features and object matching for both tracking and association. Image/Object matching has rich meaning in pairing two objects, thus deriving many specific tasks, such as sparse feature matching, dense matching (like image registration and stereo matching), patch matching (retrieval), 2-D and 3-D point set registration, and graph matching [27].

A gradient based corner response uses the first order information in image to distinguish the corner feature. The famous Harris corner detector was introduced to address the anisotropy and computation complexity problems [28]. The goal of the Harris method is to find the directions of the fastest and lowest grey value changes using a second-order moment matrix or an autocorrelation matrix; thus, it is invariant to orientation and illumination and has reliable repeatability and distinctiveness [29].

In methods based on second-order partial derivatives, the Laplacian of Gaussian (LoG) is applied based on scale space theory. The difference of Gaussians (DoG) [30] filter can be used to approximate the LoG filter, and greatly speed up the computations. Another classical blob feature detection strategy is based on the determinant of Hessian (DoH) [31]. This is more affine invariant because the eigen value and eigen vector of the second-order matrix can be applied to estimate and correct the affine region [29].

Interest point detection using DoG, DoH, and both has been widely utilized in recent visual applications. The famous Scale Invarient Feature Transform (SIFT) [30], extracts key point as the local extrema in a DoG pyramid, using the Hessian matrix of the local intensity values. Speeded up Robust Features (SURF) [32] accelerates the SIFT by approximating the Hessian matrix based detector using Haar wavelet calculation, together with an integral image strategy, thus simplifying the construction of a second order differential template [29-33].

Ucar et al. [34] put forward a novel hybrid Local Multiple system based on Convolutional Neural Networks (CNNs) and Support Vector Machines (SVMs)

with the feature extraction capability and robust classification. In the proposed system, they first divided the whole image into local regions using the multiple CNNs. Secondly, they selected discriminating features using principal component analysis (PCA) and imported them into multiple SVMs by both empirical and structural risk minimizations. Finally, they tried to fuse SVM outputs. They worked on the pre-trained AlexNet and also performed object recognition and pedestrian detection experiments on the Caltech-101 and Caltech Pedestrian datasets. Their proposed system generated better results with the low miss rate and improved object recognition and detection with an increase in accuracy. Zhou *et al.* [35] presented the architecture and the algorithms of deep learning in an application of object detection task. They worked on built-in datasets such as ImageNet, Pascal Voc, CoCo and deep learning methods for object detection. They created their own dataset and proved that using CNN for the object detection, the results are improved. Experiments proved that the deep learning is an effective tool to pass the man-made feature with the large qualitative data. Kaushal *et al.* [33] conducted a comprehensive survey on object detection and tracking in videos techniques based on the deep learning. The survey included neural network, deep learning, fuzzy logic, evolutionary algorithms required for detection and tracking. In the survey, they discussed various datasets and challenges for the object detection and tracking based on the deep neural network.

On the other hand, the application of deep learning strategies also burdens high computational cost and requires high performance computing devices and very large datasets to reach proper results. Hence, in this paper we have proposed an improved object matching method for MOT algorithm based on powerful features including Zernike Moments and combination of some distance metrics, EMD, Hausdorff and Chi-square. The results are also compared with a deep learning based approach in this paper.

3. THE PROPOSED METHOD

The main purpose of the present work is to track multiple objects in consecutive frames and solving some MOT challenges with new strategies. The tracking is performed in each frame according to the flow diagram illustrated in Figure 1. In the mentioned procedure the object is primarily obtained using background subtraction method while the Gaussian Mixture Model (GMM) is applied for object extraction in the next frames. Subsequently, the color histograms are considered for object matching and the objects' Zernike Moments are calculated for data association. In the next step, the objects are matched in the current and the previous frames based on the combination of similarity metrics: Hausdorff distance between objects, EMD distance between their color histograms, and Chi-square distance between their Zernike Moments. Eventually, the location of each object is predicted by the Kalman filter to continue tracking in subsequent frames. Thus, the predictors are updated based on the new detections, and the predicted locations are returned to the tracking process again. The same procedure continues until the last frame. Meanwhile, a new tracker starts tracking objects that do not match any of the predictions, and also the stopped trackers will be eliminated. In this paper the following challenges are considered: object fragmentation during the object detection, merging two or more objects and thus sharing a single ID, and the association of multiple identities under conditions of exit, re-entry, as well as occlusion.

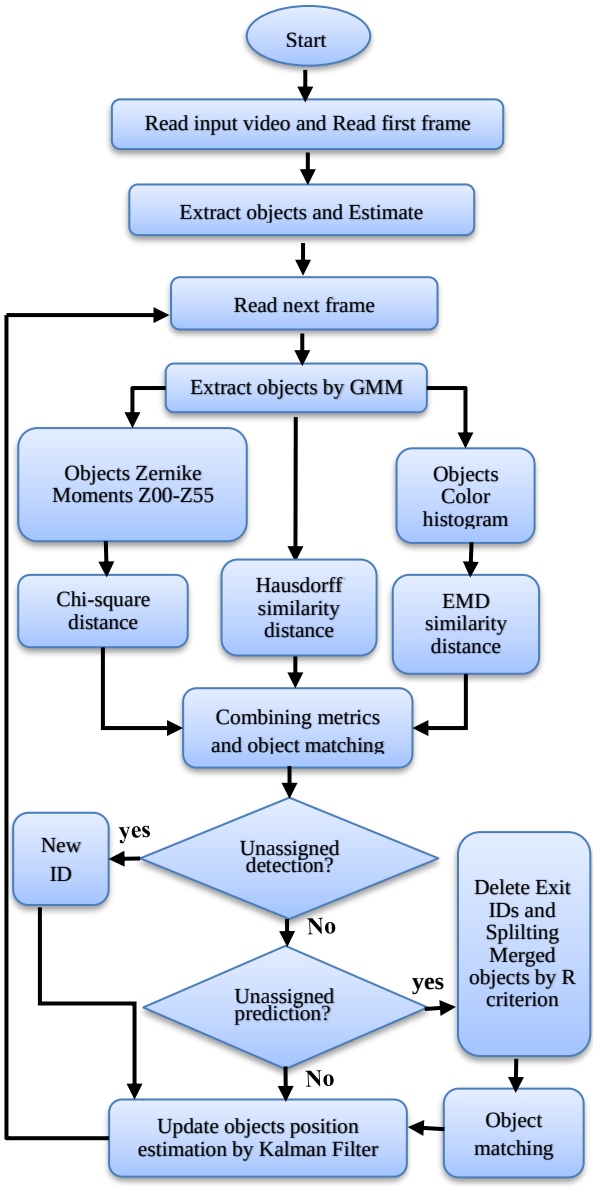

Figure 1. Flow diagram of the proposed method

To deal with the issue, an improved object matching is proposed in this work based on Zernike Moments and combination of three distance metrics e.g., EMD, Hausdorff and Chi-square that increases the multi-objects tracking accuracy. A detailed description of every step of the proposed method is put forth in the following subsections.

3. 1. Target Detection and Feature Extraction In the object tracking systems, the moving areas must be subtracted from the background, and the objects models must be created prior to the initiation of the tracking process.

The present study utilizes the GMM for object detection, which possesses decent prediction capabilities since it can accurately model any types of probability density function with a sufficient number of Gaussian functions. The GMM is among the pattern recognition systems and is defined as Equation (1) [36].

$$p(x) = \sum_{k=1}^{K} \pi_k \, N(x|\mu_k \, , \Sigma \mathrm{k}) \quad , \quad \sum_{k=1}^{K} \pi_k = 1 \qquad (1)$$

where, π_k denotes the weight of the k[th] distribution. Also, μ_k and Σk represent the mean and covariance of the k[th] cluster, respectively. In this paper, Zernike Moments (ZM), the powerful feature extractor, has been used for object matching that significantly improved the preformance of sole color features.

The ZM feature is able to determine the overall object shape in low orders and represent the object details in high orders. ZM is a powerful descriptor with features including orthogonality, low sensitivity to noise, and insensitivity to rotation. The ZM is used in numerous applications, such as character recognition, palm-print recognition, recognition of different languages in old texts, signature-based authentication, and face-based recognition. The Zernike polynomial is defined in a unit radius circle [10-37]. The mixed two-dimensional ZM of order n and with repetition m is defined as Equation (2), [38-39]. In Equation (2), $f(x,y)$ is digital image with the dimension of $M \times N$ related to intensity function of the input image and * denotes the complex conjugate.

$$ZM_{n,m}\big(f(x,y)\big) = \frac{n+1}{\pi} \sum_{i=0}^{M-1} \sum_{j=0}^{N-1} V_{n,m}^{*}(x,y) \; f(x,y) \qquad (2)$$

The order *n* is a non-negative integer and *m* is an integer which satisfies condition $|\, m \,| \leq n$. Zernike polynomials, $V_{n,m}(x,y)$ and Radial polynomials $R_{mn}(r)$, are defined as Equation (3).

$$V_{n,m}(x,y) = R_{n,m}(r)\, e^{jm\theta} \quad , \quad R_{n,m}(r) = \sum_{s=0}^{(n-|m|)/2} (-1)^s \cdot \frac{(n-s)!}{s!\left(\left(\frac{(n+|m|)}{2}-s\right)!\left(\frac{(n-|m|)}{2}-s\right)!\right)} r^{n-s} \qquad (3)$$

where; $r = \sqrt{x^2 + y^2}$ is the length of the vector that connects the origin of the coordinates to the pixel with the coordinates (x,y), and $\theta = \tan^{-1}(\frac{y}{x})$ [38-39]. It should be noted that, Zernike polynomials are defined within a unit circle, and the coordinates of the images $f(x_i, y_j)$ must be normalized into [− 1, 1] by a mapping transformation. $f(x,y)$ is the image function after mapping to a unit circle. The pixels located outside the circle are not involved in the calculations. The center of the bounding box in which the object is detected is the origin of the coordinates.

3. 2. Distance Similarity As displayed in the flow diagram of Figure 1, distance criteria based on local similarity, statistical/non-statistical similarity, or global similarity can be used to address the challenges of data association in a camera view and to perform target matching. Euclidean distance is a common method of calculating the distance between two data sets. In this study, to strengthen the separability of objects and improve the assignment of the object identities, in addition to ZM feature extractor, the EMD similarity criterion and the Hausdorff similarity metric have also been used. A number of criteria that are effective in improving the object matching results of this article are stated in the following.

The Hausdorff Distance (HD) is a similarity metric between two sets of points. The HD between two finite sets of points including A and B is the maximum of minimum distances between each point $a \in A$ to its nearest neighbor $b \in B$. HD can be calculated by, $h(A,B) = Max_{\,a \in A} \{ Min_{b \in B} \{\|a - b\|\}\}$ and $HD(A,B) = Max\,(h(A,B), h(B,A))$. In general, the values of h(A, B) and h$(B,$A) can be substantially different. So the HD, is the maximum of the directed HD in both directions and thus it is symmetric [12-13]. The EMD method begins by answering this question: What is the lowest cost to convert one distribution to another, assuming that two histograms have the same number of columns and frequecies [14].

The EMD can be stated in terms of a linear programming problem: two distributions represented by signatures P and Q, where p_i , q_i are bin centroids with frequencies w_{pi} , w_{qi}; and $D = [d_{ij}]$ is the matrix containing the Euclidean distances between p_i and q_j for all *i,j*. We ensure that *P* and *Q* have the same total mass of unity, equal to one, by normalizing each of distributions. Next, we find a $F = [f_{ij}]$ between p_i and q_j that minimizes the total cost. In Figure 2, dij represents the distance between the two columns that the value is transferred among them, and f_{ij} represents the amount of transferred value. The similarity of the two histograms can be expressed based on Equation (4). In the following equations *n* and *m* are the number of histogram bins. The objective function denotes the set of all feasible flows between bins. Equation (4) will be optimized according to the variables and constraints [14].

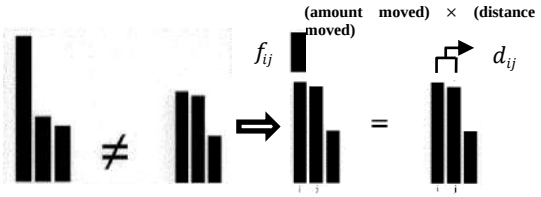

Figure 2. The histogram with different statistical distributions

$$\begin{aligned} &\textstyle\sum_{i=1}^{m}\sum_{j=1}^{n}(distance\ moved)\times(amount\ moved)\\ &Cost(P,Q,F)=\textstyle\sum_{i=1}^{m}\sum_{j=1}^{n}(d_{ij})\times(f_{ij})\\ &\textstyle\sum_{i=1}^{m}\sum_{j=1}^{n}(f_{ij}) \;=\; min(\sum_{i=1}^{n}p_i\ ,\sum_{j=1}^{n}q_j\ )\\ &EMD=\frac{\sum_{i=1}^{m}\sum_{j=1}^{n}(d_{ij})\times(f_{ij})}{\sum_{i=1}^{m}\sum_{j=1}^{n}\ f_{ij}} \end{aligned} \quad (4)$$

Solving the above linear programming problem determines the optimal flow, between the source and destination. In other words, the conversion from P to Q is performed by removing at least parts of the columns in P. Thus, the EMD method goes from an optimization problem to a minimization problem [14].

3. 3. Object Matching Data association and objects matching, in the video sequence are influential topics in the MOT. The tracking process searches for the correct association between the foreground and the predicted objects at time t. The magnitude of the ZM are calculated in the detected objects at time t and the prediction of objects in time $t-1$ and compared by the Chi-square distance according to Equation (5).

Object matching has been done according to combination of similarity distances metrics: Hausdorff distance between objects, EMD distance between their color histograms, and Chi-square distance between their Zernike Moments magnitudes. To improve the assignment of objects' identity, hard voting will be conducted between the three similarity criteria, and for each object, an identity that has been approved by the majority will be assigned.

$$D(O_t,O_{t+1})=\ \sum_{i=1}^{n}\frac{\left(O_{t_n}-O_{t_{n+1}}\right)^2}{O_{t_n}+O_{t_{n+1}}} \quad (5)$$

where; O_{t_n} and $O_{t_{n+1}}$ are the feature values of the objects.

Subsequently, object matching is conducted based on the thresholded values. Since the detected objects are less than the predictions, there is a possibility of occlusion. Hence, the merging and splitting of the bounding boxes must be evaluated. So, the shape bounding box's metric is defined as R. The R criterion is expressed according to Equation (6).

$$\begin{aligned} &R_i=\frac{Height}{Width},\\ &R_i>\tau_{RatioDown}\quad and\quad R_i<\tau_{RatioUp}\ ,\\ &\tau_{RatioDown}<R_i<\tau_{RatioUp} \end{aligned} \quad (6)$$

where; $Height$ and $Width$ are the height and the width of the bounding box of the object, respectively. The R criterion is limited by the upper bound threshold of $\tau_{RatioUp}$, and the lower bound threshold of $\tau_{RatioDown}$.

3. 4. Object Tracking In this paper, the object tracking is performed using the Kalman filter[40]. The Kalman filter is a recursive estimator with the minimum variance. Kalman filter consists of two groups of time update and measurement update equations, which are also referred to as predictive and corrective equations, respectively [40].

Equations (7)-(11) represent the Kalman equations. Equation (7) predicts the state of the system. This prediction is made without observing the current moment. Equation (8) shows the current prediction error, and Equation (9) is responsible for calculating the gain. Similarly, Equation (10) shows the estimation of the Kalman filter of the system state. The error corresponding to this estimation is given in Equation (11).

$$\hat{x}_{k+1}^{-}\ =\Phi_k\hat{x}_k \quad (7)$$

$$P_{k+1}^{-}=\Phi_kP_k{\Phi_k}^T+Q_k \quad (8)$$

$$k_k=p_k^-\ H_k^T\left(H_k\,p_k^-\ H_k^T+R_k\right)^{-1} \quad (9)$$

$$\hat{x}_k=\hat{x}_k^-+K_k(z_k-H_k\hat{x}_k^-) \quad (10)$$

$$P_k=(I-k_kH_k)P_k^- \quad (11)$$

In the above Equations, x_k is the state vector at moment k, Φ_k is the transition matrix, and Y_k is the system output. H_k is the conversion matrix, and vector Z_{k} is the sum of the output of the Y_{k} with the measurement noise of V_{k} (system observations). $\hat{x}_{\mathrm{k}}^-$ is the previous prediction, $\hat{x}_{\mathrm{k}}$ is the subsequent prediction, and $\hat{x}_{\mathrm{k+1}}^-$ is the previous prediction of $K+1$. w_{k} and v_{k} are the measurement and process noises, respectively. K_k is the Kalman gain, and p_{k} is the covariance error matrix.

4. RESULTS AND EVALUATION

In this work, the MOT in a camera view is performed by the modification of data association based on Zernike Moments features, similarity criteria, and Kalman filter. This study attempts to maintain the continuity of tracking each object during the MOT process. For this purpose, a unique and new ID is assigned to each object. The stated ID must remain constant during the tracking process even after short occlusion.

4. 1. Database and Evaluation Metrics The video sequences of the multi-camera pedestrian video

"EPFL" dataset are used in the simulations[1]. In this dataset, several videos have been recorded simultaneously from a specific location using multiple cameras at various angles. This sequence consists of people appearing one after the other, and walking in front of the cameras. It tests the ability of our algorithm to cope with a moderately crowded environment. The calibration information and homography matrices, H, are provided for each camera. The homographies given in the calibration files[4] project points in the camera views to their corresponding location on the top view of the ground plane, that is presented in Equation (12). In this equation, $\boldsymbol{X_{image}}$ is the object position in tracking process and $\boldsymbol{X\_topview}$, is the corresponding location on the top view of the ground plane.

$$H \times X_{image} = X\_topview \tag{12}$$

Accuracy and precision, along with three main parameters of False Negative, False Positive, and Identity switch (IDsw), are among the common criteria for evaluating the quality of the MOT. This study utilized the stated parameters to evaluate the tracking quality.

Multi-Objects Tracking Precision (MOTP) is stated in Equation (13). This criterion represents the overall object position error for the "object- prediction" pair in all frames. It shows the tracker's ability to estimate the precise object position [41]. Another criteria, Multi-Objects Tracking Accuracy (MOTA) is calculated according to Equation (14). In the this Equation, FN, FP, and ID_{sw} are the missing objects, false positives, and identity switches at t, respectively [41]. To evaluate the correctness of any tracker at least three entities are needed to be defined: the tracker output (or hypothesis) H_i, which is the result of the tracking algorithm, the correct result, or ground truth, g_t, and a distance function $d_{i,t}$ that measures the similarity between the true object and the prediction. C_t, is the number of matches at time t and *bbox* stands for bounding box.

$$MOTP = \frac{\sum_{i,t} d_{i,t}}{\sum_t C_t}$$
$$d(H_i, g_t) = \frac{bbox(H_i) \cap bbox(g_t)}{bbox(H_i) \cup bbox(g_t)} \tag{13}$$

$$MOTA = 1 - \frac{\sum_t (FN+FP+ID_{sw})}{\sum_t g_t} ,$$
$$\overline{FN} = \frac{\sum_t FN}{\sum_t g_t} \quad , \quad \overline{FP} = \frac{\sum_t FP}{\sum_t g_t} \quad , \quad \overline{ID_{sw}} = \frac{\sum_t ID_{sw}}{\sum_t g_t} \tag{14}$$

$\overline{FN}$ is the rate of missing objects calculated among all objects and in all frames. $\overline{FP}$ is the rate of false positives, and $\overline{ID_{sw}}$ is the rate of occurred mismatches [41].

4. 2. Simulation Details This subsection gives an overview of the results of MOT simulations using the Multi-camera pedestrian video "EPFL" dataset. During the MOT, an ID is assigned to each detected object. However, some objects may leave the scene while being tracked, or their lifespan may be less than the threshold level, or be occluded. According to the tracking process the object matching is improved based on the combination of similarity distance metrics, EMD, Hausdorff and Chi-square, each of which calculates histogram similarity distance, images distance and the object's Zernike Moments magnitudes, respectively.

Figure 3, illustrates the moments of the first object while ZM changes due to the occlusion and intersection after the 750th frame. Furthermore, an occlusion can be predicted based on the sudden changes in the magnitude of the Zernike Moments. Multiple objects in the scene may merge and be detected as a single object due to lighting, occlusion, merging of shades, or the intersection of individuals' limbs, Figure 4. Thus, the *R* ratio will be

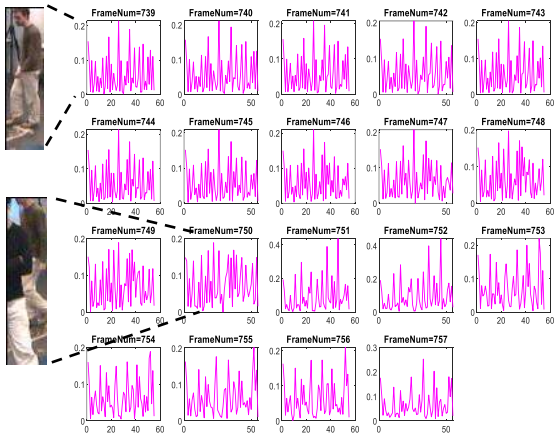

Figure 3. The illustration of the changes in Zernike Moments up to $n = 10$ order, before and after occlusion

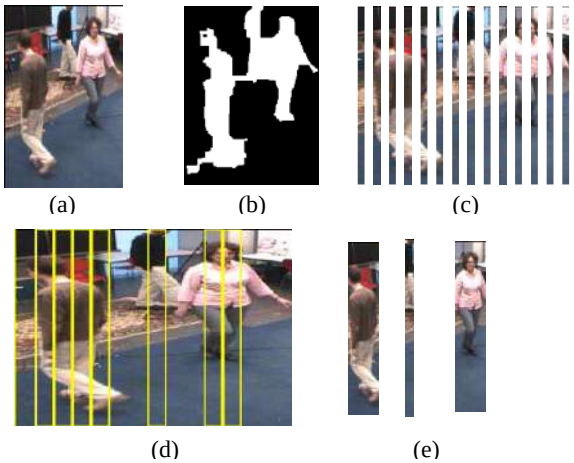

Figure 4. The separation of merged objects in the pedestrian video "EPFL" dataset, frame 1091st; (a) Three merged objects, (b) The silhouette of the merged objects, (c) Columnar segmentation, (d) Separation of merged objects, (e) Representation of the objects

[1] https://www.epfl.ch/labs/cvlab/data/data-pom-index-php/

calculated with respect to Equation (6). If the value of *R* is outside of the set thresholds, it is inferred that several objects are merged and must be separated. Consequently, the merged objects will be segmented into columnar patches, and the Zernike Moments of each patch will be calculated and compared using the Chi-Square distance. The patches with the least differences in moments magnitudes will be merged to form an object.

4. 3. Simulation Results Various studies have been performed object matching based on the SURF features [42, 43], Harris corner [44, 45], and Hungarian method [46, 47]. In Hungarian method, the objects are matched based on their optimal distance from each other. The Hungarian method tries to minimize the local distance between the target and the available predictions in each repetition. In this algorithm, each measurement will be assigned to an object by repeatedly scrolling the list of objects and allocating the closest measurement to each object. The measurement is then invalidated, and the next measuerments are processed. In SURF and Harris corner methods the objects are matched based on their key points. The SURF feature detector applies an approximate Gaussian second derivative mask to an image at many scales. Since the feature detector applies masks along each axis and at 45 degrees to the axis it is more robust to rotation than the Harris corner. The method is very fast because of the use of an integral image where the value of a pixel *(x,y)* is the sum of all values in the rectangle defined by the origin at *(x,y)*.

To detect features, the Hessian matrix, Equation (15), is applied.

$$H = \begin{bmatrix} L_{xx} & L_{xy} \\ L_{xy} & L_{yy} \end{bmatrix} \quad (15)$$

where $L_{xx}, L_{xy}, L_{yx} and\ L_{yy}$ is the convolution of the second derivative of a Gaussian with the image at the point. The Hessian determinate values are used for the range of detector windows. Valid features are found as a local maximum over a 3x3x3 range where the third dimension is detector window size, so a feature must be locally unique over a spatial range and a range of scales. The SURF uses a fast search algorithm to do non-maximum suppression.

The Harris corner detector takes horizontal and vertical derivatives of the image and looks for areas where both are high, this is quantified by the Harris corner descriptor which is defined as the matrix and descriptor, in Equations (16)-(17), respectively.

$$H = \begin{bmatrix} {D_x}^2 & D_x D_y \\ D_x D_y & {D_y}^2 \end{bmatrix} \quad (16)$$

$$c = \frac{\det(H)}{trace(H)} \quad (17)$$

We define a feature as a point that is a local maximum on a 3x3 area and is above a threshold. Also the results of the proposed method are compared with a tracking method that is implemented based on a kind of deep neural network called a Convolutional Neural Networks (CNN) [48]. This framework uses CNN to detect objects within the input frames. A state-of-the-art object detection framework [33], Faster R-CNN [49], is used for the detection of objects. The features used for the tracking are derived from a SURF and serve as a strong basis for object recognition. The approach is to match the extracted features of individual detections in subsequent frames, hence creating a correspondence of detections across multiple frames.

The images (of $227 \times 227 \times 3$ size) are applied as input to the detector model which detects and localizes individual objects [50]. According to the transfer learning, at first, a pre-trained AlexNet network is trained by the CIFAR10 dataset to regularize the network's weights and biases. Once again it is trained based on MOT: ETH-Bahnhof, ETH-Bahnhof, ETH-Linthescher datasets through the Faster R-CNN to detect humans. The developed algorithm uses SURF as a feature to make correspondences of the detections across the frames, and IDs are allocated to individual detections.

Since the results of the mentioned studies are not available in the Multi-Camera pedestrian video "EPFL" dataset, the MOT simulation and the object matching is performed based on SURF features, Harris corner, Hungarian, and Faster R-CNN methods regarding the flow diagram in Figure 5. The results of the performed tracking are presented in Table 1. The proposed method is based on Zernike Moments feature on the frame sequences from 1 to 2000, in the "EPFL" dataset.

5. DISCUSSION

Table 1 shows that tracking and matching objects with the proposed method yielded an accuracy (MOTA) of 81.6%, while the accuracy of the Hungarian, SURF, Harris corner, and Faster R-CNN methods are 74, 71.8, 50.1 and 78.6% respectively. Also, the percision of the proposed method, Faster R-CNN, Hungarian, SURF, and Harris corner methods are 54.5, 65.7 ,69.3, 72.6 and 78.1% respectively. Higher value of MOTP signifies low accuracy of the bounding boxes around the object. Higher values of MOTA signifies high accuracy in tracking. Based on the results, the Hungarian method minimizes the total distance between each object-prediction. So the false negative is less than the matching methods that operate based on points features. Also it is observed that tracking and matching processes based on the SURF or Harris corner have given poorer results compared to the rest.

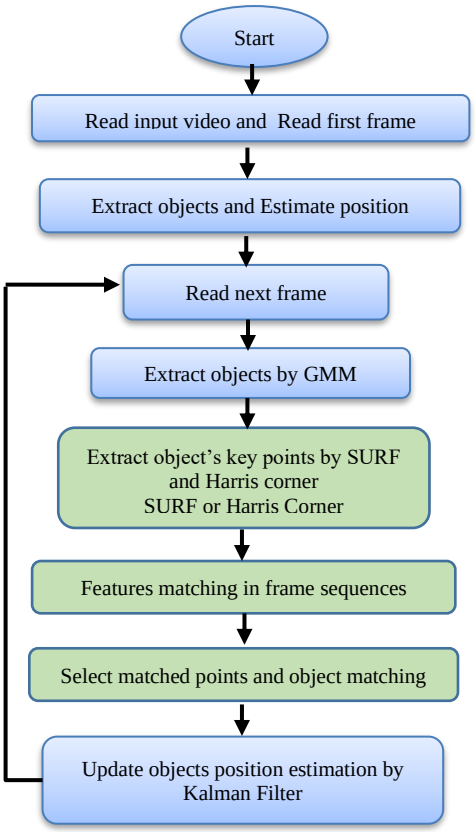

Figure 5. The flow diagram of object tracking and object matching based on SURF and Harris corner

TABLE 1. Evaluation of MOT based on data association simulated methods

MOTA	ID_{sw}	FP	FN	Method
74.4	29.8	11.3	52	Hungarian [48]
71.8	21.9	16	55.1	SURF [44]
50.1	14.6	34	97	Harris corner [45]
78.6	17.8	9.2	42.6	Faster R-CNN [51]
81.6	18	4	34	Proposed Method

The aforesaid is because the changes such as the horizontal movement of the objects, movement of limbs and deformations of object clothing will make the features points/corners extracted in frame $t-1$ disappear in frame t. Thus, the object feature points detected in frame $t-1$ are not detected and matched in frame t, so leading to a false negative error and false positives. In contrast, since the points features are used for data association, the IDsw and wrong identity allocations are less than other methods. The results in Table 1 shows the more accurate performance of the proposed method, even when comparing with a deep learning based approach.

In the proposed method, the recognition is performed based on the Zernike Moments of $n = 10$ order, and the magnitudes are obtained for Z_{00} to Z_{55}. The magnitude of the Zernike Moments indicates the overal shape of the object at low orders and object details at higher orders. Since the object feature extraction is not based on local distance or the points features, the false negatives and IDsw errors are less, resulting in higher accuracy. On the other hand, the false negative error is reduced, and fewer objects are lost in the tracking process due to the separation of merged objects. Finally, the tracking path of the first object is illustrated in Figure 6, in comparison with other methods and the groundtruth which shows the superiority of the proposed method.

It should be noted that the Epfl dataset is very famous that has different modes of challenges that happened while targets are moving. On the other hand the ground truth file, the coordinates of the objects in the scene, their path, and the homography matrix of each view is presented in a file. Hence, the proposed method has been evaluated on this dataset.

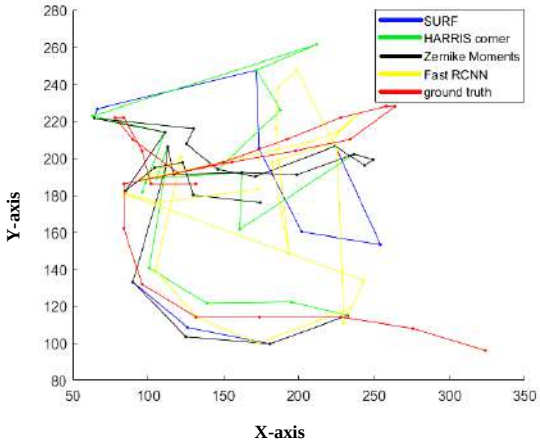

Figure 6. The trajectory of the first object in the 1st to 900^{th} frames; (blue) SURF, (green) Harris corner, (black) Zernike Moments, (yellow) Faster R-CNN and (red) Ground truth

6. CONCLUSION

This study attempted to improve the matchimg and identity association of objects according to the feature-based data association. To this end we designed a method which used Zernike Moments and similarity-based hard voting for data association and objects matching, respectively. We evaluated different criteria in various aspects between detected objects in consecutive frames. In this regard, Hausdorff and EMD distance criteria were used for distance metrics rather than Euclidean distance. Furthermore, separation of the merged objects in this work, leads to reduction of false negatives and can tackle with the dense distribution and mutual occlusion of individuals in the tracking process.

The results of this study can be used to track multiple objects using multiple cameras and detect the desired targets in the future works.

7. ACKNOWLEDGEMENT

The authors acknowledge the funding support of Babol Noshirvani University of Technology through the grant program No. BNUT/370123/00.

8. REFERENCES

1. Asvadi, A., Mahdavinataj, H., Karami, M. and Baleghi, Y., "Incremental discriminative color object tracking", in Artificial Intelligence and Signal Processing, Cham, Springer International Publishing. (2014), 71-81.
2. Ardeshir, G. and Khakpour, F., "Using a novel concept of potential pixel energy for object tracking", ***International Journal of Engineering***, Vol. 27, No. 7, (2014), 1023-1032.
3. Abbass, M.Y., Kwon, K.-C., Kim, N., Abdelwahab, S.A., El-Samie, F.E.A. and Khalaf, A.A.M., "A survey on online learning for visual tracking", ***The Visual Computer***, (2020), doi: 10.1007/s00371-020-01848-y.
4. Manafifard, M., Ebadi, H. and Abrishami Moghaddam, H., "A survey on player tracking in soccer videos", ***Computer Vision and Image Understanding***, Vol. 159, (2017), 19-46, doi: 10.1016/j.cviu.2017.02.002.
5. Asvadi, A., Karami, M. and Baleghi, Y., "Efficient object tracking using optimized k-means segmentation and radial basis function neural networks", ***Itrcjrn***, Vol. 4, No. 1, (2012), 29-39.
6. Asvadi, A. and Karami-Mollaie, M., "Object tracking using adaptive object color modeling. (2013).
7. Luo, W., Xing, J., Milan, A., Zhang, X., Liu, W. and Kim, T.-K., "Multiple object tracking: A literature review", ***Artificial Intelligence***, Vol. 293, (2021), 103448, doi: https://doi.org/10.1016/j.artint.2020.103448.
8. Xing, J., Ai, H., Liu, L. and Lao, S., "Multiple player tracking in sports video: A dual-mode two-way bayesian inference approach with progressive observation modeling", ***IEEE Transactions on Image Processing***, Vol. 20, No. 6, (2011), 1652-1667, doi: 10.1109/TIP.2010.2102045.
9. Asvadi, A., Karami-Mollaie, M., Baleghi, Y. and Seyyedi-Andi, H., "Improved object tracking using radial basis function neural networks", in 2011 7th Iranian Conference on Machine Vision and Image Processing. (2011), 1-5, doi: 10.1109/IranianMVIP.2011.6121604.
10. Khare, M., Srivastava, R.K. and Khare, A., "Object tracking using combination of daubechies complex wavelet transform and zernike moment", ***Multimedia Tools and Applications***, Vol. 76, No. 1, (2017), 1247-1290, doi: 10.1007/s11042-015-3068-5.
11. Fadaei, S. and Rashno, A., "Content-based image retrieval speedup based on optimized combination of wavelet and zernike features using particle swarm optimization algorithm", ***International Journal of Engineering***, Vol. 33, No. 5, (2020), 1000-1009, doi: 10.5829/ije.2020.33.05b.34.
12. Di Gesù, V. and Starovoitov, V., "Distance-based functions for image comparison", ***Pattern Recognition Letters***, Vol. 20, No. 2, (1999), 207-214, doi: 10.1016/S0167-8655(98)00115-9.
13. Taha, A.A. and Hanbury, A., "An efficient algorithm for calculating the exact hausdorff distance", ***IEEE Transactions on Pattern Analysis and Machine Intelligence***, Vol. 37, No. 11, (2015), 2153-2163, doi: 10.1109/TPAMI.2015.2408351.
14. Rubner, Y., Tomasi, C. and Guibas, L.J., "The earth mover's distance as a metric for image retrieval", ***International Journal of Computer Vision***, Vol. 40, No. 2, (2000), 99-121, doi: 10.1023/A:1026543900054.
15. Asvadi, A., Mahdavinataj, H., Karami, M.R. and Baleghi, Y., "Online visual object tracking using incremental discriminative color learning", ***The Csi Journal On Computer Science and Engineering***, Vol. 12, No. 2-4 (B), (2014), 16-28.
16. Dendorfer, P., Ošep, A., Milan, A., Schindler, K., Cremers, D., Reid, I., Roth, S. and Leal-Taixé, L., "Motchallenge: A benchmark for single-camera multiple target tracking", arXiv preprint arXiv:2010.07548, (2020).
17. Ciaparrone, G., Sánchez, F.L., Tabik, S., Troiano, L., Tagliaferri, R. and Herrera, F., "Deep learning in video multi-object tracking: A survey", ***Neurocomputing***, Vol. 381, (2020), 61-88.
18. Li, X., Wang, K., Wang, W. and Li, Y., "A multiple object tracking method using kalman filter", in The 2010 IEEE International Conference on Information and Automation. (2010), 1862-1866, doi: 10.1109/ICINFA.2010.5512258.
19. Xi, Z., Xu, D., Song, W. and Zheng, Y., "A* algorithm with dynamic weights for multiple object tracking in video sequence", ***Optik***, Vol. 126, No. 20, (2015), 2500-2507, doi: https://doi.org/10.1016/j.ijleo.2015.06.020.
20. Wu, Z., Thangali, A., Sclaroff, S. and Betke, M., "Coupling detection and data association for multiple object tracking, (2012), 1948-1955, doi: 10.1109/CVPR.2012.6247896.
21. Arun Kumar, N.P., Laxmanan, R., Ram Kumar, S., Srinidh, V. and Ramanathan, R., "Performance study of multi-target tracking using kalman filter and hungarian algorithm", in Security in Computing and Communications, Singapore, Springer Singapore. (2021), 213-227.
22. Li, H., Liu, Y., Lin, W., Xu, L. and Wang, J., "Data association methods via video signal processing in imperfect tracking scenarios: A review and evaluation", ***Mathematical Problems in Engineering***, Vol. 2020, (2020), 1-26.
23. Habtemariam, B.K., Tharmarasa, R., Kirubarajan, T., Grimmett, D. and Wakayama, C., "Multiple detection probabilistic data association filter for multistatic target tracking", in 14th International Conference on Information Fusion, (2011), 1-6.
24. Motro, M. and Ghosh, J., "Scaling data association for hypothesis-oriented mht", in 2019 22th International Conference on Information Fusion (FUSION), IEEE. (2019), 1-8.
25. Kim, C., Li, F., Ciptadi, A. and Rehg, J.M., "Multiple hypothesis tracking revisited", in 2015 IEEE International Conference on Computer Vision (ICCV). (2015), 4696-4704, doi: 10.1109/ICCV.2015.533.
26. Songhwai, O., Russell, S. and Sastry, S., "Markov chain monte carlo data association for general multiple-target tracking problems", in 2004 43rd IEEE Conference on Decision and Control (CDC) (IEEE Cat. No.04CH37601). (2004), 735-742 Vol.731, doi: 10.1109/CDC.2004.1428740.
27. Zhao, Z.-Q., Zheng, P., Xu, S.-t. and Wu, X., "Object detection with deep learning: A review", ***IEEE Transactions on Neural Networks and Learning Systems***, Vol. 30, No. 11, (2019), 3212-3232.
28. Bansal, M., Kumar, M. and Kumar, M., "2d object recognition techniques: State-of-the-art work", ***Archives of Computational Methods in Engineering***, (2020), doi: 10.1007/s11831-020-09409-1.
29. Ma, J., Jiang, X., Fan, A., Jiang, J. and Yan, J., "Image matching from handcrafted to deep features: A survey", ***International Journal of Computer Vision***, Vol. 129, No. 1, (2021), 23-79.
30. Lowe, D.G., "Distinctive image features from scale-invariant keypoints", ***International Journal of Computer Vision***, Vol. 60,

No. 2, (2004), 91-110.

31. Mikolajczyk, K. and Schmid, C., "Scale & affine invariant interest point detectors", ***International Journal of Computer Vision***, Vol. 60, No. 1, (2004), 63-86.
32. Bay, H., Tuytelaars, T. and Van Gool, L., "Surf: Speeded up robust features", in European conference on computer vision, Springer. (2006), 404-417.
33. Kaushal, M., Khehra, B.S. and Sharma, A., "Soft computing based object detection and tracking approaches: State-of-the-art survey", ***Applied Soft Computing***, Vol. 70, (2018), 423-464.
34. Uçar, A., Demir, Y. and Güzeliş, C., "Object recognition and detection with deep learning for autonomous driving applications", ***Simulation***, Vol. 93, No. 9, (2017), 759-769.
35. Zhou, X., Gong, W., Fu, W. and Du, F., "Application of deep learning in object detection", in 2017 IEEE/ACIS 16th International Conference on Computer and Information Science (ICIS), IEEE. (2017), 631-634.
36. Cheng, S., Luo, X. and Bhandarkar, S.M., "A multiscale parametric background model for stationary foreground object detection", in 2007 IEEE Workshop on Motion and Video Computing (WMVC'07). (2007), 18-18, doi: 10.1109/WMVC.2007.1.
37. Binh, N., "Human object tracking in nonsubsampled contourlet domain", ***International Journal of Advanced Computer Science and Applications***, Vol. 7, (2016).
38. Khare, M., Binh, N.T. and Srivastava, R.K., Human object classification using dual tree complex wavelet transform and zernike moment, in Transactions on large-scale data-and knowledge-centered systems xvi. 2014, Springer.87-101.
39. Górniak, A. and Skubalska-Rafajłowicz, E., "Object classification using sequences of zernike moments", in IFIP International Conference on Computer Information Systems and Industrial Management, Springer. (2017), 99-109.
40. Farahi, F. and Yazdi, H.S., "Probabilistic kalman filter for moving object tracking", ***Signal Processing: Image Communication***, Vol. 82, (2020), 115751, doi: 10.1016/j.image.2019.115751.
41. Bernardin, K. and Stiefelhagen, R., "Evaluating multiple object tracking performance: The clear mot metrics", ***EURASIP Journal on Image and Video Processing***, Vol. 2008, No. 1, (2008), 246309, doi: 10.1155/2008/246309.
42. Lu, X., Izumi, T., Teng, L. and Wang, L., "Particle filter vehicle tracking based on surf feature matching", ***IEEJ Journal of Industry ApplicationS***, Vol. 3, (2014), 182-191.
43. Wei, H., Takayoshi, Y., Hongtao, L. and Shihong, L., "Surf tracking", in 2009 IEEE 12th International Conference on Computer Vision. (2009), 1586-1592, doi: 10.1109/ICCV.2009.5459360.
44. Qi, Z., Ting, R., Husheng, F. and Jinlin, Z., "Particle filter object tracking based on harris-sift feature matching", ***Procedia Engineering***, Vol. 29, (2012), 924-929, doi: 10.1016/j.proeng.2012.01.065.
45. Salmane, H., Ruichek, Y. and Khoudour, L., "Object tracking using harris corner points based optical flow propagation and kalman filter", in 2011 14th International IEEE Conference on Intelligent Transportation Systems (ITSC). (2011), 67-73, doi: 10.1109/ITSC.2011.6083031.
46. Soleh, M., Jati, G. and Hilman, M., "Multi object detection and tracking using optical flow density-hungarian kalman filter (ofd-hkf) algorithm for vehicle counting. (2018).
47. Sahbani, B. and Adiprawita, W., "Kalman filter and iterative-hungarian algorithm implementation for low complexity point tracking as part of fast multiple object tracking system", in 2016 6th International Conference on System Engineering and Technology (ICSET). (2016), 109-115, doi: 10.1109/ICSEngT.2016.7849633.
48. Kim, B., Yuvaraj, N., Sri Preethaa, K., Santhosh, R. and Sabari, A., "Enhanced pedestrian detection using optimized deep convolution neural network for smart building surveillance", ***Soft Computing***, Vol. 24, (2020), 17081-17092.
49. Ren, S., He, K., Girshick, R. and Sun, J., "Faster r-cnn: Towards real-time object detection with region proposal networks", ***IEEE Transactions on Pattern Analysis and Machine Intelligence***, Vol. 39, No. 6, (2016), 1137-1149.
50. Acharya, D., Khoshelham, K. and Winter, S., "Real-time detection and tracking of pedestrians in cctv images using a deep convolutional neural network", in Proceedings of the 4th annual conference of research@ locate. Vol. 1913, (2017), 31-36.

Persian Abstract

چکیده

در نظارت ویدئویی ، رهگیری چند هدف به دلیل مشکل تطابق اهداف در فریم های متوالی ، یک مساله چالش برانگیز است. مقاله حاضر با هدف ارائه یک روش تطبیق بهبود یافته در ردیابی چند هدف بر اساس گشتاور زرنیک و ترکیبی از معیارهای فاصله شباهت ارائه شده است. در این تحقیق، ابتدا اهداف با استفاده از روش تفریق پس زمینه آشکارسازی می‌شود، همچنین مدل گاوسی مخلوط، برای استخراج اهداف در فریم های بعدی اعمال می شود. پس از آن، هیستوگرام رنگ و اندازه گشتاورهای زرنیک هر یک از اهداف محاسبه می شوند. در مرحله بعد، اهداف براساس فاصله هاسدورف ، فاصله Earth Mover بین هیستوگرام های رنگ و فاصله Chi-square بین گشتاورهای زرنیک در فریم حاضر و فریم های قبلی تطبیق داده می شوند. سپس، مکانیزم رأی گیری برای یافتن بهترین تطابق با معیارهای فوق طراحی شده است. درنهایت ، مکان هر یک از اشیا توسط فیلتر کالمن پیش بینی می‌شود تا رهگیری در فریم های بعدی ادامه یابد. نتایج نشان می دهد که رهگیری اهداف و عملکرد تطبیق با استفاده از روش پیشنهادی در توالی فریم های ویدئویی بر روی مجموعه داده ویدیویی چند دوربین عابر پیاده سایت"EPFL" ، بهبود یافته است. به طور خاص، خطاهای مثبت و منفی کاذب در رهگیری روش پیشنهادی کاهش یافته اند.

IJE TRANSACTIONS C: Aspects Vol. 34, No. 6, (June 2021) 1455-1467

International Journal of Engineering

Journal Homepage: www.ije.ir

Power Quality Improvement in Microgrids using STATCOM under Unbalanced Voltage Conditions

M. Ahmadi*, P. Sharafi, M. H. Mousavi, F. Veysi

Department of Electrical Engineering, Razi University, Kermanshah, Iran

P A P E R I N F O

Paper history:
Received 10 December 2020
Received in revised form 05 February 2021
Accepted 27 February 2021

Keywords:
Microgrid
Static Synchronous Compensator
Voltage Source Converter
Voltage Unbalance
Point of Common Coupling

A B S T R A C T

A large number of single-phase loads and sources create unbalanced voltage in microgrids. Voltage unbalance reduces the power quality, which results in misoperation or failure of customer equipment and microgrid. Also, voltage unbalance negatively impacts induction motors, power electronic converters, and adjustable speed drives. Static synchronous compensator (STATCOM), as an influential segment of the Flexible Alternative Current Transmission Systems (FACTS), has been extensively utilized as shunt compensators for controlling reactive power and regulation voltage in transmission and distribution networks. Under unbalanced conditions, an oscillating couple between the positive and negative sequence components of control loops emerge in the d-q frame. This paper suggests an innovative point of common coupling (PCC) voltage controller in Decoupled Double Synchronous Reference Frame (DDSRF) to compensate for an unbalanced PCC voltage and reduce the oscillating couple using STATCOM. Implementation of the proposed DDSRF involves several steps. Firstly, unbalance signals are rotated counterclockwise to split up the positive sequences. Secondly, those signals are rotated clockwise to separate negative sequences. Finally, by utilizing mathematical equations, the proposed DDSRF is introduced, which enables independent control of positive and negative sequence components. This study controls DC capacitor voltage for unbalanced conditions. Furthermore, the regulation voltage at PCC is performed. The control system scheme is also designed under unbalanced conditions, and simulation results guarantee the suggested control strategy.

***doi**: 10.5829/ije.2021.34.06c.09*

NOMENCLATURE

V_{sabc}	Line to neutral voltages at the PCC.	$v^{-}_{sqd\_ref}$	Negative sequence d-q components of the voltage reference.
I_{abc}	Line currents supplied by the VSC.	P^{+}, Q^{+}	Positive sequence active and reactive power.
v^{+}_{sqd}	Positive sequence d-q components of the voltage at the PCC.	L, R, C_f	Output filter of the DG.
v^{-}_{sqd}	Negative sequence d-q components of the voltage at the PCC.	k^{+}_{qdv}	Proportional controller of the positive inner voltage loop.
v^{+}_{tqd}	Positive sequence d-q components of the voltage at DG terminal.	k^{-}_{qdv}	Proportional controller of the negative inner voltage loop.
v^{-}_{tqd}	Negative sequence d-q components of the voltage at DG terminal.	k^{+}_{qdI}	Proportional integral controller of the positive inner current loop.
i^{+}_{qd}	Positive sequence d-q components of the current.	k^{-}_{qdI}	Proportional integral controller of the negative inner current loop.
i^{-}_{qd}	Negative sequence d-q components of the current.	τ_i	Time constant of the closed loop current control.
i^{+}_{lqd}	Positive sequence d-q components of the load current.	z_L	Line impedance.
i^{-}_{lqd}	Negative sequence d-q components of the load current.	C	DC-side capacitor.
$i^{+}_{qd\_ref}$	Positive sequence d-q components of the reference current.	V_{dc_ref}	References of DC voltage.
$i^{-}_{qd\_ref}$	Negative sequence d-q components of the reference current.	V_{dc}	Output of DC voltage.
$\theta^{\pm}$	Positive and negative sequence of the angle.	K_{vdc}	DC-bus compensator.

*Corresponding Author Institutional Email: Mojtabaahmadi3201@yahoo.com (M. Ahmadi)

Please cite this article as: M. Ahmadi, P. Sharafi, M. H. Mousavi, F. Veysi, Power Quality Improvement in Microgrids using STATCOM under Unbalanced Voltage Conditions, International Journal of Engineering, Transactions C: Aspects Vol. 34, No. 6, (2021) 1455-1467

$\varphi^{\pm}$	Positive and negative sequence of the initial phase.	V_g	Grid voltage.
ω_n, ξ	Natural frequency and damping ratio of notch filter.	PLL	Phase locked loop.
$v^{+}_{sqd\_ref}$	Positive sequence d-q components of the voltage reference.	PCC	Point of common coupling.

1. INTRODUCTION

In this energy-oriented era, the concept of the microgrid is of great significance. The microgrid is a power generation system with distributed generation units (DGs), loads, and energy storage systems. Although microgrids can be utilized in grid-connected mode, they also must have the capability to operate in islanding mode [1-2]. Amongst the various uncertainties of microgrids, the power quality problem is essential. One of the most challenging issues that put the power quality at high risks is voltage unbalance that may cause detrimental effects on equipment like transformers and induction motors [3]. Unbalanced voltage occurs because of the existence of unbalanced loads such as single-phase loads. Under unbalanced voltage conditions, microgrids can compensate for the unbalances so that the power delivered to sensitive loads at the PCC does not experience the quality reduction.

Accordingly, new systems are introduced to handle such obstacles and, consequently, improve the power grids performance. Flexible Alternative Current Transmission Systems (FACTS) devices are possible solutions to the above-mentioned issues. If FACTS devices are used beside proper controllers, they can enhance active and reactive power quality [4]. A static synchronous compensator (STATCOM) is a shunt FACTS device that exceedingly prominent in the power applications and voltage regulation of the PCC, and it can be employed to compensate for the unbalanced voltage [5]. To regulate the voltage at the point of common coupling (PCC), the STATCOM device controls reactive power volume. When the grid voltage is lower than what is needed, the STATCOM generates reactive power to increase the voltage. On the converse, when the system's voltage is higher than anticipated, it consumes the correct sum of reactive power to diminish the voltage [6].

In the structure of STATCOMs, voltage source converters (VSCs) are used. Considering this feature, the extra capacity of the control system of VSCs for injecting active and reactive power, voltage balancing and power quality improvement can be applied [7]. Properly injecting the power is one of the essential roles of the control system. To achieve this goal, DC-link control must be investigated. Hysa [8] used a PV system to produce power in DC side of the microgrid. Moreover, the effects of series and parallel resistances in the PV output are measured. However, the main point is to control the DC-link and how to consume this power. The feedback on controlling injected power was not provided by Hysa [8]. Besides, energy storage systems and secondary batteries are considered by Slavova et al. [9] and Sani [10], respectively. As it has already been mentioned, in previous studies, DC-link power port control was not investigated. Hence, a storage system and a PV were combined to build a microgrid [11]. AC and DC load are fed by this collection, and the main purpose of this microgrid is to control the DC port by using a PID controller. However, it should be noted that the controllers by Sagar and Debela [11] are designed in balanced conditions and without any fluctuations. It has got merit to be mentioned that under unbalanced conditions, storage systems and batteries performance are disrupted. Consequently, using a control system to cope with unbalanced condition is necessary. Therefore, many different methods have been extended to compensate for the unbalanced voltage by STATCOMs in the literature, mainly based on the separation of positive and negative sequence components. A novel form of STATCOM was introduced by Somasundaram and Rajesh Babu [12] utilizing a matrix converter in the control system to compensate for unbalanced voltage. In this method, to achieve robust performance, Particle Swarm Optimization was also added to the control system. Nevertheless, this approach eliminated dc port control, and there is no discussion of how active power is controlled because we know that the DC-link must be controlled to control the active power. It was also not a matter of separation of the asymmetric components of unbalancing. Song and Liu. [13] used the multi-level construction of STATCOM, which was star-connected to produce positive and negative components. But this approach was not appropriate for the multi-level STATCOM, and the implementation algorithm was very complicated. One strategy for unbalanced voltage compensation in STATCOMs can be based on microgrid modeling under the three-phase (Abc) frame. The dynamic phasor (DP) technique is an averaging method, which describes a time-domain waveform using DC variables [14]. That means a balance could be achieved from the dynamic phasor model in the (Abc) reference frame. A dynamic phasor concept has been presented by Shuai et al. [15] to model the unbalanced microgrid, including inverters. This dynamic phasor model has been developed in the (Abc) reference frame while the inner control loops of current and voltage have been studied through the rotating d-q coordinate.

On the other hand, some studies have proposed the Double Synchronous Reference Frame (DSRF) structure in the control system. In this method, to separate the

positive and negative sequence components, the unbalanced signals (voltage/current) are rotated counterclockwise with the system angular frequency. Doing this, 2W frequency oscillation emerges in the d-q frame. Since PI controllers are used in the inner control loops of DGs [16], oscillations with 2W frequency lead to some perturbations in the DG operation and affect the voltage control of the DC-link. Therefore, filters are applied to eliminate these oscillations [17-18]. A notch filter in the STATCOM control system was considered by Zhenglong et al. [19] to compensate the unbalanced voltage. However, the implementation of these methods cannot delete the oscillations between positive and negative components as well as the d-q frame, and it results in weakening the performance of the control system. Consequently, the DDSRF structure was suggested to remove the oscillating couple. The small-signal model of the DDSRF structure was proposed [20]. The DDSRF construction was exploited in the control system in which the current references were assumed to be completely DC and did not include oscillating components [21-22]. In fact, the current references have oscillating terms and they must be removed. Therefore, in this paper, the modified DDSRF method is introduced in the STATCOM control system to virtually eliminate the oscillating couple between positive and negative components in a case of unbalancing. The simulation results show that the proposed control approach compared to the conventional method in literature [21-22] is much more reliable and cross-coupling term effectively damped. Furthermore, the unbalanced voltage at PCC is compensated, and the voltage unbalance factor is under limited value. Also, the control system is designed so that DC-link control is not impaired by unbalanced conditions and, on the other hand, controlling and balancing the voltage of PCC are done. Finally, reactive power injection is performed to control AC voltage via a control system based on modified DDSRF.

This paper is organized as follows. In the second section, the structure of DDSRF is described. Then, in the third section, the control system of the STATCOM is presented. In the fourth section, the results of simulation of the STATCOM are discussed. The general conclusion is summarized in section five.

2. METHOD

The main goals of this paper are voltage balancing at PCC with different DDSRF-based control structures and, of course, DC-link control in the presence of unbalanced conditions. Figure 1 presents the schematic of a STATCOM in the grid-connected mode with connecting unbalanced load using an LCL filter. Moreover, in this figure, the control system of STATCOM is illustrated. To separate the positive and negative sequence components, DDSRF is used. The voltage control loop for compensating receives the positive and negative components and generates the controlling commands of the reference current. After the generation of reference currents, the current control loop is used to control the VSC current. References voltages in negative sequence *d-q* frame, $V_{sdref}{}^{-}$ and $V_{sqref}{}^{-}$ are equal to zero and $V_{sdref}{}^{+}$ is equal to the amplitude of grid voltage, i.e., 391v. These assumptions are considered because, in the unbalanced condition, the magnitude of V_d^- and V_q^- has an accountable value, but these values are about zero in the balance condition. For the after-mention reason, we consider $V_{sdref}^- = V_{sqref}^- = 0$ and utilize a proper controller in the voltage loop to achieve this purpose. The same scenario can be said for V_{sdref}^+ because, in balanced conditions, the magnitude is equal to the grid voltage. That is why $V_{sdref}^+ = 391\,v$.

3. PROPOSED CONTROL SYSTEM OF STATCOM

3. 1. DDSRF Organization in STATCOM The particular injection of negative and even the positive components of the current and voltage is vital to compensate for the unbalanced network; hence the negative and positive collection elements must be separated, which can be utilized for DSRF. In this technique, to split up the positive aspect, the current/voltage signal must turn counterclockwise. Furthermore, for any separation with the negative component, the current/voltage signal should be rotated within the clockwise direction. So, the three-phase unbalance current is considered as follows [23]:

$$i_{abc} = i_s^+ \cos(\omega t - k\frac{2\pi}{3}) + i_s^- \cos(-\omega t - k\frac{2\pi}{3}) \quad (1)$$

where superscripts + and - define the coefficients for the positive, negative sequence components, and $k = 0, 1, 2$. Using the Clarke transformation [23], the current vector in the $\alpha\beta$ plane is given by Equation (2):

$$i_{s\alpha\beta} = i_s^+ \begin{bmatrix} \cos(\omega t) \\ \sin(\omega t) \end{bmatrix} + i_s^- \begin{bmatrix} \cos(-\omega t) \\ \sin(-\omega t) \end{bmatrix} \quad (2)$$

The $\alpha\beta$ to d-q frame transformation can be obtained by multiplying $i_{s\alpha\beta}$ by Equation (3). After that, the positive and negative sequence components in the d-q axis are as follow:

$$T_{d-q} = \begin{bmatrix} \cos(\omega t) & \sin(\omega t) \\ \sin(\omega t) & \cos(\omega t) \end{bmatrix} \quad (3)$$

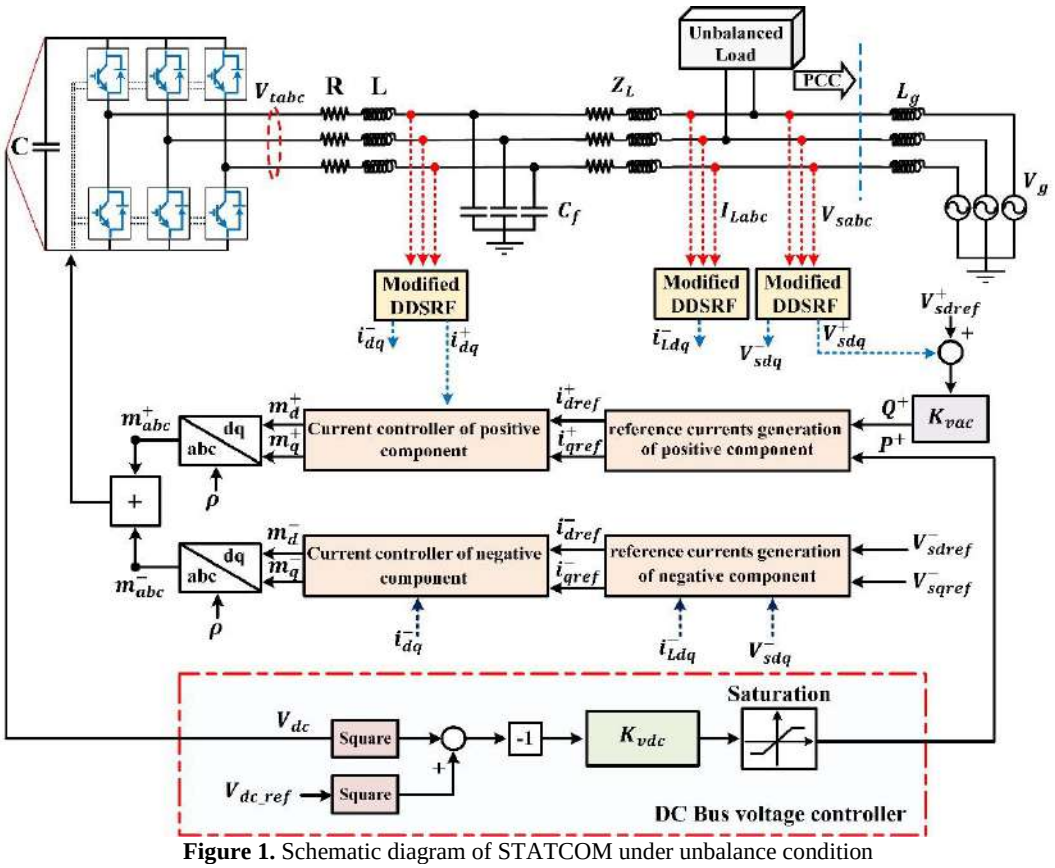

Figure 1. Schematic diagram of STATCOM under unbalance condition

$$i^+_{dq} = \underbrace{i^+_{dq}}_{DC\ term} + \underbrace{[\cos(\theta^+ - \theta^-) - j\sin(\theta^+ - \theta^-)]i^-_{dq}}_{Oscillation\ term} \quad (4)$$

$$i^-_{dq} = \underbrace{i^-_{dq}}_{DC\ term} + \underbrace{[\cos(\theta^- - \theta^+) - j\sin(\theta^- - \theta^+)]i^+_{dq}}_{Oscillation\ term} \quad (5)$$

where

$$\begin{aligned} i^+_d &= I^+\cos\left(\delta^+ - \varphi^+\right) \\ i^+_q &= I^+\sin\left(\delta^+ - \varphi^+\right) \\ i^-_d &= I^-\cos\left(\delta^- - \varphi^-\right) \\ i^-_q &= I^-\sin\left(\delta^- - \varphi^-\right) \end{aligned} \quad (6)$$

$$\begin{aligned} \theta^+ &= \omega t + \varphi^+ \\ \theta^- &= -\omega t + \varphi^- \end{aligned} \quad (7)$$

In the above equation, φ^+ and φ^- are initial phases of positive and negative sequence of voltage, respectively. Also, δ^+ and δ^- are initial phases of positive and negative sequence components.

Through Equations (4) and (5), it is clear that the components of the positive and negative sequence offer an oscillatory term and a DC term. DSRF current controllers function under unbalanced perturbations is not perfect because it cannot eliminate current and voltage oscillatory terms. To solve this problem, Decouple Double Synchronous Reference Frame (DDSRF) can be used [21] with a schematic diagram as shown in Figure 2. This method to remove oscillatory term is advantageous and stated as below:

$$\begin{aligned} i^+_{dq} = \; & \underbrace{i^+_{dq}}_{DC\ term} + \underbrace{[\cos(\theta^+ - \theta^-) - j\sin(\theta^+ - \theta^-)]i^-_{dq}}_{Oscillation\ term} - \\ & \underbrace{[\cos(\theta^+ - \theta^-) - j\sin(\theta^+ - \theta^-)].\underbrace{(i^-_{dq-ref} - \Delta i^-_{dq})}_{Dc\ term}}_{Cross-Coupling\ term} \end{aligned} \quad (8)$$

$$\begin{aligned} i^-_{dq} = \; & \underbrace{i^-_{dq}}_{DC\ term} + \underbrace{[\cos(\theta^- - \theta^+) - j\sin(\theta^- - \theta^+)]i^+_{dq}}_{Oscillation\ term} - \\ & \underbrace{[\cos(\theta^- - \theta^+) - j\sin(\theta^- - \theta^+)].\underbrace{(i^+_{dq-ref} - \Delta i^+_{dq})}_{Dc\ term}}_{Cross-Coupling\ term} \end{aligned} \quad (9)$$

In the above equations, and of course, according to Figure 2, the reference currents are assumed to be fully DC and non-oscillating. Given that, under unbalanced conditions, reference currents have oscillating components, the estimation of oscillatory components using reference currents is not as efficient as required. Therefore, according to Figure 3, in this paper the modified DDSRF, based on the measured currents is used to estimate oscillatory components:

$$i_{dq}^{+} = \underbrace{i_{dq}^{+}}_{DC\ term} + \underbrace{[\cos(\theta^{+}-\theta^{-}) - j\sin(\theta^{+}-\theta^{-})]i_{dq}^{-}}_{Oscillation\ term} - \underbrace{[\cos(\theta^{+}-\theta^{-}) - j\sin(\theta^{+}-\theta^{-})].i_{dq}^{-\prime}}_{Cross-Coupling\ term} \quad (10)$$

$$i_{dq}^{-} = \underbrace{i_{dq}^{-}}_{DC\ term} + \underbrace{[\cos(\theta^{-}-\theta^{+}) - j\sin(\theta^{-}-\theta^{+})]i_{dq}^{+}}_{Oscillation\ term} - \underbrace{[\cos(\theta^{-}-\theta^{+}) - j\sin(\theta^{-}-\theta^{+})].i_{dq}^{+\prime}}_{Cross-Coupling\ term} \quad (11)$$

where

$$i_{dq}^{+\prime} = i_{dq}^{+} \times \frac{S^2+\omega_n^2}{S^2+2\xi\omega_n+\omega_n^2}$$

$$i_{dq}^{-\prime} = i_{dq}^{-} \times \frac{S^2+\omega_n^2}{S^2+2\xi\omega_n+\omega_n^2}$$

In above equations, $\frac{S^2+\omega_n^2}{S^2+2\xi\omega_n+\omega_n^2}$ is transfer function of notch filter. ξ and ω_n are damping ratio and cut-off frequency.

3. 2. Reference Currents Generation of Positive and Negative Sequence Components

3. 2. 1. Reference Currents Generation of Positive Sequence Component After separating the positive and negative components, it is important to calculate active and reactive power delivered to the AC system based on the theory of instantaneous power.

Accordingly, active and reactive power in the d-q frame are as follow [24]:

$$P_s^{+}(t) = \frac{3}{2}\left[V_{sd}^{+}(t)i_d^{+}(t) + V_{sq}^{+}(t)i_q^{+}(t)\right] \quad (12)$$

$$Q_s^{+}(t) = \frac{3}{2}\left[-V_{sd}^{+}(t)i_q^{+}(t) + V_{sq}^{+}(t)i_d^{+}(t)\right] \quad (13)$$

As an assumption, if the PLL is in a steady state, $V_{sq}^{+} \approx 0$. Considering this, the influence between V_{sd}^{+} and V_{sq}^{+} is eliminated. Therefore, Equations (12) and (13) can be written as:

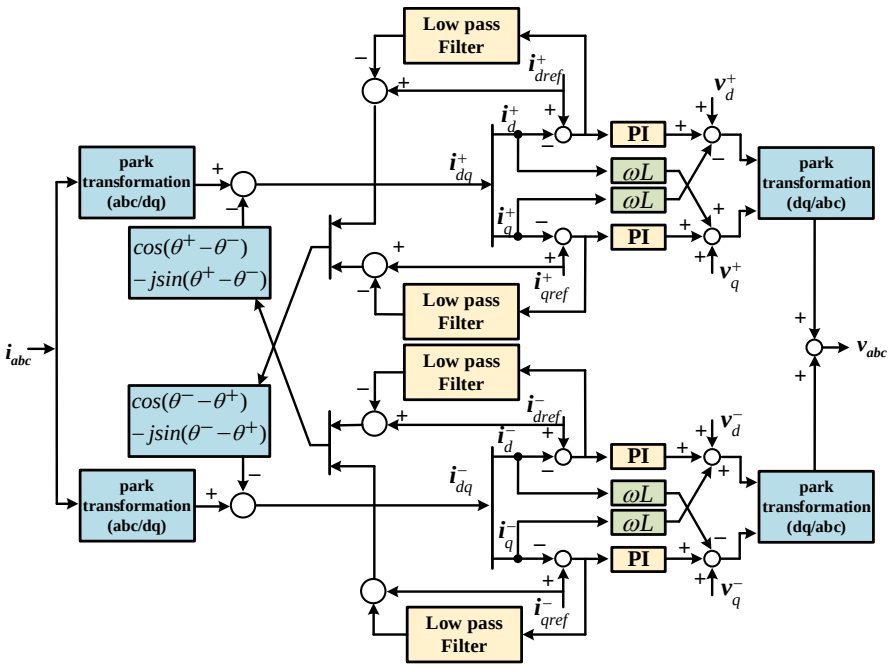

Figure 2. Presented DDSRF in reference [21]

$$P_s^+(t)=\frac{3}{2}\left[V_{sd}^+(t)i_d^+(t)\right] \quad (14)$$

$$Q_s^+(t)=\frac{3}{2}\left[-V_{sd}^+(t)i_q^+(t)\right] \quad (15)$$

Based on above equations P_s^+ and Q_s^+ can be controlled by i_d^+ and i_q^+ respectively; thus:

$$i_{dref}^+(t)=\frac{2}{3V_{sd}^+}P_s^+(t) \quad (16)$$

$$i_{qref}^+(t)=\frac{-2}{3V_{sd}^+}Q_s^+(t) \quad (17)$$

3. 2. 1. Reference Currents Generation of Negative Sequence Component The PCC open-loop control pattern can be realized using KCL on the STATCOM output capacity filter. Figure 1 shows that after converting these equations into the d-q frame, the following equations for negative sequential components are reached:

$$C_f\frac{dV_{sd}^-(t)}{dt}=I_d^-(t)-I_{Ld}^-(t)-C_f\omega(t)V_{sq}^-(t) \quad (18)$$

$$C_f\frac{dV_{sq}^-(t)}{dt}=I_q^-(t)-I_{Lq}^-(t)+C_f\omega(t)V_{sd}^-(t) \quad (19)$$

where $\omega(t)=\frac{d\rho}{dt}$ which ρ represent a phase shift in the PLL.

As it can be seen in Equations (18) and (19), there is a couple between V_{sd}^- and V_{sq}^- that this couple eliminated by feed-forward compensator (Figure 4). For the purpose of designing the $k_{d,qv}^-$ controllers, the simplified block diagram of the negative sequence components closed-loop voltage control is regarded in Figure 4. Here, τ_i is the desired time constant of the closed-loop control system, explained in the next part. The transfer function of the open-loop voltage control system has a pole leading to the coordinate; taking into account this, the steady-state error of the closed-loop system is zero, so that the $k_{d,qv}^-$ can be considered as a proportional controller with the k_{pv} value.

3. 3. Current Controllers of Positive and Negative Sequence Components The control model loop of STATCOM can be extended by applying KVL on the output inductance filter. From Figure 1, having

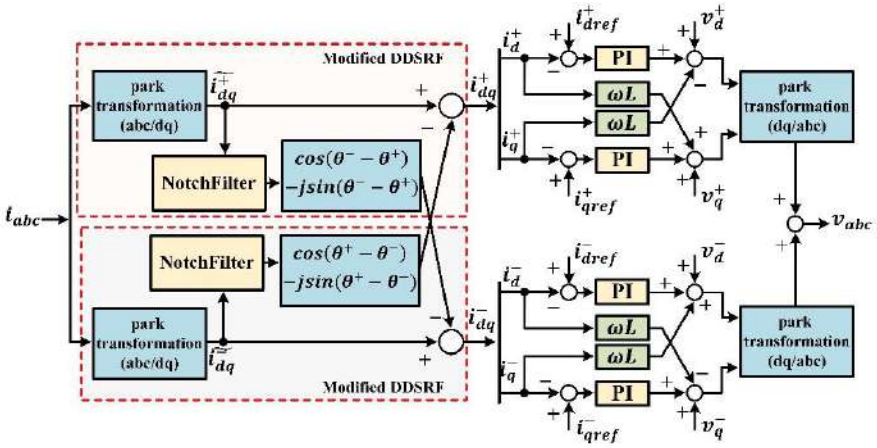

Figure 3. Modified DDSRF

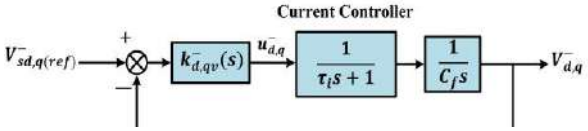

Figure 4. Simplified block diagram of the negative voltage control loop

transformed these equations into d-q frames:

$$L\frac{dI_d^+(t)}{dt}+(R+r_{on})I_d^+(t) =V_{td}^+(t)-V_{sd}^+(t)+L\omega_0 I_q^+(t) \quad (20)$$

$$L\frac{dI_q^+(t)}{dt}+(R+r_{on})I_q^+(t) = V_{tq}^+(t)-V_{sq}^+(t)-L\omega_0 I_d^+(t) \quad (21)$$

$$L\frac{dI_d^-(t)}{dt}+(R+r_{on})I_d^-(t) = V_{td}^-(t)-V_{sd}^-(t)-L\omega_0 I_q^-(t) \quad (22)$$

$$L\frac{dI_q^-(t)}{dt}+(R+r_{on})I_q^-(t) = V_{tq}^-(t)-V_{sq}^-(t)+L\omega_0 I_d^-(t) \quad (23)$$

According to principles of operation, the AC side terminal voltage of converter using in STATCOM deduced from the following equations [25]:

$$V_{td}^{\pm}(t)=\frac{V_{dc}}{2}m_d^{\pm} \quad \& \quad V_{tq}^{\pm}(t)=\frac{V_{dc}}{2}m_q^{\pm}$$

Due to the $L\omega_0$ term's presence in the above equations, there is a couple between I_d^+ and I_q^+ in both positive and negative sequence components. To decouple the dynamics, by using $u_{dq}(t)=V_{tdq}(t)-V_{sdq}(t)\pm L\omega_0 I_{dq}(t)$ in Equations (20)-(23) and rewriting equations in the Laplace domain:

$$LsI_{d,q}^{\pm}(s)=-(R+r_{on})I_{d,q}^{\pm}(s)+u_{d,q}^{\pm} \rightarrow I_{d,q}^{\pm}=\frac{u_d^+}{Ls+(R+r_{on})} \quad (24)$$

r_{on} is the converter internal resistance, and $u_{d,q}^{\pm}$ is the control command that defines in the before paragraph; other variables are defined in the NOMENCLATURE table. For the $k_{d,qI}^{\pm}$ control design, the closed-loop model of the current positive and negative components is considered functional schematics in Figure 5 and described by Equations (20)-(23). In order to equalize the steady-state error to zero, $k_{d,qI}^{\pm}$ is considered as a proportional-integral (PI) controller:

$$k_{d,qI}^{\pm}=k_p+\frac{k_i}{s} \quad (25)$$

Here k_p and k_i are the proportional and integral coefficients of the PI current controller. Thus, according to Figure 5, the transfer function of the open-loop system can be written in the following way:

$$T_{ol}(s)=\left(\frac{k_p}{Ls}\right)\left(\frac{s+\frac{k_i}{k_p}}{s+\frac{R+r_{on}}{L}}\right) \quad (26)$$

Taking into account Equation (26), the transfer function of the open-loop system has a steady pole at $p=-\frac{R+r_{on}}{L}$ Of course, this pole is partly close to the origin and is consistent with a slow response from the system. To ameliorate the system frequency response, the pole can be neutralized by the PI controller zero. For the closed-loop transfer function of the system:

$$G_i(s)=\frac{i_{d,q}^{\pm}(s)}{i_{d,q\,ref}^{\pm}(s)}=\frac{1}{\tau_i s+1} \quad (27)$$

Equation (27) is a first-order transfer function. τ_i is the desired time constant of the closed-loop control system, which should be very small to have a fast frequency response in the controller. On the other side by growing $\frac{1}{\tau_i}$, the closed-loop control system's bandwidth will rise considerably.

3. 4. DC Bus Voltage Controller The main purpose of control for the controlled DC voltage supply port is to adjust the DC bus voltage V_{dc} a feedback compensator with a required reference control. In the STATCOM system of Figure 1, the power is formulated as [25]:

$$P_{ext}-P_{loss}-\frac{d}{dt}(\frac{1}{2}CV_{dc}^2)=P_{dc} \quad (28)$$

where V_{dc}^2 is the output, P_{dc} is the control input, and P_{loss} , P_{ext} are the disturbance inputs. Equation (25) in the Laplace domain provides the voltage dynamics of the DC bus [25]:

$$G_v(s)=\frac{V_{dc}^2}{P_S}=-(\frac{2}{C})\frac{\tau S+1}{S} \quad (29)$$

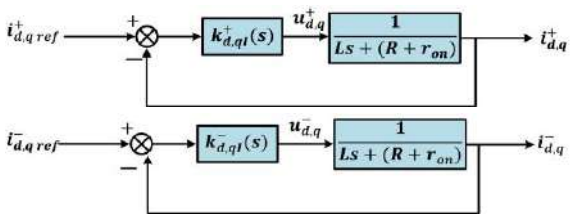

Figure 5. Simplified block diagram of the current control loop

In which the time constant τ is

$$\tau = \frac{2LP_{ext}}{3V_{sd}^2} \quad (30)$$

As shown in Figure 1 V_{dc}^2 is compared with $V_{dc\_ref}^2$; the error signal is processed by the compensator K_{vdc} , and P^+ is produced. The current controller regulates P^+ at P_{ref}^+ ; therefore, we can write:

$$G_i(s) = \frac{P^+(s)}{P_{ref}^+(s)} = \frac{1}{\tau_i s + 1}$$

Figure 6 shows a DC bus voltage regulator block diagram for the STATCOM in Figure 1. The closed-loop system is composed of the compensator $K_{vdc}(s)$, current controller $G_i(s)$, and control plant $G_v(s)$ .Thus, the open-loop transfer function is

$$\ell(s) = -K_{vdc}(s)G_i(s)G_v(s) \quad (31)$$

If consider $K_{vdc}(s) = \left(\frac{C}{2}\right)\frac{H(s)}{S}$ in (31) we found

$$\ell(s) = G_i(s)H(s)\frac{\tau S+1}{S^2} \quad (32)$$

To ensure that the phase delay due to $G_i(s)$ is negligible, $G_i(s) = 1$.

Based on defining the frequency response, the magnitude of the loop gain is infinity to the control signal frequency. To follow a control approach with zero stationary status errors, the unstable poles of the Laplace transform must be incorporated into the compensator. Likewise:

$$H(s) = h\frac{S+\alpha}{S+\beta}$$

Consequently

$$K_{vdc}(s) = h\frac{S+\alpha}{S(S+\beta)} \quad (33)$$

where h, and α , and β are coefficients of lead controller.

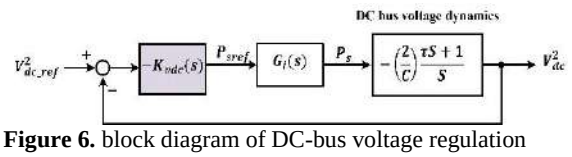

Figure 6. block diagram of DC-bus voltage regulation

4. RESULTS AND DISCUSSION

In this section, to confirm the proposed control system efficiency, the schematics presented in Figure 1 is simulated using MATLAB/SIMULINK. Here, to prove the introduction statements, a control technique based on DDSRF [21] is simulated and compared with the proposed method. The simulation details are listed in Tables 1 and 2.

4. 1. Comparison of Conventional DDSRF and Modified DDSRF As mentioned in previous sections, when reference currents are completely DC and do not have an AC sequence component, in order to decouple the sequence currents from each other, the conventional DDSRF [21] is accountable. However, when the reference currents are not DC and have an AC component, the conventional DDSRF cannot be held accountable. To demonstrate this pretension, a simulation is carried out in the condition that the reference current

TABLE 1. Parameters of simulated system

Parameter	Value
Nominal power of inverter [kW]	20
Phase voltage [v]	391 (peak)
Dc link capacitor [μF]	9812
Angular frequency [rad/sec]	377
Switching frequency [kHz]	3
Unbalance load [Ω]	0.01+j0.2
Inverter filter inductance [μH]	100
Inverter filter capacitance [μF]	2500
Distribution line [Ω]	0.01+j3.7
damping coefficient of notch filter	$\xi = 0.707$
natural frequency of notch filter	$F_n = 120\,\text{Hz}$

TABLE 2. Controller's characterization

Parameter	Value
$k_{dv}^- = k_{qv}^-$	1.6 [Ω^{-1}]
$k_{dI}^+ = k_{qI}^+ = k_{dI}^- = k_{qI}^-$	$0.2+4.14/S$ [Ω]
K_{vdc}	$1868\frac{S+19}{S(S+2077)}$ [Ω^{-1}]
K_{vac}	$\frac{2}{S}$ [MA]

of the q axis at the time t=1s is changed $i^{+}_{q\_ref} = 4 + \sin(120\pi t)$, and the reference current of the d axis at the time t=1.1s is changed to $i^{-}_{d\_ref} = 4$. Then, at t=1.2s, a sinusoidal term in form $i^{-}_{d\_ref} = \sin(120\pi t)$ is added. The results of comparison between the DDSRF and modified DDSRF are in Figures 7 and 8. As shown in Figures 7 and 8, when the reference current is not DC and has an AC component, the conventional DDSRF cannot appropriately extract the DC component. In contrast, the proposed DDSRF can correctly eliminate the ac component and extract the DC component.

4. 2. Voltage Balancing, DC Bus Voltage Control and Regulation Voltage in STATCOM with Proposed Method The results are extended to the modified DDSRF after ensuring that the conventional DDSRF cannot operate appropriately in a harmonic condition. A typical STATCOM can be used to control DC-link voltage, and of course, it can be utilized in order to regulate PCC voltage. In this paper, in addition to implementing these objectives, the voltage unbalance compensation at the PCC is performed using the modified DDSRF structure. The simulation time is organized as follows:

1. At t=0.3s, the reference of DC link voltage is changed from 1500v to 1700v.

2. At t=0.4s unbalanced load is added.

3. At t=1.9s, the reference of three-phase voltage is changed from 391v to 420v.

The unbalance load causes a voltage unbalance at the PCC. Figure 9 illustrates the PCC voltage when the proposed control system is employed for compensating the unbalanced voltage. This figure shows that the proposed control strategy effectively compensates for the unbalanced voltage.

Figure 10 presents the results of the FFT analysis of the PCC voltage. As can be observed in Figure 10a, when the conventional DDSRF method is used, the total harmonic distortion (THD) is 35.95%, which is bigger than the standard limit of 5% for distribution networks.

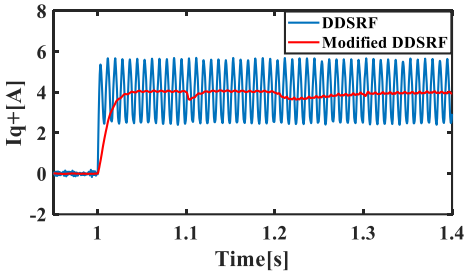

Figure 7. Positive sequence q component of the current under oscillation condition

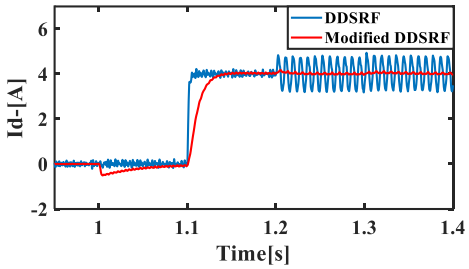

Figure 8. Negative sequence d component of the current under oscillation condition

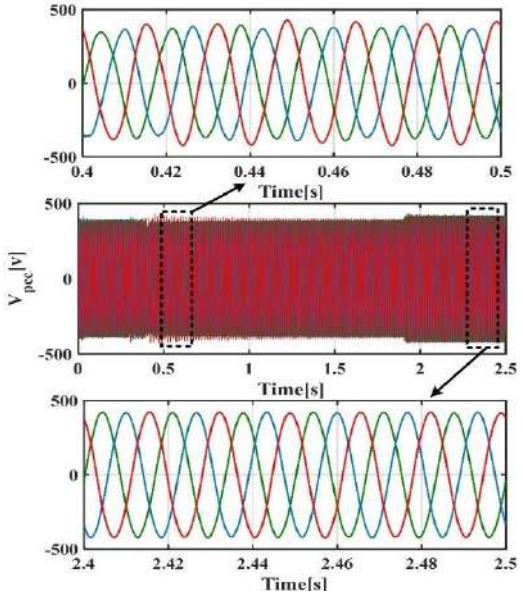

Figure 9. compensation of PCC voltage of STATCOM using modified DDSRF

The increase of the THD, in this case, is due to that the conventional DDSRF cannot effectively degrade the oscillatory coupling between the positive and negative sequence components, which leads to system instability. Using the modified DDSRF-based control method, the THD indicates that the results of FFT analysis is 1.04% within its standard limit (Figure 10b).

Figure 11 shows the voltage unbalance factor (VUF). According to the IEC description, the VUF is defined as the ratio of negative sequence voltage to the positive sequence voltage ($VUF\% = \frac{|V_-|}{|V_+|} \times 100$) [26]. This factor must be limited to under 2%. Figure 11a demonstrates that for the proposed method, after about 1.1 seconds, the VUF is reduced to less than 2%. Figure 11b shows that the control method based on conventional DDSRF causes instability. That is why suggesting the other forms of this method is avoided.

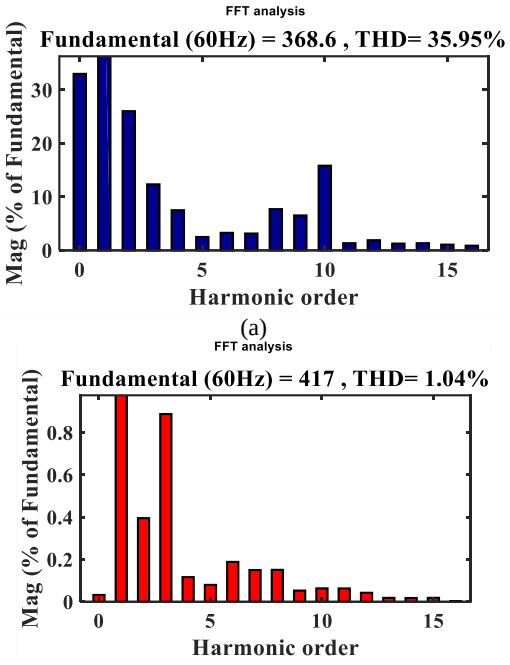

Figure 10. FFT analysis a) Modified DDSRF b) conventional DDSRF

Figures 12 and. 13 illustrate the positive and negative sequences of voltage in the d-q frame prominently. As can be seen, the positive sequence voltage in the d axis tracks its reference (391-420 V), and the positive component in the q axis and the negative components in the *d-q* axis are track zero, which proves the proper performance of the inverter control system. Furthermore, it is crystal clear that the amplitude of voltage in the negative sequence in the d and q axis decreases efficaciously. As a result, the value of the THD and the VUF remain acceptable at the steady-state.

Figure 14 shows the output active and reactive power of the STATCOM. This figure explains that, since the STATCOM is the device for controlling the reactive power and voltage control, the active power injecting it would be zero. As shown in Figure 14, at t=0.4s, when an unbalanced load is added to the system, the STATCOM control system delivers approximately 8×10^5 VAR of the reactive power to compensate for the unbalanced voltage. Also, at t=1.9s, when the AC voltage reference varies from 391v to 420v, STATCOM injected approximately 1.2×10^6 VAR of the reactive power to regulate of PCC voltage. It is noticeable that DDSRF based method has an accurate performance and provides a fast-dynamic response.

Figure 15 illustrates the controlled DC-voltage port time response when a feed-forward compensator is utilized in the DC-bus voltage control loop. At t=0.3s

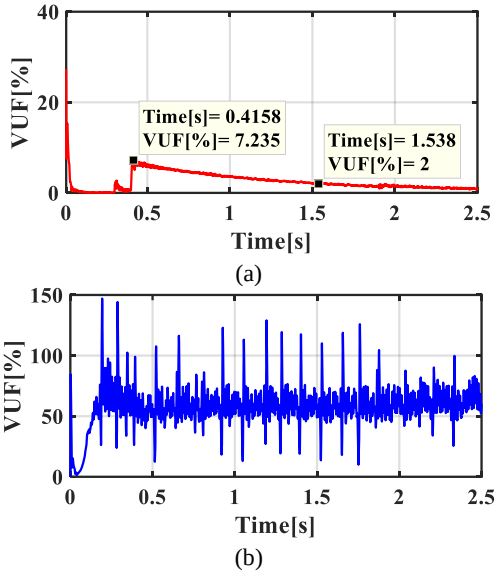

Figure 11. Voltage Unbalance Factor a) Modified DDSRF b) conventional DDSRF

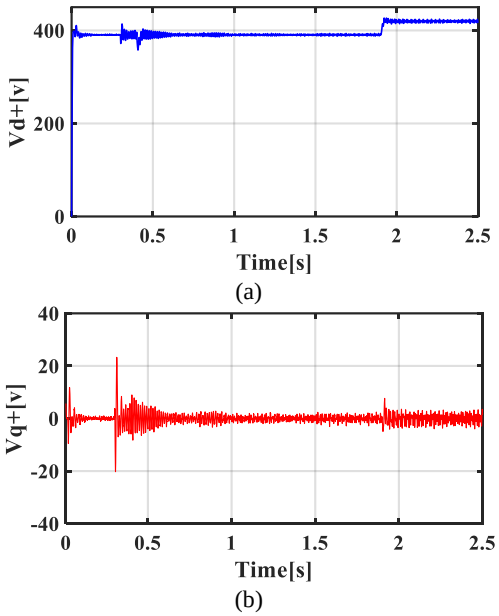

Figure12. Positive components of voltage at PCC for: a) d axis, b) q axis

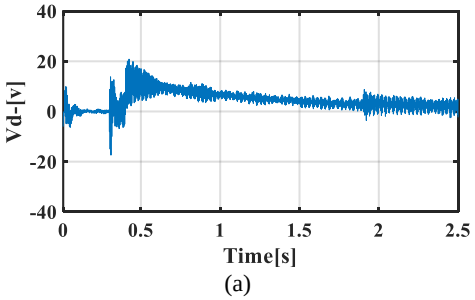

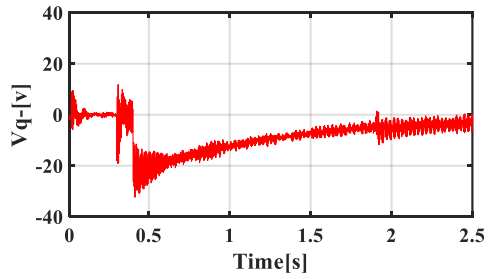

(b)

Figure 13. Negative components of voltage at PCC for: a) d axis, b) q axis

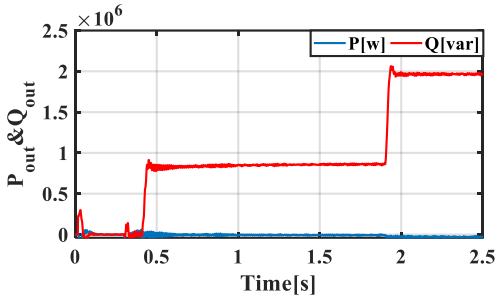

Figure14. Injected active and reactive power by STATCOM

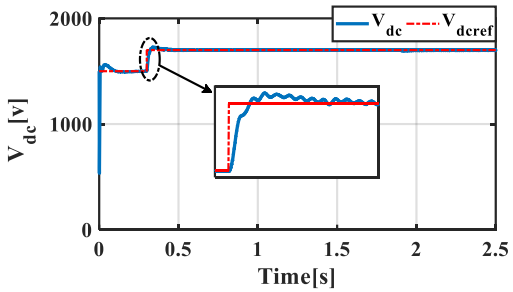

Figure 15. DC-link voltage control

reference of DC link voltage is changed stepwise from 1500v to 1700v. Consequently, to move V_{dc} up, K_{vdc} commands a negative P_{ref}^{+} to import real power from the AC system to the STATCOM DC side; P_{ref}^{+} is saturated to its negative limit for a brief period. It is perceptible that V_{dc} is regulated at $V_{dc\_ref} = 1700\,\text{v}$, and P_{ref}^{+} assumes small values corresponding to the VSC power loss.

5. CONCLUSION

This paper investigates a scheme for STATCOM control under unbalanced voltage to reduce oscillating coupled between the positive and negative sequence components using modified DDSRF. Simulation results show that the oscillating couple emerging in positive and negative sequence components of *d* and *q* frame in the conventional DDSRF is eliminated using the proposed DDSRF method and the system performance under unbalance voltage condition is improved. Applying the proposed technique, the magnitude of voltage unbalance factor and total harmonic distortion for voltage at PCC is acceptable. In addition, injected reactive power by means of STATCOM depends on PCC voltage variations. Also, regulation of AC voltage and control of DC-link voltage by employing feed-forward compensator are adequately performed to ensure the STATCOM proper functioning.

6. LIMITATION AND FUTURE WORK

The limitations of the proposed control strategy as well as the issue that need to be considered in order to extend the proposed approach are summarized as follows:
1) It is assumed that there is no load connected to DG's terminal. So, the unbalanced voltage at the DG's terminal does not negatively impact the loads.
2) It is assumed that the inverter has sufficient capacity for unbalanced voltage compensation.

As future work, a harmonic load can be added to the STATCOM and the DDSRF relations, and of course, voltage balancing and DC-link power port control can be expanded to the harmonic conditions. In this paper, only the second harmonic, 2W, is eliminated by the DDSRF, and the other harmonics must be developed and studied.

7. REFERENCES

1. Han, Yang, Pan Shen, Xin Zhao, and Josep M. Guerrero. "Control strategies for islanded microgrid using enhanced hierarchical control structure with multiple current-loop damping schemes." ***IEEE Transactions on Smart Grid***, Vol. 8, No. 3, (2015), 1139-1153, DOI: 10.1109/TSG.2015.2477698.
2. Baghaee, Hamid Reza, Mojtaba Mirsalim, Gevork B. Gharehpetian, and Heidar Ali Talebi. "Three-phase AC/DC power-flow for balanced/unbalanced microgrids including wind/solar, droop-controlled and electronically-coupled distributed energy resources using radial basis function neural networks." ***IET Power Electronics,*** Vol. 10, No. 3, (2017), 313-328, DOI: 10.1049/iet-pel.2016.0010.
3. Guerrero, Josep M., Poh Chiang Loh, Tzung-Lin Lee, and Mukul Chandorkar. "Advanced control architectures for intelligent microgrids—Part II: Power quality, energy storage, and AC/DC microgrids." ***IEEE Transactions on Industrial Electronics,*** Vol. 60, No. 4, (2012), 1263-1270, DOI**:** 10.1109/TIE.2012.2196889.
4. Aghaei, J., M. Gitizadeh, and M. Kaji. "Placement and operation strategy of FACTS devices using optimal continuous power flow." ***Scientia Iranica*** Vol. 19, No. 6, (2012), 1683-1690, DOI: 10.1016/j.scient.2012.04.021.
5. Subramanian, Sridhar Bala, Sibin Mohan, Mohammad Akbari, Hesamaldin Maleki, Reza Salehi, Wayne H. Litzenberger, and Rajiv K. Varma. "Control of STATCOMs–A review." In *2018* ***IEEE Power & Energy Society General Meeting*** *(PESGM)*,

IEEE, (2018), 1-5, DOI: 10.1109/PESGM.2018.8586479.

6. Hatano, Nobuhiko, and Toshifumi Ise. "Control scheme of cascaded H-bridge STATCOM using zero-sequence voltage and negative-sequence current." ***IEEE Transactions on Power Delivery,*** Vol. 25, No. 2, (2010), 543-550, DOI: 10.1109/TPWRD.2009.2035221.
7. Wang, Keyou, and Mariesa L. Crow. "Power system voltage regulation via STATCOM internal nonlinear control." ***IEEE Transactions on Power Systems,*** Vol. 26, No. 3, (2010), 1252-1262, DOI: 10.1109/TPWRS.2010.2072937.
8. Hysa, Azem. "Modeling and simulation of the photovoltaic cells for different values of physical and environmental parameters." ***Emerging Science Journal,*** Vol. 3, No. 6, (2019), 395-406, DOI: 10.28991/esj-2019-01202.
9. Slavova, Miglena, Elena Mihaylova-Dimitrova, Emiliya Mladenova, Borislav Abrashev, Blagoy Burdin, and Daria Vladikova. "Zeolite Based Air Electrodes for Secondary Batteries." ***Emerging Science Journal,*** Vol. 4, No. 1, (2020), 18-24, DOI: 10.28991/esj-2020-01206.
10. Sani, Mahnaz Jabbarzadeh. "Spin-Orbit Coupling Effect on the Electrophilicity Index, Chemical Potential, Hardness and Softness of Neutral Gold Clusters: A Relativistic Ab-initio Study." ***HighTech and Innovation Journal,*** Vol. 2, No. 1, (2021), 38-50, DOI: 10.28991/HIJ-2021-02-01-05.
11. Sagar, G. V. R., and T. Debela. "Implementation of optimal load balancing strategy for hybrid energy management system in dc/ac microgrid with pv and battery storage." ***International Journal of Engineering, Transactions A: Basics,*** Vol. 32, No. 10, (2019), 1437-1445, DOI: 10.5829/ije.2019.32.10a.13.
12. Somasundaram, Deepa, and Samuel Rajesh Babu. "A robust statcom controller using particle swarm optimization." ***International Journal of Engineering***, ***Transactions B: Applications,*** Vol. 27, No. 5, (2014), 731-738, DOI: 10.5829/idosi.ije.2014.27.05b.08.
13. Song, Qiang, and Wenhua Liu. "Control of a cascade STATCOM with star configuration under unbalanced conditions**."** ***IEEE Transactions on Power Electronics,*** Vol. 24, No. 1 (2009), 45-58, DOI: 10.1109/TPEL.2008.2009172.
14. Miao, Zhixin, Lakshan Piyasinghe, Javad Khazaei, and Lingling Fan. "Dynamic phasor-based modeling of unbalanced radial distribution systems." ***IEEE Transactions on Power Systems,*** Vol. 30, No. 6, (2015), 3102-3109, DOI: 10.1109/TPWRS.2014.2388154.
15. Shuai, Zhikang, Yelun Peng, Josep M. Guerrero, Yong Li, and Z. John Shen. "Transient response analysis of inverter-based microgrids under unbalanced conditions using a dynamic phasor model." ***IEEE Transactions on Industrial Electronics,*** Vol. 66, No. 4 (2018), 2868-2879, DOI: 10.1109/TIE.2018.2844828.
16. Wessels, Christian, Sönke Grunau, and Friedrich W. Fuchs. "Current injection targets for a STATCOM under unbalanced grid voltage condition and the impact on the PCC voltage." *Proc. EPE Joint Wind Energy TD Chapters Sem* (2011).
17. Nejabatkhah, Farzam, Yun Wei Li, and Bin Wu. "Control strategies of three-phase distributed generation inverters for grid unbalanced voltage compensation." ***IEEE Transactions on Power Electronics,*** Vol. 31, No. 7, (2015), 5228-5241, DOI: 10.1109/TPEL.2015.2479601.
18. Mishra, Priyanka, Ashok Kumar Pradhan, and Prabodh Bajpai. "Voltage control of PV inverter connected to unbalanced distribution system." ***IET Renewable Power Generation,*** Vol. 13, No. 9, (2019), 1587-1594, DOI: 10.1049/iet-rpg.2018.6219.
19. Zhenglong, Xia, Shi Liping, and Yang Xiaodong. "Control strategy of cascade STATCOM under unbalanced grid conditions." ***IETE Technical Review***, Vol. 31, No. 2, (2014), 177-185, DOI: 10.1080/02564602.2014.892741.
20. Bakhshizadeh, Mohammad Kazem, Jesper Hjerrild, Łukasz Kocewiak, Bo Hesselbæk, Xiongfei Wang, Frede Blaabjerg, and Claus Leth Bak. "Small-signal model of a decoupled double synchronous reference frame current controller." In *2016 IEEE 17th Workshop on Control and Modeling for Power Electronics (COMPEL)*, 1-6. IEEE, 2016, DOI: 10.1109/COMPEL.2016.7556713.
21. Reyes, Manuel, Pedro Rodriguez, Sergio Vazquez, Alvaro Luna, Remus Teodorescu, and Juan Manuel Carrasco. "Enhanced decoupled double synchronous reference frame current controller for unbalanced grid-voltage conditions." ***IEEE Transactions on Power Electronics,*** Vol. 27, No. 9, (2012), 3934-3943, DOI: 10.1109/TPEL.2012.2190147.
22. Misra, Himanshu, and Amit Kumar Jain. "Enhanced DDSRF based vector control of grid side converter using single AC side current sensor under unbalanced grid conditions." In *2016 IEEE International Conference on Power Electronics, Drives and Energy Systems (PEDES)*, 1-6. IEEE, 2016, DOI: 10.1109/PEDES.2016.7914355.
23. Rodríguez, Pedro, Josep Pou, Joan Bergas, J. Ignacio Candela, Rolando P. Burgos, and Dushan Boroyevich. "Decoupled double synchronous reference frame PLL for power converters control." ***IEEE Transactions on Power Electronics,*** Vol. 22, No. 2, (2007), 584-592, DOI: 10.1109/TPEL.2006.890000.
24. Vasquez, Juan C., Josep M. Guerrero, Mehdi Savaghebi, Joaquin Eloy-Garcia, and Remus Teodorescu. "Modeling, analysis, and design of stationary-reference-frame droop-controlled parallel three-phase voltage source inverters." ***IEEE Transactions on Industrial Electronics,*** Vol. 60, No. 4, (2012), 1271-1280, DOI: 10.1109/TIE.2012.2194951.
25. Yazdani, Amirnaser, and Reza Iravani. *Voltage-sourced converters in power systems*. Vol. 39. Hoboken, NJ, USA: John Wiley & Sons, 2010, DOI: 10.1002/9780470551578.
26. Savaghebi, Mehdi, Alireza Jalilian, Juan C. Vasquez, and Josep M. Guerrero. "Secondary control scheme for voltage unbalance compensation in an islanded droop-controlled microgrid**."** ***IEEE Transactions on Smart Grid,*** Vol. 3, No. 2, (2012), 797-807, DOI: 10.1109/TSG.2011.2181432.

Persian Abstract

چکیده

بسیاری از منابع و بارهای تکفاز سبب بروز نامتعادلی در ریزشبکه می‌شوند. نامتعادلی ولتاژ کیفیت توان ریزشبکه را کاهش می‌دهد و از تبعات آن عملکرد نادرست و قطعی بارها و تجهیزات مصرف‌کنندگان ریزشبکه است. همچنین ولتاژ نامتعادل اثرات مخربی بر موتورهای القایی، مبدل‌های الکترونیک قدرت و درایوهای تنظیم سرعت دارد. جبران‌ساز استاتیک سنکرون به عنوان یک بخش مؤثر از ادوات FACTS (سیستم انتقال جریان متناوب انعطاف‌پذیر) به طور گسترده‌ای به عنوان یک جبران‌ساز موازی در کنترل توان راکتیو و تنظیم ولتاژ در شبکه‌های توزیع کاربرد دارد. تحت شرایط نامتعادل یک کوپل نوسانی بین مولفه‌های توالی مثبت و منفی در محور d-q به وجود می‌آید. این مقاله یک کنترل کننده ولتاژ PCC (نقطه اتصال مشترک) را در قاب مرجع سنکرون دوگانه مجزا (DDSRF) را ارایه می‌دهد که نامتعادلی ولتاژ PCC را جبران می‌کند و همچنین کوپل نوسانی نیز توسط STATCOM (جبران‌ساز سنکرون استاتیک) با استفاده از حلقه‌های مجزای مثبت و منفی برطرف می‌شود. پیاده‌سازی سیستم DDSRF پیشنهاد شده شامل چندین مرحله است: ابتدا سیگنال‌های نامتعادل به منظور جداسازی مولفه‌های مثبت بر خلاف جهت عقربه‌های ساعت چرخانده می‌شوند بار دیگر همان سینگال‌ها به منظور جدا شدن مولفه‌های منفی در جهت عقربه‌های ساعت چرخانده شده و در پایان با استفاده از روابط ریاضی سیستم کنترل پیشنهادی DDSRF معرفی می‌گردد که این سیستم قادر است مولفه‌های مثبت و منفی را به طور جداگانه کنترل کند. در این مقاله علاوه بر کنترل ولتاژ خازن DC تنظیم ولتاژ PCC نیز انجام شده است. طرح سیستم کنترل پیشنهادی تحت شرایط نامتعادل طراحی شده است و نتایج شبیه‌سازی کارایی و اثربخشی استراتژی کنترلی پیشنهادی را تضمین می‌کند.

IJE TRANSACTIONS C: Aspects Vol. 34, No. 6, (June 2021) 1468-1474

International Journal of Engineering

Journal Homepage: www.ije.ir

Mitigation of Spectrum Sensing Data Falsification Attack in Cognitive Radio Networks using Trust Based Cooperative Sensing

K. Mergu*[a], H. Khan[b]

[a] *Department of Electronics and Communication Engineering, Sri Satya Sai University of Technology and Medical Sciences, Madya Pradesh, India*
[b] *Department of Electronics and Communication Engineering, K. L. Deemed to be University, India*

PAPER INFO

Paper history:
Received 08 August 2020
Received in revised form 14 April 2021
Accepted 04 May 2021

Keywords:
Cognitive Radio
Security Attacks
Spectrum Sensing Data Falsification
Cooperative Spectrum Sensing Primary User
Secondary User

ABSTRACT

One of most emerging technology in recent years in the field of wireless communication is the Cognitive Radio (CR) technology, which reduces spectrum scarcity significantly. The main function of CR technology is detecting spectrum holes or unused spectrum of primary users (PUs), also called as licensed users, and assigning this unused spectrum to the secondary users (SUs), also called unlicensed users. As the CR technology is open to every user, there are many security issues such as Primary User Emulsion Attack (PUEA), Jamming Attack, Spectrum Sensing Data Falsification (SSDF) Attack, Lion Attack, and Sink Hole Attack and so on. SSDF attack is the one of major security attack in cognitive radio in which a malicious user sends false data intentionally to the other secondary users. The main aim of the SSDF attack is to disturb the communication between the secondary users or to gain more channel resources. One of the solutions to mitigating SSDF attack is the cooperative spectrum sensing. In this paper, we propose a new algorithm of cooperative sensing based on trust values of secondary users, and compares with the conventional cooperative spectrum sensing with the proposed algorithm. In this algorithm, firstly the CR which is waiting for the channel allocation sense the information and compare the sensing information of other CRs. If any CR's sensing report not matches with the test CR's sensing with in the cluster, it will punish that CR otherwise it will give the reward. This procedure will be repeated for number of cycles. Finally test CR calculates the trust value. Based on the trust value fusion center will take the decision to include or exclude the trusting value of particular CR. The simulation of cooperative sensing also performed in both time variant channel and time invariant (Rayleigh) channel. The authors also compare the three basic hard fusion techniques such as AND, OR, MAJORITY rule.

***doi**: 10.5829/ije.2021.34.06c.10*

NOMENCLATURE

CR	Cognitive Radio	H_1	Alternative Hypothesis
SS	Spectrum Sensing	P_{fa}	Probability of False alarm
PU	Primary User	P_d	Probability of Detection
SU	Secondary User	P_m	Probability of Miss Detection
MU	Malicious User	N	Number of Cognitive Radio Users
Centralized CSS	Centralized Cooperative Sensing	**Greek Symbols**	
Distributed CSS	Distributed Cooperative Sensing	λ_{ED}	Threshold of energy detection
H_0	Null Hypothesis	σ_W	Variance of noise

1. INTRODUCTION

The applications of wireless communications networks increase rapidly in the recent years; which lead to a major problem of spectrum scarcity. Since the available spectrum is fixed. However, a large amount of assigned spectrum is not utilized efficiently by the licensed user. One solution to the spectrum scarcity and utilization of low spectrum is that opportunistic access of the valid spectrum band should be assigned to unlicensed secondary users [1].

*Corresponding Author Email: kattaswamy@gmail.com (K. Mergu)

Please cite this article as: K. Mergu, H. Khan, Mitigation of Spectrum Sensing Data Falsification Attack in Cognitive Radio Networks using Trust Based Cooperative Sensing, International Journal of Engineering, Transactions C: Aspects Vol. 34, No. 6, (2021) 1468-1474

Cognitive Radio uses a technology called spectrum sensing that sense the unused spectrum or ERD empty spectrum and assigns this spectrum to unlicensed users and avoid any collision and minimize harmful interference to the licensed users. The detection accuracy of spectrum sensing determines the performance of the whole CR systems to a great extent [2]. According to Kattaswamy [3], the spectrum user signals are categorized into primary users (PUs) signals, having licensed spectrum band and secondary users (SUs) signals, do not have any licensed spectrum band. Cognitive Radio cycle includes, spectrum sensing, spectrum decision, spectrum sharing and spectrum mobility [3].

Spectrum Sensing: sense the surrounded RF spectrum to detect unused spectrum or spectrum hole and determine the presence of the primary user.

Spectrum Decision: finding which spectrum band/hole is suitable for satisfying the requirements of application.

Spectrum Sharing: share the information about the empty spectrum to other secondary user.

Spectrum Mobility: when primary user is present, switch to another suitable empty spectrum band to avoid interference.The performance of the whole CR system can be evaluated by the detection accuracy of the spectrum sensing techniques. The time varying characteristics of wireless channel, multipath fading and shadowing effect leads to erroneous sensing decisions and result in inefficient spectrum utilization or interference with the primary user [4]. Cooperative Spectrum sensing gives the better solution to the above. It improves the reliability of spectrum utilization. In cooperative sensing, the individual sensing nodes cooperate each other by sharing detection decisions to detect the presence of primary user.

Spectrum Sensing techniques are divided into two types:

i. Local Spectrum Sensing

ii. Cooperative Spectrum Sensing

Local spectrum sensing, performed by each individual CR. It is associated with many challenges which make it difficult to detect vulnerability. Some of them are sensitivity requirement, receiver uncertainty, hidden node problem [5]. Cooperative Sensing provides better way for all the above challenges. Cooperative spectrum sensing can be classified as either centralized or distributed based on the architecture, central entity availability, quality of the control channel [6], [7].

The process of CSS includes three main steps. They are local sensing, reporting to the fusion center (FC), and global decision making [5].

Centralized CSS: It is the most popular architecture. It consists of central entity also called fusion center and a number of SUs associated with it [8,9]. In this approach, each SUs executes local spectrum sensing individually and forward their decision to the FC as one bit (hard fusion) or as raw data (soft fusion). Finally, FC collects the data and combines the result of all SUs according to fusion rule and makes final decision about the PU existence.

Distributed CSS: all the SUs share their information among each other through the multiple iterations until a consensus is reached [10]. Cognitive user sends the local spectrum sensing results to other adjacent SUs, then the cognitive user fuses the received data to make final decision. Finally, if empty spectrum is not detected, SUs repeat the process iteratively until a unanimous final decision is reached [5].

As we know that, cognitive radio technology is open to every user, it is easy to incur various kinds of security attack at different layers. Some of them are, primary emulsion attack (PUEA), spectrum sensing data falsification (SSDF) attack, jamming attack and so on.

The SSDF attack is the attack made by a malicious user by false information intentionally to other secondary users or fusion center [11] during the process of cooperative sensing. It will leads a serious damage on reliability of cooperative spectrum sensing. Hence, it is necessary design a secure and effective cooperative spectrum sensing to resist SSDF [4].

In this paper, the authors discuss the various types of ssdf attacks and proposes a new algorithm for cooperative sensing based on trust values of individual cognitive users. The author also compares the detection performance of conventional cooperative sensing and proposed cooperative spectrum sensing with different hard fusion rules.

2. SYSTEM MODEL

Consider a cognitive radio network of N cognitive/secondary users and one fusion center (FC). A CR user uses conventional energy detection (ED) with threshold λ_{ED} makes the binary decision (either '0' or '1' bit) over a fading or shadowing channel.

We assumed that all the CR users use the same threshold. The detection of primary signal presence in the spectrum band can be obtained based on the binary hypothesis given below:

$$y[k] = \begin{cases} w[k] \text{under} H_0 \\ h * x[k] + w[k] \text{under} H_1 \end{cases} \quad (1)$$

where w[k]= additive white gaussian noise with zero mean and variance.

x[k]=the primary user's signal

h=channel gain

H0=null hypothesis, indicates the primary user's signal is absent

H1=null hypothesis, indicates the primary user's signal is present

2. 1. Local Sensing by Energy Detection It is the simplest and most popular spectrum sensing technique. It is also called as blind detection technique, does not require prior information about the primary user [3]. The block diagram of spectrum sensing using energy detection is shown in Figure 1.

The test static for energy detection is [12]:

$$\text{Test Statistic}=T_{test}=\sum_{k=1}^{N}|y[k]^2| \quad (2)$$

According to the central limit theorem, if the number of samples(N) is large (N>250) enough, the pdf of any signal approach to a Gaussian distribution [3]. Hence, the probability of false alarm and probability of detection can be defined in Equation (3). The probability of false alarm is:

$$P_{fa}=\int_{\gamma}^{\infty} f(y/H_0)dy=Q\left(\frac{\lambda_{ED}-N\sigma_w^2}{\sqrt{2N\sigma_w^4}}\right) \quad (3)$$

where λ_{ED} is the threshold, Q is the Q-function and σ_W is the standard deviation of noise, P_{fa} is the probability of false alarm. The probability of detection is:

$$P_d=\int_{\gamma}^{\infty} f(y/H_1)dy=Q\left(\frac{\lambda_{ED}-N(\sigma_x^2+\sigma_w^2)}{\sqrt{2N(\sigma_x^2+\sigma_w^2)^2}}\right) \quad (4)$$

σ_x is the standard deviation of signal x form Equation (3), the threshold can be derived as:

$$\lambda_{ED}=\sigma_w^2\left(Q^{-1}(P_{fa})\sqrt{2N}+N\right) \quad (5)$$

2. 2. Hard Fusion Rule Firstly, every SU makes a decision locally and sends it to the fusion center. Then, FC applies a linear fusion rule and makes overall decision about the PU existence. Hard decision rules are classified as OR, AND, MAJORITY rules. These are special cases of Kout N rule [9]. Kout of N rule also known as counting rule. Here, N is the total number of cognitive users and K is the number of cognitive users that have decided that spectrum is used.

i. OR-Rule: The spectrum band is assumed to be occupied, if at-least one of the cognitive user decides that the channel (band) is busy i.e. K=1 [8]. Even though it increases PU protection, decreases the efficiency of spectrum utilization. Because, there is possibility that the given CR may sense the spectrum false due to shadowing and multipath fading. Hence, the final decision may be taken by fusion center that the channel is busy.

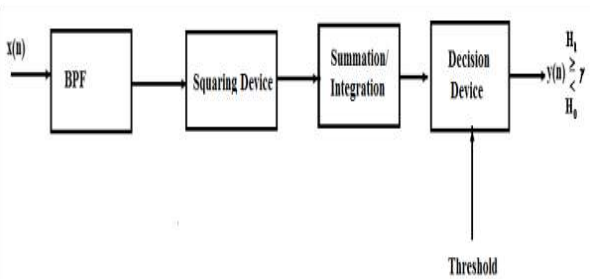

Figure 1. Block diagram of Spectrum sensing using Energy detection [3]

The global probability of detection can be obtained as:

$$Q_{dOR}=1-\prod_{k=1}^{N}(1-P_{dk}) \quad (6)$$

The global probability of false alarm can be obtained as:

$$Q_{fOR}=1-\prod_{k=1}^{N}(1-P_{fk}) \quad (7)$$

where P_{fk} and P_{dk} are the local probability of false alarm and probability of detection for k^{th} cognitive user respectively.

ii. AND-Rule: The spectrum band is assumed to be occupied, if all the cognitive users decide that the channel (band) is busy i.e. K=N. Although the AND rule based cooperative sensing increases the spectrum utilization but also it increases the risk of interference with the PU [12]. Due to the shadowing effect or multipath path there may be a possibility that any one of the CR reports false information. Then, FC declares that channel is free leads to CR inference with the PU.

The global probability of detection can be obtained as:

$$Q_{dAND}=1-\prod_{k=1}^{N}(1-P_{dk}) \quad (8)$$

The global probability of false alarm can be obtained as:

$$Q_{fAND}=1-\prod_{k=1}^{N}(1-P_{fk}) \quad (9)$$

where P_{fk} and P_{dk} are the local probability of false alarm and probability of detection for k^{th} cognitive user respectively.

iii. Majority K out of N-Rule: The spectrum band is assumed to be occupied, if at-least K cognitive users decide that the channel (band) is busy i.e. K=N/2 [12]. It compromises between the spectrum utilization and protection of PU.

The global probability of detection can be obtained as:

$$Q_{dMAJORITY}=\sum_{m=k}^{N}\binom{N}{m}P_i^m(1-P_i)^{N-m} \quad (10)$$

where P_d is probability of detection for each individual cognitive user.

3. SSDF ATTACK AND ITS MITIGATION STRATEGY

SSDF is the most effective attack in the cognitive radio networks by the malicious secondary users. An attacker may send the false local spectrum sensing results to fusion center (FC) causing the FC to make the final decision wrong. The SSDF attack is illustrated in Figure 2. The local spectrum sensing results must be robust and trusty in the CSS networks, to maintain adequate level of accuracy in the sensing decision.

Generally, SSDF attacks further classified as follows

i. Always Yes Attack: The malicious user sends the decision to the fusion center always '1' even the channel is free.

ii. Always No Attack: The malicious user sends the decision to the fusion center always '0' even the channel is occupied.

ii. Randomly False Attack: The malicious user sends the decision to the fusion center '1' when it receives '0' and '0' when it receives '1' i.e. it gives always wrong decision to the FC.

In this section, we are assumed that the local sensing technique is energy detection and also we concentrated only on mitigating randomly false SSDF attack based on the trust values of SUs.

3. 1. Proposed Algorithm

This algorithm is mainly based on trust value of the neighboring cognitive users. In this algorithm, firstly, the secondary user who want to use the spectrum hole, will find the local spectrum decision of itself. Then, it collects the spectrum result of neighboring secondary users. It compares spectrum results with the neighbor's spectrum result for number of cycles. If the spectrum decision of neighboring user's matches with its spectrum decision, it gives the trust value to them otherwise it neglects the decision of that user while performing the global decision. The flow chart of proposed trust based algorithm is shown in Figure 3.

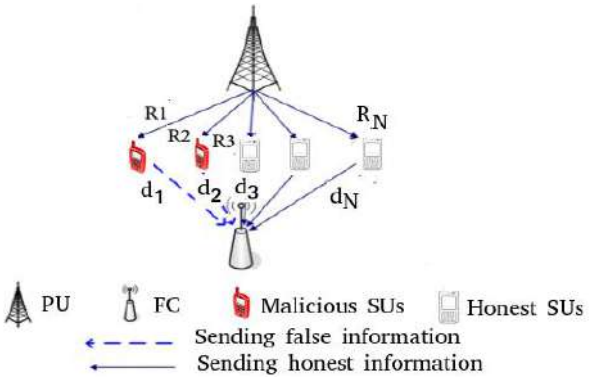

Figure 2. Random false SSDF attack

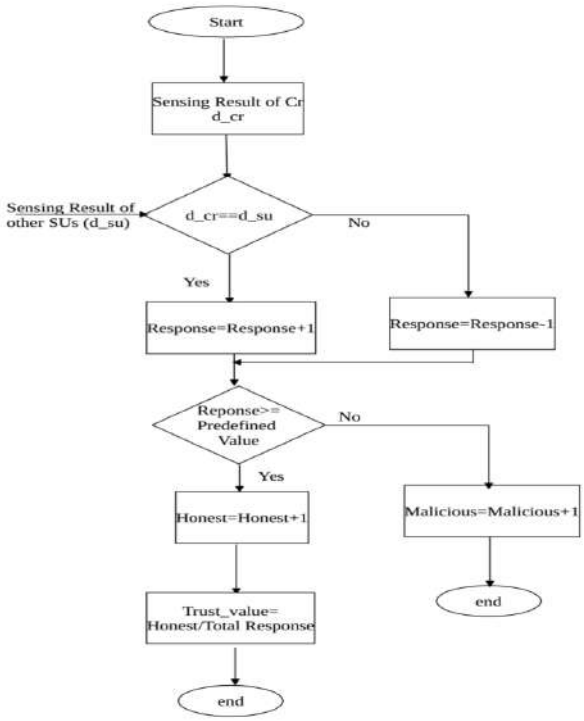

Figure 3. Flow chart of Proposed trust value algorithm

The algorithm is as follows

Input: No. of cognitive users (N), No.of cycles (Count)

Output: trust_value

Intialize: local sensing decision of cr (d_cr), local sensing decision of other secondary users (d_su), decision of malicious user (d_mu), decsion of honest user (d_hu).

1. **for** k=1 to count **do**
2. **if** d_cr==d_su **then**
3. response=response+1
4. **else**
5. response=response-1
6. **end if**
7. **if** response<= presdefined_value **then**
8. d_mu=d_mu+1
9. **else**
10. d_hu=d_hu+1
11. **end if**
12. trust_value=d_hu/total response
13. **end for**

4. RESULTS

The performance evaluation of proposed approach is obtained by using Matlab simulation. The simulation is performed based on cyclic fusion rule. At each cycle, only few of SUs are selected

for cooperation to calculate the trust value. The description of simulation elements are shown in Table 1.

Figure 4 shows the simulation of comparison between the hard fusion techniques without and without trust value. From the figure, it is clear that, OR rule based cooperative sensing gives the best probability detection and AND rule based cooperative technique gives poor performance comparing with MAJORITY rule. As we know that OR rule based cooperative technique decides that channel is busy if at-least one user decision is busy. It may gives the false decision because of misinterception of honest user due to shadowing and multipath fading.

Similarly, AND rule based cooperative technique gives false decision since it decides based on all secondary users decision. If any of honest user misinterception due to shadowing and multipath fading, it gives poor performance. Hence MAJORITY rule which takes the decision based on the majority of the secondary users. The comparison between the AND rule, OR rule and Majority rule with trust value and without trust value based cooperative sensing shown in Figure 4. It is observed that at probability of false alarm equals to 0.3, the probability of detection of AND rule, OR rule, Majority rule without trust value and with trust value are 0, 0.2, 0.5 and 1, respectively. Hence, trust value based cooperative sensing with majority rule perfoms better than the other three techniques.

The comparison of fixed threshold and adaptive threshold based on majority rule with and without trust value is shown in Figure 5. It is clear that adaptive threshold based cooperative sensing performs better than the fixed threshold based cooperative sensing. We also seen from the figure that adaptive threshold based cooperative sensing with trust value gives greater perfomance.

The performance of simulation of majority rule based cooperative sensing in both time variant and time invariant channel also compared as shown in Figure 6.

TABLE 1. Description of simulation elements

Parameter	Description	Value
N	No. of cognitive Users	10
P	No. Of PUs	2
Cycles	No. of cycle simulations	50
Mal	No. of malicious users	3
Threshold	threshold for trust value	0.6
pm	probability of misperception of malicious users	0.7
cm	probability of misperception of honest users	0.3
n	no. of CR selected randomly for cooperation	7

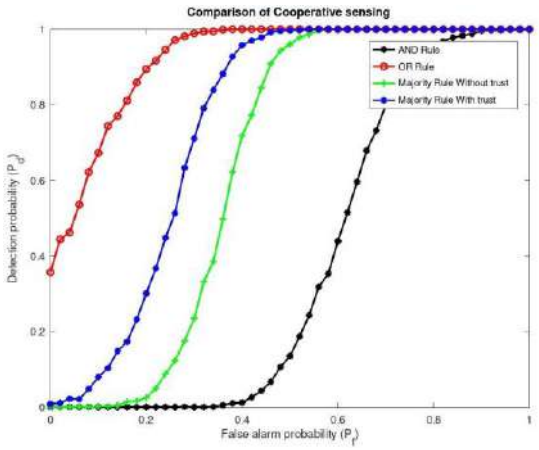

Figure 4. Comparison OF Cooperative sensing techniques with and without trust value

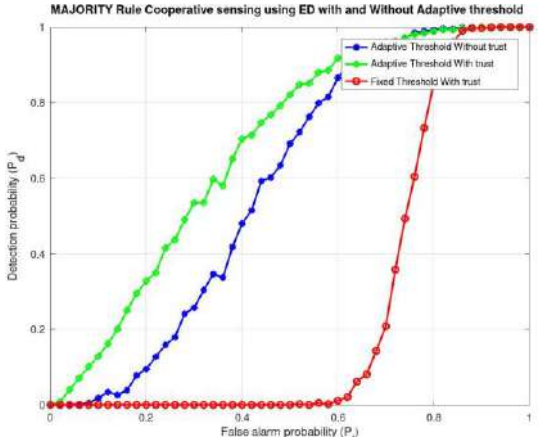

Figure 5. Comaprison of fixed threshold and adaptive threshold based majority rule with and without trust value

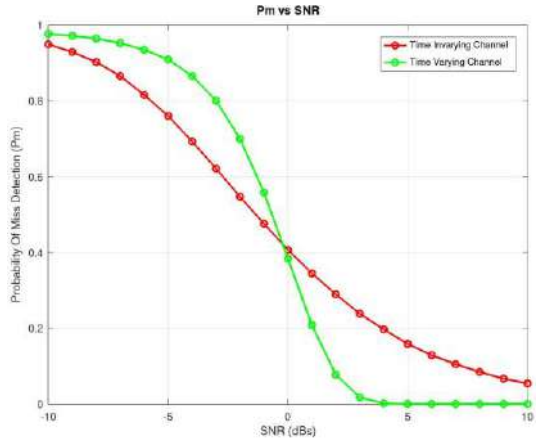

Figure 6. Comparison of Probability of miss dtection Vs SNR in both time variant and time invariant channel

The probability of miss detection in time varying channel is higher than the time in varying channel at low snr values. As SNR value increases, the probability

of miss detection decreases rapidly in time varying channel comparing with the time in varying channel based on the trust value.

The performance of three hard fusion rules such as AND, OR and MAJORITY rules with and without trust value with different probability of false alarm and probability of detection is given in Table 2.

TABLE 2. Comparison of Hard fusion cooperative sensing with and without trust

Probability of false alarm (Pf)	AND Rule		OR Rule		Majority Rule	
	P_d without trust	P_d with trust	P_d without trust	P_d with trust	P_d without trust	P_d with trust
0	0	0	0.35	0.33	0	0.08
0.2	0	0	0.86	0.83	0.01	0.52
0.4	0	0.05	1	1	0.59	0.95
0.6	0.06	0.48	1	1	1	1
0.8	0.8	0.95	1	1	1	1
1	1	1	1	1	1	1

5. CONCLUSION

The above simulation shows that the trust based cooperative sensing cognitive radio networks gives better performance comparing with conventional cooperative sensing. It is known that OR rule gives better detection probability but it suffers with the interference risk and it is not suggestible. Even though AND rule reduces the risk of interference but it suffers with another problem i.e. inefficient utilization of spectrum . Majority rule based cooperative sensing compromises the interference risk and inefficient utilization of spectrum. Hence majority rule suggestible in most of cooperative sensing cognitive networks. We also conclude that the adaptive threshold based cooperative sensing with trust value performs better than the fixed threshold cooperative sensing. In this paper we concentrated only randomly false attack. In future, we will further investigate about always yes attack and always no attack mitigation techniques.

6. REFERENCES

1. J. Mitola.,"Cognitive radio: An integrated agent architecture for software defined radio". Ph.D. Dissertation. Royal Institute of Technology (KTH), 2000, Stockholm, Sweden.
2. Ali A and Hamouda W, "Advances on spectrum sensing for cognitive radio networks: Theory and applications." ***IEEE Communications Surveys & Tutorials***, Vol. 19, No. 2, (2016), 1277-1304
3. Kattaswamy Mergu., "Spectrum sensing using Neyman Pearson based matched filter detection in cognitive radio networks". ***Journal of Basic and Applied Research International,*** Vol. 21, No. 3, (2017), 143-149
4. Runze Wan, Lixing Ding, Naixue Xiong and Xing Zhou., "Mitigation strategy against spectrum sensing data falsification attack in cognitive radio sensor networks". ***International Journal of Distributed Sensor Networks,*** Vol. 15, No. 9, (2019), 1-12.
5. I.F. Akuildiz, B.F. Lo and R. Balakrishnan, "Cooperative spectrum sensing in cognitive radio networks: A survey". ***Physical Communication,*** Vol. 4, No. 1, (2011), 40-62.
6. Youness Arjoune and Naima Kaabouch, "A Comprehensive Survey on Spectrum Sensing in Cognitive Radio Networks: Recent Advances, New Challenges, and Future Research Directions." ***Sensors,*** Sensors 2019, No. 1, 1-32. DOI: 10.3390/s19010126
7. Kenan kockaya1 and Ibrahim Develi, "Spectrum sensing in cognitive radio networks: threshold optimization and analysis". ***EURASIP Journal on Wireless Communications and Networking,*** (2020) 2020:255, 1-19. https://doi.org/10.1186/s13638-020-01870-7
8. Abdorasoul Ghasemi, and E.S. Sousa., "Collaborative spectrum sensing for opportunistic access in fading environments." ***New Frontiers in Dynamic Spectrum Access Networks,*** DYSPAN (2005).
9. E.Peh and Y.-C. Liang. "Optimization for cooperative sensing in cognitive radio networks." Wireless Communications and Networking Conference, IEEE (2007), 27-33.
10. Z.Li, F.R. Yu and M. Huang., "A cooperative spectrum sensing consensus scheme in cognitive radio." ***INFOCOM,*** (2009), 2546-2550
11. Sharifi A., "Defense against SSDF attack in cognitive radio networks: attack-aware collaborative spectrum sensing approach". ***IEEE Trans Wireless Communication,*** Vol. 9, No. 8, (2010), 2488-2497
12. Srinivas Nallagonda, Shravan Kumar Bandari, Sanjay Dhar Roy and Sumit Kundu., "On Performance of Weighted Fusion Based Spectrum Sensing in Fading Channels." ***Journal of Computational Engineering,*** (2013), DOI: 10.1155/2013/270612
13. Feng Zhao, Shaoping Li, and Jingyu Feng., "Securing Cooperative Spectrum Sensing against DC-SSDF Attack Using Trust Fluctuation Clustering Analysis in Cognitive Radio Networks." ***Wireless Communications and Mobile Computing,*** (2019), Wiley, 1-11, https://doi.org/10.1155/2019/3174304.

Persian Abstract

چکیده

یکی از فن آوری های نوظهور در سال های اخیر در زمینه ارتباطات بی سیم ، فناوری شناختی رادیو (CR) است که به طور قابل توجهی از کمبود طیف می کاهد. عملکرد اصلی فناوری CR شناسایی حفره های طیف یا طیف استفاده نشده از کاربران اصلی (PU) است که به آنها به عنوان کاربران دارای مجوز نیز گفته می شود و اختصاص این طیف بلااستفاده به کاربران ثانویه (SU) که به آنها کاربران غیر مجاز نیز گفته می شود. از آنجا که فناوری CR برای هر کاربر باز است ، بسیاری از مسائل امنیتی مانند حمله اولیه امولسیون کاربر (PUEA) ، حمله Jamming ، حمله جعل داده های سنجش داده طیف(SSDF) ، حمله شیر و حمله سوراخ سوراخ و غیره وجود دارد. حمله SSDF یکی از مهمترین حملات امنیتی در رادیو شناختی است که در آن یک کاربر مخرب داده های نادرست را عمداً برای سایر کاربران ثانویه ارسال می کند. هدف اصلی حمله SSDF ایجاد اختلال در ارتباط بین کاربران ثانویه یا به دست آوردن منابع کانال بیشتر است. یکی از راه حل های کاهش حمله SSDF ، سنجش طیف همکاری است. در این مقاله ، ما یک الگوریتم جدید سنجش تعاونی را براساس ارزش اعتماد کاربران ثانویه پیشنهاد می دهیم و با سنجش طیف تعاونی معمولی با الگوریتم پیشنهادی مقایسه می کنیم. در این الگوریتم ، ابتدا CR که منتظر تخصیص کانال است ، اطلاعات را درک کرده و اطلاعات سنجش CR های دیگر را مقایسه می کند. اگر هر گزارش سنجش CR با تست سنجش CR در خوشه مطابقت نداشته باشد ، در غیر این صورت پاداش می دهد. این رویه ها برای تعداد دوره هایی تکرار خواهد شد. سرانجام آزمون CR مقدار اعتماد را محاسبه می کند. بر اساس مرکز همجوشی ارزش اعتماد تصمیم خواهد گرفت که ارزش قابل اعتماد CR خاص را در آن گنجانده یا حذف کند. شبیه سازی سنجش تعاونی نیز در هر دو کانال نوع زمان و کانال بی تغییر زمان (ریلی) انجام می شود. نویسندگان همچنین سه روش اساسی همجوشی سخت مانند قانون AND، OR، MAJORITY را مقایسه می کنند.

IJE TRANSACTIONS C: Aspects Vol. 34, No. 6, (June 2021) 1475-1485

International Journal of Engineering

Journal Homepage: www.ije.ir

A General Framework for Estimating Channel of Orthogonal Frequency Division Multiplexing Systems by Utilizing Sparse Representation

S. H. Hashemi Rafsanjani [a], S. Ghazi-Maghrebi*[b]

[a] *Department of Digital Communication, ICT Research Center, Tehran, Iran*

[b] *Communication Department, college of Electrical Engineering, Yadegar-e-Imam Khomeini, Shahr-e-Rey branch, Islamic Azad University, Tehran, Iran*

P A P E R I N F O

Paper history:
Received 09 July 2020
Received in revised form 06 April 2021
Accepted 01 May 2021

Keywords:
Sparse Representation
Orthogonal Frequency Division Multiplexing
Sparse Channel Estiamtion
Weighted Sparse

A B S T R A C T

Channel estimation is a crucial task for orthogonal frequency division multiplexing (OFDM) modulation-based systems since this estimation is used for compensating impacts of a wireless channel. Recently, sparse representation (SR) is proposed for this task as wireless channels are considered as a sparse signal. However, SR considers sparse as the main feature and omit other features of the channel while estimating the channel. In this paper, we propose a general framework for utilizing other features of the channel in sparse channel estimation for OFDM systems, while these features are omitted in conventional sparse methods. In this regard, by utilizing maximum a posterior (MAP) estimation and defining new parameters, these features are conveyed into sparse channel estimation process to improve channel estimation. The simulation results indicate that our proposed framework not only improves the estimated parameter, but also reduces the number of resources such as the number of estimation pilots or transmitted power.

***doi**: 10.5829/ije.2021.34.06c.11*

NOMENCLATURE

$\boldsymbol{P}$	*Pilot index set*	*corr*	Correlation factor
$\tilde{\mathbf{h}}_{\mathbf{p}}^{f}$	Observed Vecotr	$\boldsymbol{\Lambda}$	an index set
$\boldsymbol{M}$	Mask Matrix	$\boldsymbol{C} = [a_i^{(-corr)}]$	Diagonal cost matrix
$\boldsymbol{A}$	Dictionary Matrix	$\boldsymbol{B}$	Weighted-dictionary
$\boldsymbol{z_P}$	Observed Noise	$\boldsymbol{h'}$	Weighted-CIR
X_{pilot}	Power of estimation pilots	T_D	Delay spread
$\boldsymbol{h}$	Channel Impulse response	a_i	Free parameter
$\boldsymbol{N}(.)$	Normal Distribution	$q = exp(-corr)$	Probability of locating at Δ
α	GGD parameter	$\Delta = (T_D / k)\ln(1/1-q)$	neighbor region
β	Scale parameter		

1. INTRODUCTION

OFDM modulation is a kind of multicarrier modulation (MCM) that utilizes orthogonal carriers to modulate data and overcome the multipath effects of the channels [1, 2]. This modulation divides a long stream of data into smaller data streams and modulates them on orthogonal carriers. This kind of modulation provides a narrowband channel for each carrier and reduces severe channel conditions [1]. In order to prepare an OFDM symbol, as indicated in Figure 1, a stream of data is passed through serial to parallel block. After passing through an inverse fast Fourier transform (IFFT) block, some specific pilots, known as estimation pilots, are inserted among them. These pilots are known at the receiver side, and their position in the stream is gathered at a set $\boldsymbol{P}=\{p_1,p_2,...,p_L\}$, which L is the number of estimation pilots. After performing some other operations such as cyclic prefix

*Corresponding Author Institutional Email: s.hadi.h.r@gmail.com (S. H. Hashemi Rafsanjani)

Please cite this article as: S. H. Hashemi Rafsanjani, S. Ghazi-Maghrebi, A General Framework for Estimating Channel of Orthogonal Frequency Division Multiplexing Systems by Utilizing Sparse Representation, International Journal of Engineering, Transactions C: Aspects Vol. 34, No. 6, (2021) 1475-1485

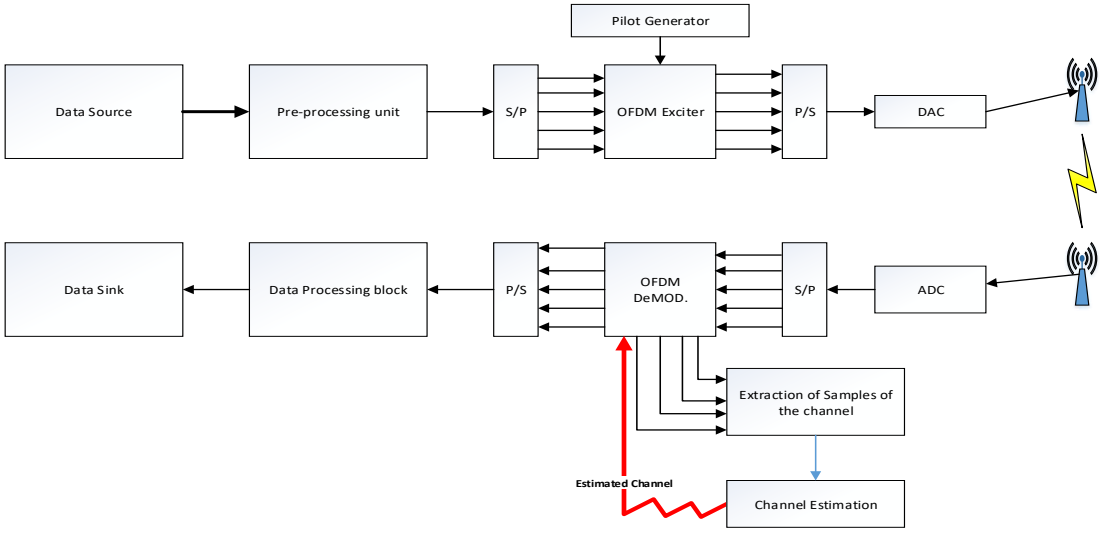

Figure 1. OFDM Modulation and Demodulation System

(CP) insertion, parallel to serial (P/S), and digital to analog conversion (DAC), an OFDM symbol is transmitted through a wireless channel [1, 3, 4]. At the receiver side, after passing through some processing blocks, estimation pilots are extracted, and the receiver estimates the wireless channel from noisy observed samples $\tilde{\mathbf{h}}_{\mathbf{p}}^{f} = \mathbf{r}_{\mathbf{p}} / X_{pilot} = \mathbf{h}_{\mathbf{p}}^{f} + \mathbf{z}_{\mathbf{p}}$, [3], [5], where $\mathbf{r}_{\mathrm{p}}$ contains received symbols at the positions of estimation-pilot $\mathbf{P}$, X_{pilot} is the estimation pilot, $\boldsymbol{h_p}^f$ contains samples of the frequency response of the channel, and $\mathbf{z}_{\mathrm{P}}$ is the channel noise at the related positions. We utilize $\boldsymbol{w}^f$ to show the Fourier transform of $\boldsymbol{w}$ in this paper. To compensate effects of the channel many algorithms discussed in literature [6, 2, 7], which utilize the noisy observed samples to estimate the channel, are proposed.

As explained by Elad [8], the relationship between observation impulse response of the channel samples, $\mathbf{h}_{\mathbf{p}}^{\mathrm{f}}$, and the wireless channel impulse response (CIR), $\boldsymbol{h}$, is $\tilde{\mathbf{h}}_{\mathbf{p}}^{f} = \mathbf{A}\mathbf{h} + \mathbf{z}_{\mathbf{p}}$, $\mathbf{A} = \mathbf{M}\mathbf{F}$, where $\boldsymbol{M}$ is a mask matrix, $\boldsymbol{F}$ is the discrete Fourier transform (DFT) matrix, and $\boldsymbol{A}$ is the DFT sub-matrix. This relation, which from now is called the observsation relation, provides an underdetermined system of linear equation relation between $\boldsymbol{h_p}^f$ and CIR $\boldsymbol{h}$. An underdetermined system of the linear equation has more unknowns than equations. For this kind of equation, there is either no answer or an infinite number of answers [9]. Similar to the atomic decomposition viewpoint [10], the matrix $\boldsymbol{A}$ is called a dictionary matrix, because the observation vector, $\boldsymbol{h_p}$, is a linear combination of columns of the dictionary matrix, $\boldsymbol{A}$. Columns of the dictionary are called atoms, and $\boldsymbol{h_p}^f$ is called the observation vector.

Nowadays sprase representation is widely used on those problems that there is an underdetermined relation between observed paramters and the desired answer has a sparse features [11, 12]. In OFDM channel estimation problem, as wireless channels are considered as a sparse signal because their taps are related to scattering objects, and these objects are sparsely located [13], and there is an underdetermined system of linear equations between the CIR of the channel and the observation vector, sparse representation is applicable to estimate the OFDM channel. In order to estimate the sparse channel, regularization method is used which define a cost function based on desired features of the answer and try to find those answers which best matches these features. Considering sparse feature as the main feature, zero-norm function is selected as the cost function and it is tried to find the solution by solving $min_{\boldsymbol{h}} \|\boldsymbol{h}\|_0 \; s.t. \left\| \tilde{\mathbf{h}}_{\mathbf{p}}^{f} - \boldsymbol{A}\boldsymbol{h} \right\|_2$. This equation is called P_0-problem and by substituing $\|\boldsymbol{h}\|_0$ with $\|\boldsymbol{h}\|_1$ the P_0-problem changes to P_1. Although zero-norm is a proper function for finding the sparse solution, it could not manipulate additional information. To clarify it, let $\boldsymbol{C}$ be a diagonal cost matrix whose diagonal elements are selected based on side information. To apply side information into the estimation process, the cost matrix $\boldsymbol{C}$ is multiplied to $\boldsymbol{h}$ to assign costs to each element of $\boldsymbol{h}$. Therefore, the regularized term changes as, $min_{\boldsymbol{h}} \|\boldsymbol{C}\boldsymbol{h}\|_0 \; s.t. \left\| \tilde{\mathbf{h}}_{\mathbf{p}}^{f} - \boldsymbol{A}\boldsymbol{h} \right\|_2$. Since $\|\boldsymbol{C}\boldsymbol{h}\|_0 = \sum_i |c_i h_i|^0 = \sum_i |h_i|^0 = \|\boldsymbol{h}\|_0$, the zero-norm function eliminates the impact of the cost matrix. Therefore, to take the impact of the side information into account, the problem formulation should be modified which in this paper we proposed a framework to present it. Many algorithms such as Basis Pursuit (BP) [9], Matching Pursuit [14], Orthogonal

Matching Pursuit (OMP) [15], and smoothed L0, SL0 [16], are proposed to find the sparse solution. These methods consider the sparsity feature of the desired parameter as the only metric and omit other features. In addition to conventional sparse algorithms, some methods discussed by Stanković [17] are proposed to employ additional information to find the sparse solution. The above algorithm proposed [17] is mainly based on OMP [15], provides a set of candidates based on additional information, and similar to the OMP algorithm, finds each element of the sparse solution step by step. At each step, the algorithm searches for finding the most correlated candidate and compares it with other elements that are not a member of the candidate set. If the correlation of the candidate element is more than other, that element is selected as nonzero elements of the sparse solution. Otherwise, the high correlated element is selected. This algorithm is an updated version of the OMP algorithm; however, its procedure of contributing side information is not applicable to other sparse representation algorithms. Zhang et al. [18] proposed to integrate the side information via maximizing the correlation between the prior information and the desired solution and tried to find the sparse solution form, $min_{\boldsymbol{h}} \|\boldsymbol{h}\|_1 + \lambda\langle \boldsymbol{h},\boldsymbol{\varphi}\rangle \; s.t. \left\| \tilde{\mathbf{h}}_{\mathrm{p}}^{f} - \boldsymbol{A}\boldsymbol{h} \right\|_2$, where λ is a free parameter. The second term calculates the similarity between prior information and the desired solution. Similarly, Mota et al. [19] concentrated on the framework of l_1-l_1-minimization and tried to utilize side information by replacing l_0-norm with l_1-norm. These methods and similar frameworks considered l_1-norm as the cost function to handle side information. However, the method didn't address utilization of side information in l_0-problem. To provide a framework that contributes other features of the solution in sparse representation process in addition to sparsity, we utilize MAP estimation and select generalized Gaussian distribution (GGD) as a probability density function (pdf) of the taps of the channel.

In this paper we assume that the wireless channel is an independent and identically distributed (i.i.d) signal and sparse. Therefore, its elements should follow those pdf covering sparse characteristics. Considering a sparse signal, most elements of it are zero, and few elements gain a nonzero amount. Consequently, the pdf of the elements should have a high density at zero and heavy tail. The concentration of the mass at zero increases the probability of selecting zero, which guaranties most elements of the signal gain zero amount while this tail guarantees that few elements are gaining huge amounts. In this paper, we select GGD distribution, as a pdf of taps of the channel, because this distribution covers wide range of pdf by changing its parameters. Distributions such as Laplacian, Gaussian, uniform distributions, and distributions that represent sparse random variables are some examples of them. This generality would also help us to present our result in a general form. The pdf of a random variable x, which obeys a GGD, is defined as follows:

$$f(x;\alpha,\beta) = \frac{\alpha}{2\beta\Gamma(1/\alpha)} \exp(-\frac{\| x \|^{\alpha}}{\beta^{\alpha}}), \quad \alpha>0,\beta>0 \tag{1}$$

where Γ(.) is the Gamma function [20]. GGD depends on two parameters α and β, which α controls the shape of the GGD distribution, varying from flat distribution to semi-δ function, shown in Figure 2. Meanwhile, β at Equation (1) is a scale parameter controlling the variance of the random variable. As indicated in Figure 2, the GGD covers a wide range of probability distribution by changing α. In this regard, for the case of $\alpha > 2$, distributions are called sub-Gaussian distributions and super-Gaussian signals for the case $\alpha < 2$. Sparse distributions are achieved for $\alpha < 1$ and uniform distribution, $U(-\beta,\beta)$, is obtained while $\alpha \to \infty$ [20].

In this paper, we try to provide a general framework to overcome the limitation of SR methods, considering sparse as the only feature and omitting other features, and estimate sparse channel while other features apart from sparse are also available. To this end, firstly, we indicate the relation between GGD parameters and sparse representation and explain how sparse representation is achieved by changing GGD parameters. Then, some parameters are defined to handle additional features and the procedure of contributing these features to sparse channel estimation is explained. Finally, we propose a new method which contributes other features of the answer in addition to sparsity while estimating sparse solution.

The rest of the paper is organized as follows. Section 2 is devoted to estimate the channel of the OFDM system by utilizing MAP estimation and considering GGD as a pdf of the wireless channel in general format. The wireless channel is calculated for a different amount of α in section 3. Section 4 is devoted to define some

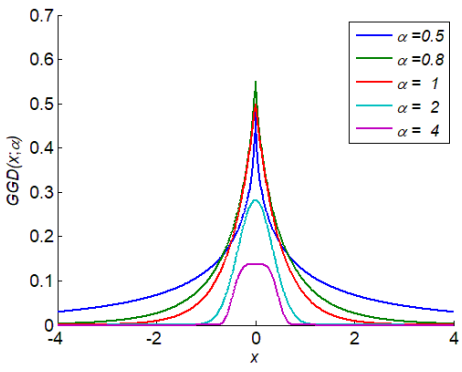

Figure 2. Generalized Gaussian Distribution

parameters to contribute other features of the answer to the channel estimation process. The simulation results are presented in section 5.

2. ESTIMATING WIRELESS CHANNEL FOR AN OFDM SYSTEM BY UTILIZING MAP

An OFDM modulation system breaks a high rate data stream into parallel low rate data streams and modulates them on orthogonal carriers [21]. In this regard, the data stream is passed through the M-QAM modulator to map digital data into digital symbols. To take samples of the channel, L deterministic symbols, which are known as estimation-pilots, are added among them. X_{pilot} indicates the transmitted power of these pilots. The position of these pilots among data samples are gathered in a set $\boldsymbol{P} = \{p_1, p_2, \ldots, p_L\}$. The estimation-pilots and data samples then pass through serial to analog block and apply to N-point IFFT block,

$$\mathbf{x}[n] = \frac{1}{N}\sum_{k=0}^{N-1}\mathbf{X}(k)\exp(\frac{j2\pi kn}{N}) \quad (2)$$

Performing some other processes such as cyclic-prefix (CP) insertion and D/A conversion, OFDM symbols are prepared to transmit through a wireless channel. At the receiver side by considering additive white Gaussian noise (AWGN), assuming semi-wide sense stationary (WSS) characteristic for the channel and omitting inter symbol interference (ISI) and inter-carrier interference (ICI) because of the CP [5], the received signal become as $\mathbf{y}[n] = \mathbf{x}[n] \otimes \mathbf{h}[n] + \mathbf{z}[n]$, where $\otimes$ represents conveloution operation. At the reciever side, the received signal is passed through an FFT block, $\mathbf{Y}(k) = \sum_{n=0}^{N-1}\mathbf{y}[n](\frac{-j2\pi kn}{N}) = \mathbf{X}(k)\mathbf{H}(k) + \mathbf{Z}(k)$, where $\boldsymbol{H(k)}$ is FFT of the channel impulse response. Since $\boldsymbol{z[n]}$ is a zero-mean white random process and FFT is a linear operator, $\boldsymbol{Z(k)}$ is also a zero-mean white process. By extracting the received samples of the estimation-pilots from other samples, and dividing them by X_{pilot} to remove their amount, the noisy observation of the channel is obtained by dividing $\boldsymbol{Y}$(k) by X_{pilot}, $\boldsymbol{Y}(k)/X_{pilot} = \boldsymbol{H}(k) + \boldsymbol{Z}(k)/X_{pilot}$, $k \in \boldsymbol{P}$. Considering that the second term is still a noise term and the observed amounts are noisy samples of the channel frequency response. For simplicity, a new parameter, $\tilde{h}_k^f \triangleq \boldsymbol{Y}(k)/X_{pilot}$ is defined to represent observed samples of the channel at the position of $k \in \boldsymbol{P}$. Replacing $\boldsymbol{H}(k)$ by its Fourier transform, the observation relation becomes,

$$\tilde{h}_k^f = \sum_{n=0}^{N-1}\mathbf{h}[n]\exp(\frac{-j2\pi nk}{N}) + \frac{\mathbf{Z}(k)}{X_{pilot}}, \qquad k \in \mathbf{P}. \quad (3)$$

The first term of Equation (3) is the k'th column of the DFT transform of $\mathbf{h}[n]$. By defining $\tilde{\mathbf{h}}_{\mathbf{P}}^f \triangleq [\,\tilde{h}_{k_1}^f, \tilde{h}_{k_2}^f, \ldots, \tilde{h}_{k_L}^f\,]^{\mathrm{T}}$, $k_i \in \boldsymbol{P}$ as an observed vector, it is possible to rewrite the observation relation in a matrix form,

$$\begin{bmatrix}\tilde{h}_{k_1}^f\\ \tilde{h}_{k_2}^f\\ \vdots\\ \tilde{h}_{k_L}^f\end{bmatrix} = \begin{bmatrix}1 & \exp(\frac{-j2\pi k_1}{N}) & \cdots & \exp(\frac{-j2\pi k_1(N-1)}{N})\\ 1 & \exp(\frac{-j2\pi k_2}{N}) & & \exp(\frac{-j2\pi k_2(N-1)}{N})\\ \vdots & \vdots & & \vdots\\ 1 & \exp(\frac{-j2\pi k_L}{N}) & \cdots & \exp(\frac{-j2\pi k_L(N-1)}{N})\end{bmatrix}\mathbf{h}[n] + \mathbf{Z}, \quad k_i \in \mathbf{P}, \quad (4)$$

$$\tilde{\mathbf{h}}_{\mathbf{P}}^f = \mathbf{A}\mathbf{h}[n] + \mathbf{Z},$$

where $\boldsymbol{A}$ in Equation (4) is a DFT sub-matrix which its columns is the k_i'th column of the DFT matrix. By defining a diagonal mask matrix, $\boldsymbol{M}$, which its diagonal elements are in associated with the elements of $\boldsymbol{P}$, and applying it on the DFT matrix, the matrix $\boldsymbol{A}$ is achieved. Equation (4) is an underdetermined system of linear equations which provides linear relation between observed samples and the channel impulse response (CIR). At follows, we use MAP to estimate the channel.

MAP estimation tries to estimate the desired parameter by utilizing prior information. This estimation tries to find the desired answer by maximizing $\boldsymbol{f}(x|y)$, where x is the desired parameter to be estimated, y is an observation parameter, and $\boldsymbol{f}(.|.)$ is a conditional pdf [22]. To estimate an OFDM channel by MAP estimation, the desired parameter, the observation vector, and observation relation are defined as $\boldsymbol{x}=\boldsymbol{h}$, $\mathrm{y}=\tilde{\mathbf{h}}_{\mathbf{P}}^f$, $\tilde{\mathbf{h}}_{\mathbf{P}}^f = \boldsymbol{Ah}+\boldsymbol{z_P}$, respectively. Considering $\boldsymbol{z_p}$ as an identical independent distributed (i.i.d) zero-mean white Gaussian noise, the conditional distribution becomes $f(\tilde{\mathbf{h}}_{\mathbf{P}}^f \mid \mathbf{h}) = f(\mathbf{Ah} + \mathbf{z}_{\mathbf{P}} \mid \mathbf{h}) = \mathbf{N}(\mathbf{Ah}, \sigma\mathbf{I})$, where $\boldsymbol{I}$ is an identical matrix, σ is the variance of observation noise, and $\boldsymbol{N}(.)$ is the normal distribution. The pdf of $f(\boldsymbol{h})$, which is prior of the desired parameter, is considered as a GGD distribution. It is assumed that the desired parameter contains N i.i.d parameters $\mathbf{h}=\{h_1, h_2, \ldots, h_N\}$. Consequently, $f(\mathbf{h}) = \Pi_{i=1}^{N}\boldsymbol{f}(h_i)$. By replacing normal and GGD distributions, the estimation relation changes to:

$$\hat{\mathbf{h}} = \arg\max_{\mathbf{h}} \mathrm{N}(\mathbf{Ah}, \sigma\mathbf{I})\prod_{i=1}^{N}\frac{\alpha}{2\beta\Gamma(\frac{1}{\alpha})}\exp(-\frac{\|h_i\|^{\alpha}}{\beta}),\ \alpha>0, \beta>0. \quad (5)$$

Since normal distribution and GGD are exponential functions and natural logarithm function (*ln*-function) is strictly increasing, performing *ln*-function on Equation (5) does not affect the maximization process. After some manipulations, the estimation relation is calculated as follows:

$$\hat{\mathbf{h}} = \arg\max_{\mathbf{h}} \ln(\frac{1}{\sqrt{2\pi\sigma^2}}\frac{\alpha}{2\beta\Gamma(1/\alpha)}) - \frac{\left\|\tilde{\mathbf{h}}_{\mathbf{P}}^f - \mathbf{Ah}\right\|_2}{\sigma^2} - \frac{\|\mathbf{h}\|_{\alpha}}{\beta^{\alpha}}, \quad (6)$$

where $\|.\|_2$, $\|.\|_{\alpha}$ are the norm-2 and norm-α, respectively. The first term of Equation (6) is constant and does not

affect the maximization process. Therefore, it is omitted. By omitting minus sign, maximization process changes to minimization process and the estimation relation changes as follows:

$$\hat{\mathbf{h}} = \arg\min_{\mathbf{h}} \frac{\left\|\tilde{\mathbf{h}}_{\mathbf{p}}^{f} - \mathbf{A}\mathbf{h}\right\|_2}{\sigma^2} + \frac{\|\mathbf{h}\|_{\alpha}}{\beta^{\alpha}}. \quad (7)$$

As explained by Elad [8], Equation (7) is also achieved, while the regularization method is used to find the desired solution of an underdetermined system of linear equation, and α-norm is selected as the cost function. Therefore, it is shown that utilizing MAP and GGD distribution provides same relation for finding sparse answer similar to regularization method. This provides us a platform to consider other features of the answer in sparse estimation. In the next section, the effect of α on the channel estimation is studied.

3. ESTIMATING OFDM CHANNEL FOR DIFFERENT AMOUNT OF PARAMETERS

The GGD distribution has two main parameters α and β, controlling shape and variance of the distribution, respectively. The parameter α controls the sharpness of the GGD distribution and provides a wide range of probability density functions. For instance, by selecting $\alpha = 2$ and $\alpha = 1$ Gaussian and Laplacian distributions are obtained, respectively. In this paper, we consider GGD distribution as a pdf of the taps of the channel because the distribution of most natural signals follows GGD distribution [23]. We estimate the channel impulse response in a general form of α at Equation (7), and in this section, we find the estimation of the channel for different amount of α. By considering $\alpha = 2$ and assuming the observation noise and $\boldsymbol{h}$ are i.i.d signals, the estimation relation is obtained as follow:

$$\hat{\mathbf{h}} = \arg\min_{h} (\tilde{\mathbf{h}}_{p}^{f} - \mathbf{A}\mathbf{h})^{T} (\sigma^2\mathbf{I})^{-1} (\tilde{\mathbf{h}}_{p}^{f} - \mathbf{A}\mathbf{h}) + \mathbf{h}^{T} (\beta I)^{-1} \mathbf{h}, \quad (8)$$

where $(.)^{T}$ is a transpose operator. Since Equation (8) is a convex relation, minimization relation is performed by derivative of Equation (8). After derivation and performing some straight forward calculation, the channel is estimated as $\hat{\mathbf{h}} = \mathbf{A}^{T} \tilde{\mathbf{h}}_{P}^{f} \beta^2 / (\sigma^2 + \beta^2)$.

By selecting $\alpha \geq 2$ non-sparse is assigned to the taps of the channel. Although this assumption is against the sparse assumption of the channel, it results in a closed-form relation for estimating the channel. Considering sparsity, α should be selected in a range $\alpha \leq 1$. By selecting $\alpha = 1$ which change GGD distribution to Laplace distribution and performing some calculation, Equation (7) changes to the following form:

$$\hat{\mathbf{h}} = \arg\min_{\mathbf{h}} \frac{\left\|\tilde{\mathbf{h}}_{\mathbf{p}}^{f} - \mathbf{A}\mathbf{h}\right\|_2}{\sigma^2} + \frac{\|\mathbf{h}\|_{1}}{\beta}. \quad (9)$$

This relation is a P_1-problem which is convex, but not strictly as discussed by Efron et al. [24]. This relation may have more than one solution, but these solutions are convex and gathered in a bounded convex set [24]. Beside it, as we are looking for the sparse answer (for example k-sparse), there exists at least one with at most k non-zero elements. The above relation can be formulated as linear programming to find the sparse solution. Algorithms such as Least Angle Regression (LARS) [24], Interior point method [25], and Least Absolute Shrinkage and Selection Operator (LASSO) [26] are used for solving it and finding the sparse solution.

Here, we consider the critical case where $\alpha \rightarrow 0$, and assume that the taps of the channel have GGD distribution with $\alpha \rightarrow 0$. In this case, the estimation relation changes as follows:

$$\hat{\mathbf{h}} = \arg\min_{\mathbf{h}, \alpha \rightarrow 0} \frac{\left\|\tilde{\mathbf{h}}_{\mathbf{p}}^{f} - \mathbf{A}\mathbf{h}\right\|_2}{\sigma^2} + \frac{\|\mathbf{h}\|_{\alpha}}{\beta^{\alpha}}. \quad (10)$$

As indicated in Equation (10) by selecting $\alpha \rightarrow 0$, the estimation relation changes to P_0-problem. This problem is complex as it is NP-Hard, and a straightforward approach is not applicable to solve it [23]. Find the sparse solution of the above relation; approximation methods are employed. Approximation methods are categorized into two main categories, such as greedy methods [27, 28] and relaxation methods. The greedy family methods, such as Matching Pursuit (MP) [14] and orthogonal MP (OMP) [15], try to build the nonzero elements of the answer one per time. While, the second method tries to approximate the zero-norm function by a smoother one [16, 22].

Therefore, it is shown that by considering GGD distribution and selecting $\alpha \rightarrow 0$, the obtained relation is same as the relation obtained from regularization method while zero-norm function is selected as the cost function. Then, MAP estimation and regularization function result in the same relation. In the next section, we explain how to contribute to other features of the answer in the OFDM channel estimation and discuss the impact of them on the channel estimation process.

4. CONTRIBUTING OTHER FEATURES OF CHANNEL AT SPARSE CHANNEL ESTIMATION PROCESS

Being sparse is the main feature of the channel, which makes sparse representation algorithms applicable for estimating the channel. Besides sparse, depending on the channel condition, there are other available features that could be considered for the channel estimation process. These features could be anything such as the number of channel taps, possible regions where taps are located, or side information of the channel, and so on. Conventional

sparse algorithms omit these features since these algorithms are designed based on just the sparsity assumption of the channel. In this paper, we mathematically model these features of the channel by defining some parameters and use these parameters to convey the impact of these features into the channel estimation process.

Based on the observation relation, to estimate the channel impulse response, an underdetermined system of the linear equation should be solved. As stated by Elad [8], the regularization method is suggested to find its solution. In this regard, a regularized-function is defined based on features of the desired answer, and the one which best satisfies it, is selected as the desired solution. In an OFDM channel estimation problem, the sparse feature of the channel is considered as the main feature, and regularization-function is defined such that the answer which best matches this condition is selected as the desired answer. The main function satiesfying sparse condition is zero-norm function [8], and many algorithms are suggested to find the sparse solution [8]. Although these algorithms are capable of finding the sparse solution, their ability to find the solution subjected to other features of the answer is not proved. As a consequence, in this section, we propose a method in general form to cover this issue. We used MAP estimation to tackle this issue, and we also propose a new method to solve it.

MAP estimation utilizes prior information to estimate the desired parameter, and features of the channel modify these priors. Mathematical parameters such as a neighbor region Δ, an index set $\boldsymbol{\Lambda}$, and a cost matrix $\boldsymbol{C}$ are defined to convey the impacts of these features into the procedure of estimating the channel. The neighbor region, Δ, indicates the length of the feasible region around nonzero taps of the channel where the next taps are more probable to be located. The index set, $\boldsymbol{\Lambda}$, contains indexes of those elements of the sparse answer located in these regions. For example, consider that $\Delta = 5$, and based on these features, it is expected that nonzero elements of the channel are located at neighborhood of $\{\lambda_8, \lambda_{55}, \lambda_{100}, \lambda_{140}\}$. Therefore, the index set, $\boldsymbol{\Lambda}$, contains indexes as $\boldsymbol{\Lambda} = \{\lambda_3, ..., \lambda_{13}, \lambda_{50}, ..., \lambda_{60}, \lambda_{95}, ..., \lambda_{105}, \lambda_{125}, ..., \lambda_{135}\}$, which $\{\lambda_{95}, \ldots, \lambda_{105}\}$ is the feasible region around λ_{100}.

As mentioned earlier, channels are represented by their channel impulse response, $\boldsymbol{h}(t,\kappa) = \sum_i \boldsymbol{h}_i(t)\delta(t-\kappa_i)$, where $\delta(t-\kappa_i)$ indicates the taps of the channel. These taps represent paths of the channel, and the number of taps indicates the number of copies of the signal received at the receiver. Additionally, $h_i(t)$ indicates channel loss of the related path. The difference time between the first and last tap is called delay spread of the channel, T_D, which indicates maximum difference between taps of the channel. Assuming that the channel has k taps and delay spread of the channel is T_D, the mean time between two consecutive taps is T_D/k, and the mean occurrence rate of taps of the channel is k/T_D. Since the expected time for receiving later copy of signal between two consecutive paths obeys exponential distribution with mean k/T_D [29], the probability of receiving next copy of the signal within period Δ is calculated as follow:

$$p(t < \Delta) = \int_0^{\Delta} e^{-\frac{k\tau}{T_D}} d\tau = 1 - e^{-\frac{k\Delta}{T_D}}. \quad (11)$$

Receiving the next copy of the signal within a period of Δ is similar to the event that tap is located within the region of Δ around the former tap of the channel. By considering the above explanation, the neighbor region for locating the next tap of the channel is calculated as $\Delta = (T_D / k)\ln(1/1-q)$, where q is the probability of locating tap at the feasible region, T_D is the delay spread, and k is the number of taps of the channel. The probability q is related to the correlation of the channel. In case of high correlation, it is expected that taps of the channel at t_2 are located closer to taps of the channel at t_1. However, in the case of low correlation, there is less dependence between samples of the channel. Therefore, taps of the former channel are located more independently, which results in larger $\boldsymbol{\Delta}$. To provide a relation between the correlation of the channel and the probability q, we select $q=exp(-corr)$, where $corr$ represents the correlation of the channel and $0 \leq corr \leq 1$. In this regard, while the correlation of the channel is decreased, the wider region should be considered for the next sample. Therefore, the probability q gains a higher amount, and Δ becomes bigger.

The diagonal cost matrix assigns proper amount of cost to each atom. Costs are selected in associated with the desired features and their impacts on the desired answer. These features indicate which atoms are more probable to be selected as a nonzero element of the channel. Accordingly, atoms are not treated uniformly, and those atoms that are more probable to be selected as nonzero elements of the answer or their indexes are in the index set, $\boldsymbol{\Lambda}$, gain lower cost. On the other hand, the higher cost is assigned to other atoms that their indexes are out of the index set, $\boldsymbol{\Lambda}$. Cost selection could be performed in various ways; for example, it is possible to define different cost levels for those elements that their indexes are in the index set, such as selecting the cost in the Gaussian form, etc. Since most features of the channel are observed from its previous samples, we need a reliable factor to indicate the reliability of these features for the current sample of the channel. Correlation is a factor that indicates correlation between different samples of the channel. The low correlation indicates the observed features from previous samples are less reliable and vice versa. To assign costs base on this parameter, we define $c_i = a_i^{(corr)}$, where $0 \leq a_i \leq 1$ is a free parameter selected based on channel conditions. In this regard,

while the correlation of the channel is low $corr \rightarrow 0$, the observed features are less reliable, and the cost assigned to elements should be gained amount around 1. In this case, the estimator omits other features of the channel and considers the sparse feature as the primary and dominant feature.

Conversely, while the correlation of the channel is high, $corr \rightarrow 1$, the observed features from previous samples are reliable, and it is expected that the current samples of the channel have similar features. Therefore, those elements that their indexes are located at the index set, Λ, gain lower cost while higher cost is assigned to others. The coefficient a_i handles the scenario of cost assignment to different elements. For example, selecting a_i based on Gaussian or stepwise formats are two forms of cost assignment. In this paper, we define two cost levels $a_i = L_1$ for $i \in \Lambda$, or $a_i = L_2$ for others,

$$\mathbf{C} = \begin{pmatrix} c_1 & \cdots & 0 \\ \vdots & \ddots & \vdots \\ 0 & \cdots & c_N \end{pmatrix}, \quad \begin{matrix} c_i = L_1^{-corr}, \ i \in \mathbf{\Lambda} \\ c_j = L_2^{-corr}, \ j \notin \mathbf{\Lambda} \end{matrix}. \tag{12}$$

To contribute impacts of these features into the estimation process, we convey their effects directly to atoms by assigning a cost to each of them. Consequently, Those atoms located at feasible regions are more probable to be selected, and lower cost is assigned to them. However, other elements located out of feasible regions are less probable to be selected, and higher cost is assigned to them. Therefore, by selecting the proper amount of cost and creating diagonal cost matrix $\boldsymbol{C}$ = diag(c_1, c_2,…, c_N), other features of the channel are conveyed to the procedure of estimating the sparse channel and estimation relation is changed as follows:

$$\hat{\mathbf{h}} = \arg\min_h \frac{\| \tilde{\mathbf{h}}_{\mathbf{P}}^f - \mathbf{A}\mathbf{h} \|_2}{\sigma^2} + \sum_{i=1}^{N} | c_i h_i |^{\alpha}. \tag{13}$$

By replacing $\sum_{i=1}^{N} |c_i h_i|^{\alpha} = \|\boldsymbol{C}\boldsymbol{h}\|_{\alpha}$, as the cost matrix $\boldsymbol{C}$ is a positive diagonal matrix, Equation (13) is changed as follows,

$$\hat{\mathbf{h}} = \arg\min_h \frac{\| \tilde{\mathbf{h}}_{\mathbf{P}}^f - \mathbf{A}\mathbf{h} \|_2}{\sigma^2} + \|C\mathbf{h}\|_{\alpha}, \tag{14}$$

by defining a weight matrix which is an inverse of the cost matrix, $\boldsymbol{W} = \boldsymbol{C}^{(-1)}$ and $\boldsymbol{h}' = \boldsymbol{C}\boldsymbol{h}$, the estimation relation becomes

$$\hat{\mathbf{h}}' = \arg\min_h \frac{\| \tilde{\mathbf{h}}_{\mathbf{P}}^f - \mathbf{A}\mathbf{W}\mathbf{h}' \|_2}{\sigma^2} + \|\mathbf{h}'\|_{\alpha}. \tag{15}$$

Here the feature is conveyed to the estimation process by applying the weight matrix $\boldsymbol{W}$. Since this matrix is diagonal, it is possible to combine it with the dictionary $\boldsymbol{A}$ and define a weighted-dictionary $\boldsymbol{B} = \boldsymbol{A}\boldsymbol{W}$. Hence, additional features affect the dictionary matrix and intensify those columns of the dictionary matrix that their indexes are in the index set Λ. Referring to the impact of additional features of the channel on the estimation relation, their impacts are conveyed to the estimation process through substituting the dictionary matrix, $\boldsymbol{A}$, with the weighted-dictionary, $\boldsymbol{B}$, and finding the answer of the below relation for different amount of α,

$$\hat{\mathbf{h}}' = \arg\min_h \frac{\| \tilde{\mathbf{h}}_{\mathbf{P}}^f - \mathbf{B}\mathbf{h}' \|_2}{\sigma^2} + \|\mathbf{h}'\|_{\alpha}. \tag{16}$$

Looking closer at Equation (16), it is clearly observed that this realtion is obtained while regularization is applied on $\tilde{\mathbf{h}}_{\mathbf{P}}^f = \boldsymbol{B}\boldsymbol{h}' + \boldsymbol{z}_{\boldsymbol{P}}$, while α-norm function is selected as the cost function. This relation which is a weighted form of the observation relation, $\tilde{\mathbf{h}}_{\mathbf{P}}^f = \boldsymbol{A}\boldsymbol{h} + \boldsymbol{z}_{\boldsymbol{P}}$, is also an underdetermined relation. For this relation other features are applied to the dictionary matrix, $\boldsymbol{A}$, and create the weighted ditionary, $\boldsymbol{B}$. Additionally, as $\boldsymbol{h}'$ is a weighted form of $\boldsymbol{h}$, and these weights are positive non-zero, $\boldsymbol{h}'$ is also a sparse signal. Therefore, the zero-norm function is a proper cost function that could be selected to find the sparse solution of $\tilde{\mathbf{h}}_{\mathbf{P}}^f = \boldsymbol{B}\boldsymbol{h}' + \boldsymbol{z}_{\boldsymbol{P}}$, and sparse algorithms are utilized to find the desired solution of Equation (16).

5. SIMULATION RESULT

In this section, simulation results of an OFDM system by utilizing the proposed channel estimation procedure are presented. For this purpose, we have simulated the complete system of Figure 1, with parameters given in "Table 1" by “MATLAB” software. In this system, we utilized a 4-tap Rayleigh fading channel. The input of this system is a stream of one thousand OFDM symbols, and for each symbol, the Rayleigh fading channel is created randomly. To create these channels, we randomly selected the channel taps in Δ, the neighbor region of the previous Rayleigh channel. For example, suppose that the Rayleigh channel for the 10'th OFDM symbol has taps at time indexes of {1, 19, 36, 100} with $\Delta = 6$. Therefore, the taps of the Rayleigh channel for the 11'th OFDM symbol, are randomly selected from $\mathbf{\Lambda}$ = {1, …,

TABLE 1. System Parameters

Parameters	Value
OFDM Symbol Duration T_u	200µ
Carrier Frequency F_c	10MHz
Symbol Modulation	16-QAM
FFT Size	2048
Maximum Number of Pilots	1700
The Number of Estimation Pilots	60
Guard band	0.25

7, 13, …, 25, 30,…,42, 94,…,106}. In this simulation, we have run this system 1000 times for each experiment, and then we computed the mean error rate as the final results. We simulated the system for two cases. For the first case, we consider sparsity as the main feature and omit other features. For the second case, although sparsity is considered as the main feature, other features are also considered.

In this regard, based on the different amounts of α, three scenarios are defined. For the first scenario, we consider $\alpha = 1$, and employ l_1-methods to estimate the channel. We have simulated different signal to noise ratio (SNR) and the different number of estimation pilots to investigate the impact of adding other features of the channel on the estimated channel. In the second scenario, by selecting $\alpha = 0$, the estimation relation is a zero-norm problem, and SL0 is selected to estimate the channel. The last scenario is devoted to employing non-sparse distribution and $\alpha = 2$. In this case, the closed-form relation for the estimated channel is provided, and we try to contribute to the impact of other features of the channel as well. To compare our proposed algorithm, we have simulated with the algorithm proposed by Stanković et al. [17] compare its result with our proposed algorithm. Since the algorithm introduced by Stanković et al. [17] is based on the OMP algorithm, we use the OMP algorithm as a sparse representation algorithm of our proposed framework and compare their results.

Figures 3 and 4 show the result of the first scenario, and present the effects of considering other features of the channel on the channel estimation, while $\alpha = 1$. Figure 3 indicates the simulation results while fixing SNR. Figure 4 presents the simulation results for the fixed number of pilots. As noted in these figures, with the same condition contributing to other features in the estimation process, channel estimation is improved. Therefore, the system experiences better performance and reduces the

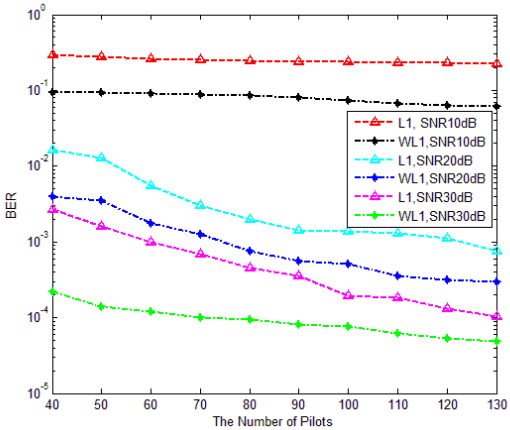

Figure 3. Comparision of performance of OFDM system, Utilizing features of the channel and fixed SNR, α=1.

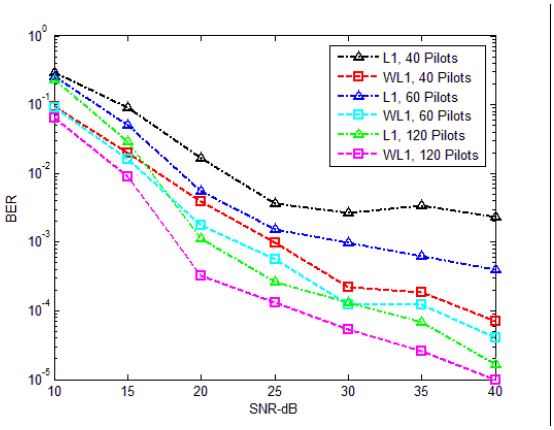

Figure 4. Comparison of Performance of OFDM system, Fixed Number of Pilots and α=1.

bit error rate. By comparing these figures, it is observed that by considering only the sparsity feature of the channel, more resources are required to provide the same performance in comparison with the case that other features take part in the estimation process. It is also indicated that, while the system is in good condition, such as high SNR value or larger amount of estimation pilots, the need for considering other features is reduced. In other words, considering them would not increase the performance of the system the same as before. This means that the mathematical computations will be decreased and also, the processing time will be decreased, and as a result, this method will be applicable in real-time data communications.

Figures 5 and 6 indicate the effects of side information while $\alpha \rightarrow 0$. Similar to the previous scenario, results are plots for fixed SNR and a fixed number of estimation pilots in these figures, respectively. To find the answer to this case, we utilize OMP and SL0 methods. Similar to the case of $\alpha = 1$, in general, form utilizing other features of the channel improves the

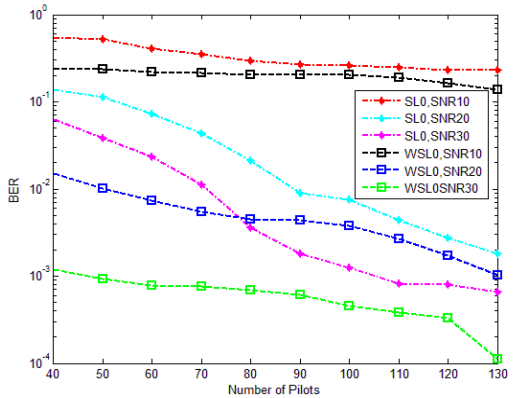

Figure 5. Comparison of Performance of OFDM system, Fixed SNR and α→0.

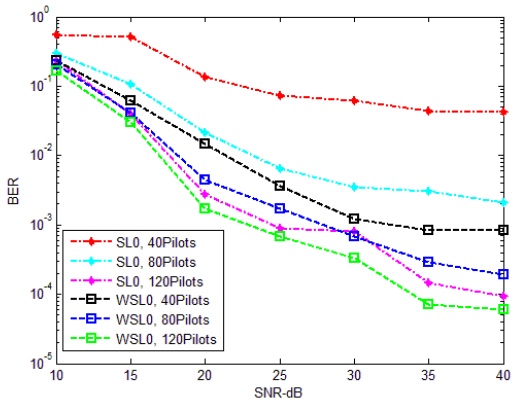

Figure 6. Comparison of Performance of OFDM system, Fixed Number of Pilots and α→0

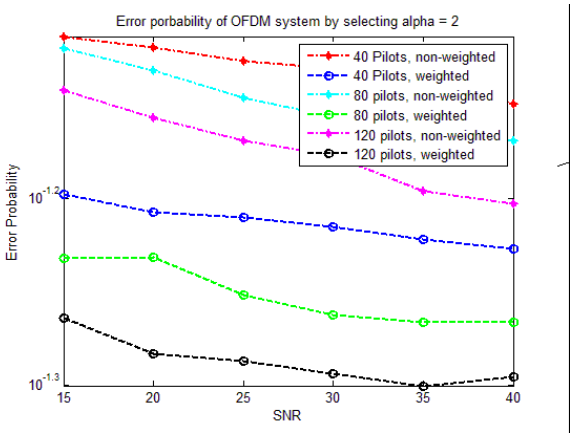

Figure 8. Comparison of Performance of OFDM system, Fixed Number of Pilots and α=2

estimation of the channel, and fewer resources are used. There is an interpretation for this improvement, which states that, by considering these features, those atoms that are more probable to be selected are bolded, and the probability of selecting these atoms increases.

Figures 7 and 8 indicate the error probability of the OFDM system while $\alpha = 2$. By selecting $\alpha = 2$, the pdf of the channel is considered as non-sparse pdf. For this system, sparse representation algorithms are not applicable. However, the relation is convex, and the complexity of calculating the channel is very low since there is a closed-form of the estimated channel. In this case, the estimated channel is less accurate than sparse methods. Despite this less accuracy, it is observed that taking into account other features, improves channel estimation, and results in improving the performance of the system.

Compare our proposed method with Stankovi's method, which estimates the sparse signal by utilizing side information [17]; we provided the same condition as our proposed method worked. In this regard, the index set $\boldsymbol{\Lambda}$ is considered as the candidate set for Stankovi's method because $\boldsymbol{\Lambda}$ indicates contains those elements that are more probable to be selected as nonzero elements of the sparse answer. Then, Stankovi's method is applied to $\tilde{\mathbf{h}}_{\mathbf{p}}^{f} = \boldsymbol{Ah}$. Meanwhile, based on our proposed method, the dictionary matrix is updated, and the OMP algorithm is applied to estimate the sparse solution of $\tilde{\mathbf{h}}_{\mathbf{p}}^{f} = \boldsymbol{Bh'}$. We have run simulations for a fixed number of pilots and fixed SNR and compare their results in Figures 9 and 10, respectively. As indicated at these figures, our proposed method provides better performance than Stankovi's method; however, at higher SNR, these two methods provide similar performance. Besides, it should also be considered that our proposed method is a general framework that could be used by any sparse representation algorithms.

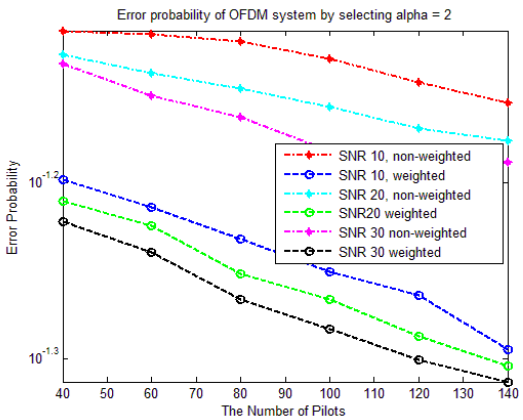

Figure 7. Comparison of Performance of OFDM system, Fixed SNR and α=2.

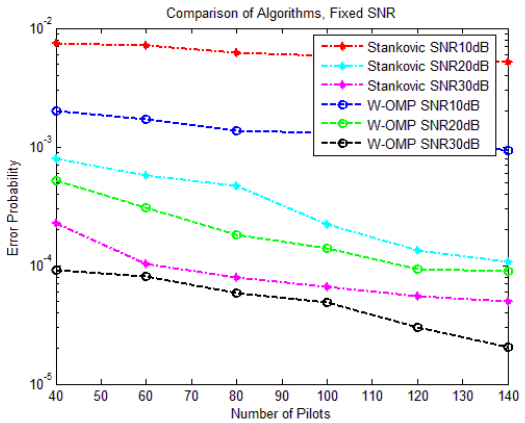

Figure 9. Comparision of the proposed algorithm and Stanikovi's algorithms, Fixed SNR

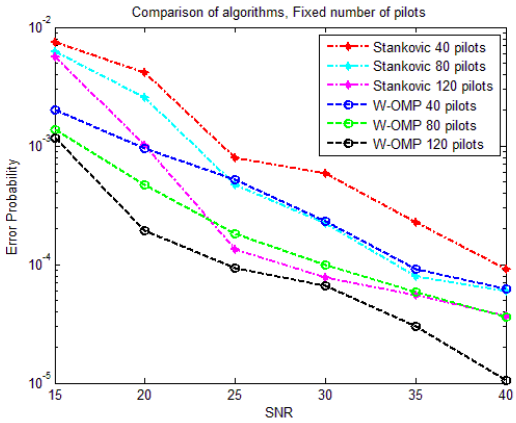

Figure 10. Comparision of the proposed algorithm and Stanikovi's algorithms, Fixed number of Pilots.

6. CONCLUSION

In this paper, we have introduced an approach to improve channel estimation for OFDM system while its complexity is not changed. In this approach, previously estimated channel samples provide information about the current status of the channel. This information is employed to provide a better estimation of the channel. To do this, we introduced a diagonal cost matrix corresponding with this information and some other related parameters such as weighted-dictionary and weighted-channel. We also utilized GGD distribution and considered different GGD's parameter amount to estimate the channel. We showed that by replacing the dictionary matrix with the weighted dictionary, not only side information is conveyed to the estimation process, but also, the computational complexity is not changed. However, in case of low correlation channel obtained information is not reliable. In this case the weight matrix is an identical diagonal matrix which doesn't have effect on the estimation process. It is also shown that utilizing this information provides the opportunity to release some parts of resources in the OFDM system, such as the number of pilots utilized to estimate the channel. For further research it is possible to utilize machine learning techniques to calculate the elements of the weight matrix. By applying the proposed method to OFDM system-based, mathematical computations and processing time will be decreased, and as a result, this method will be applicable in real-time data communications such as WiFi, WiMAX, DAB, DVB, etc.

6. REFERENCES

1. Proakis, J.G., "Digital communications, McGraw-Hill, (2001).
2. K, C.K. and J, J., "An efficient hierarchical modulation based orthogonal frequency division multiplexing transmission scheme for digital video broadcasting", ***International Journal of Engineering, Transactions A: Basics***, Vol. 31, No. 4, (2018), 574-579. doi: 10.5829/ije.2018.31.04a.08
3. Panayirci, E. and Çirpan, H.A., "Maximum a posteriori multipath fading channel estimation for ofdm systems", ***European Transactions on Telecommunications***, Vol. 13, No. 5, (2002), 487-494. doi.org/10.1002/ett.4460130509
4. Ghazi-Maghrebi, S.J.T.J.o.E.E. and Sciences, C., "An efficient ofdm-based system with an insufficient cyclic prefix via a novel constellation algorithm", ***Turkish Journal of Electrical Engineering & Computer Sciences*** Vol. 25, No. 3, (2017), 2278-2292. doi:10.3906/elk-1505-273
5. Pakrooh, P., Amini, A. and Marvasti, F., "Ofdm pilot allocation for sparse channel estimation", ***EURASIP Journal on Advances in Signal Processing***, Vol. 2012, No. 1, (2012), 59. doi: 10.1186/1687-6180-2012-59.
6. Fereydouni, A., Charmin, A., vahdaty, h. and nasiraghdam, h., "Channel estimation and cfo compensation in ofdm system using adaptive filters in wavelet transform domai". ***International Journal of Engineering Transactions A: Basics***", Vol. 33, No. 7, (2020), doi: 10.5829/ije.2020.33.07a.09
7. Komalla, A.R., Kosaraju, S. and Ette, H., "Empirical mode decomposition based adaptive filtering for orthogonal frequency division multiplexing channel estimation", ***International Journal of Engineering Transactions A: Basics*** ", Vol. 30, No. 10, (2017), 1517-1525. doi: 10.5829/ije.2017.30.10a.13
8. Elad, M., From exact to approximate solutions, in Sparse and redundant representations. 2010, Springer.79-109.
9. Candes, E.J., Romberg, J.K., Tao, T.J.C.o.P. and Sciences, A.M.A.J.I.b.t.C.I.o.M., "Stable signal recovery from incomplete and inaccurate measurements", ***Communications on Pure and Applied Mathematics: A Journal Issued by the Courant Institute of Mathematical Sciences***, Vol. 59, No. 8, (2006), 1207-1223. doi.org/10.1002/cpa.20124
10. Chen, S.S., Donoho, D.L. and Saunders, M.A., "Atomic decomposition by basis pursuit", ***SIAM Review***, Vol. 43, No. 1, (2001), 129-159. doi: 10.1137/S003614450037906X
11. Hassanpour, H. and Asadi, S., "Deblocking joint photographic experts group compressed images via self-learning sparse representation, ***International Journal of Engineering, Transaction C: Aspects***", Vol. 29, No. 12, (2016), 1684-1690. doi: 10.5829/idosi.ije.2016.29.12c.07
12. Sabzalian, B. and Abolghasemi, V., "Iterative weighted non-smooth non-negative matrix factorization for face recognition", ***International Journal of Engineering***, ***Transaction A: Basics***", Vol. 31, No. 10, (2018), 1698-1707. doi: 10.5829/ije.2018.31.10a.12
13. ETSI, T., "101 154 v2. 3.1 (2017)", Digital Video Broadcasting (DVB),
14. Mallat, S. and Zhang, Z., "Matching pursuit with time-frequency dictionaries". 1993, Courant Institute of Mathematical Sciences New York United States. doi: 10.1109/78.258082.
15. Tropp, J.A., "Greed is good: Algorithmic results for sparse approximation", ***IEEE Transactions on Information Theory***, Vol. 50, No. 10, (2004), 2231-2242. doi: 10.1109/TIT.2004.834793.
16. Mohimani, H., Babaie-Zadeh, M. and Jutten, C., "A fast approach for overcomplete sparse decomposition based on smoothed ℓ^0 Norm", ***IEEE Transactions on Signal Processing***, Vol. 57, No. 1, (2009), 289-301. Doi:10.1109/TSP.2008.2007606.
17. Stanković, V., Stanković, L. and Cheng, S., "Sparse signal recovery with side information", in 2009 17th European Signal Processing Conference, IEEE., (2009), 100-104.
18. Zhang, X., Cui, W. and Liu, Y., "Compressed sensing with prior information via maximizing correlation", in 2017 IEEE

International Symposium on Information Theory (ISIT), IEEE., (2017), 221-225. doi: 10.1109/ISIT.2017.8006522.

19. Mota, J.F., Deligiannis, N. and Rodrigues, M.R.J.I.T.o.I.T., "Compressed sensing with prior information: Strategies, geometry, and bounds", ***IEEE Transactions on Information Theory,*** Vol. 63, No. 7, (2017), 4472-4496.
20. Jorgensen, B., "Statistical properties of the generalized inverse gaussian distribution, Springer Science & Business Media, Vol. 9, (2012).
21. Coleri, S., Ergen, M., Puri, A. and Bahai, A., "Channel estimation techniques based on pilot arrangement in ofdm systems", ***IEEE Transactions on Broadcasting***, Vol. 48, No. 3, (2002), 223-229. doi: 10.1109/TBC.2002.804034.
22. Berger, J.O., "Statistical decision theory and bayesian analysis, Springer Science & Business Media, (2013).
23. Li, Y., Cichocki, A. and Amari, S.-i., "Analysis of sparse representation and blind source separation", ***Neural Computation***, Vol. 16, No. 6, (2004), 1193-1234. doi: 10.1162/089976604773717586.
24. Efron, B., Hastie, T., Johnstone, I. and Tibshirani, R., "Least angle regression", ***The Annals of Statistics***, Vol. 32, No. 2, (2004), 407-499.
25. Koh, K., Kim, S.-J. and Boyd, S., "An interior-point method for large-scale l1-regularized logistic regression", ***Journal of Machine Learning Research***, Vol. 8, No. Jul, (2007), 1519-1555.
26. Tibshirani, R., "Regression shrinkage and selection via the lasso", ***Journal of the Royal Statistical Society. Series B (Methodological)***, Vol. 58, No. 1, (1996), 267-288. doi: 10.1111/j.2517-6161.1996.tb02080.x
27. Davis, G., Mallat, S. and Avellaneda, M., "Adaptive greedy approximations", ***Constructive Approximation***, Vol. 13, No. 1, (1997), 57-98.
28. Donoho, D.L. and Elad, M., "Optimally sparse representation in general (nonorthogonal) dictionaries via ℓ1 minimization", ***Proceedings of the National Academy of Sciences***, Vol. 100, No. 5, (2003), 2197-2202.
29. Papoulis, A., "Probability & statistics, Prentice Hall, (1990). doi: 10.1073/pnas.0437847100.

Persian Abstract

چکیده

تخمین کانال یکی از اساسی‌ترین قسمتهای سیستمهای با مدولاسیون فرکانسی متعامد (OFDM) است، که بمنظور جبران اعوجاج کانال‌های بیسیم مورد استفاده قرار می‌گیرند. اخیراً با توجه به اینکه کانالهای بی‌سیم بعنوان سیستمهای تنک در نظر گرفته می‌شوند، جایگزینی تنک برای این موضوع مورد استفاده و توجه قرار گرفته است. هرچند که در روش جایگزینی تنک، خصوصیت تنک بودن بعنوان تنها خصوصیت کانال درنظر گرفته می‌شود و از سایر خصوصیتها برای یافتن و تخمین کانال چشم‌پوشی می‌شود. در این مقاله راه‌کاری را پیشنهاد داده‌ایم که با استفاده از آن قادر باشیم از سایر خصوصیت‌های کانال علاوه بر تنک بودن در تخمین کانال بهره ببریم. در این رابطه با تعریف یک سری پارامتر ریاضی و بهره بردن از تخمین MAP این خصوصیتها را بمنظور بهبود تخمین در تخمین تنک کانال OFDM استفاده کرده‌ایم. نتایج شبیه‌سازی نشان می‌دهند که ساختار پیشنهادی ما نه تنها باعث بهبود تخمین شده است، بلکه قادر بوده است که منابع کمتری، از قبیل کاهش تعداد پایلوتها و توان ارسالی، استفاده نماید.

International Journal of Engineering

Journal Homepage: www.ije.ir

Multi-conductor Transmission Line Model of Split-winding Transformer for Frequency Response and Disk-to-disk Fault Analysis

M. A. Sobouti[a], D. Azizian*[b], M. Bigdeli[a], G. B. Gharehpetian[c]

[a] *Department of Electrical Engineering, Zanjan Branch, Islamic Azad University, Zanjan, Iran*
[b] *Department of Electrical Engineering, Abhar Branch, Islamic Azad University, Abhar, Iran*
[c] *Electrical Engineering Department, Amirkabir University of Technology, Tehran, Iran*

PAPER INFO

Paper history:
Received 09 March 2020
Received in revised form 15 March 2021
Accepted 08 April 2021

Keywords:
Split-Winding Transformer
Multi-Conductor Transmission Line Model
Frequency Response Analysis
Short Circuit Fault

ABSTRACT

For transformer designers, split-winding transformer modeling in different frequency ranges is of great importance. In this paper, for the first time, a multi-conductor transmission line model is proposed for high-frequency modeling of the split-winding transformer. In this model, all the turns in layers and disks have been considered and the model's parameters have been calculated using the finite element method. In order to validate the proposed model, the results are compared with the result of a model, which is based on finite element and coupled field-circuit. It is shown that the introduced model has good accuracy and it can be employed for split-winding transformer modeling in different frequency ranges. In addition, using the validated multi-conductor transmission line model, the frequency response of the split-winding transformer and disk-to-disk short circuit fault are analyzed.

doi: *10.5829/ije.2021.34.06c.12*

NOMENCLATURE

U and I	voltage and current	ε_0	the permittivity of free space
R, L, C,* and *G	resistance, inductance, capacitance, and conductance	***S***	the conductor's cross-section
[*Z*] and [*Y*]	impedance and inductance matrix	W_{ij}	the magnetic energy
U_S ***(i)* and I_S*(i)***	sending end voltage and current of i-th transmission line	B_i	The magnetic flux density
U_R ***(i)* and I_R *(i)***	receiving end voltage and current	**Subscripts**	
l	the average length of the line	**FE**	Finite element
Y_0	the characteristic admittance matrix of the model	**MTL**	Multi-conductor transmission line
A, J	the magnetic vector potential, current density	**CC**	correlation coefficient
μ	Permeability	**FRA**	Frequency Response Analysis
ρ	the volume charge density		

1. INTRODUCTION

Nowadays, transformers are employed in different applications and a transformer designer encounters several electromagnetic and insulating complex problems [1-2]. The growing trend in the use of traction systems has increased the need for different structures of multi-winding transformers.

In a transformer, impulse overvoltages can easily cause an insulation breakdown, internal short-circuits and mechanical displacement. The special structure of a split-winding transformer may cause problems in insulating system design under different loading conditions. Investigating transformer response to different disturbances, and controlling these conditions can lead to high reliability in a traction network. Therefore, providing suitable models is important for analyzing the behavior of this type of transformers especially under high-frequency transients.

High-frequency transients have been studied in two-winding oil-immersed and dry-type transformers [3-7]. Model parameters and inductance matrix for two-

*Corresponding Author Institutional Email: d.azizian@abhariau.ac.ir

Please cite this article as: M. A. Sobouti, D. Azizian, M. Bigdeli, G. B. Gharehpetian, Multi-conductor Transmission Line Model of Split-winding Transformer for Frequency Response and Disk-to-disk Fault Analysis, International Journal of Engineering, Transactions C: Aspects Vol. 34, No. 6, (2021) 1486-1494

winding transformers have been calculated for different purposes based on analytical, finite element (FE) [8 - 13] and heuristic [14] methods.

Aghmasheh et al. have used the gray box modeling to study the transients in power transformer windings and its parameters have been obtained by applying the mathematical transfer function and the measured frequency response [15]. In literature, FE models have been employed to study high-frequency electromagnetic transients [16], frequency response [9, 17] and winding fault diagnosis [18]. Additionally, in order to model the behaviour of transformer, 2D and 3D FE models have been coupled to external electrical circuits in litetature [19-20]. The coupled field-circuit approach has also been applied for high-frequency modeling of the transformer [17, 20, 21], in which the windings have been modeled as integrated blocks that can cause a considerable error in modeling the ohmic behaviour of windings .

The multi-conductor transmission line (MTL) model has been investigated in various papers to study the transient behavior of different transformers. Also, using the optimized MTL model, the partial discharge has been studied in power transformer windings [8, 22]. Jafari et al. have introduced a modified MTL model for partial discharge localization in power transformers [23]. Zhang et al. have investigated on the distribution of very fast transient overvoltages using an analytical model based on the MTL model and finite difference time domain approach [24]. The hybrid models, which are a combination of multi and single-transmission line models, have been introduced to simulate the transients responses of transformer windings in literature [25, 26]; these models significantly reduce the number of linear equations.

The electromagnetic and thermal behaviour of the split-winding transformer has been studied in [27, 28]. Some models based on equivalent circuit and coupled field-circuit approach have been previously proposed to simulate the low-frequency behaviour of the split-winding transformer [29, 30]. Additionally, research on the design optimization of the split-winding traction transformer has been presented under normal loading conditions [31].

For the split-winding transformer, novel models based on the coupled field-circuit approach and detailed model, have been introduced and validated for high-frequency analysis by Sobouti et al. [32]. The coupled field-circuit approach is very accurate, but it needs more computational time. Additionally, detailed model is a fast method but with lower accuracy.

In order to have an accurate and fast solution, in this paper, a new model based on MTL is introduced for split-winding transformer modeling. In all previous models, only simple layers and disks have been modeled in the split-winding traction transformer. But in this paper, all the turns in layers and disks of windings have been considered and the model parameters per turns have been calculated using the FE method. The results are compared to a validated coupled field-circuit approach. It is shown that the introduced method has good accuracy and low computational time. Using the validated model, the frequency response of the split-winding transformer under normal and faulty conditions (disk-to-disk short-circuit fault) is studied. The obtained results show the higher capability of the proposed model against the older techniques

2. PROPOSED MODEL BASED ON MTL

One of the models that have been used to simulate the electromagnetic transients in transformer windings is the detailed model [32]. The validity of the detailed model depends on the accuracy of determining parameters, the number of model sections, and the selected error function. When a large number of sections are chased, although the validity ranges of the model can increase, it would be more difficult to find appropriate values for the parameters. This causes the model solution to become more time-consuming due to the larger dimensions of system equations. Thus, similar to many engineering problems, considering a compromise between modeling accuracy and calculation speed is important [33].

In the MTL model, each conductor of the winding is considered as a parallel transmission line, and all capacitive and inductive couplings are taken into account. By considering all the conductors and their lengths according to the technical specifications, the limitations of finite element models are eliminated. Thus, the validity of the model is higher than the detailed model [8].

The *N*-dimensional vectors of voltage and current of each distinct *x*-point located on each of *n* transmission lines could be formulated by the following wave equations:

$$\frac{\partial[u(x,t)]}{\partial x} = -\left([R][i(x,t)] + [L]\frac{\partial[i(x,t)]}{\partial t}\right) \quad (1)$$

$$\frac{\partial[i(x,t)]}{\partial x} = -\left([G][u(x,t)] + [C]\frac{\partial[u(x,t)]}{\partial t}\right) \quad (2)$$

where, u and i are the voltage and current vectors, respectively. In addition, R, L, C, and G are respectively the resistance, inductance, capacitance, and conductive matrices.

Because of symmetrical electrical parameters, the above equations in the frequency domain could be explained as follows [8]:

$$\frac{d^2[u(x)]}{dx^2} = [Z][Y][u(x)] = [P]^2[u(x)] \quad (3)$$

$$\frac{d^2[i(x)]}{dx^2} = [Y][Z][i(x)] = ([P]^2)^T[i(x)] \quad (4)$$

where $[Z]$ and $[Y]$ are impedance and inductance matrix respectively [8].

Figure 1 shows the MTL model of the transformer winding.

The boundary conditions of the MTL model can be defined as follows:

$$U_R(i) = U_S(i+1) \quad \text{For } i\text{=1 to } i\text{=}N\text{-1} \tag{5}$$

$$I_R(i) = -I_S(i+1) \quad \text{For } i\text{=1 to } i\text{=}N\text{-1} \tag{6}$$

By solving the equations using the boundary conditions, it is possible to calculate the currents based on voltages (7):

$$\begin{bmatrix} I_s \\ I_R \end{bmatrix} = \begin{bmatrix} Y_0.\coth([p]l) & -Y_0.cos\,ech([p]l) \\ -Y_0.cosech([p]l) & Y_0.coth([p]l) \end{bmatrix} \cdot \begin{bmatrix} U_s \\ U_R \end{bmatrix} \tag{7}$$

where, U_S *(i)* and I_S *(i)* are sending end voltage and current of *i*-th transmission line, and U_R *(i)* and I_R *(i)* are its receiving end voltage and current, $[P]$ is the product of matrices *Z* and *Y*, *l* is the average length of the line and Y_0 is the characteristic admittance matrix of the model, which is obtained from the following relation:

$$Y_0 = [Z]^{-1}.[P] \tag{8}$$

3. MTL PARAMETER CALCULATION

Figure 2 and Table 1 show the windings structure and Specifications of the dry-type split-winding transformer. The high voltage windings are paralleled to construct a single primary winding [27,32].

3. 1. FE Model Three-phase electromagnetic modeling of a transformer is time-consuming and may be impossible, but it is acceptable to employ single-phase modeling [32].

The magnetic fields can be modeled using Poison's equation, as follows:

$$\nabla^2 A - \mu\varepsilon\frac{\partial^2 A}{\partial t^2} = -\mu \cdot J, \tag{9}$$

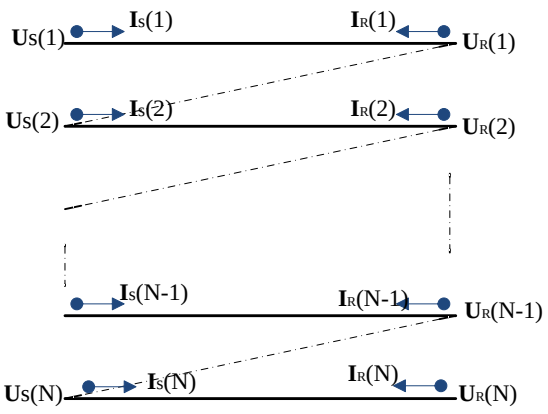

Figure 1. MTL Model

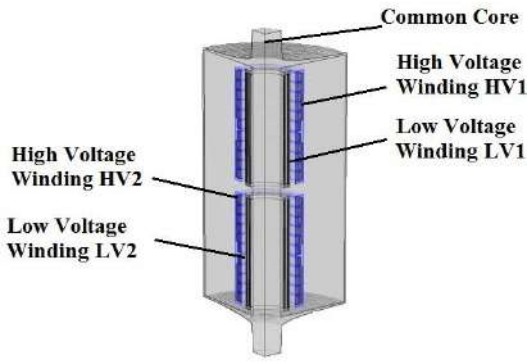

Figure 2. Single-phase view of a dry-type split-winding transformer

TABLE 1. Specifications of the transformer shown in Figure 2 [32].

	HV1	HV2	LV1	LV2
Rated power (MVA)	2	2	2	2
Line voltage (V)	20000	20000	750	750
Connection	D	D	y	D
Layer number	1	1	3	3
Axial channel (mm)	-	-	3*10	1*12
Disk number	11	11	1	1
Radial channel between disks (mm)	9*12 / 1*26	9*12 /1*26	-	-
Turns	693	693	26	15
Height (mm)	1230	1230	1240	1240
Internal diameter (mm)	654	654	332	929
External diameter (mm)	799	799	454	982
Core diameter (mm)	320			
E_s (mm)	1015			
H_f (mm)	1410			

where, *A, J,* ε and μ, are the magnetic vector potential, current density, permittivity and permeability, respectively. Also, the fundamental postulate of electrostatics in free space specifies the divergence of *E* using Equation (10):

$$\nabla . E = \frac{\rho}{\varepsilon_0}, \tag{10}$$

where ρ is the volume charge density and ε_0 is the permittivity of free space. In practical applications, the total field of an aggregate or a distribution of charges is usually calculated. The volume integral of both side of Equation (10) over an arbitrary volume *V* is given by Equation (11):

$$\int_v \nabla . E\, dv = \frac{1}{\varepsilon_0}\int_v \rho\, dv. \tag{11}$$

Using the divergence theorem, we have [34]:

$$\oint_s E \,.\, ds = \frac{Q}{\varepsilon_0}. \quad (12)$$

In this paper, the FE models are used to solve Poison's equation and to obtain magnetic fields in different positions of transformer windings. Several FE models can be employed as introduced by Sobouti *et al.* [32]. In the present research, a 2D FE model with an equivalent core model is selected for the electromagnetic field calculations, and a 2D FE model with a simple core is selected for electrostatic computations [28].

3. 2. Winding Resistance Calculation The winding losses in the transformer consist of a DC and an eddy current losses. Using the calculated magnetic field, the current and losses distribution in windings and consequently windings resistances can be calculated.

In this paper, winding losses and resistances are computed based on a semi-analytical method [32]. This quasi-numerical method employs the FE method to calculate the magnetic field distribution, and an analytical method to determine the windings losses per windings part. The obtained results are shown in Figures 3 and 4 for typical traction transformer specifications [29].

Note that the winding ohmic resistance increases with an increase in the frequency as described in literature [35, 36].

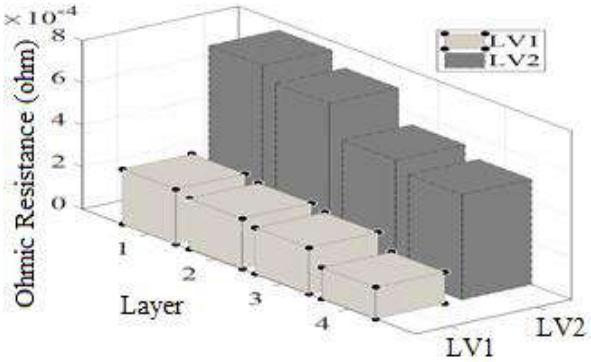

Figure 3. LV windings ohmic resistances (Ω)

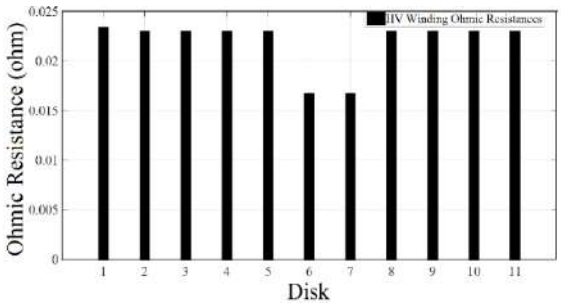

Figure 4. HV windings ohmic resistances (Ω).

3. 3. Winding Capacitors Calculation In multi-winding traction transformer modeling, the capacitances between LV and HV winding turns should be calculated in the MTL model. In this paper, the FE method has been used to calculate these capacitors. To reduces the calculation burden, a method based on FE and electrical charge calculation of each conductor is utilized to calculate capacitances [32]. Figure 5 shows electric potential (V) and electric field while the capacitancs have been calculated.

Employing voltage V_i to i-th conductor (and setting the others to zero), the electric field can be calculated using the electrostatic analysis, and the electric charge on each conductor can be calculated using Equation (13) [6, 9, 10]:

$$Q = (\varepsilon_r . \varepsilon_0)\frac{S}{d}, \quad (13)$$

where S is the conductor's cross-section, ε_0 and ε_r are free space and relative permittivity, respectively and d is the distance between conductors. Now, by calculating the electrical charges of all the conductors and forming the vector Q, the column i of the matrix C can be obtained as follows:

$$[C_{1i}, C_{2i}, \dots, C_{ni}]^T = {}^{Q}/_{V_i} \quad (14)$$

Because of the change in behavior of the electrical potential and flux distributions, studying short circuits in layers or disks is important. In the past, ohmic resistance changes have been used to detect short circuits. In this paper, capacitors are computed in both normal and faulty conditions. A fault condition in a disk or a layer can be

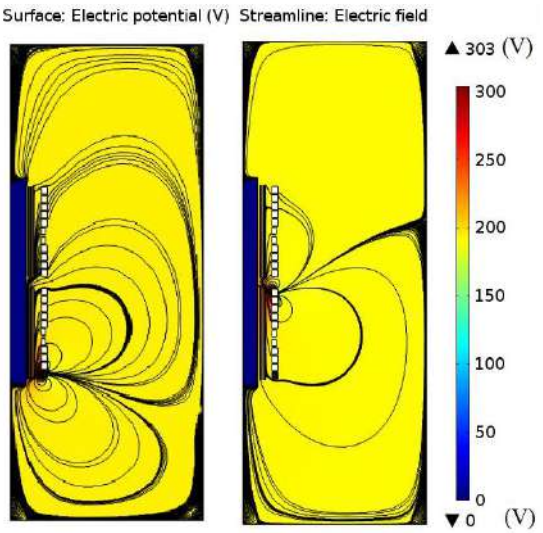

(a) (b)

Figure 5. Electric potential and electric field distribution while the capacitances between (a) Eleventh and Tenth disks of HV_1 and (b) first and second disks of HV_1 have been simulated

modeled by short-circuiting a number of turns with very low resistance. Figures 6-7 show the calculated capacitances in the normal and faulty conditions.

By comparing the results in Figures 6 and 7, it can be seen that the capacitance values decrease due to the short circuit of the layers and disks.

3. 4. Winding Inductances Calculation using Electromagnetic Field Modelling The calculation of inductive parameters includes the determination of mutual and self-inductances that are very important for impulse voltage distribution and frequency response analysis. In this paper, the energy method is used to calculate the winding inductances.

The magnetic energy can be calculated using Equation (15) by which two conductors are coupled [8, 28]:

$$W_{i,j} = \frac{1}{2}\int_{vol} B_i \cdot H_j \, dv \tag{15}$$

where, B_i is resulting magnetic flux density due to i-*th* conductor, and H_j is resulting magnetic field due to j-*th* conductor.

By employing currents I_i and I_j to a pair of intended windings and calculating the magnetic energy (W_{ij}), the mutual inductance between them is calculated using Equation (16) [8, 28]:

$$L_{ij} = \frac{2W_{ij}}{I_i I_j}. \tag{16}$$

In addition, the self-inductance can be calculated by the following equation [8]:

$$L_{ii} = \frac{2W_{ii}}{I_i^2}. \tag{17}$$

As presented in literature [32, 37], the winding inductances decrease exponentially with an increase in the frequency.

The inductances per turn for the first disk of HV_1 and the fourth layer of LV_1 in two different frequencies and under normal and short-circuit conditions are shown in Figures 8 and 9, respectively. Figure 10 shows the magnetic flux density distribution in normal and faulty conditions.

As can be seen in Figures 8 and 9, the inductance values increase as a result of the short-circuit condition. Therefore, calculated parameters have been used in the

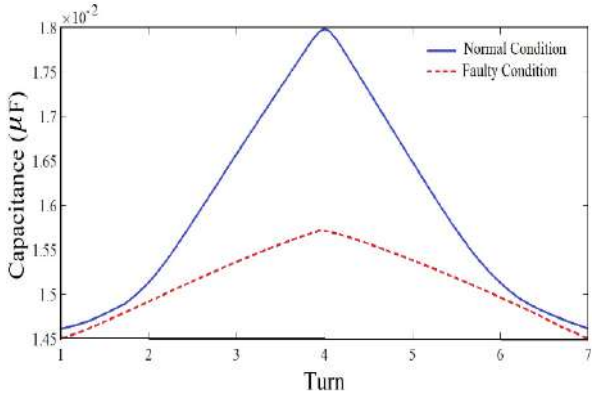

Figure 6. The first layer of LV_1 winding capacitors (F) in normal and faulty conditions

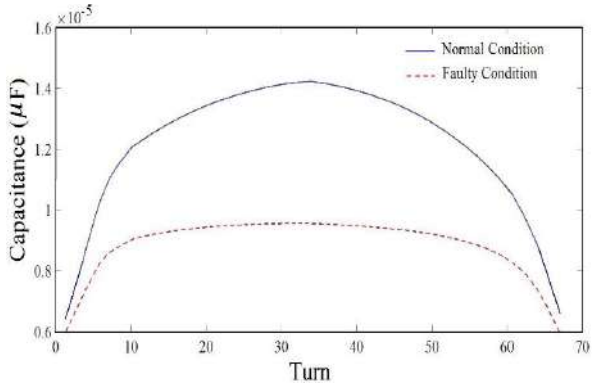

Figure 7. The first disk of HV_1 winding capacitors (F) in normal and faulty conditions

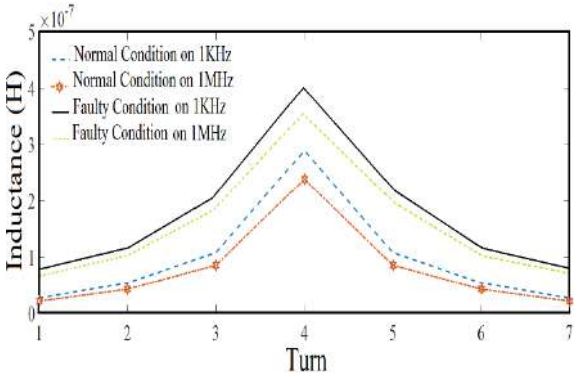

Figure 8. Inductance per turn for the fourth layer of LV1 at 1 kHz and 1 MHz

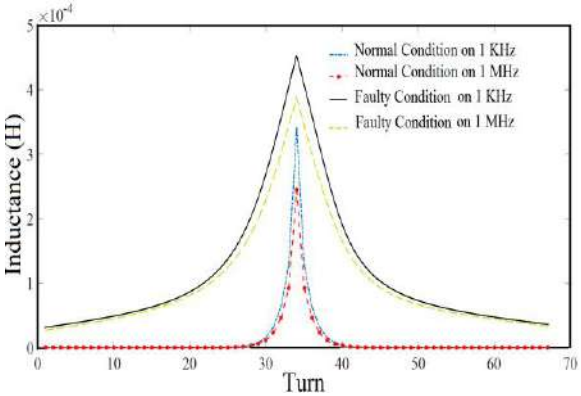

Figure 9. Inductance per turn for the first disk of HV_1 at 1 kHz and 1 MHz

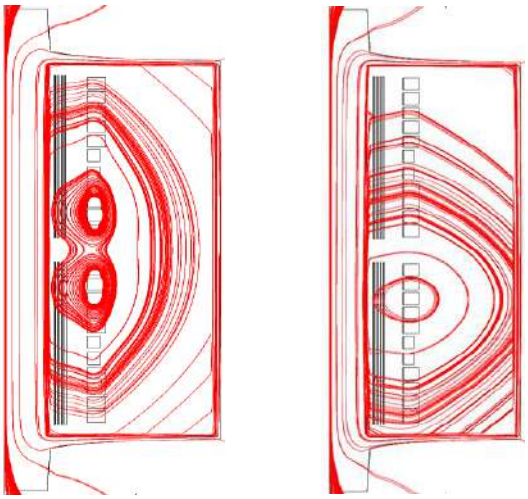

(a) (b)

Figure 10. Flux density distribution under normal loading condition: (a) normal condition and (b) fault in sample disk

MTL model and the frequency response of the split-winding transformer and disk-to-disk short circuit fault are analyzed. Figure 11 shows the flowchart of the general procdure for the current research.

4. SIMULATION RESULTS

The detailed 3D FE model with full consideration of both electromagnetic and electrostatic phenomena is the most accurate method. But, the detailed modeling of all layers and disks in the 3D model is very time-consuming, and due to the restrictions in computer hardware, it may be impossible [28, 29]. Thus, a designer may be forced to simplify the windings structure in the 3D model. This approach causes an error in high-frequency analysis. For the same structure modeling, the 3D FE model has higher accuracy. Thus, the 2D FE results are validated versus the 3D FE model with a simplified structure of the split-winding transformer as shown by Sobouti et al. [32]. In addition, the simulation time in the 2D FE model is less than the 3D model with sufficient accuracy. Therefore, a 2D model with an equivalent core can be used to model the split-winding transformer with a complete geometry for high and low-frequency electromagnetic transients studies.

To increase the accuracy in the 2D model, the 2D coupled field-circuit method has been used to model the split-winding transformer. As shown by Sobouti et al. [32], the resonant frequencies are acceptable while they are compared to the FE models. Therefore, the coupled field-circuit approach can model the transformer behavior during transients more accurately.

Also, in this paper, the MTL model is simulated using the electrical parameters determined in Section 3 in normal and faulty conditions. In this model, all the

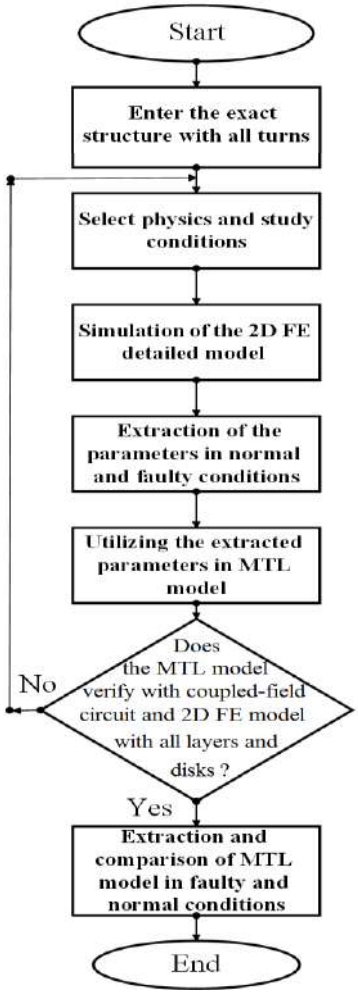

Figure 11. Flowchart for the general process of this article

conductors of the disks and layers and their average length are modeled according to the technical specifications, and validated with the FE and the coupled field-circuit method. To obtain the frequency response of the transformer, an impulse voltage is applied to the transformer input terminals (HV) and the output impulse response is obtained (LV_1 windings). Then, by dividing the output signal to the input signal and using the fast Fourier transform, the transfer function (TF) is obtained in the frequency domain [16]. Figures 12 and 13 show the results of the voltage distribution of the high-frequency MTL model in HV disks, the comparison of the results of the MTL model with the 2D FE, and the coupled-field circuit model in normal conditions. This comparison shows that the proposed method is able to model the high-frequency transient behavior of the split-winding transformer in normal conditions.

After short-circuiting the eleventh and tenth disks of the HV_1 winding, the frequency response is determined. Figure 14 shows the difference of resonant frequencies in the MTL model in faulty conditions.

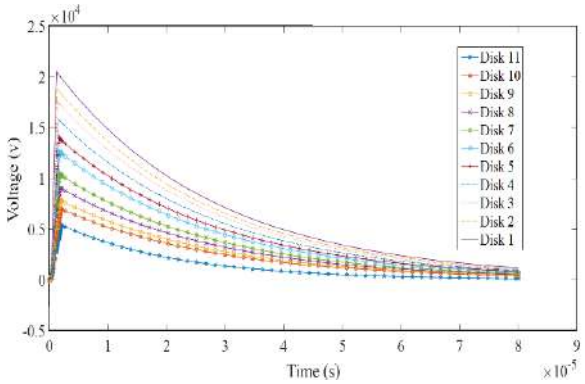

Figure 12. Voltage distribution of high-frequency MTL Model in normal condition

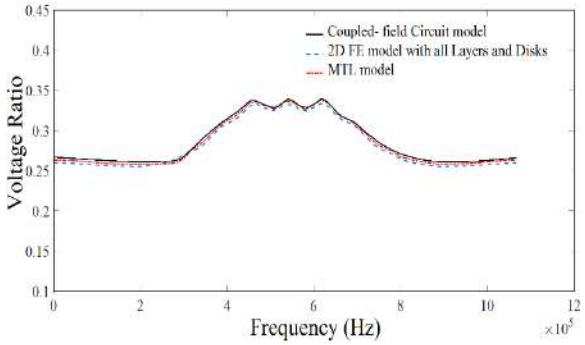

Figure 13. Comparison of MTL model with 2D FE and coupled-field circuit model in Normal condition

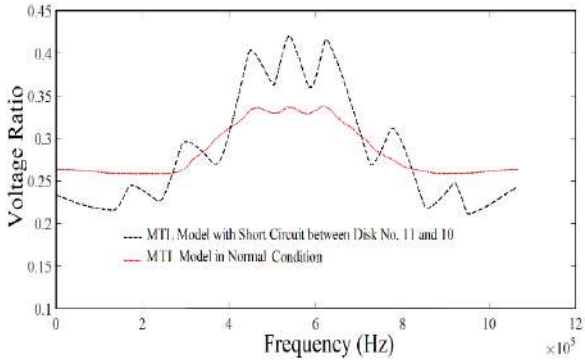

Figure 14. Comparison of MTL model in faulty and normal conditions

The data gathered in this figure can be employed for fault diagnosis of transformer winding. For this purpose, the IEEE standard [38] introduces a proper index based on correlation coefficient (CC). This index is defined as follows:

$$CC = \frac{\sum_{i=1}^{N} X(i)Y(i)}{\sqrt{\sum_{i=1}^{N}[X(i)]^2 \sum_{i=1}^{N}[Y(i)]^2}} \quad (18)$$

where, X and Y denote the healthy and the faulty conditions, and N is the number of the dataset.

As it was mentioned in literature [38], a value smaller than 0.9996 for CC means that a faulty condition is occurred. By applying Equation (18) to different disk-to-disk fault conditions such as the data presented in Fig. 14, it is seen that the CC has a value between 0.6 and 0.95. Thus, the introduced high-frequency MTL model is an efficient (fast and accurate) method for using in frequency response analysis of transformer due to different fault conditions.

5. CONCLUSIONS

In this paper, the transient behaviour of the split-winding traction transformer has been studied at high frequencies in faulty and normal conditions using an MTL model. Given that modeling all turns of disks and layers in the windings is not possible in 3D models, the 2D FE models with detailed modeling of windings was introduced to model the electromagnetic transients more accurately.

In the proposed model, all the conductors of the disks and layers and their average length have been modeled. The 2D and coupled-field circuit models have been used to model and validate the transient electromagnetic behaviour of the split-winding traction transformer in the frequency domain, and the accuracy of the methods has been confirmed. It has been discussed that the MTL model not only is fast and simple, but also can be employed to model high-frequency transient behaviour of split-winding traction transformers with much higher accuracy compared to the detailed model. In addition, its frequency range has been increased compared to the detailed model. Also, it has been shown that the FRA result of transformer winding for each short-circuit fault is different from others.

6. REFERENCES

1. Akbari, M., Yavari, M., Nemati, N., Babaee, D. J, Molavi, H., Asefi, M., "An Investigation on Stability, Electrical and Thermal Characteristics of Transformer Insulting Oil Nanofluids", ***International Journal of Engineering, Transactions A: Basics,*** Vol. 29, No. 10, (2016), 1332-1340. doi: 10.5829/idosi.ije.2016.29.10a.02

2. Siahkolah, B., Faiz, J., "Effect of solid-State on Load Distribution Transformer Tap-Changer on Power Quality Enhansement", ***International Journal of Engineering, Transactions B: Applications,*** Vol. 17, No. 2, (2004), 141-154.

3. Bigdeli, M., Vakilian, M., Rahimpour, E., "Transformer winding faults classification based on transfer function analysis by support vector machine" ***IET Electric Power Applications***, Vol. 6, No. 5, (2012), 268-276. doi: 10.1049/iet-epa.2011.0232

4. Ganji, M., Bigdeli, M., Azizian, D., "Mitigation Transformer Inrush Current Using Modified Transient Current Limiter", ***International Journal of Engineering, Transactions B: Applications,*** Vol. 32, No. 5, (2019), 701-709. doi: 10.5829/ije.2019.32.05b.12.

5. Bigdeli, M., Rahimpor, E., and Khatibi, M., "Transient-state Modelling of distribution transformers", ***International Review on Modelling and Simulations***, Vol. 4, No. 1, (2011), 295-302.
6. Eslamian, M., Vahidi, B., and Hosseinian, S. H., "Transient simulation of cast-resin dry-type transformers using FEM", ***European Transactions on Electrical Power***, Vol. 21, No. 1, (2011), 363-379. doi: 10.1002/etep.447.
7. Eslamian, M. and Vahidi, B., "New Equivalent Circuit of Transformer Winding for the Calculation of Resonance Transients Considering Frequency-Dependent Losses", ***IEEE Transactions on Power Delivery***, Vol. 30, No. 4, (2015), 1743-1751. doi: 10.1109/TPWRD.2014.2361761.
8. Hosseini, S. M., Rezaei Baravati, P., "New High Frequency Multi-conductor Transmission Line Detailed Model of Transformer Winding for PD Study***", IEEE Transactions on Dielectrics and Electrical Insulation***, Vol. 24, No. 1, (2017), 316-323. doi: 10.1109/TDEI.2016.005694.
9. Eslamian, M., Vahidi, B., and Hosseinian, S. H., "Analytical calculation of detailed model parameters of cast resin dry-type transformers", ***Energy Conversion and Management***, Vol. 52, No. 7, (2011), 2565-2574. doi:10.1016/j.enconman.2011.01.011
10. Eslamian, M., Vahidi, B., and Hosseinian, S. H., "Combined analytical and FEM methods for parameters calculation of detailed model for dry-type transformer", ***Simulation, Modelling Practice and Theory***, Vol. 18, No. 3, (2010), 390-403. doi: 10.1016/j.simpat.2009.12.005.
11. Eslamian, M., Vahidi, B. "New Methods for Computation of the Inductance Matrix of Transformer Windings for Very Fast Transients Studies", ***IEEE Transactions on Power Delivery***, Vol. 27, No. 4, (2012), 2326-2333. doi: 10.1109/TPWRD.2012.2204905.
12. Eslamian, M. and Vahidi, B., "Computation of Self-impedance and Mutual Impedance of Transformer Winding Considering the Frequency-dependent Losses of the Iron Core", ***Electric Power Components and Systems***, (2016), 1236-1247. doi: 10.1080/15325008.2016.1157111
13. Faiz, J., Naderian Jahromi, A., Mohseni, H., "A Fast Method for Calculation of Transformers Leakage Reactance Using Energy Technique", ***International Journal of Engineering, Transactions B: Applications***, Vol. 16, No. 1, (2003), 41-48.
14. Bigdeli, M. and Valii, M., Azizian, D., "Applying Intelligent Optimization Algorithms for Evaluation of Transformer Black Box Model," 6th International Conference on Soft Computing Applications, Timisoara, Romania, (2014). doi: 10.1007/978-3-319-18416-6_102
15. Aghmasheh, R., Rashtchi, V., and Rahimpour, E., "Gray Box Modelling of Power Transformer Windings for Transient Studies", ***IEEE Transactions on Power Delivery***, Vol. 32, (2017), 2350- 2359. doi: 10.1109/TPWRD.2017.2649484
16. Gunawardana, M., Fattal, F., Kordi, B., "Very Fast Transient Analysis of Transformer Winding Using Axial Multiconductor Transmission Line Theory and Finite Element Method", ***IEEE Transactions on Power Delivery***, Vol. 34, No. 5 , (2019), 1948-1956. doi: 10.1109/TPWRD.2019.2932669
17. Kumbhar, G. B., and Kulkarni, S. V., "A Directly Coupled Field-Circuit Model of a Transformer to Study Surge Phenomena and for Frequency Response Analysis", 18th National Power Systems Conference (NPSC), India, 2014. doi: 10.1109/NPSC.2014.7103838
18. Liu, S., Li, H., and Lin, F., "Diagnosis of Transformer Winding Faults based on Fem Simulation and On-site Experiments", ***IEEE Transactions on Dielectrics and Electrical Insulation*** Vol. 23, No. 6, (2016), 3752-3760. doi: 10.1109/TDEI.2016.006008
19. Wan, H., Yang, Q., Li, Y., Wang, J., Yuan, D., Hu, M., "Electromagnetic Characteristic Calculation of Several Parallel Coils for High Current Transformer Based on Field-Circuit Coupling Method", ***IEEE Transactions on Applied Superconductivity***, Vol. 29, No. 2, (2019). doi: 10.1109/TASC.2019.2893706
20. Kumbhar, G. B., Kulkarni, S. V., "Analysis of short-circuit performance of split-winding transformer using coupled field-circuit approach", ***IEEE Transaction on Power Delivery***, Vol. 22, No. 2, (2007), 936-943. doi: 10.1109/TPWRD.2007.893442.
21. Kumbhar, G. B., Kulkarni, S. V., "Analysis of sympathetic inrush phenomena in transformers using coupled field-circuit approach", ***IEEE Power Engineering Society General Meeting***, (2007), 427-432. doi: 10.1109/PES.2007.386128
22. Hosseini, S.M.H., Baravati, P. R., "Transformer Winding Modeling based on Multi-Conductor Transmission Line Model for Partial Discharge Study" ,***Electrical Engineering and Technology***, Vol. 9, No. 1, (2014), 154-161. doi: 10.5370/JEET.2014.9.1.154
23. Jafari, A.M., Akbari, A., Mirzaei, A., Kharezi, M., Allahbakhshi. M, "Investigating Practical Experiments of Partial Discharge Localization in Transformers using Winding Modeling", ***IEEE Transactions on Dielectrics and Electrical Insulation***, Vol. 15, No. 4, (2008), 1174-1182. doi: 10.1109/TDEI.2008.4591240
24. Zhang, P., Wang, Y., Nie, X., Yan, W., Zhang, H., "Transient modeling and analysis of transformer windings under VFTO", 7th World Congress on Intelligent Control and Automation, China, 2008. doi: 10.1109/WCICA.2008.4593306
25. Naderi, M. S., Vakilian, M., Blackburn, T. R., Phung, B. T., Naderi, M. S., Nasiri, A., "A hybrid transformer model for determination of partial discharge location in transformer winding", ***IEEE Transactions on Dielectrics and Electrical Insulation***, Vol. 14, No. 2, (2007), 436-443. doi: 10.1109/TDEI.2007.344625
26. Popov, M., van der Sluis, L., Paap, G. C., De Herdt, H., "Computation of very fast transient overvoltages in transformer windings", ***IEEE Transactions on Power Delivery***, Vol. 18, No. 4, (2003), 1268-1274. doi: 10.1109/TPWRD.2003.817738
27. Azizian, D., "Windings Temperature Prediction in Split-Winding Traction Transformer", ***Turkish Journal of Electrical Engineering and Computer Sciences***, Vol. 24, No. 4, (2016), 3011-3022. doi:10.3906/elk-1403-304
28. Azizian, D., Vakilian, M., Faiz, J., and Bigdeli, M., "Calculating Leakage Inductances of Split-Windings in Dry-Type Traction Transformers", ***ECTI Transaction EEC***, Vol. 10, No. 1, (2012), 99-106.
29. Azizian, D., Vakilian, M., and Faiz, J., "A New Multi-Winding Traction Transformer Equivalent Circuit for Short-Circuit Performance Analysis", ***International Transaction on Electrical Energy Systems***, Vol. 24, No. 2, (2014), 186-202. doi: 10.1002/etep.1686
30. Azizian, D., "Nonlinear Behaviour Analysis of Split-Winding Dry-Type Transformer Using a New Star Model and a Coupled Field-Circuit Approach", ***Archives of Electrical Engineering***, Vol. 65, No. 4, 773-787, 2016. doi: 10.1515/aee-2016-0054
31. Azizian, D., Gharehpetian, G. B., "Split-Winding Transformer Design Using New Hybrid Optimization Algorithm Based on PSO and I-BB-BC", ***IET Science, Measurement and Technology,*** Vol. 12, No. 6, (2018), 712-718. doi: 10.1049/iet-smt.2017.0118
32. Sobouti, M. A., Azizian, D., Begdeli, M., Gharehpetian, G. B., "Electromagnetic transients modelling of splitwinding traction transformers for frequency response analysis", ***IET Science, Measurement and Technology***, Vol. 13, No. 9, (2019). 1362-1371. doi: 10.1049/iet-smt.2019.0164
33. Gharehpetian, G. B., Mohseni, H., Moller, K., " Hybrid modelling of inhomogeneous transformer winding for very fast

transient overvoltage studies", ***IEEE Transactions on Power Delivery,*** Vol. 13, No. 1, (1998), 157-163. doi: 10.1109/61.660873

34. Gunawardana, M., Fattal, F., Kordi, B., "Very Fast Transient Analysis of Transformer Winding Using Axial Multiconductor Transmission Line Theory and Finite Element Method", ***IEEE Transactions on Power Delivery***, (2019), Vol. 34, No. 5.1948-1956. doi: 10.1109/TPWRD.2019.2932669
35. Fouineau, A., Raulet, M., Lefebvre, B., Burais, N., and Sixdenier, F., "Semi-Analytical Methods for Calculation of Leakage Inductance and Frequency-Dependent Resistance of Windings in Transformers", ***IEEE Transaction on Magnetics***, (2018), Vol. 54, No. 10, 1-10. doi: 10.1109/TMAG.2018.2858743
36. Ahour, J., Seyedtabaie, S., Gharehpetian, G. B., "Modified transformer winding ladder network model to assess non-dominant frequencies", ***IET Electric Power Applications***, (2017), Vol. 11, No. 4. 578-585. doi: 10.1049/iet-epa.2016.0635
37. Mombello, E.E., "Impedances for the calculation of electromagnetic transients within transformers", ***IEEE Transactions on Power Delivery***, (2002), Vol. 17, No. 2. 479-488. doi: 10.1109/61.997922
38. IEEE Guide for the Application and Interpretation of Frequency Response Analysis for Oil-Immersed Transformers, IEEE Std C57.149, 2012.

Persian Abstract

چکیده

برای طراحان ترانسفورماتور، مدل‌سازی ترانسفورماتورهای چندسیم‌پیچه دوطبقه در حوزه‌های فرکانسی مختلف، از اهمیت زیادی برخوردار است. در این مقاله، مدل خط انتقال چند سیمه برای مدل‌سازی فرکانس بالای ترانسفورماتورهای چند سیم‌پیچه دوطبقه برای اولین بار پیشنهاد شده است. در این مدل، تمام دورها در دیسک‌ها و لایه‌ها در نظر گرفته شده است و پارامترهای مدل توسط روش اجزای محدود محاسبه شده است. به منظور ارزیابی مدل پیشنهادی، نتایج بدست آمده با نتایج مدل اجزای محدود و تزویج میدان- مدار مقایسه شده است. مقایسهٔ نتایج نشان می‌دهد که مدل معرفی شده از دقت خوبی برخوردار بوده و می‌تواند برای مدل سازی ترانسفورماتورهای چندسیم‌پیچه دوطبقه در حوزه‌های فرکانسی مختلف مورد استفاده قرار گیرد. همچنین با استفاده از مدل خط انتقال چند سیمه تأیید شده، پاسخ فرکانسی ترانسفورماتور چند سیم‌پیچه دو طبقه و خطای اتصال کوتاه دیسک به دیسک مورد آنالیز قرار گرفته است.

IJE TRANSACTIONS C: Aspects Vol. 34, No. 6, (June 2021) 1495-1504

International Journal of Engineering

Journal Homepage: www.ije.ir

A Mathematical Model for a Blood Supply Chain Network with the Robust Fuzzy Possibilistic Programming Approach: A Case Study at Namazi Hospital

S. Tadarok[a], M. B. Fakhrzad*[a], M. Jokardarabi[a], A. Jafari-Nodoushan[b]

[a] *Department of Industrial Engineering, Faculty of Engineering, Yazd University, Yazd, Iran*
[b] *Department of Industrial Engineering, Faculty of Engineering, Meybod University, Meybod, Iran*

PAPER INFO

Paper history:
Received 13 March 2021
Received in revised form 29 April 2021
Accepted 4 May 2021

Keywords:
Blood Supply Chain
Integer Programming
Chance Constraint
Uncertainty
Robust Fuzzy Possibilistic

ABSTRAC

The main challenge in blood supply chain is the shortage and wastage of blood products. Due to the perishable characteristics of this product, saving a large number of blood units on inventory causes the spoil of these limited and infrequent resources. On the other hand, a lack of blood may lead to the cancellation of health-related critical activities, and the result is a potential increase in mortality in hospitals. In this paper, an integer programming model was proposed to minimize the total cost, shortage, and wastage of blood products in Namazi hospital by considering the different types of blood groups. The parameters in the real-world are uncertain, and this problem will be examined in the paper. The robust fuzzy possibilistic programming approach is presented, and a numerical illustration of the Namazi hospital is used to show the application of the proposed optimization model. Sensitivity analysis is conducted to validate the model for problems such as certainty level, coefficient weight, and penalty value of the objective function in the robust fuzzy possibilistic programming. The numerical results imply the model is able to control uncertainty and the robustness price is imposed on the system; therefore, the value of the objective function in the robust fuzzy possibilistic is 80% lower than probabilistic.

***doi**: 10.5829/ije.2021.34.06c.13*

NOMENCLATURE

Indeces		cpu_{tf}	Maximum capacity of the hospital for blood group *f* in period *t*
i	Production life span	M	Big number
t	Time period	θ_{itf}	The fraction of hospital blood orders at age *i* days, period *t* and the blood group *f* $0 \leq \theta_{(i.t.f)} \leq 1$
f	Blood groups	**Variables**	
Parameters		ss_{itf}	Confidence in the blood group *f* in period *t* with the age of *i* day
$\tilde{p}$	Shortage cost	u_{tf}	The amount of lesions in the blood group *f* in period *t*
$\tilde{c}$	Purchasing cost	Q_{tf}	The level of the blood group *f* deficiency in the period *t*
$\tilde{w}$	Wastage cost	ϑ_{itf}	End-of-life inventory of the blood group *f* in period *t* with the age of *i* day
$\tilde{h}$	Holding cost	O_{tf}	The rate of hospital orders to the blood group *f* in the period *t*
$\widetilde{D_{tf}}$	The demand of hospital blood group f in period t	E_{itf}	The blood group *f* received at the beginning of period *t* with the age of *i* day
$\widetilde{cap}_{tf}$	Blood centers' capacity in period *t* and the blood group *f*	Y_{itf}	A binary variable that is 1 if the patient satisfies blood from the blood group *f* in the period *t* with the age of *i* days, otherwise 0.

1. INTRODUCTION

The blood supply chain is one of the few supply chains that are also in the supply sector. In addition, it is in high uncertainty in the demand segment. This complicates the management and planning of current affairs in this supply chain [1]. On the other hand, blood products are related to the health and lives of people and management of them

*Corresponding Author Institutional Email: *mfakhrzad@yazd.ac.ir* (M. B. Fakhrzad)

Please cite this article as: S. Tadarok, M. B. Fakhrzad, M. Jokardarabi, A. Jafari-Nodoushan, A Mathematical Model for a Blood Supply Chain Network with the Robust Fuzzy Possibilistic Programming Approach: A Case Study at Namazi Hospital, International Journal of Engineering, Transactions C: Aspects Vol. 34, No. 6, (2021) 1495-1504

has a high sensitivity; so, that the occurrence of the smallest disruption in the management of supply chain issues will result in irreparable damage [2]. In recent years, the blood supply chain has been a focus of attention due to the importance of this vital product and scarce in health systems. Providing healthy blood and enough and also its management has been from particular concern for the human race, hence the collection and management of blood distribution which is proposed in the form of supply chain management requires comprehensive and accurate management and planning. The blood supply chain has complexities so that it is distinguished from the supply chain of ordinary commodities. Blood is one of the most crucial corrosive substances in nature, which is closely related to the lives of humans. One of the most important reasons for blood and blood products is its human origin, and artificially can not be produced. In addition, blood products such as red blood cells, platelets, and plasma have a different life span and require special conditions for maintenance. On the other hand, the blood supply chain, which involves processes for collection, production, storage, and distribution of blood and blood products from donors to blood recipients, is associated with uncertainty. This uncertainty in the supply and demand process is evident because blood supply from donors is relatively unplanned and uncertain, and demand for the product is not stable. Uncertainty in supply chain issues plays a crucial role in economic performance. Therefore, adjustment of supply and demand in the blood supply chain requires the design of the appropriate supply chain network to supply blood and blood derivatives.

Robust optimization optimizes at worst so that a robust approach to optimization problems has been used since the early 1970s. It has recently been studied widely [3]. Alem and Morabito [4] cited two reasons for using robust optimization. At first robust optimization is easier than possible approaches to solve the model. Also, given that we do not need explicit knowledge of data under cognitive uncertainty, historical data, and in some cases, the experiences of decision-makers can be used to infer the uncertainty interval. The reasons for the superiority of robust possibilistic programming are compared to possibilistic programming as follows [5].

1. In robust optimization, the final answer has the stability of being optimal and stable.

2. In robust optimization, the level of confidence in satisfying the constraints is determined by the model itself and its value is optimal.

3. According to the deviations of the objective function due to the uncertainty of the parameters will be prevented heavy and irreparable costs for managers and organizations. However, it is not paid much attention to the mentioned cases in the possibilistic programming approach [6]. Therefore this paper proposes robust possibilistic programming (RPP) to solve the problem, which has a considerable superiority when compared to a certain model.

In the next section, the literature review is addressed. The problem definition and mathematical model are presented in sections 3 and 4, respectively. The computational results and sensitivity analysis are mentioned in section 5. The conclusion and future research of the paper are finally indicated in section 6.

2. LITERATURE REVIEW

Brief literature is reviewed about the blood supply chain with solution methods and algorithms that are used to solve the problem. Ghandforoush and Sen [7] developed a review of some of the tactical and operational aspects of the collection, production, control of the inventory, the policy of shipment blood products, and delivery decisions. Haijema et al. [8] investigated a dynamic Markov and a simulation approach which two types of demand are presented in accordance with different types of patients and scarcity and waste is minimized. Ghandforoush and Sen [7] presented a system of initial decision support according to an unconfirmed integer programming in order to help regional blood transfusion centers to generate and collect platelets daily. The aim is to minimize the total daily cost including collection, production, and costs of shortages. They concluded that the supply and production should be on demand. Osorio et al. [9] have paid little attention to the relationship between the various stages of the supply chain and many single-level papers have been reviewed. Mansoori et al. [10] presented a bi-objective location-allocation model for blood supply under uncertainty. The objectives are minimizing the blood shortage in blood centers and also minimizing the operational costs including cost of transporting temporary blood facilities and the cost of blood collection and transportation in a multi-period context. They used the robust optimization approach in the model. Civelek et al. [11] presented a periodic inventory management system for platelet inspection so that demand varies from one age to another. The aim is to minimize the inventory, wastage, and shortage costs. Abdulwahab and Wahab [12] proposed a collection of methods used for vendor problems and linear programming in the blood bank inventory model and other methods of inventory. Abbasi and Hosseinifard [13] presented a model to evaluate the release of platelets and red blood cells in the blood supply service by using queuing theory. Pishvaee and Torabi [14] specified that traditional models can not apply the precision and logic of classical mathematical alone. Asadpour et al. [2] addressed a blood supply chain network with backup facilities and expiration date. They proposed a bi-

objective Mixed Integer Programming where the objectives are to minimize the total cost and detrimental environmental impacts.

The model is not real when uncertainty is ignored due to its structure. Conceptual concepts can not show some uncertainties; therefore, the theory of fuzzy sets has been introduced to express the uncertainties since 1980. Fuzzy concepts are the creation of the ability to definition ambiguous, inattentive, and unpleasant parameters that are defined based on personal beliefs [15]. Tanthatemee et al. [16] presented a single-product fuzzy inventory control system and a permanent overview. The presented model is based on the fuzzy logic control system for uncertain demand and resource availability. Selim and Ozkarahan [17] proposed an integrated multi-objective fuzzy scheduling model for designing a chain-of-distribution network. Handfield et al. [18] developed a model (Q, r) that Fuzzy concepts have been used to illustrate uncertainty of sources in a supply chain. Rajendran and Ravindran [19] developed stochastic models under uncertain demand for a single hospital. The models aimed to propose ordering policies to reduce shortage, wastage and purchase for different cost settings. Dilano et al. [20] proposed a two-stage stochastic programming model for explaining optimal periodic review policies for red blood cells inventory management. The objective is to minimize the operational costs, shortage and wastage by taking into account perishability and uncertain demand. Oserio et al. [21] developed integrated simulation-optimization model to account for uncertain supply and demand, blood group proportions, shelf life constraints, different collections and production methods in the blood supply chain.

Pishvaei et al. [22] presented a robust programming model for a supply chain network with social responsibility. They proposed a new approach and implemented the model under different assumptions and compared the performance of them. Zahiri et al. [23] proposed a model of robust possibilistic programming for location-allocation of organ transplant centers under the uncertainty. They used minimal costs to enhance the impact of their network design. Safaei et al. [24] formulated a closed-loop supply chain (CLSC) for the cardboard recycling network under the uncertainty of demand to maximize total profit. They used a robust optimization approach in the proposed mixed integer linear programming (MILP) model to combat uncertainty. Selma et al. [25] proposed a general MILP model for the multi-objective CLSC network due to the uncertainty of product demand. Haghjoo et al. [26] presented a a dynamic robust location–allocation model for designing a blood supply chain network under facility disruption risks and uncertainty in a disaster situation. Eskandari-Khanghahi et al. [27] developed a possibilistic optimization model for a multi-period and multi-objective sustainable blood supply chain with uncertain data where the objectives are to minimize the total cost, environmental effects and maximize the sicial effects. Kazemi et al. [28] addressed blood inventory-routing problem under uncertainty and developed a mixed integer programming formulation for the problem. Zahiri and Pishvaee [29] studied blood supply chain network design under uncertainty and developed a bi-objective mathematical programming model which minimizes the total cost as well as the maximum unsatisfied demand. Ghahremani-Nahr et al. [30] proposed a MINLP location-allocation model to design a closed-loop green supply chain under uncertainty with robust fuzzy mathematical programming and solved the model with the Wall optimization algorithm.

Although some researchers have studied uncertainty in their problems, but this uncertainty is limited to some parameters like demand. In this research, all parameters such as cost, demand and capacity are assumed uncertain and trapezoidal fuzzy distribution is considered for the uncertain parameters. A robust fuzzy possibilistic programming are used to address the uncertainty. Also, according to literature review consideration of all blood groups and expiration date simultaneously is the first study in this filed.

3. PROBLEM DEFINITION

In this paper, a blood supply chain considering different types of blood groups (O+, O-, A+, A, B+, B, AB+, AB) and expiration date has been designed simultaneously. This makes the demand for blood in the hospital more efficient and can prevent the risk of blood transfusions to patients with a variety of blood groups. It also simplifies blood demand and the blood is delivered to the hospital from the blood centers without the test of compatibility so that the hospital performs the test.The supply chain of blood consists of three levels. The first level is donors who want to donate the blood to a mobile or fixed unit of the blood transfusion organization in the city. The second level in the chain is the test and production of blood products that are performed by blood test and blood test laboratories. The third level of the chain is the distribution of blood products.

In order to design the supply chain, an initial mathematical model is proposed to minimize the total cost, shortage, and wastage in blood supply chain of Namazi hospital by considering the different types of blood groups. The model has non-deterministic parameters. Therefore, the primary model is transformed into a model with some non-deterministic parameters. A chance constraint approach and robust possibilistic programming are used to address the uncertainty. After a full explanation of the approach, we introduce a new definitive and real world model that is called the second model. The model includes the objective function and the

constraints of the first model but the trapezoidal fuzzy distribution is considered for the uncertain parameters of the problem. The assumptions considered in the model of the problem are as follows:

- all blood groups are considered
- The capacity of blood centers is limited.
- The delivery time for blood supply is zero.
- The age of blood transmitted from the blood transfusion organization is known and changes over time.
- The life of red blood cells is limited and it is 35 days which is 2 days to test.
- The policy used to send the blood is the original FIFO.
- If the demand is not met, we will be in deficit.
- If the blood expires, we will have a lost cost.
- The reviewed model is a single product and a multi-period.
- The maximum hospital blood bank capacity is predetermined.

3. 1. Mathematical Model In this section, a nonlinear integer programming model is derived from Gunpinar and Centeno [30]. In the second model, some parameters in the objective function, the technical coefficients, and the right values of some of the constraints are ambiguous therefore it is necessary to further explain. The definite model that is presented in this section is a nonlinear programming model and will be converted to a linear model. The proposed model is known NP-hard. Therefore, several algorithms are proposed to reduce the solution time for the model that will be described completely in separate sections. The mathematical model are presented and described as follows:

Objective function

$$\text{Min z} = \sum_{t=1}^{T}\sum_{f=1}^{8}\tilde{C} * O_{tf} + \sum_{i=1}^{I}\sum_{t=1}^{T}\sum_{f=1}^{8}\tilde{H} * \vartheta_{itf} + \sum_{t=1}^{T}\sum_{f=1}^{8}\tilde{W} * u_{tf} + \sum_{t=1}^{T}\sum_{f=1}^{8}\tilde{P} * Q_{tf} \quad (1)$$

Constraints

$$\sum_{f=1}^{8} O_{(t.f)} \le \sum_{f=1}^{8} Cap_{(t.f)} \quad \forall t \quad (2)$$

$$\sum_{i}(V_{i,t-1.f} + SS_{i,t.f} + e_{i,t.f}) \le cpu_{t.f} \quad \forall t, f \quad (3)$$

$$E_{(i.t.f)} = 0 \qquad \forall t.f.i = 1.2 \quad (4)$$

$$E_{(i.t.f)} = O_{(t.f)} * \theta_{(i.t.f)} \qquad \forall t.f.i \ge 3 \quad (5)$$

$$Y_{(i.t.f)} \ge Y_{(i-1.t.f)} \qquad \forall t.f.i \ge 3 \quad (6)$$

$$D_{(t.f)} = \sum_{i=3}^{I}\left[\left(\vartheta_{(i-1.t-1.f)} + E_{(i.t.f)}\right) * Y_{(i.t.f)} - ss_{(i.t.f)}\right] + Q_{(t.f)} \qquad \forall t.f \quad (7)$$

$$\left(Y_{(i.t.f)} - Y_{(i-1.t.f)}\right) * \begin{pmatrix}\vartheta_{(i-1.t-1.f)} + \\ E_{(i.t.f)}\end{pmatrix} \ge ss_{(i.t.f)} \quad \forall t.f.i \ge 3 \quad (8)$$

$$D_{(t.f)} - \sum_{i=3}^{I}\left[\vartheta_{(i-1.t-1.f)} + E_{(i.t.f)}\right] \le Q_{(t.f)} \quad \forall t.f \quad (9)$$

$$Y_{(i.t.f)} = 0 \qquad \forall t.f.i = 1.2 \quad (10)$$

$$\vartheta_{(i.t.f)} = \left(1 - Y_{(i.t.f)}\right) * \left(\vartheta_{(i-1.t-1.f)} + E_{(i.t.f)}\right) + \left(Y_{(i.t.f)} - Y_{(i-1.t.f)}\right) * ss_{(i.t.f)} \qquad \forall t.f.i \ge 3 \quad (11)$$

$$\vartheta_{(i.t.f)} = 0 \qquad \forall t.f.i = 1.2 \quad (12)$$

$$\vartheta_{(i.0.f)} = 0 \qquad \forall i.f \quad (13)$$

$$U_{(t.f)} = \vartheta_{(35.t.f)} \qquad \forall t.f \quad (14)$$

$$ss_{(i.t.f)}.\ U_{(t.f)}.\ Q_{(t.f)}.\ \vartheta_{(i.t.f)}.\ O_{(t.f)}.\ E_{(i.t.f)} \in \mathrm{Z}^{+} \quad (15)$$

$$Y_{(i.t.f)} \in \{0.1\} \quad (16)$$

The objective function of the problem consists of the cost of maintenance, waste, shortage, and purchasing shown in equation (1). Equation (2) indicates that the capacity of the blood center (supplier) is limited so that hospital demand cannot exceed the capacity of the blood centers. Equation (3) ensures that the amount of blood in the hospital cannot exceed the hospital's blood bank capacity. Constraints (4) and (5) ensure that the hospital never receives a unit of blood that one or two days left in its life span (since it takes 2 days to complete the test in a blood bank). Equation (6) shows the FIFO policy for blood delivery. Equation (7) responding to demand when blood supply is more than demand. In this case, the amount of blood in the system for all ages of blood in each period and each blood group is checked to see if it is used and we reduce the amount of confidence, then reduce the amount of deficiency which is continuously checked into the system to this value. Equation (8) implies that the value of the quantitative variable of confidence does not exceed the available blood units in its age group. Constraint (9) is intended to control the amount of blood deficiency and constraint (10) shows the allocation of blood units to each age group and also the amount of blood received from each blood group in each period. Equation (11) shows the level of inventory of the end of the blood cycle for each age group in each period. Constraint (12) ensures that two days of blood is not available in the stock. Constraint (13) specifies that no inventory is available at the beginning of the analysis period. Equation (14) shows the rate of hospital waste at the end of each course. The rest of the equations show the condition of the variables and parameters.

3. 2. Linearization of the Model Equations (7), (8) and (11) are nonlinear which leads to the complexity of the model. However, using the auxiliary variables and applying some additional constraints, the extracted model can be converted to the linear model. The linearization procedure is described below.

There is a continuous variable x and binary variable y so that variable α will be defined as nonlinear variable from multiply x by y according to Equation (17).

$$\alpha = X * y \tag{17}$$

For the linearization of the Equation (17), three constraints are added instead of it as follows [30]. The three add-ons to the model ensure that if y is zero, the variable α will equal to zero. Otherwise, if y is equal one then the variable α will equal x according to Equations (18) to (20). The limitations are linearized that Gupte et al., is using [31].

$$\alpha \leq M * y \tag{18}$$

$$\alpha \leq X \tag{19}$$

$$\alpha \geq X - M(1 - y) \tag{20}$$

3. 3. Chance Constraint Programming In order to face uncertainty, several approaches have been developed in mathematical optimization problems such as randomization, fuzzy optimization, robust optimization, and hybrid approaches. In this section, the model and concepts are derived from the paper by Pishvaee and Torabi [14] Fuzzy programming models use fuzzy confidence coefficients and membership functions to express the lack of knowledge about the parameters and are divided into possibilistic and flexible programming.

In probable planning, the lack of knowledge about the exact amounts of the model parameters with probabilistic distribution functions is modeled using available target data and decision-making knowledge. In flexible programming, the objective function and constraints are used to control the uncertainty of the flexible value, and modeling will be based on fuzzy sets or priorities. In the paper, probabilistic planning of the limits of chance is used to address the uncertainty of the various parameters in the problem.

The chance constraint method is one of the primary techniques for solving optimization problems under various uncertainties. This formulation method is an optimization problem that assures that the probability of a specific limit is higher than a certain level. In other words, it restricts space to a high level of confidence. In particular, the distribution of trapezoidal probability according to Figure 1, is used to represent non-deterministic parameters in the proposed model. For a more detailed and simplistic introduction, the compact

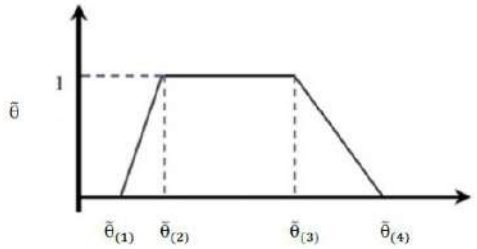

Figure 1. trapezoidal fuzzy distribution

form of the proposed model is presented as follows:

Objective function

$$Min\ Z = fy + cx \tag{21}$$

Subject to:

$$Ax \geq d$$
$$Bx = d$$
$$Sx \leq Ny$$
$$Y_{i,t,f} \in \{0,1\}$$
$$x \geq 0$$

Assume that the vector f (fixed cost) is a definite parameter, and the vectors c (variable costs) and d (hospital demand) and the matrix of coefficients N (capacity of facilities) are unknown parameters of the problem. To build a basic fuzzy programming curve, chance constraint, we use the "expected value" factor to non-deterministic model parameters of the objective function and the necessity (Nec) scale for modeling losing constraints. The Nec scale can be applied directly to convert the fuzzy odds limits to equivalent equations.

Subject to:

$$Nec\{Ax \geq \tilde{d}\} \geq \alpha_m \qquad \forall m \in M$$
$$Nec\{Bx = \tilde{d}\} \geq \alpha_m \qquad \forall m \in M$$
$$Nec\{Sx \leq \tilde{N}y\} \geq \alpha_m \qquad \forall m \in M \tag{22}$$
$$Y \in \{0,1\}$$
$$x \geq 0$$

Since the objective function and constraints have non-deterministic parameters and are considered by fuzzy distributions, and the constraints with non-deterministic parameters must be formed with the minimum level of α_i, the model Definite can be defined as follows:

Objective function

$$\text{Min } E[Z] = fy + \left(\frac{c_{(1)}+c_{(2)}+c_{(3)}+c_{(4)}}{4}\right) x$$

Subject to:

$$Ax \geq (1-\alpha_m)\, d_{(3)} + \alpha_m d_{(4)}$$

$$Bx \leq (\frac{\alpha_m}{2})\, d_{(3)} + (1-\frac{\alpha_m}{2})\, d_{(4)}$$

$$Bx \geq (\frac{\alpha_m}{2})\, d_{(2)} + (1-\frac{\alpha_m}{2})\, d_{(1)} \quad (23)$$

$$Sx \leq [(1-\alpha_m)\, N_{(2)} + \alpha_m N_{(1)}]Y$$

$$Y \in \{0,1\}$$

$$x \geq 0$$

According to the said articles, the definitive equivalent model of the proposed model will be as follows:

$$\text{Nec}\{\sum_{f=1}^{8} O_{(t.f)} \leq \sum_{f=1}^{8} \widetilde{CAP_{(t.f)}}\} \geq \alpha_1 \quad (24)$$

$$\text{Nec}\{\widetilde{D_{(t.f)}} = \sum_{i=3}^{I}\left[\left(\vartheta_{(i-1.t-1.f)} + E_{(i.t.f)}\right) * Y_{(i.t.f)} - ss_{(i.t.f)}\right] + Q_{(t.f)}\} \geq \alpha_2 \quad (25)$$

$$\text{Nec}\{\widetilde{D_{(t.f)}} \leq Q_{(t.f)} + \sum_{i=3}^{I}(\vartheta_{(i-1.t-1.f)} + E_{(i.t.f)})\} \geq \alpha_3 \quad (26)$$

The definition of the limits of this section is the same as in the previous section, and we included uncertainty in only three constraints that included demand and capacity. The objective function, like the last section, minimizes the available costs.

Objective function

$$MinE[Z] = \sum_{t=1}^{T}\sum_{f=1}^{8}\left(\frac{C1+C2+C3+C4}{4}\right) * O_{tf} + \sum_{i=1}^{I}\sum_{t=1}^{T}\sum_{f=1}^{8}(\frac{H1+H2+H3+H4}{4}) * \vartheta_{(i.t.f)} + \sum_{t=1}^{T}\sum_{f=1}^{8}\left(\frac{W1+W2+W3+W4}{4}\right) * u_{(t.f)} + \sum_{t=1}^{T}\sum_{f=1}^{8}(\frac{P1+P2+P3+P4}{4}) * Q_{(t.f)} \quad (27)$$

Subject to:

$$\sum_{f=1}^{8} O_{(t.f)} \leq [(1-\alpha_1) * \sum_{f=1}^{8} CAP_2 + \alpha_1 * \sum_{f=1}^{8} CAP_1] \quad \forall t \quad (28)$$

$$\sum_i (V_{i,t-1.f} + SS_{i,t.f} + e_{i,t.f}) \leq cpu_{t.f} \quad \forall t, f \quad (29)$$

$$E_{(i.t.f)} = 0 \quad \forall t.f.i = 1.2 \quad (30)$$

$$E_{(i.t.f)} = O_{(t.f)} * \theta_{(i.t.f)} \quad \forall t.f.i \geq 3 \quad (31)$$

$$Y_{(i.t.f)} \geq Y_{(i-1.t.f)} \quad \forall t.f.i \geq 3 \quad (32)$$

$$\sum_{i=3}^{I}\left[\alpha_{(i.t.f)} + \beta_{(i.t.f)} - ss_{(i.t.f)}\right] + Q_{(t.f)} \leq \left[\left(\frac{\alpha_2}{2}\right) * D_{3(t.f)} + \left(1-\frac{\alpha_2}{2}\right) * D_{4(t.f)}\right] \quad \forall t.f.i \geq 3 \quad (33)$$

$$\sum_{i=3}^{I}\left[\alpha_{(i.t.f)} + \beta_{(i.t.f)} - ss_{(i.t.f)}\right] + Q_{(t.f)} \geq \left[\left(\frac{\alpha_2}{2}\right) * D_{2(t.f)} + \left(1-\frac{\alpha_2}{2}\right) * D_{1(t.f)}\right] \quad \forall t.f.i \geq 3 \quad (34)$$

$$\alpha_{(i.t.f)} + \beta_{(i.t.f)} - \mu_{(i.t.f)} - \varphi_{(i.t.f)} \geq ss_{(i.t.f)} \quad \forall t.f.i \geq 3 \quad (35)$$

$$[(1-\alpha_3) * D_{3(t.f)} + \alpha_3 * D_{4(t.f)}] \leq Q_{(t.f)} + \sum_{i=3}^{I}\left[\vartheta_{(i-1.t-1.f)} + E_{(i.t.f)}\right] \quad \forall t.f \quad (36)$$

$$Y_{(i.t.f)} = 0 \quad \forall t.f.i = 1.2 \quad (37)$$

$$\vartheta_{(i.t.f)} = \vartheta_{(i-1.t-1.f)} + E_{(i.t.f)} - \alpha_{(i.t.f)} - \beta_{(i.t.f)} + \Delta_{(i.t.f)} - \gamma_{(i.t.f)} \quad \forall t.f.i \geq 3 \quad (38)$$

$$\vartheta_{(i.t.f)} = 0 \quad \forall t.f.i = 1.2 \quad (39)$$

$$\vartheta_{(i.0.f)} = 0 \quad \forall t.f.i = 1.2 \quad (40)$$

$$U_{(t.f)} = \vartheta_{(35.t.f)} \quad \forall t.f \quad (41)$$

$$ss_{(i.t.f)}.\ U_{(t.f)}.\ Q_{(t.f)}.\ \vartheta_{(i.t.f)}.\ O_{(t.f)}.E_{(i.t.f)}.\ \gamma_{(i.t.f)}.\Delta_{(i.t.f)}.\ \varphi_{(i.t.f)}.\mu_{(i.t.f)}.\ \beta_{(i.t.f)}.\ \alpha_{(i.t.f)} \in Z^{+} \quad (42)$$

$$Y_{(i.t.f)} \in \{0.1\} \quad (43)$$

3. 4. Robust Fuzzy Possibilistic Similar to the chance constraint possibilistic model, the first part in the objective function is the expected value of z "E[z]". The second part of the objective function is the difference between the maximum and minimum possible values of z based on trapezoidal distribution. The method finds the desired value for the confidence levels, and the confidence levels are considered as a variable. In the model, the coefficient γ indicates the significance of the difference between the minimum and maximum values of the objective function and can be used in the range of [0,1]. Therefore, the presence of the section in the target function leads to a minimization of the maximum deviation of the maximum and minimum optimal values of z. It is worth noting that this optimally stable part controls the answer to the problem.

The third part, added to the objective function, indicates the level of confidence in any random constraint in which the penalty for deviating from the limit values is the uncertain parameters. It shows the difference between the worst value of the uncertain parameter and the value used in the random constraint. Therefore, using the part, the condition of the answers will be established. It should be noted that in the stable model, the expression γ (z_{max}, E[z]) minimizes the maximum deviation of the highest and lowest optimal expected value of the objective function, but in some cases, the decision-maker only select one of these. Two values of sensitivity deviation are shown as follows.

$$
\begin{aligned}
&min\, E[Z] + \gamma(z_{max} - E[z]) + \delta\big(d_{(4)} - (1-\alpha)d_{(3)} - \alpha d_{(4)}\big) + \varphi\big[\big(\beta N_{(1)} + (1-\beta)N_{(2)} - N_{(1)}\big)\big]\\
&Ax \geq (1-\alpha)d_{(3)} + \alpha d_{(4)}\\
&Bx \leq \left(\frac{\alpha_m}{2}\right) d_3 + (1 - \frac{a_m}{2}) d_4\\
&Bx \geq \left(\frac{\alpha_m}{2}\right) d_2 + (1 - \frac{a_m}{2}) d_1 \qquad (44)\\
&Sx \leq [\beta N_{(1)} + (1-\beta)N_{(2)}]\\
&Tx \leq 1\\
&Z_{max} = f_4 * x + c_4 * y\\
&x \geq 0.\ \ 0\cdot 5 \leq \alpha.\beta \leq 1
\end{aligned}
$$

Therefore, the complete model is as follows so that the constraints are like 28-43.

Objective function

$$
\begin{aligned}
&MinE[Z] = \sum_{t=1}^{T}\sum_{f=1}^{8}\left(\frac{C1+C2+C3+C4}{4}\right) * O_{tf} +\\
&\sum_{i=1}^{I}\sum_{t=1}^{T}\sum_{f=1}^{8}\left(\frac{H1+H2+H3+H4}{4}\right) * \vartheta_{(i.t.f)}\\
&+ \sum_{t=1}^{T}\sum_{f=1}^{8}\left(\frac{W1+W2+W3+W4}{4}\right) * u_{(t.f)} +\\
&\sum_{t=1}^{T}\sum_{f=1}^{8}\left(\frac{P1+P2+P3+P4}{4}\right) * Q_{(t.f)} +\\
&\gamma\left[\sum_{t=1}^{T}\sum_{f=1}^{8} C_4 * O_{tf} + \sum_{i=1}^{I}\sum_{t=1}^{T}\sum_{f=1}^{8} H_4 * \vartheta_{(i.t.f)} + \sum_{t=1}^{T}\sum_{f=1}^{8} W_4 * u_{(t.f)} + \sum_{t=1}^{T}\sum_{f=1}^{8} P_4 * Q_{(t.f)}\right) - \sum_{t=1}^{T}\sum_{f=1}^{8}\left(\frac{C1+C2+C3+C4}{4}\right) * O_{tf} +\\
&\sum_{i=1}^{I}\sum_{t=1}^{T}\sum_{f=1}^{8}\left(\frac{H1+H2+H3+H4}{4}\right) * \vartheta_{(i.t.f)} +\\
&\sum_{t=1}^{T}\sum_{f=1}^{8}\left(\frac{W1+W2+W3+W4}{4}\right) * u_{(t.f)} +\\
&\sum_{t=1}^{T}\sum_{f=1}^{8}\left(\frac{P1+P2+P3+P4}{4}\right) * Q_{(t.f)}\Big] + \delta_1 \sum_{t.f}\left(\left(1 - \frac{\alpha_2}{2}\right) d_{(4)tf} - \frac{\alpha_2}{2} d_{(3)tf} - d_{(3)tf}\right) + \delta_2 \sum_{t.f}\left(d_{(2)tf} - \left(1 - \frac{\alpha_2}{2}\right) d_{(1)tf} - \frac{\alpha_2}{2} d_{(2)tf}\right) + \delta_3 \sum_{t.f}\big(d_{(4)tf} - (1-\alpha_3)d_{(3)tf} - \alpha_3 d_{(4)tf}\big) + \delta_4 \sum_{t.f}\left((1-\alpha_1)cap_{(2)tf} + \alpha_1 cap_{(1)tf} - cap_{(1)tf}\right)
\end{aligned} \qquad (44)
$$

4. COMPUTATIONAL RESULTS

In this section, a numerical example from the Namazi hospital is presented to study the efficiency of the proposed model. Both programming and scheduling programs are coded with GAMS software using the CPLEX solver. It should be noted that all the necessary tests were performed on a CORE i5 computer with 1 T of RAM. The formulation of the described chain involves a large number of definite and non-deterministic parameters. Therefore, displaying all parameters is not possible due to space constraints. As a result, some essential uncertain parameters such as customer demand, shortage, holding, wastage, and purchasing costs, the capacity of the blood center and maximum hospital capacity are presented in Tables 1, 2, and 3, respectively.

To investigate the effect of the three factors of demand, the maximum capacity, and the shortage cost, various issues have been considered in which two factors are considered constant and the other one is considered variable. Figures 2 to 4 show how the objective function changes in relation to maximum capacity, demand, and shortage cost where scale objective function values according to Million. Figure 2 show the objective function changes are very high about the amount of demand, while the sensitivity of the objective function to the maximum capacity is small and negligible based on Figure 2.

TABLE 1. Fuzzy Demand for each blood group

Blood group	Demand
O^+	(15,22,28.35)
O^-	(5,7,9,11)
A^+	(8,12,17,21)
A^-	(1,2,3,4)
B^+	(11,15,20,24)
B^-	(0,1,2,3)
AB^+	(0,2,4,6)
AB^-	(1,2,3,4)

TABLE 2. Fuzzy costs

Purchasing cost	(30000,35000,40000,45000)
Holding cost	(3000,4000,5000,6000)
Wastage cost	(3000,5000,7000,9000)
Shortage cost	(400000,500000,600000,700000)

TABLE 3. Fuzzy Capacity blood center for each blood group

Blood group	Capacity
O^+	(221,231,241,251)
O^-	(190,218,230,240)
A^+	(185,192,200,207)
A^-	(175,185,195,205)
B^+	(180,190,200,210)
B^-	(170,180,190,200)
AB^+	(143,150,157,202)
AB^-	(132,138,144,152)

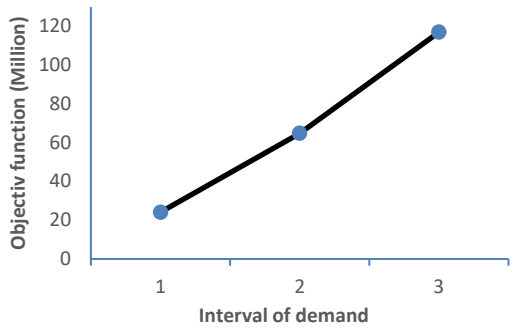

Figure 2. Objective function changes with increasing demand

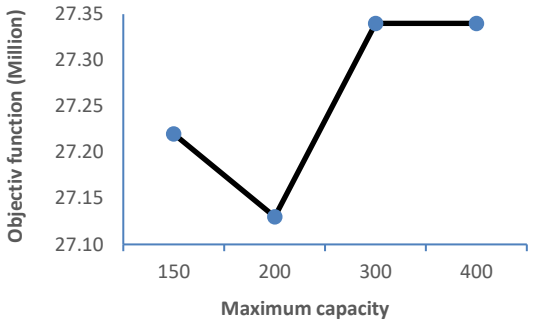

Figure 3. Objective function changes with increasing maximum capacity

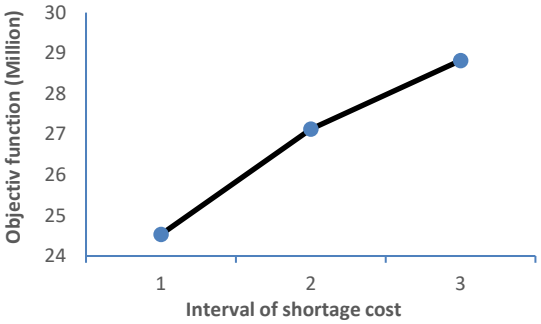

Figure 4. Objective function changes with increasing shortage cost

The objective function changes with respect to increasing maximum capacity is shown in Figure 3. As shown in Figure 4 the objective function increases with increasing shortage cost.

Figure 5 also shows the comparison of the objective function obtained from the problem taking into different values of α_i. According to the Figure 5, the objective function increases with increasing α-values. Based on this diagram, it can be concluded that with increasing values of α_i, the scope of the restrictions will be smaller, and thus the value of the objective function increases.

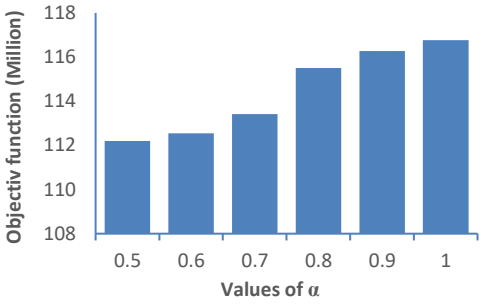

Figure 5. Objective function changes with increasing α_i

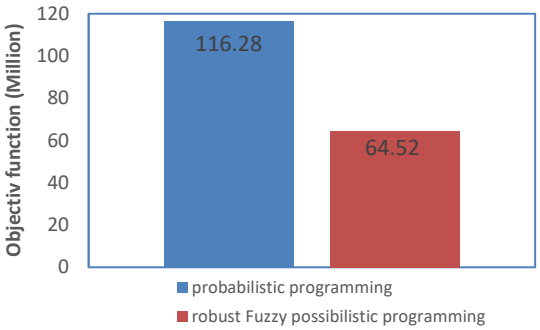

Figure 6. Comparison of the objective function of two models

Figure 6 illustrates the value of robust fuzzy possibilistic programming objective function with maximum confidence level α is less than the value of probabilistic programming objective function with the lowest level of penalty γ coefficient.

As shown in Table 4 the value of the objective function and run time of the problem is escalating with increasing the penalty coefficient. As can be seen, α_2 and α_3 have a value of 0.5 which indicates the high risk of the restriction and a low level of confidence. Therefore, the decision-maker must be risk-free against this constraint. In this case, the decision-maker must consider the maximum amount of demand so that we are less deficient in a crisis.

TABLE 4. Sensitivity analysis on weight factor parameter γ

$\delta_1.\delta_2.\delta_3.\delta_4 = 10$					
γ = 0.3		**γ = 0.6**		**γ = 0.9**	
Run time (s)	60	Run time (s)	79	Run time (s)	95
E[Z]	66/77	E[Z]	71/67	E[Z]	75/99
α_1	1	α_1	1	α_1	1
α_2	0.5	α_2	0.5	α_2	0.5
α_3	0.5	α_3	0.5	α_3	0.5

5. CONCLUSION

In the paper, we will focus on a single-level inventory model for blood supply chain in the Namazi hospital and an optimization model designed to manage the resources of the hospital that ultimately reduce costs and improves patient services. The focus of this study is on the whole blood because its demand is higher and it is a non-replaceable substance. We used integer programming to the model. The first model was a nonlinear definite model which we linearized it. The second model was an uncertain model that was more closely related to the real world and solved it by a robust fuzzy possibilistic method.

The examined model was a single-product and multi-cycle model. The delivery time for blood supply was zero and the blood centers were limited and the policy was to send the product using the FIFO principle. By reducing the maximum capacity, you can not order a lot because less blood can be stored, so there will be shortage costs which will increase costs, as well as increased capacity will also increase orders. It imposes the cost of maintenance and waste on the system but its enormous increase does not affect the cost and costs constant because we can not be more than the capacity of the blood transfusion organization. Therefore, considering the appropriate limit for maximum capacity requires strong management. By increasing the shortage cost, the hospital maintains more blood units, therefore levels of deficiency reduces and inventory levels increases in leading to an increase in casualties and an increase in total hospital costs. The results showed with increasing demand for patients the total expected cost of the hospital increases, because the number of orders and the likelihood of deficiency to the hospital increases. In future research, we can use other optimization approaches. The following could be presented as suggested paths for future research.

- Extends the model and makes it a multi-product model, adding another level to the problem and reducing the cost of blood transfusion centers.
- Blood componenet or products e.g. platet and plasma is considered in the problem.
- A closed-loop supply chain is designed to accommodate a refund for blood that has not been used by the hospital and has expired.
- Patient satisfaction is also considered in the model.

6. REFERENCES

1. Khalifehzadeh, S., Fakhrzad, MB., A Modified Firefly Algorithm for optimizing a multi stage supply chain network with stochastic demand and fuzzy production capacity, ***Computers & Industrial Engineering,*** Vol. 133, (2019), 42-56.
2. Asadpour, M., Boyer, O., Tavakkoli-Moghaddam, R. "A Blood Supply Chain Network with Backup Facilities Considering Blood Groups and Expiration Date: A Real-world Application", ***International Journal of Engineering, Transactions B: Applications***, Vol. 34, No. 2, (2021), 470-479. doi: 10.5829/ije.2021.34.02b.19
3. Eslamipoor, R., Fakhrzad, MB., Zare Mehrjerdi, Y., A new robust optimization model under uncertainty for new and remanufactured products, ***International Journal of Management Science and Engineering Management***, Vol. 10, No. 2, (2015), 137-142.
4. Alem, D.J., Morabito, R. "Production planning in furniture settings via robust optimization", ***Computers & Operations Research***, Vol. 39, No. 2, (2012), 139-150. doi.org/10.1016/j.cor.2011.02.022
5. Nourzadeh, F., Ebrahimnejad, S., Khalili-Damghani, K., Hafezalkotob, A. "Development of a Model for Locating Hubs in a Competitive Environment under Uncertainty: A Robust Optimization Approach", ***International Journal of Engineering, Transactions A: Basics***, Vol. 33, No. 1, (2020), 124-133. doi: 10.5829/ije.2020.33.01a.14
6. Sadra Abarqhouei, N., Hosseini Nasab, H., Fakhrzad, MB., Macro ergonomics interventions and their impact on productivity and reduction of musculoskeletal disorders: including a case study, ***Iran Occupational Health***, Vol. 9, No. 2, (2012), 27-39.
7. Ghandforoush, P., Sen, T. K. "A DSS to manage platelet production supply chain for regional blood centers". ***Decision Support Systems***, Vol. 50, No. 1, (2010), 32-42. doi.org/10.1016/j.dss.2010.06.005
8. Haijema, R., der Wal, J., van Dijk, N.M. "Blood platelet production: Optimization by dynamic programming and simulation", ***Computers & Operations Research***, Vol. 34, No. 3, (2007), 760-779. doi.org/10.1016/j.cor.2005.03.023
9. Osorio, A.F., Brailsford, S.C., Smith, H.K. "A structured review of quantitative models in the blood supply chain: a taxonomic framework for decision-making", ***International Journal of Production Research***, Vol. 53, No. 24, (2015), 7191-7212. doi.org/10.1080/00207543.2015.1005766
10. Mansoori, S., Bozorgi Amiri, A., Bayatloo, F. "A Bi-Objective Robust Optimization Model for Emergency Blood Supply Network Design under Uncertainty", ***Modern Researches in Decision Making***, Vol. 3, No. 2, (2018), 249-274. https://www.sid.ir/en/journal/ViewPaper.aspx?id=791256
11. Civelek, I., Karaesmen, I., Scheller-Wolf, A. "Blood platelet inventory management with protection levels", ***European Journal of Operational Research***, Vol. 243, No. 3, (2015), 826-838. doi.org/10.1016/j.ejor.2015.01.023
12. Abdulwahab, U., Wahab, M. "Approximate dynamic programming modelling for a typical blood platelet bank", ***Computers & Industrial Engineering***, Vol. 78, No. 1, (2014), 259-270. doi.org/10.1016/j.cie.2014.07.017
13. Abbasi, B., Hosseinifard, S.Z. "On the issuing policies for perishable items such as red blood cells and platelets in blood service", ***Decision Sciences***, Vol. 45, No. 5, (2014), 995-1020. doi.org/10.1111/deci.12092
14. Pishvaee, M.S., Torabi, S.A. "A possibilistic programming approach for closed-loop supply chain network design under uncertainty", ***Fuzzy Sets and Systems***, Vol. 161, No. 20, (2010), 2668-2683. doi.org/10.1016/j.fss.2010.04.010
15. Gutiérrez, G.J., Kouvelis, P., Kurawarwala, A.A. "A robustness approach to uncapacitated network design problems", ***European Journal of Operational Research***, Vol. 94, No. 2, (1996), 362-376. doi.org/10.1016/0377-2217(95)00160-3
16. Phruksarphanrat, B., Tanthatemee, T. "Fuzzy logic approach to inventory lot-sizing problem under uncertain environment",

IAENG Transactions on Engineering Technologies, Vol. 186, (2013), 203-216. doi:10.1007/978-94-007-5651-9-15

17. Selim, H., Ozkarahan, I. "A supply chain distribution network design model: an interactive fuzzy goal programming-based solution approach", ***The International Journal of Advanced Manufacturing Technology***, Vol. 36, No. 3, (2008), 401-418. doi.org/10.1007/s00170-006-0842-6
18. Handfield, R., Warsing, D., Wu, X. "(Q, r) Inventory policies in a fuzzy uncertain supply chain environment", ***European Journal of Operational Research***, Vol. 197, No. 2, (2009), 609-619. doi.org/10.1016/j.ejor.2008.07.016
19. Rajendran, S., Ravindran, A.R. "Platelet ordering policies at hospitals using stochastic integer programming model and heuristic approaches to reduce wastage", ***Computers & Industrial Engineering***, Vol. 110, (2017), 151-164. doi.org/10.1016/j.cie.2017.05.021
20. Dillon, M., Oliveira, F., Abbasi, B. "A two-stage stochastic programming model for inventory management in the blood supply chain", ***International Journal of Production Economics***, Vol. 187, (2017), 27-41. doi.org/10.1016/j.ijpe.2017.02.006
21. Osorio, A.F., Brailsford, S.C., Smith, H.K., Forero-Matiz, S.P., Camacho-Rodríguez, B.A. "Simulation-optimization model for production planning in the blood supply chain", ***Health Care Management Science***, Vol. 20, No. 4, (2017), 548-564. doi: 10.1007/s10729-016-9370-6
22. Pishvaee, M.S., Razmi, J., Torabi, S.A., "Robust possibilistic programming for socially responsible supply chain network design: A new approach", ***Fuzzy Sets and Systems***, Vol. 206, No. 1, (2012), 1-20. doi.org/10.1016/j.fss.2012.04.010
23. Zahiri, B., Tavakkoli-Moghaddam, R., Pishvaee, M.S. "A robust possibilistic programming approach to multi-period location–allocation of organ transplant centers under uncertainty", ***Computers & Industrial Engineering***, Vol. 74, No. 1, (2014), 139-148. doi.org/10.1016/j.cie.2014.05.008
24. Safaei, A.S., Roozbeh, A., Paydar, M.M. "A robust optimization model for the design of a cardboard closed-loop supply chain", ***Journal of Cleaner Production***, Vol. 166, No. 10, (2017), 1154-1168. doi.org/10.1016/j.jclepro.2017.08.085
25. Salema, M.I.G., Barbosa-Povoa, A.P., Novais, A.Q. "An optimization model for the design of a capacitated multi-product reverse logistics network with uncertainty", ***European Journal of Operational Research***, Vol. 179, No. 3, (2007), 1063-1077. doi.org/10.1016/j.ejor.2005.05.032
26. Haghjoo, N., Tavakkoli-Moghaddam, R., Shahmoradi-Moghadam, H., Rahimi, Y. "Reliable blood supply chain network design with facility disruption: A real-world application", ***Engineering Applications of Artificial Intelligence***, Vol. 90, No. C, (2020), 103493. doi.org/10.1016/j.engappai.2020.103493
27. Eskandari-Khanghahi, M., Tavakkoli-Moghaddam, R., Taleizadeh, A.A., Hassanzadeh Amin, S. "Designing and optimizing a sustainable supply chain network for a blood platelet bank under uncertainty", ***Engineering Applications of Artificial Intelligence***, Vol. 71, (2018), 236-250. doi.org/10.1016/j.engappai.2018.03.004
28. Kazemi, S.M., Rabbani, M., Tavakkoli-Moghaddam, R., Abolhassani-Shahreza, F. "Blood inventory-routing problem under uncertainty", ***Journal of Intelligent and Fuzzy Systems***, Vol. 32, No. 1, (2017), 467-481. Doi.org/10.3233/JIFS-152175
29. Zahiri, B., Pishvaee, M.S. "Blood supply chain network design considering blood group compatibility under uncertainty", ***International Journal of Production Research***, Vol. 55, No. 7, (2017), 2013-2033. doi.org/10.1080/00207543.2016.1262563
30. Ghahremani-Nahr, J., Kian, R., Sabet, E. "A robust fuzzy mathematical programming model for the closed-loop supply chain network design and a whale optimization solution algorithm", ***Expert Systems with Applications***, Vol. 116, (2019), 454-471. doi.org/10.1016/j.eswa.2018.09.027
31. Gunpinar, S., Centeno, G. "Stochastic integer programming models for reducing wastages and shortages of blood products at hospitals", ***Computers & Operations Research***, Vol. 54, (2015), 129-141. doi.org/10.1016/j.cor.2014.08.017
32. Gupte, A., Ahmed, S., Cheon, M.S., Dey, S. "Solving mixed integer bilinear problems using MILP formulations", ***SIAM Journal on Optimization***, Vol. 23, No. 2, (2013), 721-744. doi.org/10.1137/110836183

Persian Abstract

چکیده

چالش اصلی در زنجیره تامین خون، کمبود و هدر رفتن فراورده‌های خونی می‌باشد. به دلیل ویژگی‌های فاسدشدنی این محصول، نگهداری تعداد زیادی از واحدهای خونی به عنوان موجودی باعث خراب شدن این منابع محدود و نادر می‌شود. از طرف دیگر کمبود خون ممکن است باعث لغو فعالیت‌های مهم مرتبط با سلامتی شود و نتیجه آ« افزایش بالقوه مرگ و میر در بیمارستان‌ها است. در این مقاله یک مدل برنامه‌ریزی عدد صحیح با هدف حداقل کردن هزینه کل، کمبود و هدر رفت فراورده‌های خونی در بیمارستان نمازی ارائه شده است. پارامترها در دنیای واقعی نامشخص هستند و این مساله در این مقاله مورد بررسی قرار می‌گیرد. رویکرد برنامه‌ریزی محدودیت احتمال ارائه شده است و یک تصویر عددی از بیمارستان نمازی برای نشان دادن کاربرد مدل بهینه پیشنهادی استفاده گردیده است. تجزیه و تحلیل حساسیت برای اعتبارسنجی مدل در مورد مسائلی مانند سطح اطمینان در مدل احتمالی، وزن ضریب و مقدار جریمه تابع هدف در مدل فازی استوار انجام شده است. نتایج عددی نشان می‌دهد که مدل قادر به کنترل عدم قطعیت می‌باشد و قیمت مقاومتی بر سیستم تحمیل می‌شود؛ بنابراین مقدار تابع هدف در فازی استوار ۸۰ درصد کمتر است.

International Journal of Engineering

Journal Homepage: www.ije.ir

Electromagnetic Wave Absorption Properties of Barium Ferrite/Reduced Graphene Oxide Nanocomposites

M. Moslehi Niasar[a], M. J. Molaei*[b], A. Aghaei[a]

[a] *Materials and Energy Research Center, Karaj, Iran*
[b] *Faculty of Chemical and Materials Engineering, Shahrood University of Technology, Shahrood, Iran*

PAPER INFO

Paper history:
Received 19 September 2020
Received in revised form 26 January 2021
Accepted 05 April 2021

Keywords:
Barium Ferrite
Reduced Graphene Oxide
Magnetic Properties
Electromagnetic Wave Absorption

ABSTRACT

Reduced graphene oxide (rGO) and M-type hexagonal ferrites such as $BaFe_{12}O_{19}$ have attracted great attention as electromagnetic (EM) wave absorbing materials in recent years. In this research, different weight percents of $BaFe_{12}O_{19}$/rGO nanocomposites were incorporated into the microwave absorbing layers and their EM wave absorption was investigated. Barium ferrite was synthesized through the co-precipitation method. Graphene oxide (GO) was synthesized through the modified Hummers' method. The synthesized GO was reduced to rGO nanosheets using a reducing agent. The synthesized barium ferrite and rGO were then mechanically milled to form $BaFe_{12}O_{19}$/rGO nanocomposite. The chemical bondings, phase analysis, magnetic properties, particle morphology, and EM wave absorbing properties were investigated using FTIR, XRD, Vibration Sample Magnetometer (VSM), FESEM, and Vector Network Analyzer (VNA), respectively. The saturation magnetization (M_s) and the coercivity (H_c) of the synthesized $BaFe_{12}O_{19}$/rGO nanocomposite were 31 emu/g and 1.5 kOe, respectively. The EM absorption properties in the X-band (8.2-12.4 GHz) showed that the maximum reflection loss (RL) of -7.39 dB could be obtained for the nanocomposite containing only 10 wt. % of $BaFe_{12}O_{19}$/rGO nanocomposite in a resin matrix with a thickness of 2 mm.

***doi**: 10.5829/ije.2021.34.06c.14*

1. INTRODUCTION

In recent years, electronic devices and wireless communications which act in the range of microwave frequency or X-band (8-12 GHz) are widely developed [1]. With the development of electronic devices, electromagnetic interference (EMI) has become a serious concern. Furthermore, the improvements in the technology of radar detection have increased the demand for microwave absorbing layers [2]. The microwave absorbing materials should be able to attenuate and dissipate the microwave energy through dielectric loss and magnetic loss mechanisms [1]. An ideal absorbing material should possess a broad absorption frequency, strong absorption capability, and lightweight [3]. The basic design criteria for the absorbing materials are impedance matching characteristics and attenuation capability [4, 5]. Generally, weak attenuation leads to a low reflection loss. Furthermore, weak impedance matching results in an increased reflection from the surface [5].

Most of the microwave absorbing materials have consisted of dielectric loss components such as conducting polymers or carbon material and magnetic loss materials such as nickel, cobalt, and ferrite [6]. Hexagonal ferrites with the chemical formula of $MFe_{12}O_{19}$ (M= Ba, Pb, and Sr) are the widely used hard magnetic materials in different applications [7]. Barium ferrite ($BaFe_{12}O_{19}$) as a hard magnetic material with enhanced saturation magnetization (M_s) and high coercivity (H_c) has received wide applications [8-17]. Barium ferrite has EM wave absorption properties as well [18]. However, due to the low dielectric loss and high density, the EM absorbing applications of hexagonal ferrites are restricted. In order to enhance the EM absorbing properties of hexagonal ferrites, versatile

*Corresponding Author Institutional Email: *m.molaei@shahroodut.ac.ir* (M. J. Molaei)

Please cite this article as: M. Moslehi Niasar, M. J. Molaei, A. Aghaei, Electromagnetic Wave Absorption Properties of Barium Ferrite/Reduced Graphene Oxide Nanocomposites, International Journal of Engineering, Transactions C: Aspects Vol. 34, No. 6, (2021) 1505-1513

dielectric loss fillers such as carbon nanotubes (CNTs) and graphene have been applied together with these ferrites [19].

Carbon-based materials such as CNTs, porous carbon, carbon spheres, graphene, and rGO have superior electromagnetic wave reflection loss efficiency. The rGO with a high dielectric loss is a great candidate for use in EM wave absorber materials [20]. Graphene, a monolayer sheet of carbon atoms in the form of a hexagonal two-dimensional structure with sp^2 hybridization, has attracted extensive attention due to its mechanical, electrical, and thermal properties. Graphene-based materials provide application potential in the fields of biomedical, supercapacitors, energy, catalysts, batteries, and EM wave absorption [21-23]. The graphene absorption properties can be enhanced if are used with other appropriate EM absorbing materials [24]. The graphene can act as a dielectric loss EM wave absorption material with an absorption performance better than CNTs [25]. The residual groups and defects on the rGO nanosheets introduce groups' electronic dipole relaxation and defect polarization relaxation. The rGO nanosheets have higher microwave absorption in comparison to CNT or graphite. The rGO nanosheets can also be a better microwave absorbing material compared to high-quality graphene [3]. However, graphene cannot be used as an appropriate microwave absorption material since it has a high dielectric loss while misses to have a high magnetic loss. In order to overcome this shortage, magnetic materials can be incorporated into graphene [26]. There have been some efforts to incorporate magnetic materials into rGO for enhancement of EM wave absorption properties including rGO/Fe_3O_4 [27], rGO/α-Fe_2O_3 [28], rGO/γ-Fe_2O_3 [29], rGO/$MnFe_2O_4$ [30], rGO/$ZnFe_2O_4$ [26], rGO/$CoFe_2O_4$ [31], rGO/Co_3O_4 [32], rGO/nitrogen-doped cobalt/cobalt oxide/carbon [33], rGO/Co_3Ni [34], rGO/ferroferric oxide-carbon [35], rGO/ hybrid C@CoFe nanoparticles [36].

While different magnetic materials have been used to enhance the microwave absorption properties of the rGO, barium ferrite as an effective microwave absorbing magnetic material, with different weight percents has not been used together with rGO to enhance the microwave absorption. Therefore, in this research, different weight percents of $BaFe_{12}O_{19}$/rGO nanocomposites were incorporated into a microwave absorbing layer, and their EM wave absorption properties were investigated. The barium ferrite was synthesized through the co-precipitation method while rGO nanosheets were synthesized by reduction of graphene oxide with hydrazine hydrate.

2. EXPERIMENTAL PROCEDURE

2. 1. Materials Graphite powder (purity 99.3%), hydrochloric acid (HCl, 10%), sulfuric acid (H_2SO_4, 98%), sodium nitrate ($NaNO_3$), potassium permanganate ($KMnO_4$), hydrogen peroxide (H_2O_2, 30%), ferric chloride ($FeCl_3.6H_2O$), barium chloride ($BaCl_2.2H_2O$), sodium hydroxide (NaOH), cetyltrimethyl ammonium bromide ($C_{19}H_{42}BrN$), and hydrazine hydrate ($NH_2NH_2{\cdot}xH_2O$, 98%) were purchased from Merck. The epoxy (viscosity=1.75 MPa.s and density =1150 kg/m^3 at room temperature) and the hardener (viscosity=1.1 MPa.s and density=1000 kg/m^3 at room temperature) were also purchased from Shell company. All materials were reagent grade and were used without any further purification process.

2. 2. Synthesis of Barium Ferrite For the production of barium ferrite nanoparticles, $FeCl_3.6H_2O$ and $BaCl_2.2H_2O$ were added to 50 mL deionized water in a manner to reach to Fe:Ba molar ratio of 10. The cetyltrimethyl ammonium bromide (CTAB) surfactant was added (10 ppm) to decrease the agglomeration of the precipitates. The solution was stirred for 30 min. Then sodium hydroxide (5 M) solution added dropwise in 1 h to reach the pH of 11. During the addition of the sodium hydroxide, the ferrite precursors precipitate. The precipitates then were collected and washed using a 4000 rpm centrifuge and dried at 100 ◦C overnight. The dried precursors (reddish solids) were calcined at 1150 ◦C for 2 h in air.

2. 3. Synthesis of rGO Synthesis of rGO was conducted through chemical reduction of GO. The GO was synthesized by a modified Hummers' method [23]. Briefly, graphite (1 g) and $NaNO_3$ (2 g) were added into a flask containing H_2SO_4 (80 mL) and after stirring for 1 h, the mixture was transferred to an ice bath. Then $KMnO_4$ (3 g) was added to the flask under vigorous stirring. Subsequently, after continuous stirring for 48 h at room temperature, deionized water (400 mL) and H_2O_2 (15 mL) were added to the flask. The precipitate was washed with HCl (10%) and then with water to reach to pH of almost 7. The precipitate was dried at 80ºC in an oven overnight. Part of the resultant GO (0.4 g) was dissolved in deionized water (50 mL) using an ultrasonic bath. The GO was reduced to rGO with the aid of hydrazine hydrate (0.5 mL) under stirring for 1 h. The resultant rGO was collected and washed with deionized water for several times using an 11000 rpm centrifuge.

2. 3. Synthesis of $BaFe_{12}O_{19}$/rGO Nanocomposites The $BaFe_{12}O_{19}$/rGO nanocomposites were synthesized using a high energy mechanical milling. The weight ratio of the barium ferrite to rGO was 60/40. The powder mixtures were milled for 1 h in a SPEX-8000D milling machine with a ball to powder mass ratio of 7:1.

2. 4. Characterization Techniques Phase analysis was done using a Siemens model D500 XRD

machine. The XRD patterns were obtained with a step size of 0.02 degrees using Cu-K_α radiation. The analysis was completed with the help of X'pert software. Scherrer's equation [37] was used to calculate the mean crystallite size of the phases. Fourier-transform infrared spectroscopy (FTIR) analysis was performed on a PerkinElmer spectrometer (400-4000 cm^{-1}). The particle morphology was studied by a field emission scanning electron microscope (MIRA3TESCAN-XMU). Magnetic hysteresis loops of the samples were obtained by a vibrating sample magnetometer (VSM, Meghnatis Daghigh Kavir) at room temperature. The magnetization at the maximum applied field of 1.5 kOe was considered as the saturation magnetization. The EM wave absorption properties of the synthesized nanocomposites were measured by a vector network analyzer device (VNA, HP Network Analyzer, USA, model 8720) in the frequency range of 8.2-12.4 GHz at room temperature. For VNA measurements, the samples were prepared with different weight ratios of barium ferrite/rGO nanocomposites to the epoxy resin by the aid of slow mechanical agitation. The samples were prepared in similar thicknesses. The contents and thicknesses of the samples are listed in Table 1.

3. RESULTS AND DISCUSSIONS

Figure 1 shows the XRD patterns of the synthesized GO and barium ferrite/rGO nanocomposite. As can be seen in Figure 1, A sharp diffraction peak at $2\theta=12^\circ$ is detected in the pattern (a) which reveals the formation of GO. The pattern (b) merely consists of barium ferrite peaks, which implies that the milling of rGO and barium ferrite phases does not result in chemical reactions and the formation of new phases [37]. The electronic structure of the graphene nanosheets is modified by the lattice defects and attached functional groups. The defects and functional groups are scattering centers that alter the electrical properties. The reduction of GO to rGO removes the bonded oxygen-containing functional groups and also atomic-scale lattice defects. Furthermore, the reduction process recovers the conjugated network of the graphitic lattice. These change in the structure of the graphene sheets recovers the conductivity of the graphene [38]. The mechanism of the formation of barium ferrite is based on two competing processes: indirectly via crystalline intermediates and directly from the amorphous precursors. However, the direct formation of barium ferrite happens at lower temperatures because of its lower activation energy compared to the indirect route which posses higher activation energy [39].

Figure 2 displays the FTIR spectrum of the $BaFe_{12}O_{19}$/rGO nanocomposite. The peaks that are observed at 590 cm^{-1}, 545 cm^{-1}, and 442 cm^{-1} could be assigned to the Fe-O stretching vibrations [40]. The hydroxyl and carboxyl groups of the GO are absent on the FTIR spectrum of the synthesized nanocomposite. The peaks at 2914 cm^{-1}, 2842 cm^{-1}, and 1570 cm^{-1} due to C-H stretching and C=C stretching is evidence of the restoration of the graphitic structure [19].

FESEM images of the rGO nanosheets and $BaFe_{12}O_{19}$/rGO nanocomposite are shown in Figure 3. As can be seen in Figure 3(a), the lamellar structure has been conserved even after the chemical reduction of the GO.

TABLE 1. weight ratios of ferrite/rGO to epoxy resin in the samples alongside sample thicknesses

Samples	Barium ferrite/rGO content in the samples (wt%)	Epoxy resin content in the samples (wt%)	Thickness
I	10%	90%	2mm
II	20%	80%	2mm

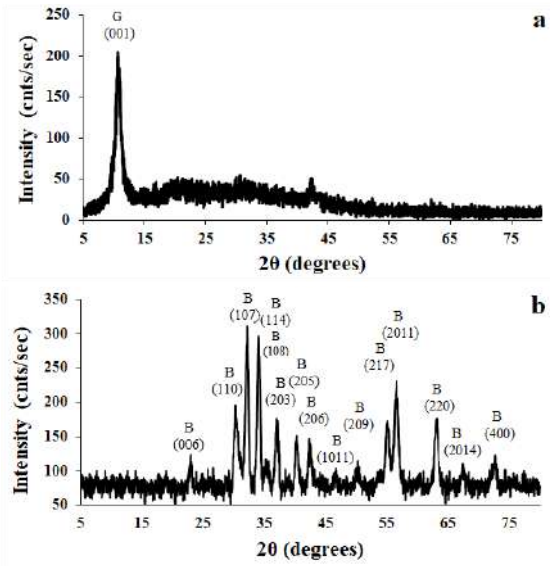

Figure 1. XRD patterns of the a) synthesized GO and b) $BaFe_{12}O_{19}$/rGO nanocomposite

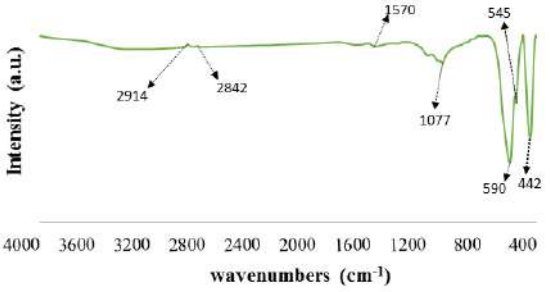

Figure 2. FTIR spectrum of $BaFe_{12}O_{19}$/rGO nanocomposite

Figure 3(b) shows rGO flakes that are decorated by barium ferrite nanoparticles which might have occurred due to an electrostatic attraction between rGO and $BaFe_{12}O_{19}$ [19].

Figure 4 shows the magnetic hysteresis loop of the synthesized $BaFe_{12}O_{19}$/rGO nanocomposites compared to barium ferrite. The nanocomposite of $BaFe_{12}O_{19}$ magnetic nanoparticles on the rGO flakes can reach a saturation magnetization (M_s) of 31 emu/g and coercivity (H_c) of 1.5 kOe.

Figure 5(a) shows the complex permittivity real part (ε′) and the imaginary part (ε″) of the $BaFe_{12}O_{19}$/rGO/epoxy nanocomposites with different weight ratios of $BaFe_{12}O_{19}$/rGO nanocomposite to epoxy at room temperature in the range of 8.2–12.4 GHz. It can be observed that the ε′ and ε″ values of the nanocomposites increased with an increase in the rGO content from 4 wt% to 8 wt%. Figure 5(b) shows the complex permeability real part (μ′) and the imaginary part (μ″) of the magnetic loss with different weight ratios of $BaFe_{12}O_{19}$/rGO nanocomposite to epoxy. The values of μ′ were in the range of 0.93–1.25 and the values of μ" were in the range of -0.03–0.25.

Considering the relative complex permeability which consists of real and imaginary parts, the real part (μ′) shows the storage capability and the imaginary part (μ″) represents the loss capability of the EM wave energy. The real and imaginary parts of permittivity (ε´ and ε″) also show energy storage and energy attenuation, respectively [30]. The values of ε´ and ε″ for the sample (Π) is high due to high conductivity. The chemical reduction of the graphene oxide results in an increase in the electrical conductivity and also dipolar induction. In fact, the relative complex permittivity is a measure of the polarizability [19]. The dielectric properties of the materials depend on ionic, electronic, space charge, interfacial, and orientational polarization. The sample with a higher content of rGO has enhanced conductivity and increased space charge polarization. The sample (Π) included more interfaces between rGO and barium ferrite nanoparticles that lead to more virtual charge accumulation at the interfaces. This results in interfacial polarization charges at the interface between phases with different dielectric constants. Therefore, the increased ε´ value is due to intrinsic dielectric properties and the increased ε″ value is due to enhanced space charge and interfacial polarization [41]. It is not advantageous for materials to have high values of permittivity since it may result in strong reflection and reduced absorption. On the other hand, for microwave absorbing properties low real part of permittivity and enhanced conductivity are preferred [42].

It can be seen in Figure 5(b) that the μ′ values show a slight increase by increasing the $BaFe_{12}O_{19}$/rGO content in the nanocomposites while μ″ values of the nanocomposite samples are almost unchanged. These

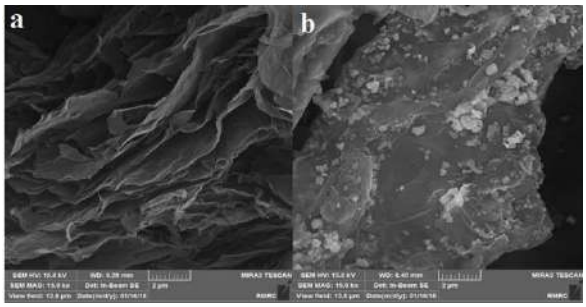

Figure 3. FESEM images of a) rGO flakes, b) rGO flakes decorated with barium ferrite nanoparticles

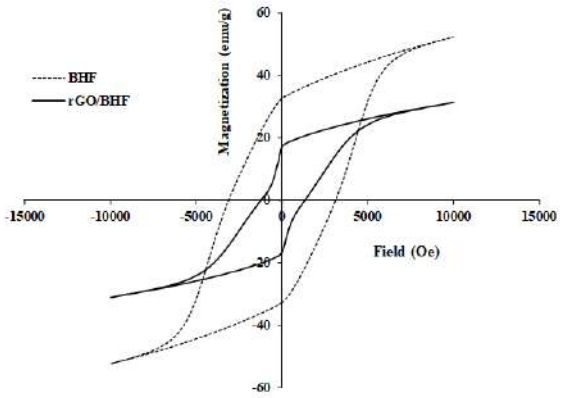

Figure 4. Magnetic hysteresis loop of pure $BaFe_{12}O_{19}$ (BHF) compared to $BaFe_{12}O_{19}$/rGO nanocomposite

data mean that the magnetic loss performance of the samples is nearly unchanged while the ability of the storage of the magnetic energy for the nanocomposites improves by increasing the $BaFe_{12}O_{19}$/rGO content.

The dielectric loss tangent ($\tan\delta_\varepsilon = \varepsilon''/\varepsilon'$) and the magnetic loss tangent ($\tan\delta_\mu = \mu''/\mu'$) variations of the synthesized nanocomposites in the measured frequency range are calculated and plotted in Figure 6. It can be seen in Figure 6(a) that $\tan\delta_\varepsilon$ values $BaFe_{12}O_{19}$/rGO/epoxy nanocomposites of the sample (Π) are higher than that of the sample (I). The higher values of $\tan\delta_\varepsilon$ in the sample with higher rGO content might be due to a) increased polarization as a result of surface functional groups which leads to higher dielectric loss and b) the role of rGO in contracting more conductive paths that result in higher dielectric loss [41]. As can be seen in Figure 6(b) both samples have nearly the same $\tan\delta_\mu$ curve that shows both samples have almost identical magnetic loss properties. Part of the dielectric loss is due to the conductivity loss and polarization loss. The electronic polarization and ionic polarization are significant in higher ranges of frequency (10^3–10^6 GHz) and are not considered for the current investigated frequency range [43]. The higher number of interfaces that exist between different phases in the sample with higher nanocomposite

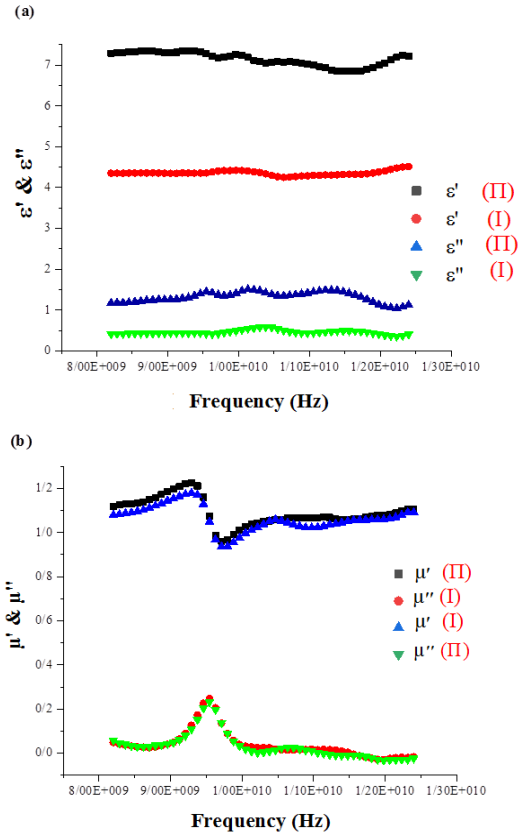

Figure 5. a) real and imaginary parts of the permittivity and b) real and imaginary parts of the permeability variations with different ratios of $BaFe_{12}O_{19}$/rGO nanocomposite to epoxy (samples I an II) in the range of 8.2-12.4 GHz

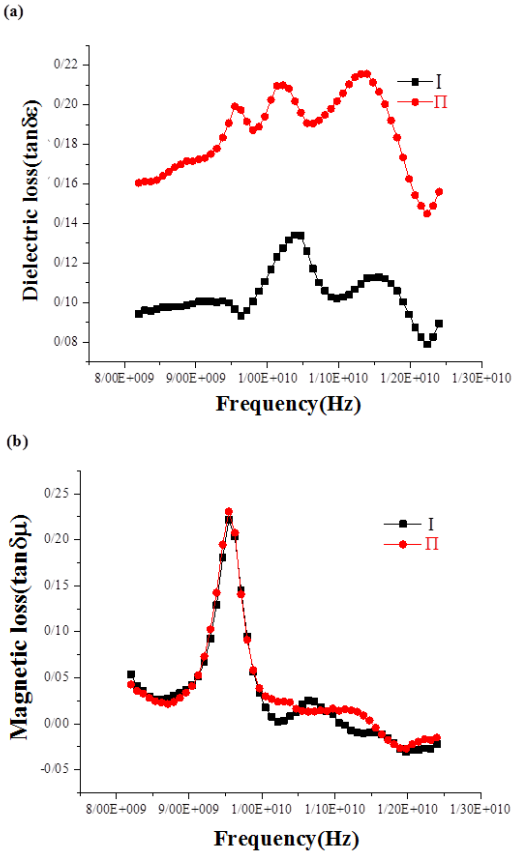

Figure 6. a) dielectric loss factor and b) magnetic loss factor of $BaFe_{12}O_{19}$/rGO/epoxy nanocomposites in the range of 8.2-12.4 GHz for the samples I and II

content, as well as charge transfer that can happen through $BaFe_{12}O_{19}$ nanoparticles and rGO interfaces, are responsible for the higher dielectric loss for sample II. These free carriers vibrate with stimuli of EM wave and cause electric polarization in the rGO [41].

A preferable $\tan\delta_e$ does not necessarily result in high absorption properties. There is another important criterion that should be satisfied for reaching a high microwave absorption efficiency. The characteristic impedance of the layer that is expected to absorb microwaves, should be equal or close to that of free space which is 377 Ωsq^{-1}. Under the impedance matching condition, the absorbing material will have zero-reflection of the incident EM wave at the front surface. For characteristic impedance matching, the complex permeability and complex permittivity should not differ greatly since in the case of large difference, the wave will reflect strongly at the surface of the absorbing material [44].

The reflection loss (RL) can be calculated by the following equation [20]:

$$RL(db) = 20\log\left|\frac{Z_{in}-Z_0}{Z_{in}+Z_0}\right| \quad (1)$$

where Z_0 is the impedance of air and Z_{in} is the input impedance at the interface between the absorber and air. This parameter is related to the EM parameters of the absorber material as follow [20]:

$$Z_{in} = Z_0\left(\frac{\mu_r}{\varepsilon_r}\right)^{\frac{1}{2}}\tanh\left\{j\left(\frac{2\pi ft}{c}\right)(\mu_r\varepsilon_r)^{\frac{1}{2}}\right\} \quad (2)$$

in which μ_r is complex permeability and ε_r is complex permittivity. The parameter c is the velocity of light in free space, *t* is the thickness of the absorbing sample, and *f* is the frequency.

In order to reach enhanced absorption, the incidence of the EM wave on the materials should be without front-end reflection and the EM wave should also be attenuated strongly during propagation in the material. The condition of impedance matching (Z_{in}/Z_0 =1) requires equal values of relative permittivity and permeability [45]. The calculated reflection loss of the $BaFe_{12}O_{19}$/rGO/epoxy nanocomposites with barium ferrite/rGO contents to epoxy weight ratios of 10% and 20% with the sample thicknesses of 2 mm, in the range of 8.2-12.4 GHz, is shown in Figure 7. The curves indicate that the maximum RL for the sample with

barium $BaFe_{12}O_{19}$/rGO content to epoxy of 20 wt% (sample Π) reaches 3.93 dB at 9.5 GHz. Furthermore, the RL of the sample with $BaFe_{12}O_{19}$/rGO content to epoxy of 10 wt% (sample I) reaches 7.39 dB at 9.5 GHz. It can be concluded from Figure 6 and RL data that the maximum absorption occurs at the frequency range in which $\tan\delta_\mu$ is higher than $\tan\delta_\varepsilon$ [45]. Table 2 summarizes microwave absorption of graphene-containing nanocomposites with different filling percents and thicknesses. The data in Table 2 shows that the $BaFe_{12}O_{19}$/rGO/epoxy resin nanocomposite synthesized in this research, shows better microwave absorption in low filling percent and thickness, compared to some other GO- and rGO-containing nanocomposites.

Figure 8 shows input impedance (Z_{in}) for the nanocomposite samples with respect to frequency. The blue curve reveals the conditions where the best impedance matching occurs. Impedance matching occurs when $Z_{in}/Z_0=1$. It can be seen in Figure 8 that the impedance matching in sample II is lower than that of sample I. This caused sample I to display better absorption performance rather than the other sample in all frequency ranges.

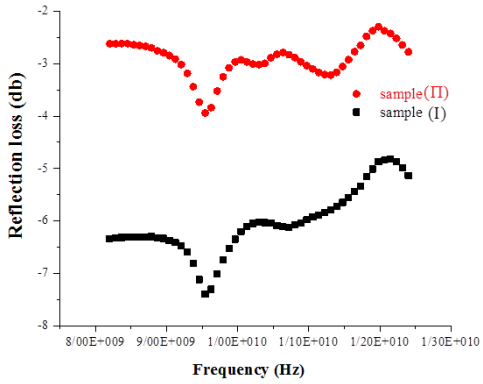

Figure 7. Reflectivity curves of $BaFe_{12}O_{19}$/rGO/epoxy nanocomposites with different barium ferrite/rGO contents to epoxy weight ratios

TABLE 2. Comparison of the microwave absorption of graphene-containing nanocomposites with different filling percents and thicknesses

Absorbing material	Filling percent	Thickness (mm)	Minimum reflection loss	Ref.
Functionalized rGO/γ-Fe_2O_3/Epoxy nanocomposite	60% wt	3	-10.2	[29]
Acid-imidazolium based dicationic ionic liquid (PTA@Imid diIL) interlocked on the surface of fluorinated GO/epoxy resin	20%	4	-5.8	[46]
Al@RGO/paraffin	60%	3	-7.7	[47]
Fe_3O_4-NH_2/GO nanocomposite	100%	4	-8	[48]

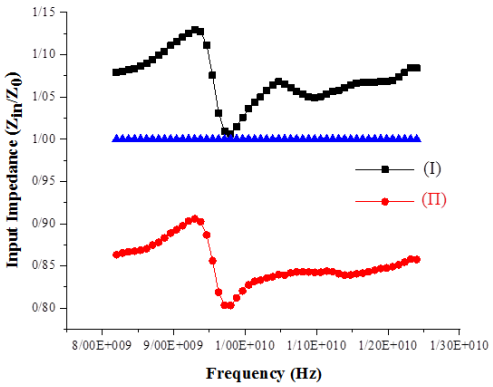

Figure 8. The impedance of $BaFe_{12}O_{19}$/rGO/epoxy nanocomposites in the range of 8.2-12.4 GHz for the samples I and Π

4. CONCLUSION

In this research, different contents of $BaFe_{12}O_{19}$/rGO nanocomposites were incorporated into epoxy resin and the microwave absorption properties of the absorbing layers were investigated.

Microstructural studies revealed a fine distribution of barium ferrite nanoparticles on the surface of rGO nanosheets forms through the coprecipitation method. The synthesized $BaFe_{12}O_{19}$/rGO nanocomposite was found to possess suitable magnetic properties (M_s=33 emu/g and H_c=2.1 kOe) to be used in EM wave absorption applications. The results of EM wave absorption measurements showed that the RL values of the $BaFe_{12}O_{19}$/rGO/epoxy nanocomposite are strongly influenced by their absorber material ratio in the sample. The sample with barium ferrite/rGO content of 10 wt% in the resin epoxy exhibits a maximum RL of 7.39 dB at 9.54 GHz. The results show that $BaFe_{12}O_{19}$/rGO nanocomposite is promising for the application in microwave absorbing layers.

5. ACKNOWLEDGMENT

The authors would like to acknowledge Materials and Energy Research Center, Shahrood University of Technology, and Iranian Nanotechnology Initiative Council for the financial support of present research.

6. REFERENCES

1. Widanarto, W., Khaeriyah, S., Ghoshal, S.K., Kurniawan, C., Effendi, M. and Cahyanto, W.T., "Selective microwave absorption in nd3+ substituted barium ferrite composites", ***Journal of Rare Earths***, Vol. 37, No. 12, (2019), 1320-1325, doi: 10.1016/j.jre.2019.01.008
2. Liu, C., Zhang, Y., Tang, Y., Wang, Z., Ma, N. and Du, P., "The tunable magnetic and microwave absorption properties of the Nb^{5+}–Ni^{2+} co-doped m-type barium ferrite", ***Journal of Materials Chemistry C***, Vol. 5, No. 14, (2017), 3461-3472, doi: 10.1039/C7TC00393E
3. Li, Y., Yu, M., Yang, P. and Fu, J., "Enhanced microwave absorption property of fe nanoparticles encapsulated within reduced graphene oxide with different thicknesses", ***Industrial & Engineering Chemistry Research***, Vol. 56, No. 31, (2017), 8872-8879, doi: 10.1021/acs.iecr.7b01732
4. Lv, H., Ji, G., Liang, X., Zhang, H. and Du, Y., "A novel rod-like MnO_2@ Fe loading on graphene giving excellent electromagnetic absorption properties", ***Journal of Materials Chemistry C***, Vol. 3, No. 19, (2015), 5056-5064, doi: 10.1039/C5TC00525F
5. Zhang, X., Ji, G., Liu, W., Zhang, X., Gao, Q., Li, Y. and Du, Y., "A novel co/tio 2 nanocomposite derived from a metal–organic framework: Synthesis and efficient microwave absorption", ***Journal of Materials Chemistry C***, Vol. 4, No. 9, (2016), 1860-1870, doi: 10.1039/C6TC00248J
6. Wang, C., Han, X., Xu, P., Zhang, X., Du, Y., Hu, S., Wang, J. and Wang, X., "The electromagnetic property of chemically reduced graphene oxide and its application as microwave absorbing material", ***Applied Physics Letters***, Vol. 98, No. 7, (2011), 072906, doi: 10.1063/1.3555436
7. Singhal, S., Garg, A. and Chandra, K., "Evolution of the magnetic properties during the thermal treatment of nanosize bamfe11o19 (m= Fe, Co, Ni and Al) obtained through aerosol route", ***Journal of Magnetism and Magnetic Materials***, Vol. 285, No. 1-2, (2005), 193-198, doi: 10.1016/j.jmmm.2004.07.039
8. Molaei, M., Ataie, A. and Raygan, S., "Synthesis of barium hexaferrite/iron oxides magnetic nano-composites via high energy ball milling and subsequent heat treatment", in International Journal of Modern Physics: Conference Series, World Scientific. Vol. 5, (2012), 519-526, doi: 10.1142/S2010194512002425
9. Molaei, M., Ataie, A. and Raygan, S., "Synthesis of magnetic nano-composite by partial reduction of barium hexaferrite via high-energy ball milling", in Key Engineering Materials, Trans Tech Publ. Vol. 434, (2010), 354-356, doi: 10.4028/www.scientific.net/KEM.434-435.354
10. Molaei, M., Ataie, A., Raygan, S., Picken, S. and Tichelaar, F., "Investigation on the effects of milling atmosphere on synthesis of barium ferrite/magnetite nanocomposite", ***Journal of Superconductivity and Novel Magnetism***, Vol. 25, No. 2, (2012), 519-524, doi: 10.1007/s10948-011-1322-2
11. Molaei, M., Ataie, A., Raygan, S. and Picken, S., "Role of intensive milling in the processing of barium ferrite/magnetite/iron hybrid magnetic nano-composites via partial reduction of barium ferrite", ***Materials Characterization***, Vol. 101, (2015), 78-82, doi: 10.1016/j.matchar.2015.01.006
12. Molaei, M., Ataie, A., Raygan, S., Picken, S. and Tichelaar, F., "The effect of heat treatment and re-calcination on magnetic properties of bafe12o19/Fe_3O_4 nano-composite", ***Ceramics International***, Vol. 38, No. 4, (2012), 3155-3159, doi: 10.1016/j.ceramint.2011.12.018
13. Molaei, M., Ataie, A., Raygan, S., Picken, S., Mendes, E. and Tichelaar, F., "Synthesis and characterization of bafe12o19/Fe_3O_4 and bafe12o19/Fe/Fe_3O_4 magnetic nano-composites", ***Powder Technology***, Vol. 221, (2012), 292-295, doi: 10.1016/j.powtec.2012.01.015
14. Molaei, M., Ataie, A., Raygan, S., Rahimipour, M., Picken, S., Tichelaar, F., Legarra, E. and Plazaola, F., "Magnetic property enhancement and characterization of nano-structured barium ferrite by mechano-thermal treatment", ***Materials Characterization***, Vol. 63, (2012), 83-89, doi: 10.1016/j.matchar.2011.11.004
15. Molaei, M., Ataie, A., Raygan, S. and Picken, S., "Exchange bias in barium ferrite/magnetite nanocomposites", ***Applied Physics A***, Vol. 123, No. 6, (2017), 437.
16. Molaei, M., Ataie, A., Raygan, S. and Picken, S., "The effect of different carbon reducing agents in synthesizing barium ferrite/magnetite nanocomposites", ***Materials Chemistry and Physics***, Vol. 219, No. 1, (2018), doi: 10.1016/j.matchemphys.2018.07.027
17. Zhang, Y., Chuyang L., Kangsen P., Yufan C., Gang F., and Yujing Z. "Synthesis of broad microwave absorption bandwidth Zr^{4+}-Ni^{2+} ions gradient-substituted barium ferrite." ***Ceramics International,*** Vol. 46, No. 16, (2020), 25808-25816, doi: 10.1016/j.ceramint.2020.07.062
18. Molaei, M. and Rahimipour, M., "Microwave reflection loss of magnetic/dielectric nanocomposites of bafe12o19/TiO_2", ***Materials Chemistry and Physics***, Vol. 167, (2015), 145-151, doi: 10.1016/j.matchemphys.2015.10.022
19. Verma, M., Singh, A.P., Sambyal, P., Singh, B.P., Dhawan, S. and Choudhary, V., "Barium ferrite decorated reduced graphene oxide nanocomposite for effective electromagnetic interference shielding", ***Physical Chemistry Chemical Physics***, Vol. 17, No. 3, (2015), 1610-1618, doi: 10.1039/C4CP04284K
20. Su, Z., Tan, L., Tao, J., Zhang, C., Yang, R. and Wen, F., "Enhanced microwave absorption properties of feni nanocrystals decorating reduced graphene oxide", ***Physica Status Solidi (b)***, (2018), 1700553, doi: 10.1002/pssb.201700553
21. Badiei, E., P. Sangpour, M. Bagheri, and M. Pazouki. "Graphene oxide antibacterial sheets: Synthesis and characterization (research note)." ***International Journal of Engineering, Transactions C: Aspects,*** Vol. 27, No. 12, (2014), 1803-1808, doi: 10.5829/idosi.ije.2014.27.12c.01
22. Allahyari, E., and M. Asgari. "Vibration Behavior of Nanocomposite Plate Reinforced by Pristine and Defective Graphene Sheets; an Analytical Approach." ***International Journal of Engineering, Transactions A: Basics,*** Vol. 31, No. 7 (2018), 1095-1102, doi: 10.5829/ije.2018.31.07a.13
23. Asemaneh, H. R., Laleh Rajabi, Farzad Dabirian, Neda Rostami, Ali Ashraf Derakhshan, and Reza Davarnejad. "Functionalized Graphene Oxide/Polyacrylonitrile Nanofibrous Composite: Pb^{2+} and Cd^{2+} Cations Adsorption." ***International Journal of Engineering, Transactions C: Aspects,*** Vol. 33, No. 6, (2020), 1048-1053, doi: 10.5829/ije.2020.33.06c.01
24. Durmus, Z., Durmus, A. and Kavas, H., "Synthesis and characterization of structural and magnetic properties of graphene/hard ferrite nanocomposites as microwave-absorbing material", ***Journal of Materials Science***, Vol. 50, No. 3, (2015), 1201-1213, doi: 10.1007/s10853-014-8676-3
25. Meng, F., Wang, H., Huang, F., Guo, Y., Wang, Z., Hui, D. and Zhou, Z., "Graphene-based microwave absorbing composites: A review and prospective", ***Composites Part B: Engineering***, Vol. 137, (2018), 260-277, doi: 10.1016/j.compositesb.2017.11.023
26. Yang, Z., Wan, Y., Xiong, G., Li, D., Li, Q., Ma, C., Guo, R. and Luo, H., "Facile synthesis of $ZnFe_2O_4$/reduced graphene oxide nanohybrids for enhanced microwave absorption properties", ***Materials Research Bulletin***, Vol. 61, (2015), 292-297, doi: 10.1016/j.materresbull.2014.10.004
27. Song, W.-L., Guan, X.-T., Fan, L.-Z., Cao, W.-Q., Zhao, Q.-L., Wang, C.-Y. and Cao, M.-S., "Tuning broadband microwave

absorption via highly conductive Fe_3O_4/graphene heterostructural nanofillers", ***Materials Research Bulletin***, Vol. 72, (2015), 316-323, doi: 10.1016/j.materresbull.2015.07.028

28. Chen, D., Wang, G.-S., He, S., Liu, J., Guo, L. and Cao, M.-S., "Controllable fabrication of mono-dispersed rgo–hematite nanocomposites and their enhanced wave absorption properties", ***Journal of Materials Chemistry A***, Vol. 1, No. 19, (2013), 5996-6003, doi: 10.1039/C3TA10664K
29. Jaiswal, R., Agarwal, K., Kumar, R., Kumar, R., Mukhopadhyay, K. and Prasad, N.E., "Emi and microwave absorbing efficiency of polyaniline-functionalized reduced graphene oxide/γ-Fe_2O_3/epoxy nanocomposite", ***Soft Matter***, Vol. 16, No. 28, (2020), 6643-6653, doi: 10.1039/D0SM00266F
30. Zhang, X.-J., Wang, G.-S., Cao, W.-Q., Wei, Y.-Z., Liang, J.-F., Guo, L. and Cao, M.-S., "Enhanced microwave absorption property of reduced graphene oxide (rgo)-$MnFe_2O_4$ nanocomposites and polyvinylidene fluoride", ***ACS Applied Materials & Interfaces***, Vol. 6, No. 10, (2014), 7471-7478, doi: 10.1021/am500862g
31. Zong, M., Huang, Y., Wu, H., Zhao, Y., Wang, Q. and Sun, X., "One-pot hydrothermal synthesis of rgo/$CoFe_2O_4$ composite and its excellent microwave absorption properties", ***Materials Letters***, Vol. 114, (2014), 52-55, doi: 10.1016/j.matlet.2013.09.113
32. Liu, P., Huang, Y., Wang, L., Zong, M. and Zhang, W., "Hydrothermal synthesis of reduced graphene oxide–Co_3O_4 composites and the excellent microwave electromagnetic properties", ***Materials Letters***, Vol. 107, (2013), 166-169, doi: 10.1016/j.matlet.2013.05.136
33. Shu, R., Wu, Y., Zhang, J., Wan, Z. and Li, X., "Facile synthesis of nitrogen-doped cobalt/cobalt oxide/carbon/reduced graphene oxide nanocomposites for electromagnetic wave absorption", ***Composites Part B: Engineering***, (2020), 108027, doi: 10.1016/j.compositesb.2020.108027
34. Guo, X., Bai, Z., Zhao, B., Zhang, R. and Chen, J., "Tailoring microwave-absorption properties of CoxNiy Alloy/rGO nanocomposites with tunable atomic ratios", ***Journal of Electronic Materials***, Vol. 46, No. 4, (2017), 2164-2171, doi: 10.1007/s11664-016-5152-7
35. Shu, R., Wu, Y., Li, W., Zhang, J., Liu, Y., Shi, J. and Zheng, M., "Fabrication of ferroferric oxide–carbon/reduced graphene oxide nanocomposites derived from Fe-based metal–organic frameworks for microwave absorption", ***Composites Science and Technology***, (2020), 108240, doi: 10.1016/j.compscitech.2020.108240
36. Li, J., Yang, S., Jiao, P., Peng, Q., Yin, W., Yuan, Y., Lu, H., He, X. and Li, Y., "Three-dimensional macroassembly of hybrid c@ cofe nanoparticles/reduced graphene oxide nanosheets towards multifunctional foam", ***Carbon***, Vol. 157, (2020), 427-436, doi: 10.1016/j.carbon.2019.10.074
37. Hakimi, M., Alimard, P. and Yousefi, M., "Green synthesis of reduced graphene oxide/Sr2CuMgFe28O46 nanocomposite with tunable magnetic properties", ***Ceramics International***, Vol. 40, No. 8, (2014), 11957-11961, doi: 10.1016/j.ceramint.2014.04.032
38. Pei, S. and Cheng, H.-M., "The reduction of graphene oxide", ***Carbon***, Vol. 50, No. 9, (2012), 3210-3228, doi: 10.1016/j.carbon.2011.11.010
39. Lisjak, D. and Drofenik, M., "The mechanism of the low-temperature formation of barium hexaferrite", ***Journal of the European Ceramic Society***, Vol. 27, No. 16, (2007), 4515-4520, doi: 10.1016/j.jeurceramsoc.2007.02.202
40. Ohlan, A., Singh, K., Chandra, A. and Dhawan, S.K., "Microwave absorption behavior of core− shell structured poly (3, 4-ethylenedioxy thiophene)− barium ferrite nanocomposites", ***ACS Applied Materials & Interfaces***, Vol. 2, No. 3, (2010), 927-933, doi: 10.1021/am900893d
41. Zhao, C., Shen, M., Li, Z., Sun, R., Xia, A. and Liu, X., "Green synthesis and enhanced microwave absorption property of reduced graphene oxide-SrFe12O19 nanocomposites", ***Journal of Alloys and Compounds***, Vol. 689, (2016), 1037-1043, doi: 10.1016/j.jallcom.2016.08.078
42. Wang, L., Huang, Y., Li, C., Chen, J. and Sun, X., "A facile one-pot method to synthesize a three-dimensional graphene@ carbon nanotube composite as a high-efficiency microwave absorber", ***Physical Chemistry Chemical Physics***, Vol. 17, No. 3, (2015), 2228-2234, doi: 10.1039/C4CP04745A
43. Zhou, C., Geng, S., Xu, X., Wang, T., Zhang, L., Tian, X., Yang, F., Yang, H. and Li, Y., "Lightweight hollow carbon nanospheres with tunable sizes towards enhancement in microwave absorption", ***Carbon***, Vol. 108, (2016), 234-241, doi: 10.1016/j.carbon.2016.07.015
44. Qiang, R., Du, Y., Wang, Y., Wang, N., Tian, C., Ma, J., Xu, P. and Han, X., "Rational design of yolk-shell c@ c microspheres for the effective enhancement in microwave absorption", ***Carbon***, Vol. 98, (2016), 599-606, doi: 10.1016/j.carbon.2015.11.054
45. Narang, S.B., Pubby, K. and Singh, C., "Thickness and composition tailoring of k-and ka-band microwave absorption of BaCoxTixFe12−2xO19 ferrites", ***Journal of Electronic Materials***, Vol. 46, No. 2, (2017), 718-728, doi: 10.1007/s11664-016-5059-3
46. Mohamadi, M., Kowsari, E., Yousefzadeh, M., Chinnappan, A. and Ramakrishna, S., "Highly-efficient microwave absorptivity in reduced graphene oxide modified with pta@ imidazolium based dicationic ionic liquid and fluorine atom", ***Composites Science and Technology***, Vol. 188, (2020), 107960, doi: 10.1016/j.compscitech.2019.107960
47. Fan, Q., Zhang, L., Xing, H., Wang, H. and Ji, X., "Microwave absorption and infrared stealth performance of reduced graphene oxide-wrapped al flake", ***Journal of Materials Science: Materials in Electronics***, Vol. 31, No. 4, (2020), 3005-3016, doi: 10.1007/s10854-019-02844-2
48. Ebrahimi-Tazangi, F., Hekmatara, S.H. and Seyed-Yazdi, J., "Synthesis and remarkable microwave absorption properties of amine-functionalized magnetite/graphene oxide nanocomposites", ***Journal of Alloys and Compounds***, Vol. 809, (2019), 151779, doi: 10.1016/j.jallcom.2019.151779

Persian Abstract

چکیده

فریت های هگزاگونال نوع M همانند $BaFe_{12}O_{19}$ ترکیبات فوق العاده ای در مواد جاذب امواج الکترومغناطیسی (EM) هستند. گرافن احیاء شده نیز یکی از مواد دو بعدی با جذب بالای امواج الکترومغناطیسی است. در این تحقیق خواص جذب امواج الکترومغناطیسی درصدهای وزنی مختلف از نانوکامپوزیت $BaFe_{12}O_{19}/rGO$ در لایه جاذب مایکروویو مورد استفاده بررسی قرار گرفت. هگزافریت باریم با استفاده از روش همرسوبی سنتز شد. اکسید گرافن (GO) با استفاده از روش هامرز سنتز شد. اکسید گرافن احیاء و به همراه هگزافریت باریم تحت آسیاکاری مکانیکی قرار گرفت. پیوندهای شیمیایی، آنالیز فازی، خواص مغناطیسی، مورفولوژی ذرات و خواص جذب مایکروویو به ترتیب با استفاده از طیف سنجی تبدیل فوریه مادون قرمز، پراش اشعه ایکس، مغناطش سنج نمونه مرتعش، میکروسکوپ الکترونی روبشی نشر میدانی و آنالایزر شبکه برداری مورد بررسی قرار گرفتند. تصاویر میکروسکوپ الکترونی روبشی نشان داد که نانوذرات هگزافریت باریم با موفقیت روی نانوصفحه های گرافن احیاء شده نشسته اند. مغناطش اشباع و نیروی پسماندزدا برای نانوکامپوزیت سنتز شده به ترتیب ۳۱ emu/g و ۱/۵ kOe بود. لایه جاذب امواج حاوی ۱۰٪ وزنی از نانوکامپوزیت $BaFe_{12}O_{19}/rGO$ در یک زمینه رزینی با ضخامت mm حداکثر اتلاف انعکاسی برابر ۷/۳۹ dB- در بازه X نشان داد.

IJE TRANSACTIONS C: Aspects Vol. 34, No. 6, (June 2021) 1514-1525

International Journal of Engineering

Journal Homepage: www.ije.ir

A Continuum Damage Mechanics-based Piecewise Fatigue Damage Model for Fatigue Life Prediction of Fiber-reinforced Laminated Composites

P. Gholami[a], M. A. Kouchakzadeh*[b], M. A. Farsi[a]

[a] *Aerospace Research Institute (Ministry of Science, Research and Technology), Tehran, Iran*
[b] *Department of Aerospace Engineering, Sharif University of Technology, Tehran, Iran*

PAPER INFO

Paper history:
Received 11 January 2021
Received in revised form 18 April 2021
Accepted 02 May 2021

Keywords:
Piecewise Fatigue Damage Model
Continuum Damage Model
Degradation Growth Function
Composite Laminate

ABSTRACT

The purpose of this study is to define a piecewise fatigue damage model (PFDM) for the prediction of damage in composite laminates under cyclic loading based on the continuum damage mechanics (CDM) model. Assuming that damage in fiber-reinforced plastic structures accumulates nonlinearly, a piecewise degradation growth function is defined and coupled with CDM and micromechanics approaches. The model divides the damage behavior of fiber, matrix, and fiber/matrix debonding at the ply scale, into three different stages. For generality, a fully multi-stage damage formulation on a single-ply level is employed. The unknown parameters of the PFDM are estimated according to obtained experimental data of damage mechanisms associated with the composites laminate under cyclic loading. To predict multidirectional composite laminates' fatigue life, the proposed model was implemented in Abaqus software by the subroutine. In a validation against experimental data on carbon fiber reinforced material, the model proves to provide a good numerical approximation of the damage during the fatigue loading. The results reveal that by considering the multi-stage process in stiffness reduction, the proposed model can estimate the fatigue life of composite laminate under multiaxial cyclic loading conditions more accurately than the similar model in the literature.

doi: *10.5829/ije.2021.34.06c.15*

NOMENCLATURES

Material parameter	a	**Greek Symbols**	Γ
Material constant	A	Gibbs free energy	ε
Material parameter	b	Normal strain	γ
Material constant	B	Shear strain	v
Material constant	C	Poisson ratio	ρ
Damage variable	D	Mass density	σ
Young's modulus of elasticity	E	Normall stress	τ
Variance ratio	F	Shear stress	v
Shear modulus	G	Poisson ratio	ω
Number of cycles	N	Piecewise degradation growth function	**Subscripts**
Probability value	p	Fiber	f
Volume fraction	V	Matrix	m
Conjugate forces of damage variable	Y	Critical	cr

1. INTRODUCTION

Composites are one of the most well-known materials that reduce the structure's weight without reducing the strength for various functions [1-4]. Polymer composites exploit a wide range of applications (such as electronic, aerospace, automobile, etc.) due to their all-around excellent performance in mechanical, thermal, and electrical properties [5-9]. One of the main concerns in using these materials is their relatively unknown and

*Corresponding Author Institutional Email: mak@sharif.edu (M. A. Kouchakzadeh)

Please cite this article as: P. Gholami, M. A. Kouchakzadeh, M. A. Farsi, A Continuum Damage Mechanics-based Piecewise Fatigue Damage Model for Fatigue Life Prediction of Fiber-reinforced Laminated Composites, International Journal of Engineering, Transactions C: Aspects Vol. 34, No. 6, (2021) 1514-1525

complicated damage process. The mechanisms of local damage usually initiate in the early stages of loading and propagate over time according to the loading, environmental, and boundary conditions. The composites' damage mechanisms can be classified into fiber breakage, matrix cracking, fiber/matrix debonding, and delamination. In the past, many researchers have made efforts to assess the damage behavior of composite structures under different loading conditions experimentally [10-12] and theoretically [13]. While considerable progress was achieved in this area, no single method is currently available that precisely estimates degradation at all levels of damage mechanism, for all loading conditions, and all types of laminated composites. On the other hand, in the last decades, due to the stochastic nature of composite damage behavior, data analysis methods [14] and Bayesian framework [15], etc. have been coupled with fatigue models to obtain the real scatter of the predicted results, similar to the scatter of experimental data.

The composites used in the structures can experience fatigue and degradation due to cyclic loads. Compared to static loading, less attention has been paid to fatigue conditions. Tools and methods that simulate the response of fiber-reinforced plastic structures under cyclic loading are required to design structures that can tolerate such failure. The response of structures made of composites under cyclic loads has been studied by several authors, which has led to the expansion of some fatigue damage models. These models can be classified into various categories; fatigue life concepts [16, 17], phenomenological models [18, 19], strength degradation models [20, 21], micromechanics models [22, 23], and continuum damage mechanics (CDM) models [24].

The fatigue life models are based on the usage of stress versus life, the so-called *S-N* procedures [25]. These approaches cannot simulate the various failure mechanisms occurring in composites [16]. These models' limitation is that they require extensive empirical data to evaluate each new laminate [26].

The phenomenological models describe material damage by modeling the reduction of specific mechanical properties (strength/stiffness) of composites during fatigue loading. Based on these approaches, some mathematical definition of strength/stiffness reduction versus the number of fatigue loading is introduced by curve-fitting on empirical data. Some methods have been developed in this area for stiffness reduction [19] and strength reduction [21] under fatigue loading. These models' main problems are the need for comprehensive empirical data and the deficiency of particular fracture criteria.

The strength degradation models are generally a composition of fracture criteria, fatigue life approaches, and degradation laws for mechanical properties [25]. Stress analysis is carried out in each load cycle and failure is investigated based on the fracture criteria. If the failure occurs, the mechanical properties of the relevant failed area are abruptly dropped; otherwise, the entire material's mechanical properties are gradually reduced based on the number of loading cycles. This procedure continues until all layers experience catastrophic fracture mode [20, 27].

To apply the micromechanical method, a suitable unit cell is selected from the composite material, and the stress and strain fields are obtained based on micromechanics [28]. At the micro-level, the stress components in the constituents need to be calculated [29]. Micromechanical models may be used in a multiscale analysis to predict the onset and propagation of cracks and stiffness reduction. These models include stress-transfer mechanisms [30], shear-lag approach [31], and variational methods [32]. The limitation of these procedures is their dependence on the micromechanical models' ability to analyze the diverse damage mechanisms associated with the composites and their limited performance with different boundary conditions, loads, and various lay-up configurations [33].

The CDM models are based on thermodynamic potential (Gibbs free energy function) to express material constitutive equations. In the composite area, the CDM approach was first introduced by Ladeve'ze [34] and Ladeve'ze et al. [35] for static loading. In recent decades, this model is developed to calculate the behavior of damage in fiber-reinforced plastic structures subjected to cyclic loading. Payan and Hochard [36] proposed a new CDM approach to predict static and fatigue damage. This approach was based on the hypothesis that fibers experience brittle failure, where the matrix experiences elastic-plastic failure. Xiong and Shenoi [37] studied the fatigue damage process in a compressive cyclic loading using a CDM base model. They presented that the reduction in stiffness occurs in two different phases. The first stage is the onset of failure, which has little efficacy on mechanical properties. The second stage is the propagation of failure, which directly affects the destruction of mechanical properties. Kawai and Honda [38] suggested a fatigue damage model for composite laminates relying on the CDM approach coupled with in situ strength and the plastic deformation of the layers. Based on the CDM approach and the definition of two variables of damage in the fiber and matrix, Shi et al. [39] presented a fatigue damage approach for the reinforced polymer lamina, which is according to the characterization process of the model proposed by Zhang and Zhao [40]. Using a single scalar damage variable in the framework of irreversible thermodynamics, Movaghghar and Lvov [41], by considering plane stress, presented an energy-based model to predict fatigue life and assessed progressive damage. Based on the CDM model and using three variable damage variables, Salimi-Majd and colleagues [42] modified Movaghghar's model

to estimate intralaminar fatigue damage of fibrous composites. To evaluate the life of fiber-reinforced laminated composites under fatigue loading, Mohammadi et al. [43] by defining three damage variables for the fiber, matrix, and fiber/matrix debonding, proposed a CDM approach relying on effective average local stresses so that it can estimate the fatigue life of multidirectional composites with acceptable accuracy. The characterization of their model is based on Zhang's law, according to *S-N* and material stiffness reduction diagrams in different directions. Based on the CDM method, Mahmoudi et al. [44], using micromechanics, suggested a fatigue damage approach to estimate the life of carbon/epoxy laminate, which considers both damage variables because of static and fatigue load conditions. To validate the proposed model, they utilized the experimental method and showed that considering static damage under the cyclic loading process is necessary. Hohe and his colleagues [45] assumed that the damage of material results from microplastic work and defined a brittle damage model based on the CDM approach that describes the degradation of the laminate composite under harmonic cyclic loading.

In recent years, models based on entropy and thermodynamic laws have been developed that use the maximum entropy to predict composite laminate failure and life under fatigue load conditions. Naderi and Khonsari [46], using an empirical method based on a thermodynamic approach, showed that fatigue is an irreversible process of increasing entropy that accumulates until it achieves a significant value, called fracture fatigue entropy at the beginning of fracture. In another study, the fatigue behavior of glass/epoxy composite laminate using the dissipated energy via different mechanisms was investigated by Naderi and Khonsari [47]. Mohammadi and Mahmoudi [48] proposed a novel method relying on the thermodynamic entropy model to estimate cross-ply laminates' fatigue life and examined variables such as different stacking sequences, loading frequency, and ambient temperature. Considering that dissipated entropy during fatigue conditions can be used to measure the composite damage, they proposed [49] a theoretical approach based on the first and second thermodynamics laws, which consider work of irreversible deformations.

Because of the occurring and mixing of several damage accumulation mechanisms under fatigue loading, the damage behavior of composites must be considered as a combination of micro-damage mechanics (MIDM) and macro-damage mechanics (MADM). In the laminated composites, damage usually starts at the matrix material with the cracks and is accompanied by the fiber/matrix debonding to eventually fiber breakage occurred. On the other hand, according to experimental observations, damage evolution in fatigue conditions occurs in different stages. In the first stage, due to the rapid growth of micro-defects, stiffness reduction occurs nonlinearly. In the next step, stiffness reduction reduces linearly with partial degradation by the loading cycle. Finally, in the third stage, and before the final failure, a rapidly increasing stiffness degradation occurs. Based on a review of the literature, it can be seen that most fatigue models do not explicitly consider the multi-stage process for damage caused by cyclic loading in the formulation of the damage accumulation law. The present study is concerned with a modified model, applicable to multi-stage damage due to fatigue loading in the fatigue process, which leads to more accurate estimations about fatigue life. For this purpose, a generalization of a CDM-based constitutive model coupled with micromechanics constitutive equations and degradation growth function is proposed.

In this paper, three in-plane damage mechanisms based on the CDM approach is discussed, while the out-of-plane damage mechanism, i.e., delamination, is ignored. Based on the literature's experimental data, a degradation growth function is used to modify Mohammadi's model [43] that satisfies the laminate composite's multi-stage damage process under fatigue loading. In this study, this revised model is called the piecewise fatigue damage model (PFDM). In recent decades, damage models relying on the finite element method (FEM) have found the most attention [50, 51]. These models directly predict composite materials' damage and fracture for any stacking sequence and material properties [52]. The CDM approach has been developed increasingly in the FEM. Therefore, to show the ability of the PFDM to estimate the life of composite laminates under tension fatigue loading, a numerical approach was used and implemented in Abaqus software by the subroutine. Besides, the results of the modified model were compared to numerical and experimental data available in the literature, and it is shown that the results are consistent with the empirical data.

2. CONTINUUM DAMAGE MODEL

In the CDM approach, an irreversible thermodynamic theory is used as a logical base to formulate constitutive equations with damage. According to this concept, the free energy and the dissipation function must first be expressed. The free energy indicates the relationship between the variables of the internal variable and their conjugate forces, while the dissipation function describes the development of internal variables.

The CDM approach considered in this work is at a ply scale. In this scale, the damage is supposed to be in the form of fiber breakage, matrix cracking, or fiber/matrix interface debonding. This model describes damage by reducing the stiffness of the material. In this paper, plastic

strain due to the brittle response of fiber-reinforced plastic composites is ignored. A degradation growth function is used to predict stiffness reduction in fiber-reinforced plastic composites under cyclic loading. The suggested formulas in the system are based on the materials' principal coordinates so that 1 and 2 show the fiber direction and perpendicular direction of the fibers, respectively.

2. 1. Damage Mechanism The Young's modulus of the undamaged ply in the fiber direction and perpendicular direction is expressed by E_{11}^0 and E_{22}^0, while in the -plane shear modulus is represented by G_{12}^0. In addition, the Poisson's ratio in fibers direction and in its perpendicular directions are expressed by ν_{12} and ν_{21}, respectively. To model various modes of damage, i.e., the fiber breakage, matrix cracking, and the fiber/matrix interface debonding, the values of E_{11}^0, E_{22}^0 and G_{12}^0 may be reduced. Therefore, if the damage variables of E_{11}^0, E_{22}^0 and G_{12}^0 is shown by D_1, D_2 and D_{12}, (indicating fracture in fiber, microcracking in matrix and debonding of fiber/matrix, respectively), then the Gibbs free energy for the ply in damaged state is defined as follows [53]:

$$\rho\Gamma = \frac{1}{2}\left[\frac{\sigma_{11}^2}{E_{11}^0(1-D_1)} - \frac{2\nu_{12}\sigma_{11}\sigma_{22}}{E_{11}^0(1-D_1)} + \frac{\langle\sigma_{22}\rangle_+^2}{E_{22}^0(1-D_2)} + \frac{\langle\sigma_{22}\rangle_-^2}{E_{22}^0} + \frac{(\tau_{12})^2}{G_{12}^0(1-D_{12})}\right] \quad (1)$$

where

$$\langle a\rangle_+ = a \quad \text{if } a \geq 0; \quad \text{otherwise} \langle a\rangle_+ = 0$$
$$\langle a\rangle_- = a \quad \text{if } a \leq 0; \quad \text{otherwise} \langle a\rangle_- = 0 \quad (2)$$

The elastic constitutive equation is:

$$\varepsilon_{11}^e = \rho\frac{\partial\Gamma}{\partial\sigma_{11}} = \frac{\sigma_{11}}{E_{11}^0(1-D_1)} - \frac{\nu_{12}}{E_{11}^0}\sigma_{22} \quad (3\text{-a})$$

$$\varepsilon_{22}^e = \rho\frac{\partial\Gamma}{\partial\sigma_{22}} = \frac{\langle\sigma_{22}\rangle_+}{E_{22}^0(1-D_2)} + \frac{\langle\sigma_{22}\rangle_-}{E_{22}^0} - \frac{\nu_{12}}{E_{11}^0}\sigma_{11} \quad (3\text{-b})$$

$$\gamma_{12}^e = \rho\frac{\partial\Gamma}{\partial\tau_{12}} = \frac{\tau_{12}}{G_{12}^0(1-D_{12})} \quad (3\text{-c})$$

Damage development is controlled by three conjugate forces Y_1, Y_2, and Y_{12} calculated from the partial derivatives of the Gibbs free energy, relative to D_1, D_2, and D_{12}, respectively:

$$Y_1 = \rho\frac{\partial\Gamma}{\partial D_1} = \frac{\sigma_{11}^2}{2E_{11}^0(1-D_1)^2} \quad (4\text{-a})$$

$$Y_2 = \rho\frac{\partial\Gamma}{\partial D_2} = \frac{\sigma_{22}^2}{2E_{22}^0(1-D_2)^2} \quad (4\text{-b})$$

$$Y_{12} = \rho\frac{\partial\Gamma}{\partial D_{12}} = \frac{\tau_{12}^2}{2G_{12}^0(1-D_{12})^2} \quad (4\text{-c})$$

2. 2. Damage Variables Damage variable in terms of stiffness reduction in fiber and matrix is:

$$D_k = \frac{E_k^0 - E_k}{E_k^0} \quad (5)$$

where $k = f, m$ indicating the fiber and matrix, while E_k^0 and E_k represent the undamaged and damaged stiffness state, respectively. Damage variable in shear is:

$$D_{12} = \frac{G_{12}^0 - G_{12}}{G_{12}^0} \quad (6)$$

where G_{12}^0 and G_{12} represent the undamaged and damaged shear modulus, respectively.

To simulate the damage evolution, the micromechanical theory is used to compute the average stress distributions in each direction. The stress-strain relationship is defined [54]:

$$\left[\sigma_i^m\right] = \left[A_{ij}\right]\left[\sigma_j^f\right] \quad (7)$$

and $\left[A_{ij}\right]$ is:

$$\left[A_{ij}\right] = \begin{bmatrix} a_{11} & a_{12} & a_{13} & 0 & 0 & 0 \\ 0 & a_{22} & 0 & 0 & 0 & 0 \\ 0 & 0 & a_{33} & 0 & 0 & 0 \\ 0 & 0 & 0 & a_{44} & 0 & 0 \\ 0 & 0 & 0 & 0 & a_{55} & 0 \\ 0 & 0 & 0 & 0 & 0 & a_{66} \end{bmatrix} \quad (8)$$

where

$$a_{11} = \frac{E_m}{E_f} \quad (9\text{-a})$$

$$a_{22} = a_{33} = a_{44} = \frac{1}{2} + \frac{E_m}{2E_f} \quad (9\text{-b})$$

$$a_{55} = a_{66} = \frac{1}{2} + \frac{G_m}{2G_f} \quad (9\text{-c})$$

$$a_{12} = a_{13} = (a_{11} - a_{22})\left[\left(\frac{V_m}{E_m} - \frac{V_f}{E_f}\right)\Big/\left(\frac{1}{E_f} - \frac{1}{E_m}\right)\right] \quad (9\text{-d})$$

E_f and E_m are Young's modulus of fiber and matrix, while V_f and V_m represent the volume fractions of fiber and matrix, respectively. The stress matrix in fiber and matrix is [54]:

$$\left[\sigma_i^f\right]=\left[B_{ij}\right]\left[\sigma_j\right] \tag{10-a}$$

$$\left[\sigma_i^m\right]=\left[A_{ij}\right]\left[B_{ij}\right]\left[\sigma_j\right] \tag{10-b}$$

where $\left[\sigma_j\right]$ represents the stress of lamina, and $\left[B_{ij}\right]=\left(V_f\left[I\right]+V_m\left[A_{ij}\right]\right)^{-1}$, and $\left[I\right]$ is a unit matrix.

The undamaged elastic modulus E_{11}^0 in the longitudinal direction and E_{22}^0 in the perpendicular direction are:

$$E_{11}^0=V_fE_f^0+V_mE_m^0 \tag{11-a}$$

$$E_{22}^0=\frac{\left(V_f+V_ma_{11}\right)\left(V_f+V_ma_{22}\right)}{\left(V_f+V_ma_{11}\right)\left(\frac{V_f}{E_f^0}+\frac{a_{22}V_m}{E_m^0}\right)+V_fV_m\left(\frac{V_f}{E_f^0}-\frac{V_m}{E_m^0}\right)a_{12}} \tag{11-b}$$

The elastic modulus in the damaged state is:

$$E_{11}=V_f\left(1-D_f\right)E_f^0+V_f\left(1-D_m\right)E_m^0 \tag{12-a}$$

$$E_{22}=\frac{\left(V_f+V_ma_{11}\right)\left(V_f+V_ma_{22}\right)}{\left(V_f+V_ma_{11}\right)\left(\frac{V_f}{\left(1-D_f\right)E_f^0}+a_{22}\frac{V_m}{\left(1-D_m\right)E_m^0}\right)+V_fV_m\left(\frac{V_f}{\left(1-D_f\right)E_f^0}-\frac{V_m}{\left(1-D_m\right)E_m^0}\right)a_{12}} \tag{12-b}$$

$$G_{12}=G_{12}^0\left(1-D_{12}\right) \tag{12-c}$$

So, the damage variables in longitudinal and perpendicular directions are:

$$D_1=\frac{E_{11}^0-E_{11}}{E_{11}^0} \tag{13-a}$$

$$D_2=\frac{E_{22}^0-E_{22}}{E_{22}^0} \tag{13-b}$$

2. 3. Proposed Method In recent years, there has been much effort to develop a damage evolution model under fatigue loading conditions based on the CDM approach. In this study, to estimate the damage evolution of composite laminate material under cyclic loading, the following model is used [39]:

$$\frac{dD_k}{dN}=\frac{A_kY_k^{B_k}}{\left(1-D_k\right)^{C_k}} \tag{14}$$

where k represents the fiber, perpendicular, and fiber/matrix debonding direction, and A_k , B_k and C_k are the material constants. The conjugate forces of the damage variable are:

$$Y_k=\frac{\sigma_k^2}{2E_k\left(1-D_k\right)^2} \tag{15}$$

According to experimental observations, stiffness reduction starts with the application of fatigue loading. In the initial loading cycles, due to the rapid growth of micro-defects, stiffness reduction occurs nonlinearly. In the second stage, the initial stiffness reduction is followed by degradation as the loading cycles increase. Finally, before the final degradation, in the third stage, a rapidly increasing stiffness reduction occurs. The stiffness reduction process under fatigue loading is shown in Figure 1. Based on the mentioned degradation process in laminate composite, in the present paper, to estimate multi-stage stiffness reduction under cyclic loading, the damage evolution law in Equation (14) is expanded to:

$$\frac{dD_k}{dN}=\frac{A_k\omega\left(D\right)Y_k^{B_k}}{\left(1-D_k\right)^{C_k}} \tag{16}$$

where $\omega(D)$ is the piecewise degradation growth function:

$$\omega\left(D\right)=\begin{cases}b+a_I\left(D-D_I\right)^2 & D\le D_1\\ b & D_I\le D\le D_{II}\\ b+a_{II}\left(D-D_{II}\right)^2 & D\ge D_{II}\end{cases} \tag{17}$$

D_I , D_{II} , a_I , a_{II} and b are the material parameters, which should be obtained based on empirical observations, considering:

$$\int_0^{D_{cr,k}}\omega\left(D\right)dD=D_{cr,k} \tag{18}$$

According to experimental results available in the literature, various models are proposed for the

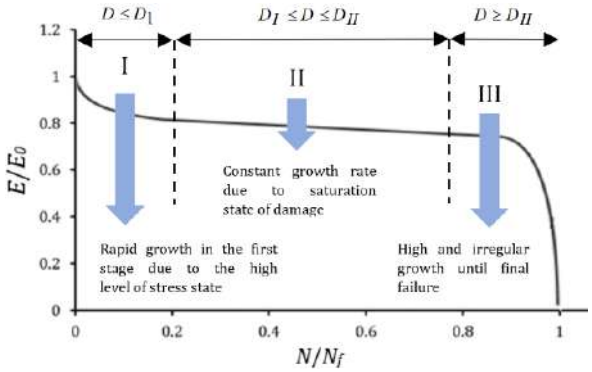

Figure 1. Overall stiffness reduction in fatigue loading

degradation growth function [45]. In this study, the introduced model is called the piecewise fatigue damage model (PFDM), which can fit each of the degradation phases.

3. PARAMETER IDENTIFICATION

Fatigue models need to characterize the material parameters, and many procedures have been developed by authors. The PFDM approach contains two type constants; (1) damage model parameters (i.e., *A*, *B*, *C* for fiber, matrix, and shear damage), and (2) degradation growth function parameters (i.e., a_I, b_{II}, b, D_I, D_{II}).

For the fatigue damage model presented in Equation (14), Shi and his colleagues [39] have proposed characterization parameter. Mohammadi et al. [43] suggested a modified approach for the characterization of material constants. In this study, the modified material characterization procedure suggested by Mohammadi et al. [43] is used. Based on this model, a simple form of the proposed fatigue model is considered in which the degradation growth function can be discarded by assuming $\omega(D)=1$. The damage evolution law is:

$$\frac{dD_k}{dN}=\frac{A_k}{\left(2E_k^0\right)^{B_k}}\frac{\sigma_{\max k}^{2B_k}}{\left(1-D_k\right)^{2B_k+c_k}} \tag{19}$$

where $\sigma_{\max k}$ represents the maximum applied stress in each direction. The integration of Equation (19) from $D=0$ to $D=D_{cr}$ is:

$$\sigma_{\max k}^{2B_k}\cdot N = \frac{\left(2E_k\right)^{B_k}}{A_k\left(2B_k+C_k+1\right)}\left(1-\left(1-D_{cr,k}\right)^{2B_k+C_k+1}\right) \tag{20}$$

where $D_{cr,k}$ is the critical damage parameter in each direction and is calculated experimentally. The logarithm of Equation (20) is:

$$\log N_k = \log\left[\frac{\left(2E_k\right)^{B_k}}{A_k\left(2B_k+C_k+1\right)}.\left(1-\left(1-D_{c,cr}\right)^{2B_k+C_k+1}\right)\right] - 2B_k\log\sigma_{\max,k} \tag{21}$$

By plotting $\log N_k$ versus $\log\sigma_{\max,k}$, the slope B_k is obtained. On the other hand, by plotting $\log dD_k/dN$ versus $\log\left(1-D_k\right)^{-1}$, the parameters A_k and C_k can be specified.

$$\log\frac{dD_k}{dN}=\log\left(\frac{A_k}{\left(2E_k\right)^{B_k}}\sigma_{\max k}^{2B_k}\right) + \left(2B_k+c_k\right)\log\left(1-D_k\right)^{-1} \tag{22}$$

This method for characterization of material constants is applied for fiber, matrix, and fiber/matrix debonding damages, and model constants are obtained. Then, based on the experimental data, the degradation growth function is obtained for each direction to be combined with the fatigue model.

For characterization of the damage model parameters, tensile, transverse, and shear loadings are required. For this purpose, the results of experiments for measuring the residual stiffness of a unidirectional 0°, 90° plies, and cross-ply laminate under tension-tension fatigue on AS4/3501-6, obtained by Shokrieh and Lessard [27] are used. The characterization of material constants for AS4/3501-6 composites under longitudinal, transverse, and shear loading are adapted from reference [43] and listed in Table 1.

The parameters in the degradation growth function are chosen by means of diagrams of damage versus the number of cycles (*D*-*N*) and Young's modulus versus the number of cycles (*E*-*N*), so that Equation (18) is satisfied. For characterization of fiber, based on the experimental data of Shokrieh and Lessard [27] for measuring the stiffness reduction of a unidirectional $[0]_{16}$ laminate subjected to tension-tension cyclic loading, the

D_f-*N*, and *E*-*N* diagrams are plotted in Figure 2**.** As can be seen, the D_f-*N* diagram is divided into three stages. The values of D_I and D_{II} are obtained as 0.09 and 0.18, respectively. At the intersection of the two segments (cycles N_I and N_{II}), according to Equation (18) the constants a_I, a_{II} and b are 50.93, 91.50, and 0.38. For a description of material constants of the degradation growth function for the matrix and fiber/matrix debonding damages, according to experimental data of $[90]_{16}$ and $[0/90]_s$ laminates under tension-tension fatigue, the D_f-*N* and *E*-*N* diagrams are drawn in Figures 3 and 4. Based on the same previous procedure, the unknown parameters of the degradation growth function are obtained and listed in Table 1. It is worth mentioning

TABLE 1. Unknown parameters of PFDM approach

Function	Parameter	Fiber	Matrix	Shear
Damage model	*A*	3.2304×10^{-15}	3291	$1.1269\text{X}10^{-4}$
	B	7.84	7.754	6.28
	C	-19.75	-18.21	-21.72
	D_{cr}	0.2	0.56	0.28
Degradation growth	a_I	50.93	12.00	142.72
	a_{II}	91.50	43.92	110.51
	b	0.38	0.47	0.42
	D_I	0.09	0.42	0.15
	D_{II}	0.18	0.55	0.23

that these diagrams are depicted in a stress ratio of 0.1 and different maximum stresses.

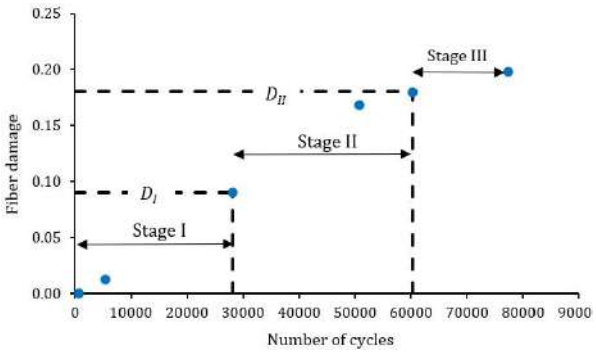

(a) Fiber damage

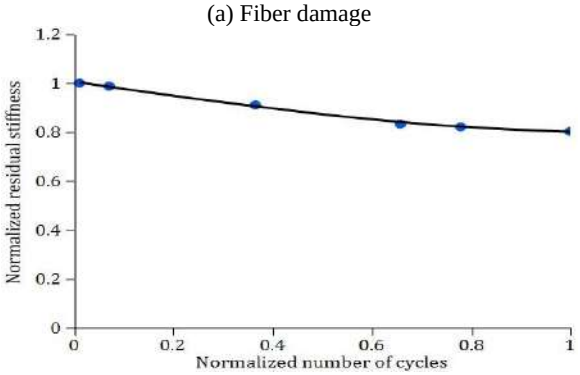

(b) Normalized residual stiffness

Figure 2. Longitudinal direction damage

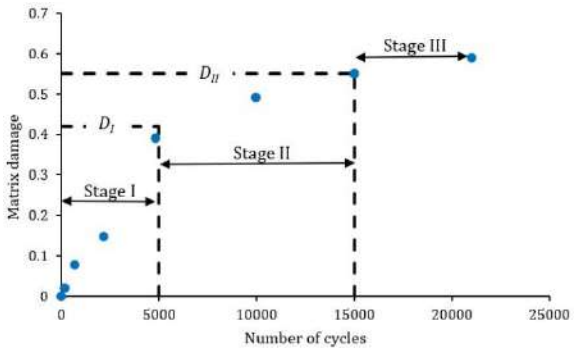

(a) Matrix damage

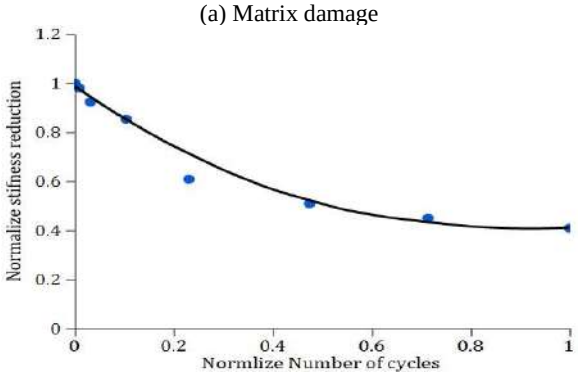

(b) Normalized residual stiffness

Figure 3. Perpendicular direction damage

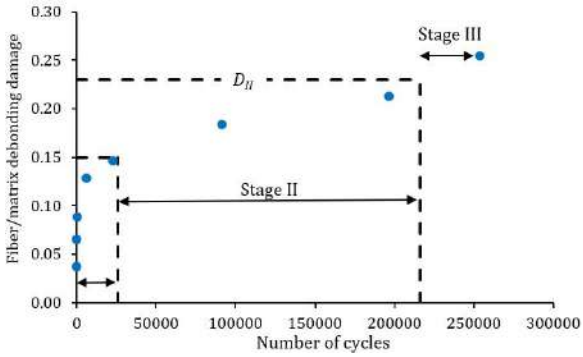

(a) Shear damage

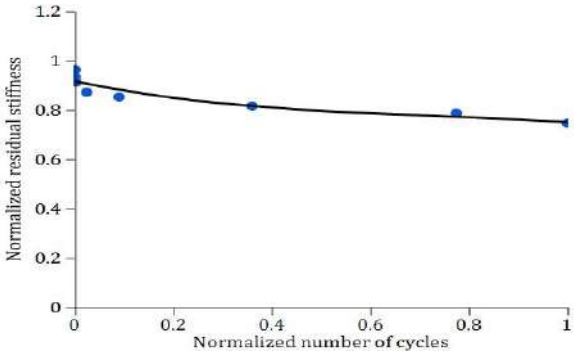

(b) Normalized residual stiffness

Figure 4. Fiber/matrix debonding damage

4. RESULTS AND DISCUSSION

To show the ability of the PFDM approach, the fatigue damage model proposed in section 2.3, the experimental results of AS4/3501-6 composite laminate [55, 56] are investigated. Based on the PFDM approach and parameter identification, for the prediction of laminated composite fatigue life, a numeral procedure is extended and implemented in Abaqus software by USERMAT subroutine. Figure 5 shows the overall flowchart of the process.

In this section, firstly a comparison between the results obtained of the PFDM approach and numerical analysis by other researchers is performed. For this purpose, the fatigue failure test results on $[30]_{16}$ AS4/3501-6 composite laminate [55] are used under uniaxial tension-tension at different stress levels, load ratio of 0.1, and frequency of 10 Hz. Figure 6 illustrates the estimated fatigue life of $[30]_{16}$ AS4/3501-6 composite laminate by different models. As shown in this figure, there is a good agreement between experimental results and estimated fatigue life by the PFDM approach. In addition, as can be seen from Figure 6, the fatigue life results of the PFDM approach same as the 3D finite element model [57] lay in the range of experimental data at different stress levels. Thus, the comparison of these two numerical models shows an acceptable agreement

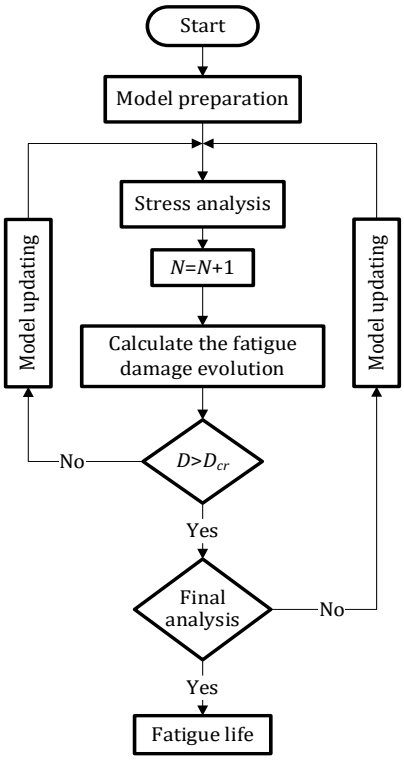

Figure 5. Flowchart of the simulation process using the PFDM approach

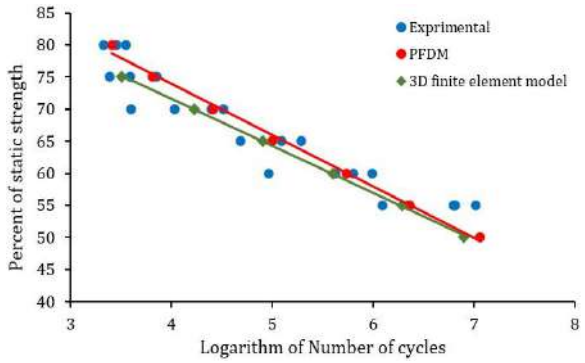

Figure 6. Comparison between fatigue life prediction of $[30]_{16}$ laminate from different numerical models

between them with less difference, and both models have made reliable predictions.

For further verification and assessments of the transferability of the PFDM approach and the parameter set exhibited in Table 1, the model with the previously specified parameter set is compared with the fatigue damage model proposed by Mohammadi et al. [43]. The fatigue life of the $[30]_{16}$ [55] and $[90/45/-45/0]_s$ [56] laminates made of AS4/3501-6 under fatigue loading conditions with stress ratio equal to 0.1 and different maximum stresses are studied. Figures 7 and 8 show the results. Furthermore, a regression model is used to fit experimental data and fatigue behavior is predicted. It can be seen from these figures that the predicted life of the PFDM approach is more accurate than the fatigue model proposed by Mohammadi et al. [43]. The differences between the two models are because of considering multi-stage stiffness reduction with the number of cycles.

In order to visualize the difference between the results obtained from the numerical approach and the experimental approach, the Analysis of Variance (ANOVA) is helpful. ANOVA is a statistically-based decision tool for detecting differences in the average performance of experimental and simulated data groups. Based on reported data in litertaure [58], some basic information about the ANOVA can be found. For an ANOVA, the null hypothesis is considered that between the groups there is no significant difference, and the alternative hypothesis considers that there is a significant difference between the groups. So, in the ANOVA after cleaning the data, assumptions of ANOVA should be tested. According to this, the F-ratio and the associated probability value (p- value) must be calculated. In general, observed probabilities of 0.05 or less are often assumed evidence that there are differences in the group means.

The fatigue life prediction of PFDM, Mohammadi's model, and experimental approach are then post-processed by using ANOVA, and the results of the implementation of ANOVA are shown in Table 2. With ANOVA for $[30]_{16}$ and $[90/45/-45/0]_s$ composite

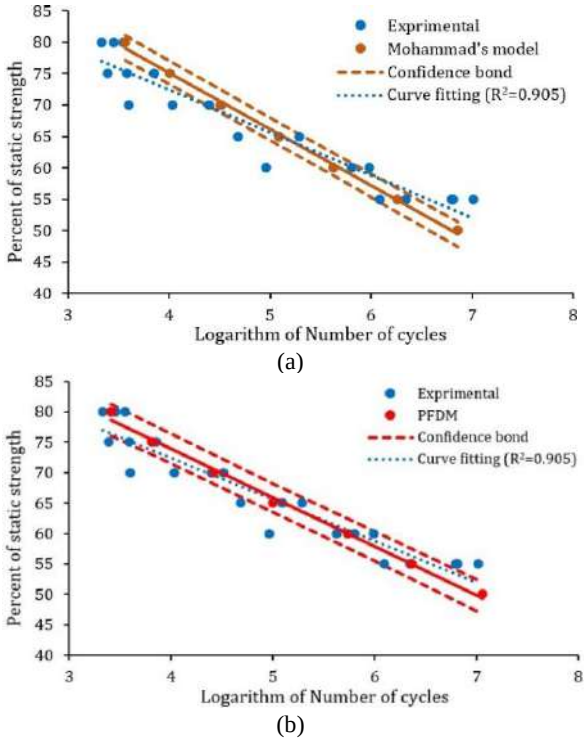

Figure 7. Fatigue life simulation and experimental results of $[30]_{16}$ laminate

laminates, only 22 experiments are used. As shown in Table 2, the *p*-values of the numerical model are more than 0.05, showing no statistically significant differences between the PFDM approach and experimental data.

It can be concluded that considering the multi-stage stiffness reduction in longitudinal, transverse, and fiber/matrix debonding direction, more accurate results can be achieved. It is evident that if the experimental data for material characterization is more, a more exact estimate of the unknown parameters in the PFDM approach can be obtained. The prediction of the multidirectional composite laminate's fatigue life will be more consistent with the experimental data. On the other hand, by considering variations of the properties and re-running the model several times under different states of stress, the PFDM approach can be developed to achieve the real scatter of the simulation results, similar to the scatter of experimental data. Besides, the investigation should be given to the delamination analysis in the present work and can be improved by taking into account the proper cohesive zone model between the layers in the current model to simulate the separation of two layers.

The presented results are only for AS4/3501-6 Carbon-Epoxy composites under a specific load. These results will be different for other materials, loading, and geometry conditions. Investigating the fatigue life of composite laminate with various properties, considering experimental data scattering, and plastic strain and hardening process using the PFDM approach and probabilistic methods may be recommended for further studies.

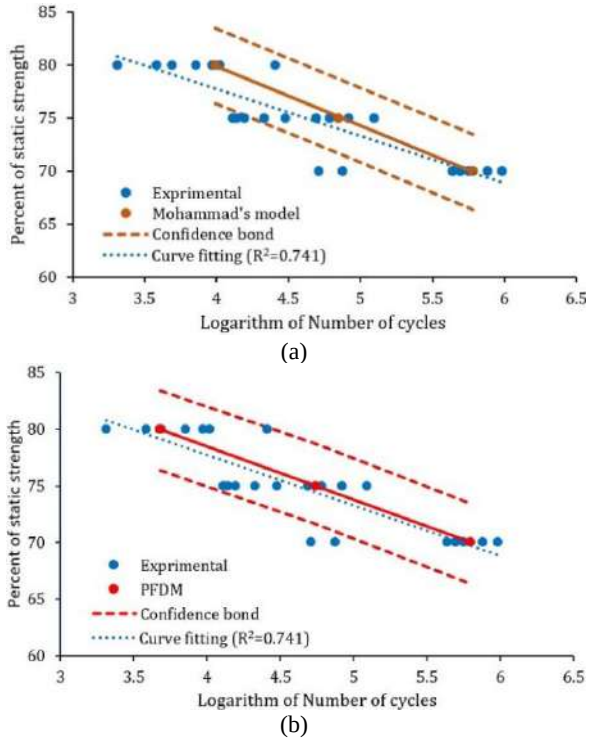

Figure 8. Fatigue life simulation and experimental results of $[90/45/-45/0]_s$ laminate

TABLE 2. Results of ANOVA for the Variation of fatigue life of $[30]_{16}$ and $[90/45/-45/0]_s$ laminates

Model 1	Model 2	$[30]_{16}$		$[90/45/-45/0]_s$	
		***F* ratio**	***p*-value**	***F* rario**	***p*-value**
PFDM	Experimental	1.225	0.274	0.348	0.558
Mohammadi	Experimental	1.780	0.189	0.370	0.545
PFDM	Mohammadi	0.235	0.630	5.7×10^{-6}	0.998

4. CONCLUSION

The objective of the present work is to study the fatigue behavior of fiber-reinforced laminated composites by a continuum damage mechanics (CDM) model relying on the finite element method (FEM). The simulation results agree with the experiment well. The following concluding remarks are pertinent:

- The model is enhanced by the introduction of the degradation growth function.
- The current model is capable of taking to account multi-stage stiffness reduction in laminated composites during a fatigue loading.
- The model is capable to provide a reasonable qualitative approximation of the experimental data for a wide range of fatigue life of laminated composites.
- The prediction capability depends on the maturity of damage evolution law, micromechanics model, degradation growth function, identification of unknown parameters, etc. integrated into the proposed frame.
- In the current model, delamination has been ignored, which can be improved by applying a proper cohesive model current model to capture the delamination of different modes of fracture.

5. REFERENCES

1. Asyraf, M., Ishak, M.R., Sapuan, S., Yidris, N., Shahroze, R., Johari, A., Rafidah, M. and Ilyas, R., "Creep test rig for cantilever beam: Fundamentals, prospects and present views", ***Journal of Mechanical Engineering and Sciences***, Vol. 14, No. 2, (2020), 6869-6887, doi: 10.15282/jmes.14.2.2020.26.0538.
2. Asyraf, M., Ishak, M., Sapuan, S., Yidris, N., Ilyas, R., Rafidah, M. and Razman, M., "Potential application of green composites for cross arm component in transmission tower: A brief review", ***International Journal of Polymer Science***, Vol. 2020, (2020), doi: 10.1155/2020/8878300.
3. Asyraf, M., Ishak, M., Sapuan, S., Yidris, N. and Ilyas, R., "Woods and composites cantilever beam: A comprehensive

review of experimental and numerical creep methodologies", ***Journal of Materials Research and Technology***, Vol. 9, No. 3, (2020), 6759-6776, doi: 10.1016/j.jmrt.2020.01.013.

4. Mohd Nurazzi, N., Muhammad Asyraf, M., Khalina, A., Abdullah, N., Sabaruddin, F.A., Kamarudin, S.H., Ahmad, S., Mahat, A.M., Lee, C.L. and Aisyah, H., "Fabrication, functionalization, and application of carbon nanotube-reinforced polymer composite: An overview", ***Polymers***, Vol. 13, No. 7, (2021), 1047, doi: 10.3390/polym13071047.
5. Ha, K., "Innovative blade trailing edge flap design concept using flexible torsion bar and worm drive", ***HighTech and Innovation Journal***, Vol. 1, No. 3, (2020), 101-106, doi: 10.28991/HIJ-2020-01-03-01.
6. Battistelli, D., Ferreira, D.P., Costa, S., Santulli, C. and Fangueiro, R., "Conductive thermoplastic starch (tps) composite filled with waste iron filings", ***Emerging Science Journal***, Vol. 4, No. 3, (2020), 136-147, doi: 10.28991/esj-2020-01218.
7. Asyraf, M., Ishak, M., Sapuan, S., Yidris, N., Ilyas, R., Rafidah, M. and Razman, M., "Evaluation of design and simulation of creep test rig for full-scale crossarm structure", ***Advances in Civil Engineering***, Vol. 2020, (2020), doi: 10.1155/2020/6980918.
8. Alsubari, S., Zuhri, M., Sapuan, S., Ishak, M., Ilyas, R. and Asyraf, M., "Potential of natural fiber reinforced polymer composites in sandwich structures: A review on its mechanical properties", ***Polymers***, Vol. 13, No. 3, (2021), 423, doi: 10.3390/polym13030423.
9. Nurazzi, N., Asyraf, M., Khalina, A., Abdullah, N., Aisyah, H., Rafiqah, S., Sabaruddin, F., Kamarudin, S., Norrrahim, M. and Ilyas, R., "A review on natural fiber reinforced polymer composite for bullet proof and ballistic applications", ***Polymers***, Vol. 13, No. 4, (2021), 646, doi: 10.3390/polym13040646.
10. Wu, Q. and Wang, Y., "Experimental detection of composite delamination damage based on ultrasonic infrared thermography", ***International Journal of Engineering, Transactions B: Applications***, Vol. 27, No. 11, (2014), 1723-1730. doi: 10.5829/idosi.ije.2014.27.11b.10
11. Mohammad Zaheri, F. and Majzoubi, G., "Numerical and experimental study of ballistic response of kevlar fabric and kevlar/epoxy composite", ***International Journal of Engineering, Transactions B: Applications***, Vol. 30, No. 5, (2017), 791-799. doi: 10.5829/idosi.ije.2017.30.05b.20
12. Jhanji, K. and PVN, L., "Influence of circular and square cut-outs on fiber glass/epoxy composite laminate under tensile loading", ***International Journal of Engineering, Transactions A: Basics***, Vol. 31, No. 1, (2018), 104-109. doi: 10.5829/ije.2018.31.01a.15
13. Askaripour, K. and Fadaee, M., "Diagnosis of delaminated composites using post-processed strain measurements under impact loading", ***International Journal of Engineering, Transactions A: Basics***, Vol. 32, No. 1, (2019), 54-61. doi: 10.5829/ije.2019.32.01a.07
14. Rastegarian, S. and Sharifi, A., "An investigation on the correlation of inter-story drift and performance objectives in conventional rc frames", ***Emerging Science Journal***, Vol. 2, No. 3, (2018), 140-147, doi: 10.28991/esj-2018-01137.
15. Fazelabdolabadi, B. and Golestan, M.H., "Towards bayesian quantification of permeability in micro-scale porous structures–the database of micro networks", ***HighTech and Innovation Journal***, Vol. 1, No. 4, (2020), 148-160, doi: 10.28991/HIJ-2020-01-04-02.
16. Hashin, Z. and Rotem, A., "A fatigue failure criterion for fiber reinforced materials", ***Journal of Composite Materials***, Vol. 7, No. 4, (1973), 448-464, doi: 10.1177/002199837300700404.
17. Vassilopoulos, A.P., Manshadi, B.D. and Keller, T., "Influence of the constant life diagram formulation on the fatigue life prediction of composite materials", ***International Journal of Fatigue***, Vol. 32, No. 4, (2010), 659-669, doi: 10.1016/j.ijfatigue.2009.09.008.
18. Whitworth, H., "A stiffness degradation model for composite laminates under fatigue loading", ***Composite Structures***, Vol. 40, No. 2, (1997), 95-101, doi: 10.1016/S0263-8223(97)00142-6.
19. Zhang, Y., Vassilopoulos, A.P. and Keller, T., "Stiffness degradation and fatigue life prediction of adhesively-bonded joints for fiber-reinforced polymer composites", ***International Journal of Fatigue***, Vol. 30, No. 10-11, (2008), 1813-1820, doi: 10.1016/j.ijfatigue.2008.02.007.
20. Shokrieh, M.M. and Lessard, L.B., "Progressive fatigue damage modeling of composite materials, part i: Modeling", ***Journal of Composite Materials***, Vol. 34, No. 13, (2000), 1056-1080, doi: 10.1177/002199830003401301.
21. Philippidis, T. and Passipoularidis, V., "Residual strength after fatigue in composites: Theory vs. Experiment", ***International Journal of Fatigue***, Vol. 29, No. 12, (2007), 2104-2116, doi: 10.1016/j.ijfatigue.2007.01.019.
22. Reifsnider, K.L. and Stinchcomb, W., A critical-element model of the residual strength and life of fatigue-loaded composite coupons, in Composite materials: Fatigue and fracture. 1986, ASTM International.
23. Pineda, E.J., Bednarcyk, B.A. and Arnold, S.M., "Validated progressive damage analysis of simple polymer matrix composite laminates exhibiting matrix microdamage: Comparing macromechanics and micromechanics", ***Composites Science and Technology***, Vol. 133, (2016), 184-191, doi: 10.1016/j.compscitech.2016.07.018.
24. Krüger, H. and Rolfes, R., "A physically based fatigue damage model for fibre-reinforced plastics under plane loading", ***International Journal of Fatigue***, Vol. 70, (2015), 241-251, doi: 10.1016/j.ijfatigue.2014.09.023.
25. Vassilopoulos, A.P., Fatigue life prediction of composites and composite structures, Woodhead publishing, (2019).
26. Fawaz, Z. and Ellyin, F., "Fatigue failure model for fibre-reinforced materials under general loading conditions", ***Journal of Composite Materials***, Vol. 28, No. 15, (1994), 1432-1451, doi: 10.1177/002199839402801503.
27. Shokrieh, M.M. and Lessard, L.B., "Progressive fatigue damage modeling of composite materials, part ii: Material characterization and model verification", ***Journal of Composite Materials***, Vol. 34, No. 13, (2000), 1081-1116, doi: 10.1177/002199830003401302.
28. K Ahmaditabar, K., Ahmadi, I. and Hashemi, M., "Stiffness prediction of beech wood flour polypropylene composite by using proper fiber orientation distribution function", ***International Journal of Engineering, Transactions A: Basics***, Vol. 30, No. 4, (2017), 582-590. doi: 10.5829/idosi.ije.2017.30.04a.17
29. Bagheri, R., Peason, R. and Marouf, B., "Modeling of stiffening and strengthening in nano-layered silicate/epoxy (research note)", ***International Journal of Engineering, Transactions A: Basics***, Vol. 30, No. 1, (2017), 93-100. doi: 10.5829/idosi.ije.2017.30.01a.12
30. Ogi, K., Yashiro, S., Takahashi, M. and Ogihara, S., "A probabilistic static fatigue model for transverse cracking in cfrp cross-ply laminates", ***Composites Science and Technology***, Vol. 69, No. 3-4, (2009), 469-476, doi: 10.1016/j.compscitech.2008.11.023.
31. McCartney, L., "Energy methods for fatigue damage modelling of laminates", ***Composites Science and Technology***, Vol. 68, No. 13, (2008), 2601-2615, doi: 10.1016/j.compscitech.2008.04.044.
32. Zhang, H. and Minnetyan, L., "Variational analysis of transverse cracking and local delamination in [θm/90n] s laminates", ***International Journal of Solids and Structures***, Vol. 43, No. 22-23, (2006), 7061-7081, doi: 10.1016/j.ijsolstr.2006.03.004.
33. Rafiee, R. and Elasmi, F., "Theoretical modeling of fatigue phenomenon in composite pipes", ***Composite Structures***, Vol. 161, (2017), 256-263, doi: 10.1016/j.compstruct.2016.11.054.

34. Ladeveze, P., "A damage computational method for composite structures", ***Computers & Structures***, Vol. 44, No. 1-2, (1992), 79-87, doi: 10.1016/0045-7949(92)90226-P.
35. Allix, O. and Ladevèze, P., "Interlaminar interface modelling for the prediction of delamination", ***Composite Structures***, Vol. 22, No. 4, (1992), 235-242, doi: 10.1016/0263-8223(92)90060-P.
36. Payan, J. and Hochard, C., "Damage modelling of laminated carbon/epoxy composites under static and fatigue loadings", ***International Journal of Fatigue***, Vol. 24, No. 2-4, (2002), 299-306, doi: 10.1016/S0142-1123(01)00085-8.
37. Xiong, J. and Shenoi, R., "A two-stage theory on fatigue damage and life prediction of composites", ***Composites Science and Technology***, Vol. 64, No. 9, (2004), 1331-1343, doi: 10.1016/j.compscitech.2003.10.006.
38. Kawai, M. and Honda, N., "Off-axis fatigue behavior of a carbon/epoxy cross-ply laminate and predictions considering inelasticity and in situ strength of embedded plies", ***International Journal of Fatigue***, Vol. 30, No. 10-11, (2008), 1743-1755, doi: 10.1016/j.ijfatigue.2008.02.009.
39. Shi, W., Hu, W., Zhang, M. and Meng, Q., "A damage mechanics model for fatigue life prediction of fiber reinforced polymer composite lamina", ***Acta Mechanica Solida Sinica***, Vol. 24, No. 5, (2011), 399-410, doi: 10.1016/S0894-9166(11)60040-2.
40. Zhang, X. and Zhao, J., "Applied fatigue damage mechanics of metallic structural members", ***National Defence Industry Press, Beijing***, (1998).
41. Movaghghar, A. and Lvov, G., "An energy model for fatigue life prediction of composite materials using continuum damage mechanics", in Applied Mechanics and Materials, Trans Tech Publ. Vol. 110, (2012), 1353-1360, doi: 10.4028/www.scientific.net/AMM.110-116.1353.
42. Salimi-Majd, D., Helmi, M. and Mohammadi, B., "Damage growth prediction of unidirectional layered composites under cyclic loading using an energy based model", ***Modares Mechanical Engineering***, Vol. 15, No. 7, (2015), 173-180.
43. Mohammadi, B., Fazlali, B. and Salimi-Majd, D., "Development of a continuum damage model for fatigue life prediction of laminated composites", ***Composites Part A: Applied Science and Manufacturing***, Vol. 93, (2017), 163-176, doi: 10.1016/j.compositesa.2016.11.021.
44. Mahmoudi, A., Mohammadi, B. and Hosseini-Toudeshky, H., "Damage behaviour of laminated composites during fatigue loading", ***Fatigue & Fracture of Engineering Materials & Structures***, Vol. 43, No. 4, (2019), doi: 10.1111/ffe.13152.
45. Hohe, J., Gall, M., Fliegener, S. and Hamid, Z.M.A., "A continuum damage mechanics model for fatigue and degradation of fiber reinforced materials", ***Journal of Composite Materials***, Vol. 54, No. 21, (2020), 0021998320904142, doi: 10.1177/0021998320904142.
46. Naderi, M. and Khonsari, M., "Thermodynamic analysis of fatigue failure in a composite laminate", ***Mechanics of Materials***, Vol. 46, (2012), 113-122, doi: 10.1016/j.mechmat.2011.12.003.
47. Naderi, M. and Khonsari, M., "On the role of damage energy in the fatigue degradation characterization of a composite laminate", ***Composites Part B: Engineering***, Vol. 45, No. 1, (2013), 528-537, doi: 10.1016/j.compositesb.2012.07.028.
48. Mohammadi, B. and Mahmoudi, A., "Developing a new model to predict the fatigue life of cross-ply laminates using coupled cdm-entropy generation approach", ***Theoretical and Applied Fracture Mechanics***, Vol. 95, (2018), 18-27, doi: 10.1016/j.tafmec.2018.02.012.
49. Mahmoudi, A. and Mohammadi, B., "On the evaluation of damage-entropy model in cross-ply laminated composites", ***Engineering Fracture Mechanics***, Vol. 219, (2019), 106626, doi: 10.1016/j.engfracmech.2019.106626.
50. Emeka, A.E., Chukwuemeka, A.J. and Okwudili, M.B., "Deformation behaviour of erodible soil stabilized with cement and quarry dust", ***Emerging Science Journal***, Vol. 2, No. 6, (2018), 383-387, doi: 10.28991/esj-2018-01157.
51. Nadjafi, M. and Gholami, P., "Reliability analysis of notched plates under anisotropic damage based on uniaxial loading using continuum damage mechanics approach", ***International Journal of Engineering, Transactions A: Basics***, Vol. 34, No. 01, (2021), 253-262, doi:10.5829/ije.2021.34.01a.28.
52. Choupani, N. and Heydari, M.H., "A new comparative method to evaluate the fracture properties of laminated composite", ***International Journal of Engineering, Transactions C: Aspects***, Vol. 27, No. 6, (2014), 991-1004. doi:10.5829/idosi.ije.2014.27.06c.18
53. Ladeveze, P. and LeDantec, E., "Damage modelling of the elementary ply for laminated composites", ***Composites Science and Technology***, Vol. 43, No. 3, (1992), 257-267, doi: 10.1016/0266-3538(92)90097-M.
54. Huang, Z.-M., "Simulation of the mechanical properties of fibrous composites by the bridging micromechanics model", ***Composites Part A: Applied Science and Manufacturing***, Vol. 32, No. 2, (2001), 143-172, doi: 10.1016/S1359-835X(00)00142-1.
55. Shokrieh, M.M. and Lessard, L.B., "Multiaxial fatigue behaviour of unidirectional plies based on uniaxial fatigue experiments—ii. Experimental evaluation", ***International Journal of Fatigue***, Vol. 19, No. 3, (1997), 209-217, doi: 10.1016/S0142-1123(96)00068-0.
56. Yang, S., *Stiffness degradation of composite laminates*. 1987, George Washington Univ., Washington, DC (USA).
57. Naderi, M. and Maligno, A., "Fatigue life prediction of carbon/epoxy laminates by stochastic numerical simulation", ***Composite Structures***, Vol. 94, No. 3, (2012), 1052-1059, doi: 10.1016/j.compstruct.2011.11.013.
58. Dunn, O.J. and Clark, V.A., *Applied statistics: Analysis of variance end regression*. 1987, John Wiley & Sons.

Persian Abstract

چکیده

هدف از این مطالعه، تعریف مدل آسیب خستگی چندضابطه‌ای برای پیش‌بینی آسیب چندلایه‌های مواد مرکب تحت بارگذاری خستگی بر اساس مدل مکانیک آسیب پیوسته است. با فرض این‌که آسیب در سازه‌های تقویت_شده با الیاف پلیمری، به صورت غیرخطی انباشته می‌شود، یک تابع رشد تخریب چندضابطه‌ای تعریف شده است و با رویکرد مکانیک آسیب پیوسته و میکرومکانیک ترکیب می‌شود. این مدل رفتار آسیب الیاف، ماتریس و جدایش فصل مشترک الیاف/ماتریس در مقیاس یک لایه را به سه مرحله مختلف تقسیم می‌کند. به طور کلی، یک فرمول آسیب کاملاً چندمرحله‌ای در سطح یک لایه استفاده می‌شود. ابتدا با توجه به داده‌های تجربی به دست آمده از مکانیسم‌های آسیب چندلایه مواد مرکب تحت بارگذاری خستگی، پارامترهای ناشناخته مدل آسیب خستگی چندضابطه‌ای به‌دست می‌آید و سپس برای پیش_بینی عمر خستگی چندلایه چندجهته، این مدل با استفاده از سابروتین در نرم‌افزار آباکوس اجرا می‌شود. در یک اعتبارسنجی در برابر داده‌های تجربی مواد تقویت‌شده با الیاف کربن، مدل اثبات می‌کند که یک تقریب عددی خوب از رفتار آسیب تحت شرایط بارگذاری خستگی ارائه می‌دهد. نتایج نشان می‌دهد که با در نظر گرفتن کاهش سفتی چندمرحله‌ای، مدل پیشنهادی می‌تواند عمر خستگی چندلایه مواد مرکب تحت شرایط بارگذاری خستگی چندمحوره را با دقت بیشتری نسبت به مدل مشابه در سایر مقالات تخمین بزند.

International Journal of Engineering

Journal Homepage: www.ije.ir

Study of the Fracture Behavior under the Effect of Cross-ply and Angle-ply Arrangement of FRP Composite Laminate Subjected to Central Circular Cut-out with Mechanical and Thermal Loading Conditions

V. V. Venu Madhav[a], A. V. S. S. K. S. Gupta[b], S. R. More[a]

[a] *V R Siddhartha Engineering College, Vijayawada, A.P, India*
[b] *Department of Mechanical Engineering, JNTU College of Engineering, Hyderabad, Telengana, India*

P A P E R I N F O

Paper history:
Received 01 April 2021
Received in revised form 18 April 2021
Accepted 02 May 2021

Keywords:
Strain Energy Release rate
Virtual Crack Closure Technique
Angle-ply
Cross-ply
Circular edge crack
Thermal Loading
Finite Element Analysis

A B S T R A C T

In advance composite material the propagation of crack is a regular failure problem in various engineering applications especially in aircrafts body. The aircraft body components are subjected to various thermal and mechanical loading conditions. It is very difficult, time-consuming and costly process of testing the aircrafts components failure due to various thermal and mechanical conditions. Strain energy release rate (SERR) is the significant parameter for the composite materials and quality of composite materials depends on SERR values.The present investigation is based on ANSYS analysis for finding the strain energy release rate (SERR) value using Virtual Crack Closure Technique (VCCT) to understand the fracture behavior of the composite lamina. The circular crack present in the middle of the composite plate and subjected to pressure and temperature loading for different angle (cross-ply and angle-ply) composite structure laminas. The angle-ply shows less SERR in mode I & II while cross-ply shows less SERR in mode III under the constant pressure loading conditions. Mode II shows the maximum SERR in cross-ply compared to mode I and III for temperatures 30ºC, , 130 ºC and 180ºC. SERR for mixed-mode was found by considering the total mode of fracture and validation based on published literature for SERR due to the thermal load of mode I (G_I) for different fiber layup configurations of the circular cut-out.

***doi**: 10.5829/ije.2021.34.06c.16*

1. INTRODUCTION

Composite materials play an essential role in various Engineering applications because of their beauty related to their material properties. Composites have properties like low coefficient of thermal expansion and density, higher strength, good resistance to fatigue, corrosion, wear and creep. The properties of composite do not only depend on its materials properties; they widely vary with composite construction. The Automotive and Aerospace Industries fiber-reinforced composite (FRP) is used to develop the structural and nonstructural components [1-3]. Reasreschers are used biopolymer and natural fibers [1], natural fiber reinforced polymer composites (NFRPCs) [2], carbon nanotube-reinforced polymer composite [3], and wood and another composite [4] for various application armor structure system and electrical transmission system application [5]. For structural applications, the fracture toughness of composite materials plays an important role. Many researchers tried to improve the fracture toughness, creep, energy absorption characteristics, creep, and other mechanical properties by changing the use of materials for developing the composite and adopting various changes with construction methods like sandwich [6] and various orientations of the composite materials. Also, the researchers work on the various loading (mechanical, thermal, and thermo-mechanical) conditions and their effect on fracture behaviors of composite materials.

*Corresponding Author Institutional Email: moresatish11@yahoo.co.in (S. R. More)

Please cite this article as: V. V. Venu Madhav, A. V. S. S. K. S. Gupta, S. R. More, Study of the Fracture Behavior under the Effect of Cross-ply and Angle-ply Arrangement of FRP Composite Laminate Subjected to Central Circular Cut-out with Mechanical and Thermal Loading Conditions, International Journal of Engineering, Transactions C: Aspects Vol. 34, No. 6, (2021) 1526-1532

Wang et al. [7] studied the effect of course loading on the graphite-epoxy cross-ply laminates and their various cracking events. They observed 0.3% lower strains induced at the transverse crack at 90º ply. The crack increased continuously with continuously increasing applied tension. Also, they observed matrix dominant cracking modes are emerging before breaking of fiber at 0º ply. Bae et al. [8] used aluminum, polymetheyl-methacrylate samples used to investigate the effect of thermo-mechanical loads on the samples interfacial cracks with mismatches in thermal and mechanical loading. They observed the propagation path of cracks to be occurred due to the effect of temperature. It could be the measure of crack tip stresses that occurred while loading. Aiello et al. [9] proposed the analytical model for finding the temperature rise (ΔT) to initiate the cracking phenomenon to complete concrete failure. They found the FRP reinforced concrete elements under Thermal loads. The nonmetallic rebars were presented with high transverse coefficients of thermal expansion, which increased the temperature of concrete when tensile stresses act. Camanho and Catalanotti [10] studied the fracture toughness of a multidirectional carbon–epoxy composite with 0º ply angle. The model developed was the combination of lamination theory and linear-elastic fracture mechanics. Fracture toughness of any material would play an important role in offering considerable resistance to cracks. Shi et al. [11] developed a method to predict the compressive strength and failure of the silica fiber-reinforced phenolic composites under thermo-mechanical loading. They got results with good agreement between the experimental measured strength values and curve obtained by calculated values. Shi et al. [12] proposed a model for predicting FRP composite degradation behavior supporting static compressive loading under high temperatures. They found that the proposed model can be good for predicting FRP composite properties based on the temperature.

Le and Gardin [13] studied the propagation of a surface crack due to the cyclic thermal loading over a stainless steel specimen. They introduce the analytical and numerical approach for kinematics of the crack and crack shape evolution. They found the results are in good agreement with the analytical approach and numerical approaches supported by experimental results. Barroso et al. [14] provided a general procedure for evaluating fracture toughness value with different experimentation techniques. The process, explained in their work, was apt to apply it for anti-symmetric models that possessed dual singularity of multi-material corners. Berto et al. [15] conducted more than 70 fracture tests on specimens with notches made of polymethyl-methacrylate at room temperature. The notch root radius varies from 0.1 to 7mm for semicircular notches, U-shaped and V-shaped notches to conduct the static test.

Pinto et al. [16] developed a method to measure inter-laminar cracks that occurred due to extreme temperatures. The double-edge notched (DEN) specimen is used to find the crack resistance curve. Li et al. [17] analyzed the dynamic nature of crack growth in elastic-plastic solids numerically when the local heating and temperatures raised the whole phase transition of crack-tip stress and deformation from elastic to plasticity by estimating the work done due to heat generation. Rolfes and Rohwer [18] estimated temperature distribution in the thickness direction. They developed suitable elements for numerical analysis and experimentally verified the same with the problems about both steady-state and transient cases. The researchers also tried to improve the flexural and shear strength of RC Beam Reinforced by Glass Fiber-Reinforced Polyurea (GFRPU) [19]. They observe significant improvement in resistive capacity and ductility for non reinforce beams over reinforced beams. Also, the change in design like blade edge and adding edged on the torsional bar helps improve mechanical properties of components used in various engineering applications [20].

From the literature survey, it is clear that most researchers are tried to investigate the fractural toughness of various composite materials. For the investigation, researchers are used numerical simulations and experimental methodologies depending on various conditions and applications. Researchers used some thermal, mechanical, and thermo-mechanical loading conditions and the different types of composite construction conditions. But there is still scope to introduce the effect of cross-ply and angle-ply composite laminated structures on thermal, mechanical, and thermo-mechanical loading combination in the single composition of composite materials. Therefore, the present investigation is based on the study of the fracture toughness of FRP composite effect on composite laminate (cross-ply and angle-ply) under the thermal, mechanical, and thermo-mechanical loading conditions finite element analysis methodology. FEA results validate with published literature.

2. FEA WORK

2. 1. Problem Configuration, Geometry and Fracture Mode A cross-ply and angle-ply composite laminate along a virtual crack and circular hole at its center was considered. Figure 1 shows the application of circular cut-out in a composite panel used in the Aircraft. For the present investigation, two types of cases i.e., pure thermal and structural loading was

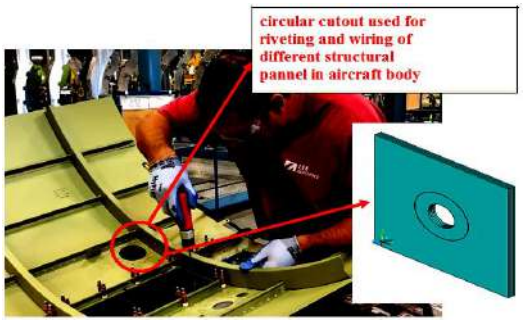

Figure 1. Circular Cut-out in a Composite panel used in the Aircraft

considered. The angle (+45º/-45º) and (0º/90º) is considered for the angle-ply and cross-ply, respectively. Figure 2 shows the angle-ply and cross-ply representation used in the development of composite lamina. A volume has been created with 100 mm X100 mm X5 mm of length, width, and thickness, and a circular cut-out of 20mm diameter is modeled at the geometrical center of the plate. Figure 3 shows the geometry of the composite laminate along with dimensional details and arrangements. A crack is modeled with 20 mm around the circular cut-out periphery-out with a virtual crack of a 0.22 mm diameter around it and between the second and third layers of the laminate. The thickness of the laminate 5mm is divided into four laminas i.e.5/4= 1.25 mm, with each layer having a thickness of 1.25 mm. In this 1.25 mm layer, the desired fiber angle is maintained.

During the analysis the three different ways (Modes) fracture are considered of presenting a force to enable a crack to propagate. These ways are famously termed as modes of fracture as shown in Figure 4. Mode I fracture, where the tensile stress acts normal to the plane of crack. It is also termed as opening mode, as it creates an opening to the crack to propagate further. It is representing by G_I during the present investigation. Mode II fracture, where the shear stress is acting parallel to the plane of the crack and perpendicular to the crack front. It is represented by G_{II} during the present investigation. Mode III fracture, where a shear stress acting parallel to the plane of the crack and parallel to the crack front. It is represented by G_{III} during the present investigation. Mixed Mode fractures, in general structures are subjected to not only simple tension or compression loadings but also to shear as well as torsion loads. This combination of different type of loading patterns will lead to combination of three basic modes, known as mixed mode. Mixed modes can be a result of different types of interactions such as mixed mode I/II or mode II/III or mode I/III. The summation of all three modes i.e. total mode it is denoted by G_T.

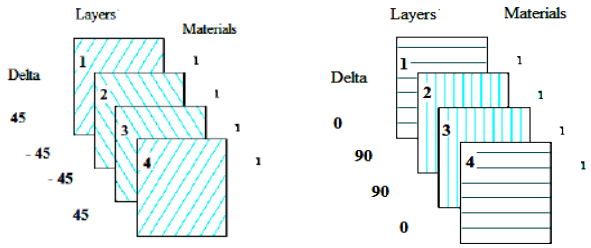

a) Angle-ply b) Cross-ply

Figure 2. Angle-ply and Cross-ply representation[21]

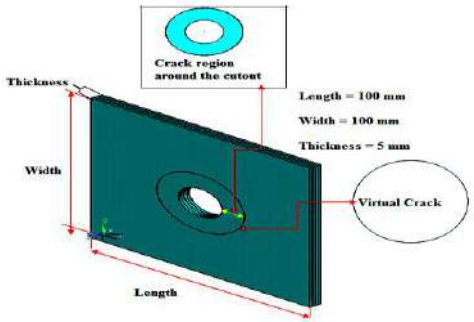

Figure 3. Circular cut-out composite laminate layup with the virtual crack

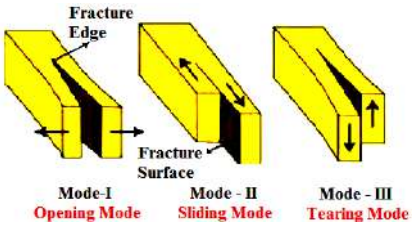

Figure 4. Fracture modes [21]

2. 2. FE Model Figure 5 shows the geometry of composite lamina and virtual crack which is considered for the analysis. The solid 20 node 186 elements are used for the present investigation along with refinement and suitable meshing.

2. 3. Material Properties The composite modeling was done using lamina material 3501-6 epoxy along AS4 carbon fiber inside surrounded. From I.

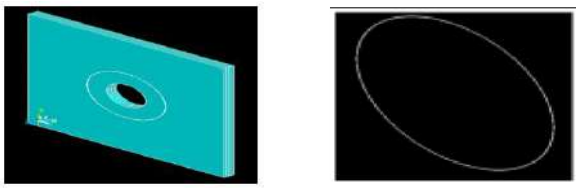

Figure 5. Geometry of the Composite Laminate and virtual crack

Daniel and Oriish [21] required material properties are used for the analysis. Initially composite lamina at 0º fiber angle are considered for the materials properties from reference, then material properties of composite lamina for 45º and 90º find using a simple MATLAB code. Table 1 shows the properties of the AS4/3501-6 Carbon/Epoxy lamina.

2. 4. Boundary and Loading Conditions Figure 6 shows the composite lamina after applying meshing and boundary conditions. The ANSYS software is used for the meshing and applying the boundary conditions. The displacement constraints are applied on all four edges of the composite lamina by considering similar supported conditions. The two loading conditions are considered i.e., Thermal and Mechanical. Initially, in the first case, Mechanical loading is applying to geometry; for this loading, a pressure of 5 MPa is considered. The 5 MPa load pressure is applied on the top face of the composite lamina, and the direction of loading is downward. The thermal loading is considered in the second case of analysis. Thermal loading is applied on the geometry; for this loading 30˚C temperature is considered starting temperature, then temperature increases up to 180ºC. Results are finding with the interval of 50ºC temperature difference applied on the composite lamina.

3. RESULTS AND DISCUSSION

3. 1. Mechanical Load (Angle-ply Vs Cross-ply) Figure 7 shows that the variation of G_I, G_{II} and G_{III} with respect to the S.E.R.R. for Angle-ply (+45º/-45º)s and cross-ply (0º/90º)s under Mechanical loading. As represented in Figure 7, the shearing mode energy release rate (G_{II}) is more and the shearing action of the laminate with cut-out will be minimized by arranging the fibre in cross layup. For the case of G_I, the Angle-ply laminated yielded maximum SERR as compare to Cross-ply laminate. In the case of G_{II}, the Angle-ply laminate setup showed maximum SERR and Cross-ply laminate showed minimum SERR. In the G_{III} case, the Cross-ply SERR is maximum and angle-ply SERR is minimum. Therefore, the cross-ply is significant useful and good results for mode I and II failure while for mode III angle play having an important role as compare to crass-ply.

TABLE 1. Material Properties considered for FEA

As4/3501-6 Epoxy carbon Composite Properties										
E_{11} (Gpa)	E_{22} (Gpa)	E_{33} (Gpa)	G_{12} (Gpa)	G_{23} (Gpa)	G_{13} (Gpa)	ν_{12}	ν_{23}	ν_{13}	$\alpha 1$ (10^{-6}/ºC)	$\alpha 2 = \alpha 3$ (10^{-6}/ºC)
147	10.3	10.3	7.0	3.48	7.0	0.27	0.51	0.27	-0.9	27

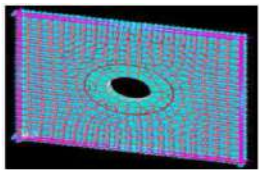

Figure 6. Boundary Conditions applied for the composite laminate

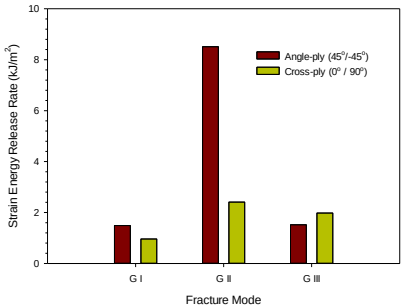

Figure 7. Modification in SERR with different modes of fracture under Mechanical Load of 5 MPa for Angle-ply and Cross-ply

3. 2. Thermal Load (Angle-ply Vs Cross-ply) Figure 8 shows the change in SERR with the increase of temperature under thermal load for different layup of composite laminas. The three different mode of fracture is considered for investigating the effect of thermal loading on different layup of composite laminas. The GI, GII, &GIII are the fracture modes consider for change in SERR with respective temperature under thermal loading for different layup of composite laminas. The investigation is based on the temperature range 30^0C to 180^0C. The SERR is check for the point of 50^0C temperature interval point under the given temperature range. Figure 8 mode I, II and III shows the SERR results with respect to fracture mode G_I, G_{II}, &G_{III} respectively for the angle-ply (+45º/-45º)s and cross-ply (0º/90º)s . The similar kind of graphical trend observed of all three type of fracture mode I, II and III. The angle-ply gives better results in terms of SERR for all three mode of fracture as compare to cross-ply. The fracture mode II is having maximum SERR for angle-ply and cross ply as compare to remaining mode. Mode III and II are having results of SERR followed by mode I. The mode I having SERR range 0.0002 to 0.0064

kg/m^2 for angle and cross-ply composite laminas. Similarly, the results of SERR range (0.03 to 0.8 kg/m^2) and (0.0005 to 0.015 kg/m^2) for mode II and III respectively.

Figure 8 mode I show the approximately 10, 8.3 and 7.9 time higher SERR for cross-ply as compare to angle-play. Similarly, mode II results show the approximately 11.52, 9.59 and 8.72 time higher SERR for cross-play as compare to angle-ply. At mode III the SERR approximately 8.5, 8.4 and 6 times higher for cross-ply as compare to angle-play. The SERR at mode II is higher side for all temperature points for cross-ply as compare to angle-ply. Therefore, angle-ply is more reliable as compare to cross-ply for change in temperature from range 30^{0}C to 180^{0}C as SERR concern.

3. 3. Thermal Load in Mixed Mode (Angle-plyVsCross-ply) Figure 9 shows the variation of SERRfor mixed mode i.e. (G_I/G_T, G_{II}/G_T and G_{III}/G_T) with the increase of temperature under thermal load for different layup of composite laminas. There is a falling in G_I/G_T with respect to the temperature and a slight higher value is observed for cross-ply $(0^o/90^o)_S$ of fibre angle. Similar type observations and graph trend appear for G_{II}/G_T with respect to temperature for cross-ply and angle-ply. There is ascending trend in G_{III}/G_T with respect to the temperature and slight higher value is observed for cross-ply $(0^o/90^o)_S$ of fibre angle. G_{III}/G_T ratio shows the reverse trend as compare to result obtained for G_I/G_T & G_{II}/G_T this is because of less contribution of G_{III} for overall fracture of given composite laminas i.e. angle-ply and cross-ply. The ratio G_{II}/G_T result shows the maximum variation between the angle-ply and cross-ply because mode II having maximum SERR for both the type of angle composite laminas.

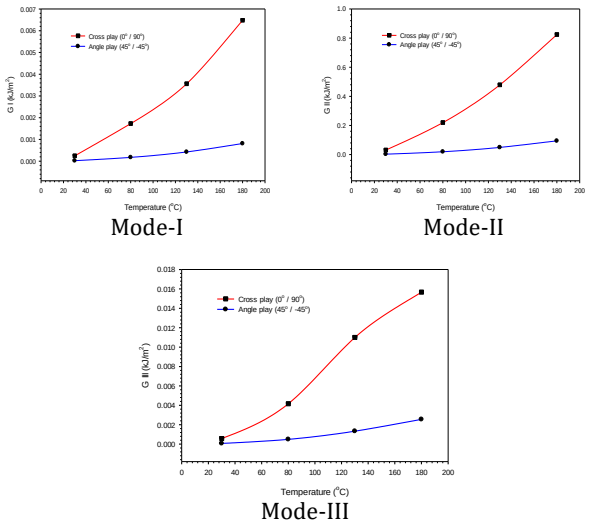

Figure 8. Discrepancy in SERR with the increase of temperature under Thermal Load between different layup configurations in three different modes

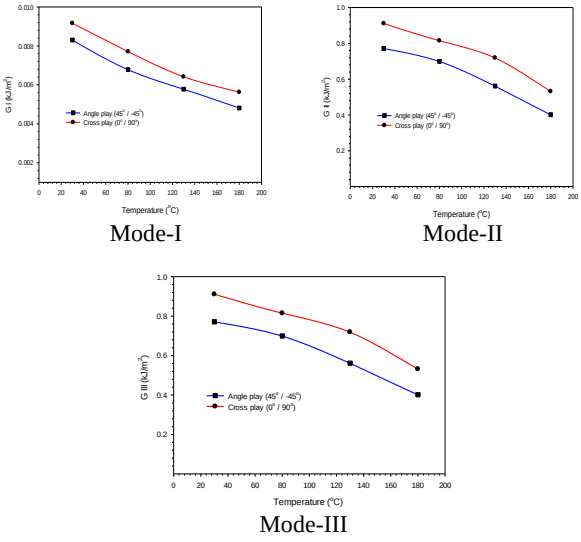

Figure 9. Difference in SERR with the increase of temperature under Thermal load between different layup configurationsof mixed mode fracture in three different modes

3. 4. Validation for Circular Cut-out The results obtained by FEA are validated with results available in published literature. Table 2 shows that the SERR values for cross-ply (0^o/90^o) and angle-ply (+45^o/-45^o) layup are 0.02 J/m^2 and 0.003 J/m^2, respectively machetes with published literature of Ramesh Babu and Pradhan [22]. The percentage error between results of present investigation and publishes literature are within the considerable range under 5%.

4. CONCLUDING REMARKS

In mechanical loading conditions, G_{II}, i.e., mode II shows the maximum SERR for both angle and cross-ply composite laminas compared to G_I & G_{III}. This is because mode II is base on sliding movement and

TABLE 2. SERR due to Thermal Load of Mode I (G_I) for different fibre layup configuration of circular cut-out

Layup configuration	SERR Value obtained SERR (J/m^2)	SERR Value Ramesh Babu& Pradhan (22) SERR (J/m^2)	Percentage Error
Cross-ply ($0^0/90^0$)	0.0206	0.02	2.91 %
Angle-ply ($+45^0/-45^0$)	0.00305	0.003	1.64 %

action. Angle-ply shows less SERR for mode I and II, but at mode III, cross-ply shows less SERR for mode III composite laminas subjected under mechanical loading conditions. G_{III}, the cross-ply value is higher than angle-ply in normal load.

Same composite laminas are tested for the thermal loading condition result shows an increase in SERR with respect to increases in temperature. The forgiven composite material increase in temperature toughness and stiffness decreases, i.e., an increase in SERR. In thermal loading mode II, results show the approximately 11.52, 9.59, and 8.72 times higher SERR in cross-play compared to angle-play for temperature 80ºC, 130ºC & 180ºC, respectively.

In mixed mode and thermal loading conditions, G_I/G_T and G_{II}/G_T show the same trend of SERR results. G_{III}/G_T mixed-mode III shows a reverse trend as compare to other modes this is because less contribution of SERR in mode III, i.e., GIII in G total mode, i.e., in G_T

6. REFERENCES

1. M. R. M. Asyraf, M. R. Ishak, S. M. Sapuan, N. Yidris, R. A. Ilyas, M. Rafidah, and M. R. Razman, "Potential Application of Green Composites for Cross Arm Component in Transmission Tower: A Brief Review", ***International Journal of Polymer Science,*** Vol. 2020, https://doi.org/10.1155/2020/8878300.
2. N. M. Nurazzi, M. R. M. Asyraf, A. Khalina, N. Abdullah, H. A. Aisyah, S. Ayu Rafiqah, F. A. Sabaruddin, S. H. Kamarudin, M. N. F. Norrrahim, R. A. Ilyas, and S. M. Sapuan, "A Review on Natural Fiber Reinforced Polymer Composite for Bullet Proof and Ballistic Applications", ***Polymers,*** Vol. 13, 646, (2021), https://doi.org/10.3390/polym13040646
3. Norizan Mohd Nurazzi, M.R.M. Asyraf, Abdan Khalina, Norli Abdullah, Fatimah Athiyah Sabaruddin, Siti Hasnah Kamarudin, So'bah Ahmad, Annie Maria Mahat, Chuan Li Lee, H. A. Aisyah, Mohd Nor Faiz Norrrahim, R. A. Ilyas, M. M. Harussani, M. R. Ishak, and S. M. Sapuan, "Fabrication, Functionalization, and Application of Carbon Nanotube-Reinforced Polymer Composite: An Overview", ***Polymers,*** Vol. 13, 1047, (2021), https://doi.org/10.3390/polym13071047
4. M.R.M. Asyrafa, M.R. Ishaka, S.M. Sapuand, N. Yidris, R.A. Ilyas, "Woods and composites cantilever beam: A comprehensive review of experimental and numerical creep methodologies", ***Journal of Material Research and Technology***, Vol. 9, No. 3, (2020), 6759-6776.
5. M. R. M. Asyraf, M. R. Ishak, S. M. Sapuan, N. Yidris, R. M. Shahroze, A. N. Johari, M. Rafidah and R. A. Ilyas, " Creep test rig for cantilever beam: Fundamentals, prospects and present views", ***Journal of Mechanical Engineering And Sciences*** (JMES), Vol. 4, (2020), 6869-6887.
6. S. Alsubari, M. Y. M. Zuhri, S. M. Sapuan, M. R. Ishak, R. A. Ilyas, and M. R. M. Asyraf, "Potential of Natural Fiber Reinforced Polymer Composites in Sandwich Structures: A Review on Its Mechanical Properties", ***Polymers***, Vol. 13, 423, (2021), https://doi.org/10.3390/polym13030423
7. D. Wang, N. N. Kishoret and C. A. Li, "Crack Development in Graphite-Epoxy Cross-ply Laminates under Uni axial Tension", ***Composites Science and Technology***. Vol. 24, (1985) 1-31.
8. Joon-Soo Bae, Sridhar Krishnaswamy, "Subinterfacial cracks in biomaterial systems subjected to mechanical and thermal loading", ***Engineering Fracture Mechanics***, Vol. 68, (2001), 1081-1094.
9. Maria A. Aiello, Francesco Focacci2 and Antonio Nanni3, "Effects of Thermal Loads on Concrete Cover of FRP Reinforced Elements: Theoretical and Experimental Analysis", ***ACI Materials Journal***, Vol. 98, (2001), 332-339.
10. P.P. Camanho, G. Catalanotti, "On the relation between the mode I fracture toughness of a composite laminate and that of a 0_ ply: Analytical model and experimental validation", ***Engineering Fracture Mechanics***, Vol. 78, (2011), 2535-2546.
11. Shengbo Shi, Jun Liang, LiangxianGu, Chunlin Gong, Lihua Wen, Yifan Wang, "Degradation in compressive strength of silica/phenolic composites subjected to thermal and mechanical loading", ***Journal of Reinforced Plastics and Composites***, Vol. 35, No. 7, (2016), 579-588.
12. Shengbo Shi, LiangxianGu, Jun Liang, Guodong Fang, Chunlin Gong, Cunxi Dai, "A mesomechanical model for predicting the degradation in stiffness of FRP composites subjected to combined thermal and mechanical loading", ***Materials and Design***, Vol. 89, (2016), 1079-1085.
13. Hoai Nam Le, C.Gardin,"Analytical prediction of crack propagation under thermal cyclic loading inducing a thermal gradient in the specimen thickness-comparison with experiments and numerical approach", ***Engineering Fracture Mechanics***, Vol. 78, (2011), 638-652.
14. A. Barroso, D. Vicentini, V. Mantic, F. Paris, "Determination of Generalized Fracture Toughness in composite multimaterial closed corners with two singular terms - Part I: Test proposal and numerical analysis", ***Engineering Fracture Mechanics***, Vol. 89, (2012), 1-14.
15. F. Berto, M. Elices, P. Lazzarin, M. Zappalorto, "Fracture behaviour of notched round bars made of PMMA subjected to torsion at room temperature", ***Engineering Fracture Mechanics***, Vol. 90, (2012), 143-160.
16. R.F. Pinto. Catalanotti, P.P. Camanho, "Measuring the intralaminar crack resistance curve of fibre reinforced composites at extreme temperatures", ***Composites: Part A***, Vol. 91, (2016), 145-155.
17. Wen Li, Xiaomin Deng, Ares J Rosakis, "Determination of temperature field around a rapidly moving crack-tip in an elastic-plastic solid", ***International Journal of Mass Transfer***, Vol. 39, (1996), 677-690.
18. R. Rolfes, K. Rohwer, "Integrated thermal and mechanical analysis of A. S. composite plates and shells", ***Composites Science and Technology***, Vol. 60, (2000), 2097-2106.
19. Jun-Hyeok Song, and Hee-Chang Eun, "Improvement of Flexural and Shear Strength of RC Beam Reinforced by Glass Fiber-Reinforced Polyurea (GFRPU)", ***Civil Engineering Journal***, Vol. 7, No. 3, (2021), 407-418.
20. Kwangtae Ha, "Innovative Blade Trailing Edge Flap Design Concept using Flexible Torsion Bar and Worm Drive", HighTech and Inn, Vol. 3, No. 2, (2020), 101-106.
21. I.M.Daniel, Isaac M., OriIshi, 2006. ***Engineering Mechanics of Composite Materials***, Oxford University Press.
22. P. Ramesh Babu, B. Pradhan, "Thermo elastic effects on mixed-mode delamination growth emanating from circular holes in laminated FRP composites", ***Composite Structures***, Vol. 82, (2008), 50-60.

Persian Abstract

از قبل مواد ترکیبی انتشار ترک یک مشکل خرابی منظم در کاربردهای مختلف مهندسی خصوصاً در بدنه هواپیما است. اجزای بدنه هواپیما تحت شرایط بارگیری حرارتی و مکانیکی مختلفی قرار دارند. آزمایش خرابی اجزای هواپیماها به دلیل شرایط مختلف حرارتی و مکانیکی بسیار دشوار ، زمانبر و پرهزینه است. میزان انتشار انرژی کرنش (SERR) پارامتر قابل توجهی برای مواد کامپوزیتی است و کیفیت مواد کامپوزیتی به مقادیر SERR بستگی دارد. تحقیق حاضر بر اساس تجزیه و تحلیل ANSYS برای یافتن مقدار سرعت انتشار انرژی کرنش با استفاده از تکنیک بستن ترک مجازی (VCCT) برای درک رفتار شکست لایه کامپوزیت. ترک دایره ای موجود در وسط صفحه کامپوزیت و تحت فشار و بارگذاری دما برای ورقه های مختلف ساختار کامپوزیت زاویه دار (ورق ضخیم و ورق زاویه ای) است. زاویه پیچ در حالت I و II SERR کمتری را نشان می دهد در حالی که ضربدری در شرایط بارگذاری فشار ثابت SERR کمتری را در حالت III نشان می دهد. حالت II در دمای ۳۰ ، ۱۳۰ و ۱۸۰ درجه سانتیگراد حداکثر SERR را در مقطع نسبت به حالت I و III نشان می دهد. SERR برای حالت مخلوط با در نظر گرفتن حالت کلی شکستگی و اعتبارسنجی بر اساس ادبیات منتشر شده برای SERR به دلیل بار حرارتی حالت I (GI) برای پیکربندی های مختلف شکل دهی فیبر برش دایره ای ، مشاهده گردید.

IJE TRANSACTIONS C: Aspects Vol. 34, No. 6, (June 2021) 1533-1539

International Journal of Engineering

Journal Homepage: www.ije.ir

Ratcheting Analysis of Steel Plate under Cycling Loading using Dynamic Relaxation Method Experimentally Validated

S. I. Shahraini, M. Kadkhodayan*

Department of Mechanical Engineering, Ferdowsi University of Mashhad, Mashhad, Iran

P A P E R I N F O

Paper history:
Received 26 November 2020
Received in revised form 02 April 2021
Accepted 24 April 2021

Keywords:
Ratcheting
Dynamic Relaxation Method
Bending Loading
Elastic-plastic Deformation

A B S T R A C T

The present study aimed to introduce a numerical method to study ratcheting strains of rectangular plates. A new numerical analysis was conducted by development of dynamic relaxation method combined with MATLAB software to evaluate the ratcheting behavior of the thin steel plate under mentioned loading condition. In order to verify the results, experimental tests were performed under stress-controlled conditions by a zwick/roell amsler HB100 machine and bending ratcheting of CK45 steel plate at room temperature was studied. Under stress-controlled conditions with non-zero mean stress, ratcheting behavior occurred on thin plate. Moreover, a finite element analysis was carried out by Abaqus using nonlinear isotropic/kinematic (combined) hardening model. The results showed that the rate of ratcheting strain decreased with an increase in cycle number. It was found that the hysteresis loops were wider in experimental method than those of other methods because of more energy dissipation. The numerical results are in a good agreement with the simulation and experimental data. Comparison of errors between these methods obviously demonstrate high accuracy of the new introduced method.

***doi**: 10.5829/ije.2021.34.06c.17*

1. INTRODUCTION

Cyclic plastic deformation as an important source of the fatigue life-limiting factor can lead to catastrophic failure in critical engineering installations [1, 2]. On account of applied load and symmetric or asymmetric strain/stress cycling, materials will fail by high or low cycle fatigue, mean stress relaxation and ratcheting [3]. Ratcheting corresponds on progressive plastic deformation under stress-controlled cyclic loading with asymmetric stress (non-zero mean stress), if applied load is kept high enough for inelastic deformation [1, 4]. Ratcheting or cyclic creep is related to cyclic accumulation of strain, in the direction of mean stress [5]. Accumulation of ratcheting strain, formation and shifting of stress-strain hysteresis loop can lead to fatigue damage [2]. Therefore, simulations of hysteresis loop curves are highly important in numerical modeling of cyclic plastic deformation [6]. Investigation of ratcheting phenomena is important to estimate remaining life, assess safety of components and design the structures [2].

As ratcheting has the highest detrimental influence on fatigue life in comparison between other forms of cyclic plastic deformation, numerous investigations have been conducted based on determination of effective controlling factors of ratcheting. Recent studies in the field of ratcheting are devoted to three categories including: (1) experimental studies on the influence of loading amplitude, temperature, loading rate, mean stress, etc. [7-10], (2) experimental studies on ratcheting behavior under uniaxial or multiaxial loading [11-13], and (3) numerical studies on development of ratcheting models [14, 15].

Considering necessity of research cost reduction and on account of ratcheting importance, it is noteworthy to numerically investigate the nonlinear ratcheting event. Dynamic Relaxation (DR) method as an approximate iterative technique, which is suitable for nonlinear analysis, explicitly solves the simultaneous system of equations and can be used for ratcheting investigation. So far, various studies have been conducted on using

*Corresponding Author Institutional Email: kadkhoda@um.ac.ir (M. Kadkhodayan)

Please cite this article as: S. I. Shahraini, M. Kadkhodayan, Ratcheting Analysis of Steel Plate under Cycling Loading using Dynamic Relaxation Method Experimentally Validated, International Journal of Engineering, Transactions C: Aspects Vol. 34, No. 6, (2021) 1533-1539

DR method to solve different problems. Collins and Cosgrove [16] used DR modeling for braced bending active grid shells with rectangular sections. Their model was validated by reference to closed form benchmark solutions and finite element models. The results exhibited major stiffness variations in various bracing and joint models. DR method was utilized by Golmakani and Kadkhodayan to solve non-linear thermo-mechanical bending behavior of thin and moderately thick functionally graded sector plates [17]. They compared the bending analysis results of sector plate based on first order shear deformation theory and classical plate theory. Zhang et al. [18] investigated the post-buckling analysis of compressed rods in cylinders by introducing a DR method. They proved that the results of numerical simulation were in good agreement with the analytical ones. DR method was used to compute the structural buckling limit load by Rezaiee Pajand and Estiri [19]. They stated that their method can successfully estimate the buckling limit load of structures. Esmaeilzadeh and Kadkhodayan [20] analyzed the stiffened porous bi-directional functionally graded plates by DR method.

Besides of using DR method in solving problems, its modifications and combination of this method with other numerical techniques were taken into consideration in recent literature. Kadkhodayan and Alamatian [21] developed DR method by introducing a modified fictitious time increment determined by minimizing the residual force after each iteration. They demonstrated the advantages, potentiality and high efficiency of this new method. They also showed that the modified fictitious time optimized the convergence rate of the DR method. Namadchi and Alamatian [22] combined DR method with the explicit-implicit time integrations. They found that applying the proposed strategy led to excellent accuracy in comparison with the well-known implicit Newmark and Wilson schemes. They concluded that their method reduced the computational efforts and it had a potential to combine with any explicit-implicit time integration method. Rezaiee-Pajand and Estiri [23] explored the capability of mixing DR method with load factor and displacement increments to trace the complex structural equilibrium path. They proved this suggested approach by applying it on several 3D trusses and 2D frames, with geometrical nonlinear behavior. The results demonstrated the successful trace of the complex structural equilibrium path. Rezaiee Pajand and Estiri [24] found the buckling points for nonlinear structures by implementing DR scheme. Setting the external work zero, they introduced a new scheme to calculate the load factor. The results of their study indicated that the quick proposed approach could trace the complex structural static paths, even in the snap-back and snap-through parts.

In order to generate accurate cutting patterns for tensile fabric structures, Gale and Lewis [25] proposed a new patterning method by using a discrete element model, advanced flattening methods, DR and re-meshing. They stated that the proposed model as a simple alternative was suitable for cutting pattern generation. Based on a DR algorithm, Wang et al. [26] presented a novel numerical form-finding method for cable nets in mesh reflectors. They demonstrated that the presented method could predetermine the uniform distribution of forces and also, it had a much higher calculating efficiency and a much less total calculating time for mesh reflectors than the existing algorithms.

In view of importance of ratcheting and considering precision of DR method, it is worth to use DR in the studies of ratcheting phenomena, which has not been reported yet in the literature. In this paper, ratcheting behavior of CK45 steel plate is experimentally investigated and also, ratcheting of mentioned plate is simulated by Abaqus. Then, as the main objective of this paper, a proposed numerical method by development of DR technique is introduced and the obtained results of Abaqus model, experimental investigation and proposed method were compared.

2. MATERIALS AND METHODS

2. 1. Geometrical and Mechanical Properties

The rectangular plate used in this investigation is made of CK45 steel. The chemical composition of the material is Mn 0.65%, C 0.46%, Si 0.25%, P 0.05% and S <0.05%. The geometry of the rectangular plate is taken as 180 mm length, 50 mm width and 3 mm thickness. The standard tensile test of material was performed by Shariati and Mehrabi [27]. On the other hand, the specimen of the present study is prepared from the other part of mentioned material. Therefore, the mechanical properties of specimen are extracted from stress-strain curve obtained from previous study [27] as summarized in Table 1.

2. 2. Experimental Setup and Procedure

The device used in this research is a zwick/roell amsler HB100 machine shown in Figure 1. The apparatus is connected to a computer for the test control as well as

TABLE 1. Mechanical properties of CK45 [27]

Property	Values
Young's modulus	E = 204 GPa
Yield stress	σ_y = 384 MPa
Ultimate stress	S_u = 690 MPa
Poisson's ratio	ϑ = 0.3

data acquisition. Experiments were carried out at room temperature and under stress-controlled condition with mean load of 350N and load amplitude of 350N. To apply the cyclic bending load a proper fixture is designed. It is used to exert the sinusoidal load to the center of rectangular plate. This type of loading causes bending of plate cyclically. Figure 2 shows the schematic of rectangular plate placed on the bending fixture.

2. 3. Development of DR Method for Ratcheting Analysis To analyze the structures using DR method, the static system of equations is converted to fictitious dynamic space. As can be seen in Equation (1), the dynamic system achieved by adding fictitious mass and damping factor to the static system of equations,

$$[M]\{\ddot{X}\} + [C]\{\dot{X}\} + [S]\{X\} = \{P\} \quad (1)$$

where $[M]$, $[C]$, $[S]$ and $\{P\}$ denote mass, damping and stiffness matrices and vector of the forces, respectively. The factors of $\{x\}$, $\{\dot{x}\}$, $\{\ddot{x}\}$ refer to displacement, velocity and the system acceleration. For simplification purpose, the matrix of fictitious mass is considered to be diagonal. Additionally, the factors of acceleration and velocity are obtained approximately by using the techniques of finite differences as follows:

$$\dot{X}^{n+\frac{1}{2}} = \frac{1}{t^{n+1}}(\{X^{n+1}\} - \{X^n\}) \quad (2)$$

$$\dot{X}^n = \frac{1}{2}\left(\left\{\dot{X}^{n-\frac{1}{2}}\right\} + \left\{\dot{X}^{n+\frac{1}{2}}\right\}\right) \quad (3)$$

$$\ddot{X}^n = \frac{1}{t^n}\left(\left\{\dot{X}^{n+\frac{1}{2}}\right\} - \left\{\dot{X}^{n-\frac{1}{2}}\right\}\right) \quad (4)$$

Furthermore, damping matrix is defined as a coefficient of mass matrix. This relation can be written as $[c^n] = c^n[M]$ where the factor of c^n is the damping coefficient of n^{th} step. Substituting the values of velocity and acceleration and defining damping matrix in equilibrium equation of dynamic system of step n, the velocity is obtained in time $t^{n+\frac{1}{2}}$ and then the result of the next step is computed as follows:

$$\{X^{n+1}\} = \{X^n\} + \tau^{n+1}\left\{\dot{X}^{n+\frac{1}{2}}\right\} \quad (5)$$

In most strategies of DR, time step is assumed to be constant (equal to 1). Mass matrix is diagonal in DR method; Hence, the results of $[M^n]^{-1}\{R^n\}$ can be calculated in the form of R_i^n/m_{ii}^n where the R_i^n and m_{ii}^n are respectively the residual force of i^{th} degree of freedom and i^{th} diagonal entry from mass matrix in n^{th} step. The residual is computed by:

$$\{R^n\} = \{P^n\} - \{f^n\} = [M]\{\ddot{X}^n\} + [C]\{\dot{X}^n\} \quad (6)$$

In this equation, mass matrix, damping and time step are unspecified. General relation for mass values are obtained by [28]:

$$m_{ii} = \frac{(\tau^n)^2}{4}\text{Max}\left[\sum_{i=1}^{ndof}|S_{ij}|\ ,\ 2S_{ii}\right] \quad (7)$$

where the factor of *ndof* is the indicator of the number of degree of freedom.

In view of dynamic systems, the critical damping of the system leads to maximize the convergence rate. Therefore, the critical damping is estimated by Rezaee Pajand and Taghavian Hakkak [29]:

$$c^n = 2\sqrt{\frac{\{X^n\}^T\{f(X^n)\}}{\{X^n\}^T[M]\{X^n\}}} \quad (8)$$

With the determination of these parameters, it is possible to utilize DR method in ratcheting analysis. In the current study, DR algorithm is developed to be able

Figure 1. Zwick/roell amsler HB100 machine

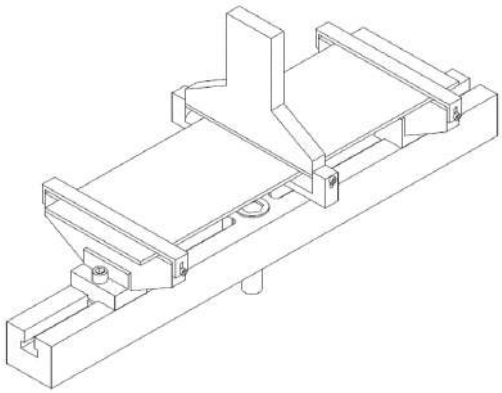

Figure 2. Schematic of rectangular plate placed on the bending fixture

to solve cyclic problems. So, when loading reaches to a certain defined maximum value, reverse loading (unloading) is applied to the specimen sinusoidally. Maximum and minimum loads are kept constant in all cycles to impose stress-controlled conditions to the ratcheting analysis. Based on kinetic or combined hardening model, yield stress is modified after each loading or unloading. Finally, some additional actions are applied to numerical code to run analysis properly. The steps of ratcheting analysis using DR process are:

1. Let initial velocity $\{\dot{X}^0\} = 0$ and $n = 0$; specify Number of Cycles (NoC), initial displacement $\{x^0\}$, N_{max}, e_R and e_k where e_R and e_k are the convergence indexes of residual force and energy, respectively.
2. Apply boundary conditions.
3. Form stiffness matrix $[S]$ and mass matrix $[M]$.
4. Calculate residual force $\{R^n\}$.
5. If $|R_i^{Ln}| \leq e_R$, go to step 10; otherwise continue.
6. Calculate c^n and $\dot{X}^{n+\frac{1}{2}}$.
7. If the kinetic energy $(\sum_{L=u}^{w}\sum_{i=1}^{n}(\dot{x}_i^{Ln+\frac{1}{2}})^2 \leq e_R$, go to step 10; otherwise continue.
8. Calculate X^{n+1}.
9. Exert boundary conditions.
10. Print the displacements for this increment.
11. $n = n + 1$; if $n > N_{max}$ start new loading/ unloading analysis (step12); otherwise return to step 4.
12. Apply reverse loading (unloading).
13. Modify yield stress based on desired hardening model.
14. If number of cycles < *NoC*, go to step 4; otherwise stop.

2. 4. Finite Element Simulation The finite element simulation is carried out using Abaqus software to analyze the ratcheting behavior of rectangular plate. The plate is modeled using 3D deformable solid elements. To mesh the model, eight-noded C3D8R elements with reduced integration and hourglass control is utilized. This type of meshing improves the convergence rate [30, 31]. A mesh convergence study is conducted for model to ensure accurate simulation results and appropriate mesh density. To eliminate undesired stress concentration, distributed loading is applied to small central area of the plate. A nonlinear isotropic/kinematic (combined) hardening model is applied to obtain ratcheting data. All required data are extracted from stress-strain curve of a recent study [27].

3. RESULTS AND DISCUSSION

The results of ratcheting analysis of CK45 steel plate subjected to cyclically bending load are discussed in this section. Data are obtained from numerical, experimental and Abaqus analyses. Moreover, numerical investigation based on developed DR method, is validated by the results of experimental and Abaqus studies. Figure 3 illustrates the experimental response of bending load on the plate during 50 cycles in comparison with the results of Abaqus simulation and numerical analysis. It is seen that similar plastic deformation occurred in the plate for all three cases. Figure 4 presents the applied sinusoidal load versus cycles. Considering stress-controlled conditions, maximum and minimum load are kept in the range of 0-700 N with mean load of 350 N and load amplitude of 350 N. The relationship between applied load and displacement in the experimental bending ratcheting study is plotted in Figure 5(a). It reveals that the hysteresis loops are converging with increase in the number of cycles. Hysteresis loops are not closed exactly at the maximum load in initial cycles, i.e. intersections of curves are not located at the maximum load as marked by circles in enlarged view of hysteresis loops, Figure 5(b). Therefore, increasing the number of cycles leads to a development in ratcheting displacement and strain accumulation as shown in Figure 5(b).

The ratcheting strain is defined as the average of maximum and minimum strain (ε_{max} and ε_{min}) in each cycle of loading as stated in Equation (9):

$$\varepsilon_r = \frac{\varepsilon_{max} + \varepsilon_{min}}{2} \quad (9)$$

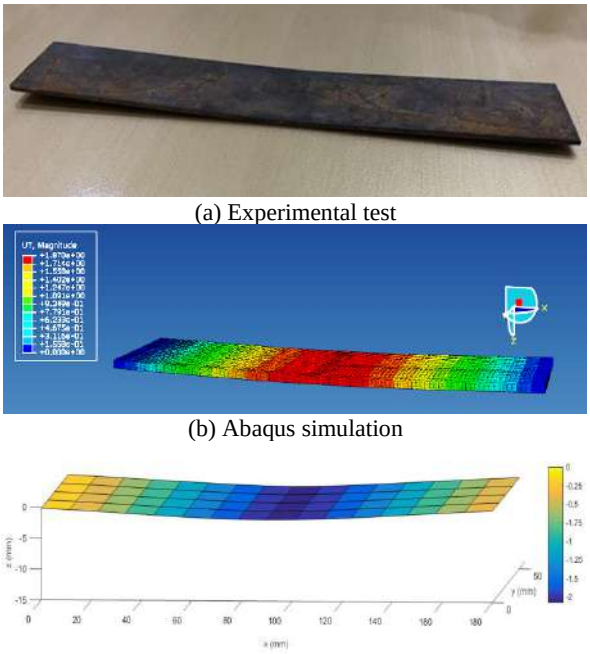

(a) Experimental test

(b) Abaqus simulation

(c) Numerical code

Figure 3. Plate response after 50 cycles, a) Experimental test b) Abaqus simulation, c) Numerical code

The variation of strain accumulation and ratcheting strain with cycles for various methods are demonstrated in Figures 6(a) and 6(b), respectively. It is seen that the ratcheting rate declines with growing number of cycles in the beginning. Then, it remains constant at a steady value and ratcheting strain increases with this constant rate. According to Figures 6(a), 6(b) and comparison between the results of numerical method, experimental study and Abaqus simulation it is obvious that the ratcheting strain values of numerical method are in a good agreement with the those of Abaqus simulation and experimental study. Besides, the results of numerical method gradually become closer to the experimental data. These results clearly validate accuracy of the proposed numerical method. At cycle 50, the error of numerical method is approximately 5.5% whereas the Abaqus simulation has an error of 9.5%.

Experimental hysteresis loops at cycles 1, 5 and 50 are shown in Figure 7. In the range of tested cyclic number, loading and unloading curves does not overlap. It means that the ratcheting strain occurs during loading process and also, strain does not reach the shakedown state. Moreover, it is observed that a rise in the number of cycles decreases the strain rate rapidly. At the higher cycles, the loading and unloading curves are closer than the initial cycles because it is more difficult to produce plastic deformation at higher cycles.

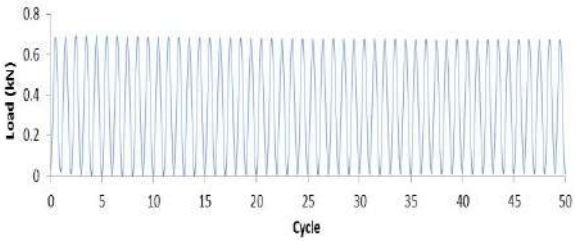

Figure 4. Applied load against cycle

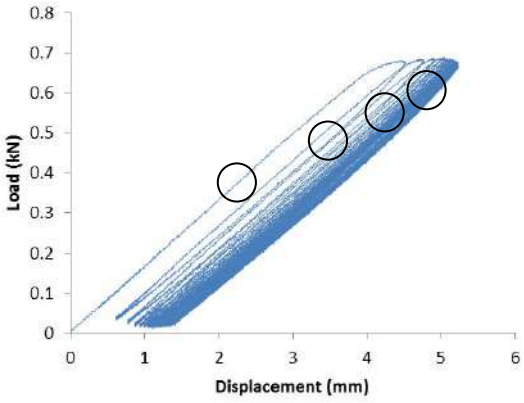

(a) Applied load versus displacement

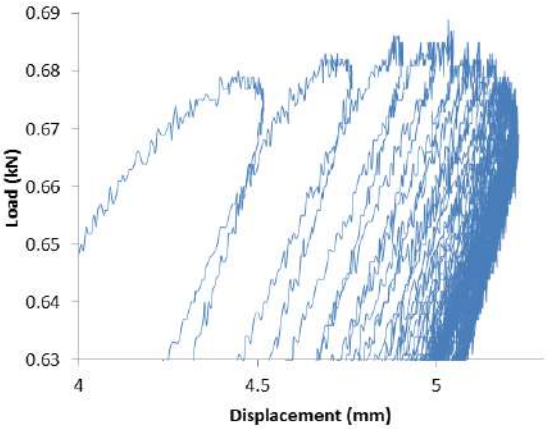

(b) Intersections of curves and development of ratcheting displacement in enlarged view of hysteresis loops

Figure 5. (a) Applied load versus displacement, (b) Enlarged view of hysteresis loops

Figure 8 presents the hysteresis loops for numerical method, experimental study and Abaqus simulation at cycles 1 and 50. The results indicate that the experimental study and Abaqus simulation precisely verify the results of the proposed numerical method, for both cycles. The area of hysteresis loops of experimental study is larger than those of other methods, which is due to existence of more energy dissipation in the experimental study.

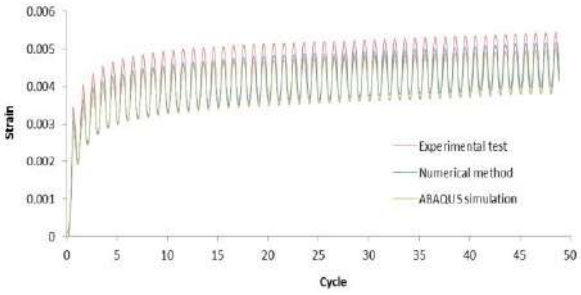

(a) Variation of strain accumulation with number of cycles

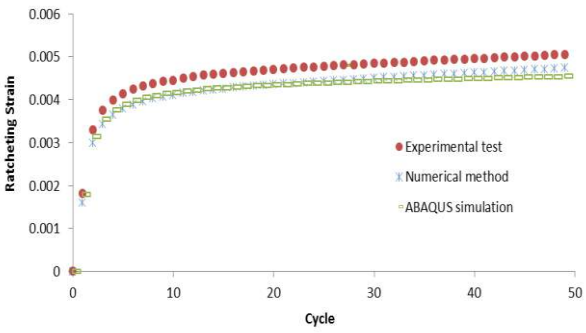

(b) Ratcheting strain against number of cycles

Figure 6. a) Variation of strain accumulation with number of cycles, b) Ratcheting strain against cycles

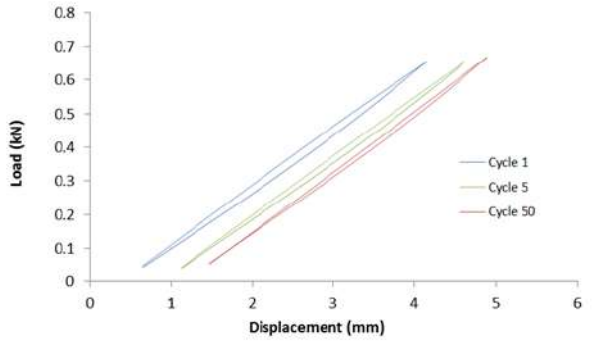

Figure 7. Experimental hysteresis loops at cycles 1, 5 and 50

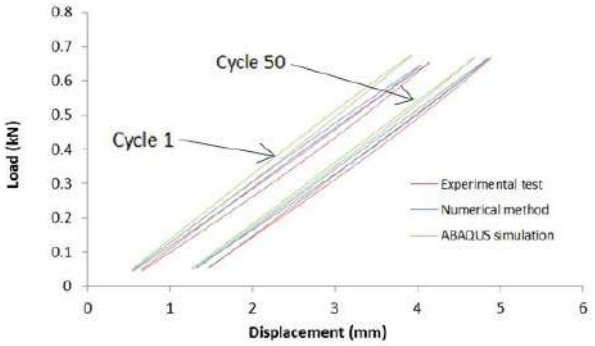

Figure 8. Comparison of hysteresis loops

4. CONCLUSIONS

In this study numerical, experimental and Abaqus simulation of bending ratcheting analysis of CK45 steel plate were conducted. Numerical method was carried out by development of DR method and Abaqus simulation was performed using nonlinear isotropic/ kinematic (combined) hardening model. All the mentioned methods were achieved under stress-controlled conditions. The major findings of this study are as follows:

1. The proposed numerical method for the analysis of ratcheting phenomena is able to predict the results of experimental method more accurate than the Abaqus simulation.
2. The results of numerical method gradually become closer to the experimental ones.
3. The hysteresis loops area of experimental study is larger than those of other methods due to more energy dissipation in experimental study.
4. Dissipated energy per cycle decreases when the number of cycles increases.
5. At the higher cycles, loading and unloading curves are closer and narrower than the initial cycles.
6. Ratcheting rate decreases with increase in the number of cycles.

5. REFERENCES

1. Zeinoddini, M., Ezzati, M., and Fakheri. J., "Uniaxial strain ratcheting behavior of dented steel tubular: An experimental study", ***Engineering Failure Analysis,*** Vol. 44, (2014), 202-216. DOI: 10.101/j.engfailanal.2014.05.016
2. Paul, S.K., "A critical review of experimental aspects in ratcheting fatigue: microstructure to specimen to component", ***Journal of Materials Research and Technology,*** Vol. 8, No. 5 (2019), 4894-4914. DOI: 10.1016/j.jmrt.2019.06.014
3. Paul, S.K. "Effect of anisotropy on ratcheting: an experimental investigation on IFHS steel sheet." ***Materials Science and Engineering: A,*** Vol. 538, (2012), 349-355. DOI: 10.1016/j.msea.2012.01.058
4. Zhu, J., Chen, X., Xue, F., and Yu. W.,"Bending ratcheting tests of Z2CND18. 12 stainless steel." ***International Journal of Fatigue,*** Vol. 35, No. 1, (2012), 16-22. DOI: 10.1016/j.ijfatigue.2011.04.008
5. Abdel-Karim, M., "Effect of elastic modulus variation during plastic deformation on uniaxial and multiaxial ratchetting simulations." ***European Journal of Mechanics-A/Solids,*** Vol. 30, No. 1, (2011), 11-21. DOI: 10.1016/j. euromechsol.2010.08.002
6. Khademia, E., Majzoobib, G. H., Bonora, N., "A Strain range dependent cyclic plasticity model", ***International Journal of Engineering Transactions B: Applications***, Vol. 30, No. 2, (2017), 321-329. DOI: 10.5829/idosi.ije.2017.30.02b.20
7. Dutta, K., Ray, K K., "Ratcheting strain in interstitial free steel", ***Materials Science and Engineering: A,*** Vol. 575, (2013), 127-135. DOI: 10.1016/j.msea.2013.02.052
8. Yu, X. J., Kumar, K. S., "Uniaxial, load-controlled cyclic deformation of recrystallized molybdenum sheet", ***Materials Science and Engineering: A,*** Vol. 540, (2012), 187-197. DOI: 10.1016/j.msea.2012.01.124
9. Zhang, J., Jiang, Y., "An experimental investigation on cyclic plastic deformation and substructures of polycrystalline copper" ***International Journal of Plasticity,*** Vol. 21, No. 11 (2005): 2191-2211. DOI: 10.1016/j.ijplas.2005.02.004
10. Paul, S. K., Sivaprasad, S., Dhar, S., Tarafder,S., "True stress controlled ratcheting behavior of 304 L N stainless steel" ***Journal of Materials Science,*** Vol. 47, (2012), 4660-4672. DOI: 10.1007/s10853-012-6334-1
11. Portier, L., Calloch, S., Marquis, D., Geyer, P., "Ratchetting under tension–torsion loadings: experiments and modelling" ***International Journal of Plasticity,*** Vol. 16, No. 3, (2000), 303-335. DOI: 10.1016/S0749-6419(99)00056-X
12. Lin, Y. C., Chen, X. M., Chen, G., "Uniaxial ratcheting and low-cycle fatigue failure behaviors of AZ91D magnesium alloy under cyclic tension deformation" ***Journal of Alloys and Compounds,*** Vol. 509, No. 24, (2011), 6838-6843. DOI: 10.1016/j.jallcom.2011.03.129
13. Rezaiee-Pajand, M. and Sinaie S., "Calibration of hardening rules for cyclic plasticity", ***International Journal of Engineering Transactions A: Basics,*** Vol. 26, No. 4, (2013), 351-364. DOI: 10.5829/idosi.ije.2013.26.04a.04
14. Dong, Y., Kang, G., Liu, Y., Jiang, H., "Multiaxial ratcheting of 20 carbon steel: Macroscopic experiments and microscopic observations", ***Materials Characterization,*** Vol. 83, (2013), 1-12. DOI: 10.1016/j.matchar.2013.05.014
15. Kang, G., Dong, Y., Liu, Y., Jiang, H., "Macroscopic and microscopic investigations on uniaxial ratcheting of two-phase Ti–6Al–4V alloy", ***Materials Characterization,*** Vol. 92, (2014), 26-35. DOI: 10.1016/j.matchar.2014.02.014
16. Collins, M., and Cosgrove, T., "Dynamic relaxation modelling of braced bending active gridshells with rectangular sections."

Engineering Structures, Vol. 187, (2019), 16-24. DOI: 10.1016/j.engstruct.2019.02.001

17. Golmakani, M. E. and Kadkhodayan, M., "Non-linear thermo-mechanical bending behavior of thin and moderately thick functionally graded sector plates using dynamic relaxation method", ***International Journal of Engineering Transactions C: Aspects***, Vol. 29, No. 6, (2016), DOI: 10.5829/idosi.ije.2016.29.06c.00
18. Zhang, Q., Jiang B., Xiao, Zh., Cui, W., and Liu J., "Post-buckling analysis of compressed rods in cylinders by using dynamic relaxation method." ***International Journal of Mechanical Sciences,*** Vol. 159 (2019), 103-115. DOI: 10.1016/j.ijmecsci.2019.05.040
19. Rezaiee-Pajand, M., and Estiri, H., "Computing the structural buckling limit load by using dynamic relaxation method." ***International Journal of Non-Linear Mechanics,*** Vol. 81, (2016), 245-260. DOI: 10.1016/j.ijnonlinmec.2016.01.022
20. Esmaeilzadeh, M., and Kadkhodayan M., "Dynamic analysis of stiffened bi-directional functionally graded plates with porosities under a moving load by dynamic relaxation method with kinetic damping." ***Aerospace Science and Technology,*** Vol. 93, (2019), 105333. DOI: 10.1016/j.ast.2019.105333
21. Kadkhodayan, M., Alamatian J., "A new fictitious time for the dynamic relaxation (DXDR) method", ***International Journal for Numerical Methods in Engineering,*** Vol. 74, No. 6, (2008), 996-1018. DOI: 10.1002/nme.2201
22. Namadchi, A. H., and Alamatian. J., "Explicit dynamic analysis using Dynamic Relaxation method." ***Computers & Structures,*** Vol. 175, (2016), 91-99. DOI: 10.1016/j.compstruc.2016.07.008
23. Rezaiee-Pajand, M., and Estiri H., "Mixing dynamic relaxation method with load factor and displacement increments." ***Computers & Structures,*** Vol. 168, (2016), 78-91. DOI: 10.1016/j.compstruc.2016.02.011
24. Rezaiee-Pajand, M., and Estiri H., "Finding buckling points for nonlinear structures by dynamic relaxation scheme." ***Frontiers of Structural and Civil Engineering,*** Vol. 14, No. 1 (2020), 23-61. DOI:10.1007/s11709-019-0549-z
25. Gale, S., and Lewis, W.J., "Patterning of tensile fabric structures with a discrete element model using dynamic relaxation." ***Computers & Structures,*** Vol. 169, (2016), 112-121. DOI: 10.1016/j.compstruc.2016.03.005
26. Wang, X., Cai, J., Yang, R., and Feng J., "Form-finding of deployable mesh reflectors using dynamic relaxation method." ***Acta Astronautica,*** Vol. 151, (2018), 380-388. DOI: 10.1016/j.actaastro.2018.06.017
27. Shariati, M., Mehrabi, H., "Energy-based prediction of low-cycle fatigue life of CK45 steel and SS316 stainless steel", ***Journal of Solid Mechanics,*** Vol. 6, No. 3, (2014), 278-288.
28. Rezaiee-Pajand, M., Alamatian, J., "The dynamic relaxation method using new formulation for fictitious mass and damping", ***Structural Engineering and Mechanics,*** Vol. 34, No.1, (2010), 109-133. DOI: 10.12989/sem.2010.34.1.109
29. Rezaee Pajand, M., and Taghavian Hakkak, M., "Nonlinear analysis of truss structures using dynamic relaxation", ***International Journal of Engineering Transactions B: Applications,*** Vol. 19, No.1 (2006), 11-22.
30. Shafabakhsh G., Motamedi M., "Sensitivity analysis of road actual conditions to evaluate the optimal positioning of geogrid using finite elements and dynamic methods", ***International Journal of Engineering Transactions C: Aspects***, Vol. 29, No. 9, (2016), 1235-1241. DOI: 10.5829/idosi.ije.2016.29.09c.08
31. Jamal-Omidi, M., Mohammadi Suki M.R., "A numerical study on aluminum plate response under low velocity impact", ***International Journal of Engineering Transactions C: Aspects***, Vol. 30, No. 3, (2017), 440-448. DOI: 10.5829/idosi.ije.2017.30.03c.14

Persian Abstract

چکیده

در این پژوهش روش عددی جدیدی برای بررسی رچتینگ در صفحات مستطیلی معرفی می‌شود. به منظور بررسی صحت این روش، آزمایشاتی در شرایط تنش کنترل توسط دستگاه zwick/roell amsler HB100 در دمای محیط انجام و پدیده رچتینگ در صفحه فولادی CK45 تحت بارگذاری خمشی سیکلی مورد بررسی قرار گرفت. در شرایط تنش کنترل و تنش میانگین غیرصفر، رچتینگ در صفحه فولادی نازک اتفاق افتاد. سپس تحلیل المان محدود توسط نرم افزار آباکوس با مدل سخت شوندگی ترکیبی انجام گرفت. در نهایت یک روش عددی جدید که با توسعه روش رهایی پویا به دست آمده است، جهت تحلیل رفتار رچتینگ در صفحه نازک فولادی تحت بارگذاری اشاره شده، مورد استفاده قرار گرفت. نتایج نشان می‌دهند، نرخ رچتینگ در ابتدا زیاد و سپس با افزایش سیکل ها به تدریج کاهش می‌یابد. همچنین سطح حلقه‌های هیسترزیس در روش آزمایشگاهی (به دلیل اتلاف انرژی)، بزرگ‌تر از دو روش المان محدود و عددی است. نتایج روش عددی هماهنگی مناسبی با نتایج روش‌های آزمایشگاهی و شبیه‌سازی دارد. مقایسه نتایج بین این سه روش دقت بالای روش عددی معرفی شده را نشان می‌دهد.

IJE TRANSACTIONS C: Aspects Vol. 34, No. 6, (June 2021) 1540-1547

International Journal of Engineering

Journal Homepage: www.ije.ir

Sensitivity Analysis on Thermal Performance of Gas Heater with Finned and Finless Tubes using Characteristics-based Method

S. E. Razavi[a], T. Adibi[b], H. Hassanpour*[c]

[a] School of Mechanical Engineering, University of Tabriz, Tabriz, Iran
[b] School of Mechanical Engineering, University of Bonab, Bonab, Iran
[c] School of Automotive Engineering, Iran University of Science and Technology, Tehran, Iran

PAPER INFO

Paper history:
Received 16 April 2021
Received in revised form 04 May 2021.
Accepted 06 May 2021

Keywords:
Thermal Performance
Characteristics-based Method
Fin
Natural Gas
Gas Station
Navier-Stokes's Equations

ABSTRACT

Natural gas must be preheated to prevent phase change and gas hydrate in pressure reduction stations. This paper aims to investigate the effect of the fins of gas tubes and their configuration, arrangement, and shape on the heat transfer and thermal efficiency of gas. To conduct a parametric study, two tube cases with fins and without fins, and in the finned case for the fin's configuration, two longitudinal and circular arrangements, and the formation of the fins, two solid and interrupted forms were analyzed. Also, three types of cross-sections, including rectangular, convergent parabolic, and divergent parabolic, for the shape of the fins have been studied. For this simulation, the three-dimensional, incompressible, and steady flow was considered, and for analysis and discretization of convective heat equations, the characteristic-based method was applied. FORTRAN software was also used to implement and solve the equations. The results show that in solid and interrupted fins and increasing the number of fins in parallel, the dimensionless heat transfer coefficient increases. Also, the dimensional heat transfer coefficient decreases with increasing the ratio of fin height to the tube's diameter. Also, the most significant heat transfer improvement was related to the divergent parabolic cross-section.

***doi**: 10.5829/ije.2021.34.06c.18*

1. INTRODUCTION

Optimal energy consumption is the main issue in recent years, and researchers had many studies in this field [1]. The consumption of natural gas as a fuel in the heaters of the pressure reduction stations has drawn attention to the use of solutions to reduce fuel consumption and increase the efficiency of heaters. Researchers have proposed numerous methods and, in some cases, implemented them. Recycling power from the chimney outlet, using various fluids to transfer heat, modifying the combustion chamber, using a catalytic heater, using nanofluids, solar cells, temperature control equipment for the output of the heater, and controlling fuel consumption are some of the solutions. Using nano-fluids is another way to increases the heat transfer rate[2]. Natural gas is one of the primary sources of energy called sour gas when extracted from tanks containing impurities such as H_2S and CO_2. Before consumption, during the gas sweetening process in the gas treating unit, acid gases are separated, and sweet gas is obtained [3]. In 2012, 24% of the world's electricity was generated by natural gas compared to other energy sources such as oil, coal, nuclear energy, hydroelectricity, and renewable energy sources [4].

Free convection heat transfer is a common physical phenomenon that is important in the design and operation of heat exchangers. Researchers have studied different types of fins in vertical and horizontal plates and cylinders and their effect on increasing free convection. Ahmadi et al. [5] examined and compared the transfer of free transfer heat from vertical heating wells with solid and interrupted longitudinal fins. Their research included a comprehensive empirical and numerical study of the effect of interrupting fins and the longitudinal distance of two fins on heat transfer. Sajedi et al. [6] examined the optimal number of longitudinal fins in a vertical

*Corresponding Author Institutional Email: h_hassanpur@alumni.iust.ac.ir (H. Hassanpour)

Please cite this article as: S. E. Razavi, T. Adibi, H. Hassanpour, Sensitivity Analysis on Thermal Performance of Gas Heater with Finned and Finless Tubes using Characteristics-based Method, International Journal of Engineering, Transactions C: Aspects Vol. 34, No. 6, (2021) 1540-1547

cylindrical heat exchanger. The temperature distribution of the heat exchanger and the total heat transfer indicate the optimal number of fins to increase the heat transfer. Sebastian and Shine [7] studied layered free convection around a heated cylinder with or without a horizontal barrier. Numerical modeling consists horizontal barriers above and below the cylinder at different vertical distances, and the finite volume method was used to solve two-dimensional governing equations. Innella and Rodgers [8] investigated the Benefits of a Convergence between art and engineering by compiling and analyzing a review of the literature and creative works spanning from the renaissance to contemporary art; their paper presents the potential benefits of combining engineering and art research. Fazelabdolabadi and Golestan [9] developed a Bayesian framework to quantify the absolute permeability of water in a porous structure from the geometry and clustering parameters of its underlying pore-throat network. Bayareh et al. [10] studied the effects of stator boundary conditions and fin geometry on the efficiency of a scraped surface heat exchanger numerically. Matsunaga and Sumitomo [11] studied pressure loss and heat transfer in a double-tube type heat exchanger with rotating fins. They used the corn syrup water solution as a test process fluid. Shahsavar Goldanlou et al. [12] studied the turbulent forced convection heat transfer of Fe_3O_4/-CNT/water hybrid nanofluid (HNF) in a heat exchanger (HE) equipped with fin-shape turbulators. They solved the 3D governing equations with the SIMPLE algorithm and solution domain by employing the control volume method (CVM). Zhang et al. [13] studied a gas engine-driven heat pump (GEHP) performance experimentally for space heating and cooling and investigated the effect of critical parameters on system performance under both cooling and heating modes. Kostikov and Romanenkov [14] performed an estimating the convergence rate of an algorithm for numerically solving the optimal control problem for the three-dimensional heat equation. A variety of longitudinal and peripheral fins are used to increase the heat transfer of free convection. Kuma et al. [15] modeled the transient convection of a horizontal fin tube inside a furnace in OpenFOAM software. They studied the effect of fin diameter, the ratio of fin diameter to tube diameter, furnace height, and ambient temperature difference, and the surface area of the tube on heat transfer by considering 8 circular fins in the middle of a tube with an outer diameter of 24.9 mm. Kiatpachai [16] studied the effect of serrated circular fins on the hydrothermal performance of fin-tube heat exchangers. Considering the physical parameters, they experimented with several arrays of fins. A specific type of longitudinal Fin was investigated in Lorenzini's work [17]. They introduced longitudinal T-shaped fins to increase the cooling rate of a horizontal cylinder. The purpose of their study was to reduce the maximum difference between the temperature of the cylinder and the environment.

Another way to reduce energy consumption in heaters at a pressure reduction station is to release gas at the minimum acceptable temperature. The minimum temperature required to prevent gas condensate and hydrate formation can be calculated using thermodynamic relations according to the thermo-physical conditions of natural gas and the pressure drop rate. Using this idea, Ashouri et al. [18] Proposed a temperature control system to determine the gas output conditions. There is not any analytical solution for the thermo-flow governing equation in general. As a result, experimental and numerical methods were used to simulate flows with heat transfer in different cases. An experimental method is expensive, and most of the simulations in the recent decade are done numerically by investigators [19-21].

In this paper, for the first time, it is proposed to use different fins for a shell-tube heat exchanger that contains gas transmission tubes. Numerical simulations are done by a new characteristics-based method that the authors introduced in their previous works [22, 23]. This characteristic-based numerical scheme was developed for three-dimensional flow [24]. As a result, it can be used in the three-dimensional flow with heat transfer. According to previous research in improving heat transfer from horizontal cylinders in pressure reduction station heaters, the suitable types of fins and their thermal role are studied in the present study. The proposed fins have been in different shapes and dimensions. The Fin effect on the improvement of free convection from the tubes and the increase of heat transferred to the gas inside the tube have been studied. Optimum cases that have high efficiency have been found and reported in this work. The study originated and was designed based on a need in natural gas stations to prevent phase change and hydrate formation. In the introduction, the purpose of the article was presented by stating the problem and reviewing the literature. In the modeling section, the geometric model of the system and mathematical equations will be extracted, and after stating the initial conditions and boundary conditions, the solution method will be expressed. Finally, after the simulation and parametric analysis of the model, the results of the simulation and analysis will be presented and discussed in the results section.

2. MATERIALS AND METHODS

The steps of the research process, including research methodology as a flowchart are shown in Figure .

2. 1. Geometric Modeling As seen in Figure 2, to the parametric analysis of the effect of fins on gas tubes

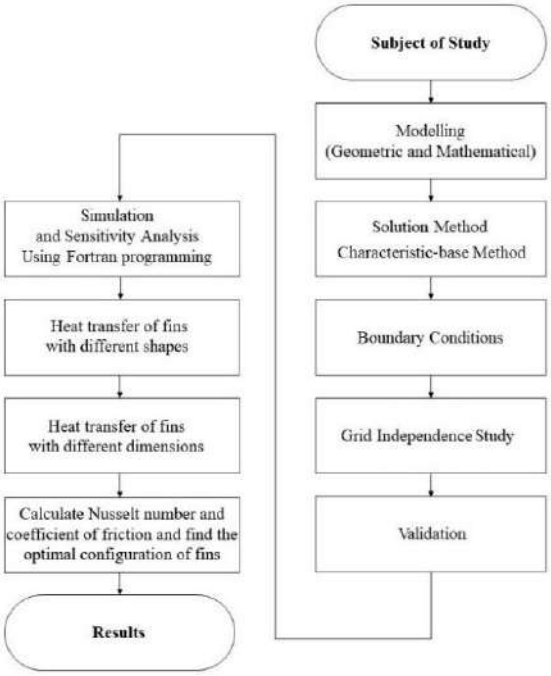

Figure 1. Research process steps

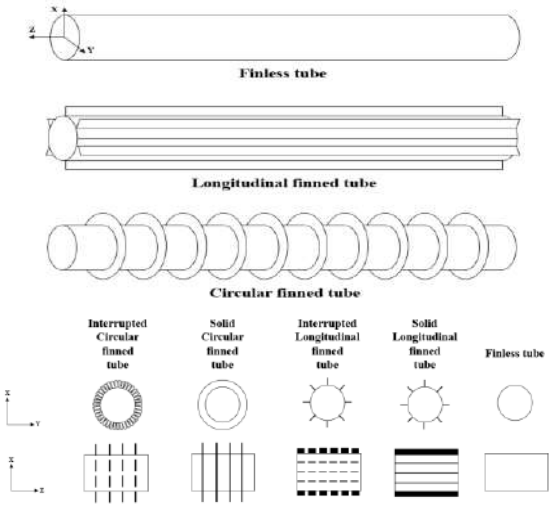

Figure 2. Finless and finned tubes configurations

heat transfer, two tube-cases with fins and without fins, and in the finned case for the fins configuration, two longitudinal and circular arrangements, And for the fins formation of the fins, two solid and interrupted forms are studied. As shown in Figure , three shapes, including rectangular cross-section, convergent parabolic, and divergent parabolic for the fins, are also examined.

2. 2. Mathematical Modeling The governing equations of the incompressible fluid along with heat transfer are as follows:

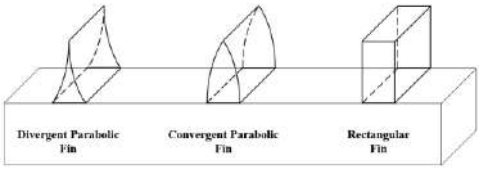

Figure 3. Fins sections and shapes

$$\vec{\nabla}\vec{V}=0,\ \frac{D\vec{V}}{Dt}=-\frac{\vec{\nabla}p}{\rho}+\upsilon\nabla^2\vec{V}$$
$$\frac{DT}{Dt}=\frac{k}{\rho C_p}\nabla^2 T. \quad (1)$$

In the above equation, V is the velocity, p is the pressure, T is the temperature, ρ is the density, ϑ is the kinematic viscosity, g is gravity acceleration, and C_P is the thermal coefficient. In free and mixed convection, density is not constant, but the Boussinesq assumption can be used. The governing equations are solved numerically by a new finite volume method. A new three-dimensional characteristics-based scheme is used to obtain convective fluxes [24]. The used numerical method is one of the novel numerical methods. Due to the use of virtual waves propagating inside the incompressible fluid, it is more stable to find convective fluxes than the averaging method. Convective terms at the cell boundary were calculated in the finite volume method. The second-order averaging scheme is used to calculate viscous fluxes, and the fifth-order Runge-Kutta method is applied to time marching [23, 25]. For validation, the accuracy of the numerical results of the free convection heat transfer from a horizontal tube enclosed in the chamber was examined. Nusselt numbers at different Rayleigh numbers were obtained by the explained numerical method and are compare by Cesini et al. [26] results. Cesini et al. [26] performed a three-dimensional experimental work. Air is used as the working fluid. The interval vertical walls were made of aluminum and cooled by coolant fluid. Plexiglass made the top and the bottom walls. The last vertical wall was made of glass to allow optical work. After validating the numerical model and studying the effect of the fins on heat transfer, simulation was performed for a horizontal tube enclosed in the chamber, and the effect of the fins on heat transfer is investigated. Cesini et al. [26] considered the horizontal tube enclosed in the chamber containing the air and examined the effect of the Rayleigh number and the chamber's geometry on the heat transfer coefficient. Their study was experimental, and they used numerical analysis to ensure the accuracy of the experiments. The temperature of the tube was constant and kept above room temperature. The temperature of the surrounding walls was assumed to be constant and uniform. Neumann boundary condition was applied at the upper level of the chamber, and the overall heat transfer coefficient from

the upper level was $10\,W/m^2k$. This comparison is displayed at Table 1. Good agreement between results was observed. According to the results the maximum error was 9.2%. No slip conditions were considered at wall. The velocity and temperature are given at the inlet, and pressure is calculated by second-order extrapolation. The pressure is given at the outlet, and temperature and velocities are calculated by second-order extrapolation

This problem is considered a steady state problem. Hence it does not need the real initial condition. The initial condition in this numerical simulation is defined as inlet and outlet boundary conditions. After numerical simulations and determining the temperature, pressure, and velocity fields, the Nusselt number and friction coefficient were calculated numerically by second-order methods. The Nusselt number and the friction coefficient are compared, and the fin efficiency is determined. Finally, the optimum fin is introduced by comparing the fin efficiency. Experimental and numerical studies focused on calculating the average Nusselt number of cylinders calculated from the following equation.

$$Nu = \left(\frac{\partial T}{\partial r}\right)_{r=D/2} \frac{D}{\theta},\ \overline{Nu} = \frac{1}{\pi D}\int_0^{\pi D} Nu\, ds \qquad (2)$$

In the above equation, Nu is Nusselt number, $\overline{Nu}$ is the mean Nusselt number, D is the diameter of the tubes. The heater has a length of 5600 mm and a diameter of 2100 mm. The thickness of the applied fins on the tubes is 5 mm. In Figure , the position of two middle tubes relative to the fire tube is the most exposed to heat. Also, the close distance between the tubes makes it difficult to dissipate heat from the two pipelines. Therefore, the two middle tubes have the most critical conditions for heat load tolerance and heat transfer limitation. One of these two tubes and the fluid around it is intended for modeling, and its results can be generalized to other tubes collections. The used grid is shown in Figure . A tetrahedron grid is used in this work, and due to the boundary layer effect, the velocity and temperature gradient is high near the wall. Then clustering near the wall is done in this grid to improve the accuracy of the results.

The heater's walls are thermal insulation to reduce energy loss. If the torch operates continuously at its rated load, constant heat flux is transferred from the fire tubes to the fluid. Applying a constant flux to the set keeps the water bath temperature constant at about 80℃. The outlet temperature of the heater should also be higher than the dew point of the water. During the year, the inlet and outlet temperatures of natural gas can be assumed to be 10℃ and 38℃, respectively. In the present simulation, the internal surface temperature of the tubes is assumed to be the average gas inlet and outlet temperature, 24℃. If the Fin is used, the outer surface of the tube and the fins is in heat exchange with the surrounding convection medium. The front, rear, and top panels are insulated. Fixed heat flux is applied from the low level. The initial velocity field at the computational domain is zero, and the walls are subject to non-slip conditions. Rayleigh numbers are between 10^9 and 10^{11} according to the industrial data.

TABLE 1. Comparison results of mean Nusselt number of cylindrical with Cesini results [26]

Rayleigh numbers	Present paper	Cesini Results [26]	Difference, %
1300	29.2	36.2	9.2
2400	57.2	61.2	5.1
3400	67.2	77.2	6.3

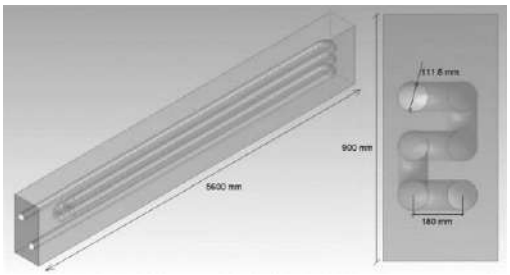

Figure 4. The geometry of the tube position

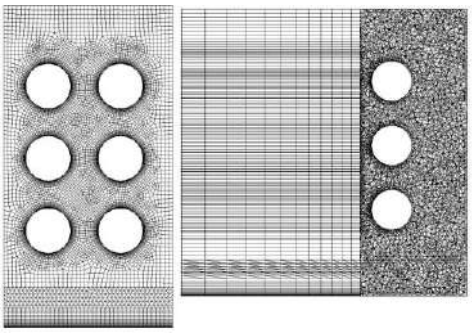

Figure 5. The front cross-section (left) and lateral cross-section (right) of grid

3. RESULTS AND DISCUSSION

The enclosed horizontal cylinder-shaped tube in the chamber is modeled. Grid independence for finless tube case at Rayleigh number of 750,000 in four different grid forms studied. The average Nusselt numbers of the tube are obtained in each case and are plotted in Figure 1. The number of elements was selected to be 250,000 for calculations.

In this section, the effect of applying two types of longitudinal and peripheral fins on heat transfer has been studied. The development of heat flow and heat transfer

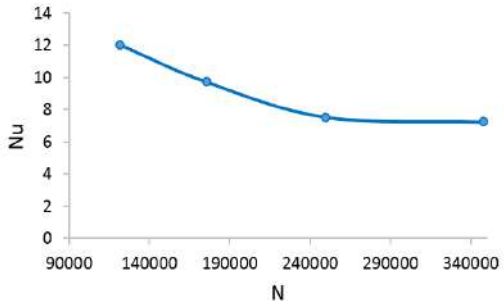

Figure 1. Grid independence study of the finless tube for Ra=750,000

for three large Rayleigh numbers in the layered heat transfer range was studied. The Rayleigh numbers are 750,000, 7,500,000, and 15,000,000, respectively, corresponding to the temperature differences of 1℃, 10℃, and 20℃ between the tube and the environment. Two different arrays are modeled for each type of Fin. A comparison is made between the Nusselt numbers of different modes with a tube without a fin. The ratio of the Nusselt number for the finless and with finned case is shown in Figure 2. An increase in 8 to 18 percent and 7 to 16 percent for the dimensionless heat transfer coefficient due to solid and interrupted fins can be seen in the range of Rayleigh numbers studied. In the modeled geometry, the ratio of $H / D = 0.5$ has the optimum improvement on heat transfer, and its effect increases with increasing Rayleigh number. As the ratio of the height of the Fin to the diameter of the tube increases, the existence of the fins acts as a heat trap and prevents the flow of stagnation. For this reason, the trend of increasing the heat transfer coefficient for $H / D = 0.7$ is reduced by the Rayleigh number. In this case, the use of 4 and 2 fins increases 10 to 17% and 8 to15% in the dimensionless heat transfer coefficient. It can be concluded that the use of fins to improve the heat transfer of free convection is a function of the geometry of the fins, the dimensions and number of fins, and the Rayleigh number.

In the indirect water heater bath, the set is under free convective heat transfer. In the following, the effect of using two types of fins with different arrays on improving heat transfer from the surrounding fluid to the tube wall has been studied. Average Nusselt number of the pipeline in the presence of longitudinal and circular fins with an increase compared to the finless case. Figures 8-10 show the average Nusselt number ratio of the finless to fin mode for the three rectangular sections, convergent and convergent, respectively. An increase in 3 to 20% is seen for the dimensionless heat transfer coefficient. Among the three cases selected for fin height, H = 15 mm has the highest increase in noise. The fins with a divergent parabolic profile are optimum heat transfer improvement. The heat enters the Fin from the wide surface in contact with the fluid and travels through it to the narrow

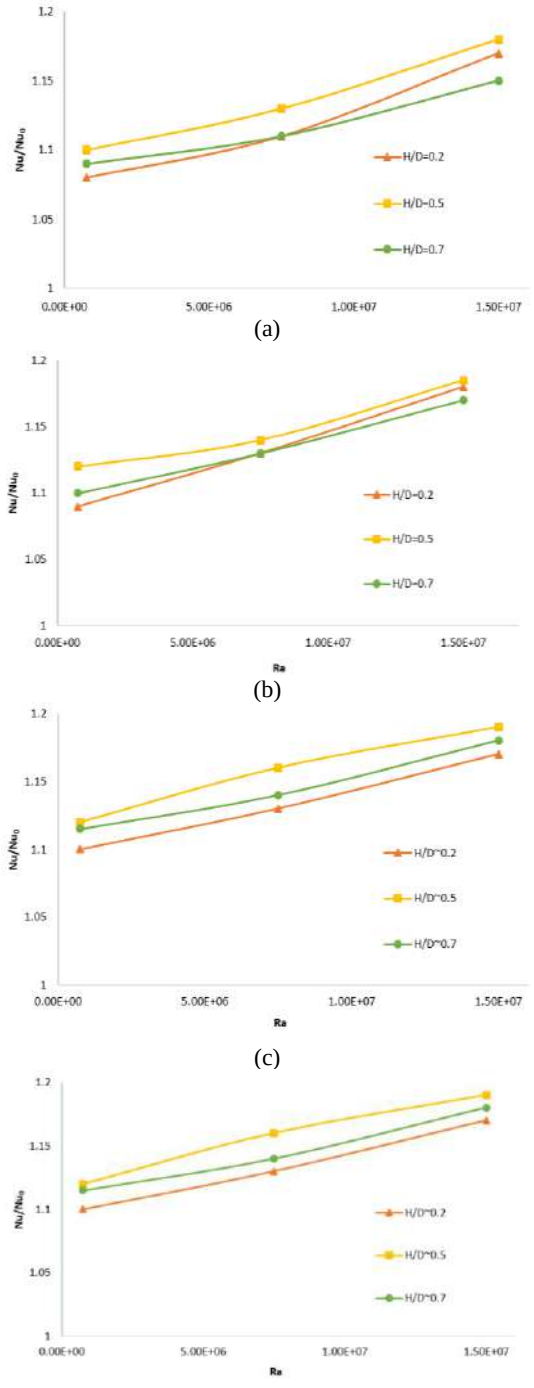

Figure 2. Average Nusselt number of finned tube relative to the finless tube (a) Solid longitudinal (b) Interrupted longitudinal (c) Quadruple circular (d) Dual circular

section leading to the tube. According to the principle of energy conservation, the input heat to the Fin and the output heat are equal; therefore, the heat flux coming out of the Fin is larger than the heat flux entering it, and a larger Nusselt number is obtained at the base of the Fin.

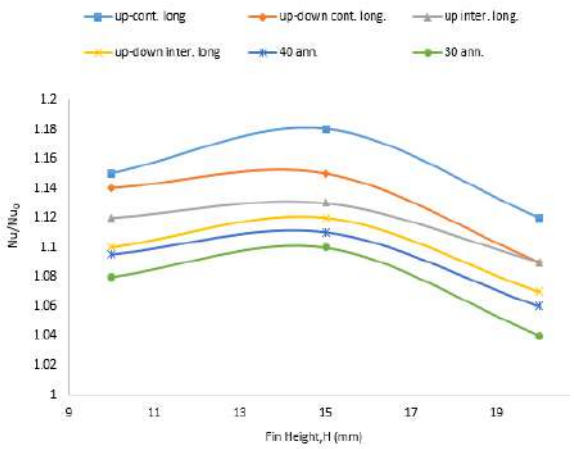

Figure 3. Average Nusselt number of finned tube relative to the finless tube with rectangular shaped fins

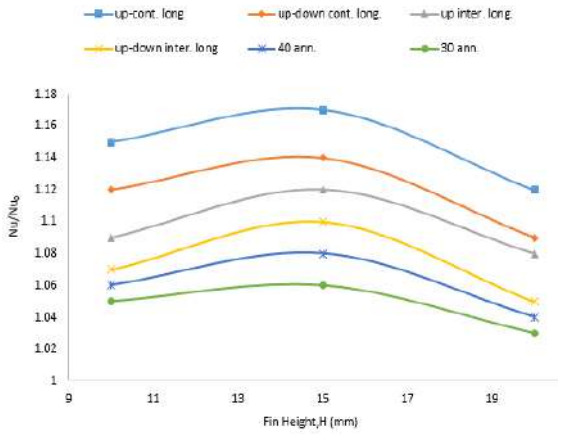

Figure 4. Average Nusselt number of finned tube relative to the finless tube with convergent parabolic shaped fins

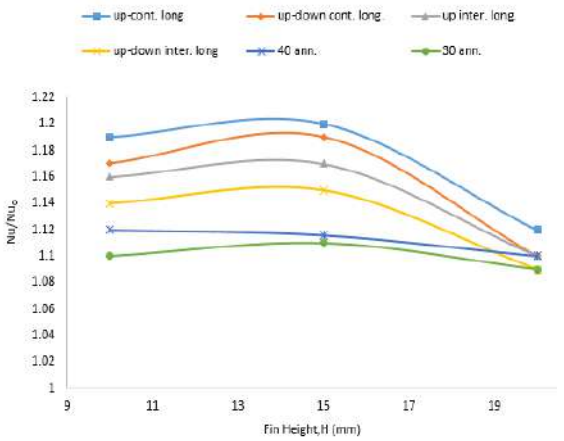

Figure 5. Average Nusselt number of finned tube relative to the finless tube with divergent parabolic shaped fins

The thermal enhancement factor is a parameter that considers changes in heat transfer and flows properties simultaneously. When it comes to choosing the optimal temperature for maximum heat transfer and the lowest coefficient of friction, it is essential to determine the thermal enhancement factor. Because, the executive and economic justification of the optimal state is conditional on having $\eta > 1$ [27].

$$\eta = \frac{\frac{Nu}{Nu_0}}{(\frac{f}{f_0})^{1/3}} \quad (3)$$

In Equation (3), Nu_0 and $f_0$are the Nusselt number and the coefficient of friction of the reference state without Fin, respectively. Also, Nu and f are the Nusselt number and the coefficient of friction of the tube with Fin, respectively. Figures 11-13 demonstrate the thermal enhancement factor for different types and profiles of fins. The highest parameter of thermal enhancement factor is related to the divergent parabolic profile, which,

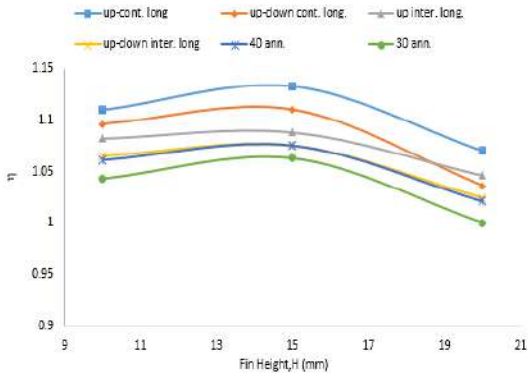

Figure 11. The thermal enhancement factor with rectangular shaped fins

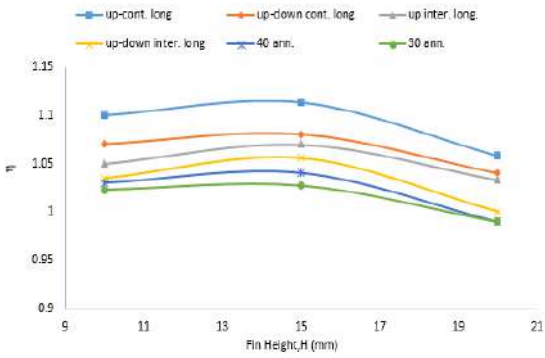

Figure 12. The thermal enhancement factor with convergent parabolic shaped fins

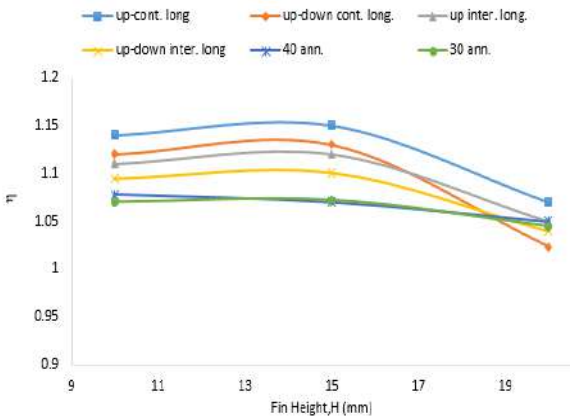

Figure 13. The thermal enhancement factor with divergent parabolic shaped fins

despite the high-pressure drop, an increase in heat transfer coefficient leads to the maximum thermal enhancement factor. In the convergent parabolic section, the thermal enhancement factor for circular fins with an H = 20 mm height is less than one. The rest of the cases show that improving the heat transfer coefficient overcomes the increase in the coefficient of friction, and the application of fins from the optimization point of view is justified.

4. CONCLUSION

In pressure reduction stations, before the constant enthalpy process of pressure failure, the indirect water bath heater preheats the natural gas to prevent phase change and gas hydrate formation. This paper studies the feasibility of applying fins along tubes to increase the transferred heat to the natural gas and increase thermal efficiency. Two longitudinal and circular fins are selected according to the condition of the tube. Three different profiles for fins are considered in the simulations. The flow was considered three-dimensional, incompressible, and steady. For simulation and analysis, a first-order characteristics-based scheme is used to obtain convective fluxes, and the second-order averaging method is used to calculate the viscous fluxes in the numerical method. The fifth-order Runge-Kutta method is applied for time marching. FORTRAN was also utilized to solve the governing equations. The Rayleigh number lies within the beginning of the transition range ($10^9 - 10^{11}$). Experimental results of similar articles were used to validate the numerical results in this paper.

The results show that for the dimensionless heat transfer coefficient, due to the use of the fin, compared to the finless case, for three sections, including rectangular, convergent parabolic, and divergent parabolic, it increases by 3 to 20%. Also, the dimensionless heat transfer coefficient increases from 8 to 18% due to using solid fins, from 7 to 16% due to the use of interrupted fins, and from 10 to17%, and 8 to 15% due to the use of 4 and 2 blades, respectively. Increasing the ratio of fin height to tube diameter, the presence of the fin, acts the role of heat trap and prevents the flow motion. Hence, H/D has the most significant improvement on heat transfer, and with increasing Rayleigh number, its effect also increases. Among the three cases selected for fin height, H=15 mm has the highest Nusselt increase. The highest heat recovery parameter is related to the divergent parabolic cross-section. Despite the high-pressure drop, increasing the heat transfer coefficient leads to the maximum heat recovery parameter. It shows that the improvement of the heat transfer coefficient overcomes the increase of the coefficient of friction, and the application of the fin is justified from the optimization point of view.

5. REFERENCES

1. Adibi, T., "Evaluation of using solar ammonia absorption cooling system for major cities of the middle east", ***International Journal of Heat and Technology***, Vol. 36, No. 3, (2018), 840-846. doi: https://doi.org/10.18280/ijht.360309.
2. Adibi, T., Razavi, S.E. and Adibi, O., "A characteristic-based numerical simulation of water-titanium dioxide nano-fluid in closed domains", ***International Journal of Engineering, Transactions A: Basics***, Vol. 33, No. 1, (2020), 158-163. doi: https://doi.org/10.5829/ije.2020.33.01a.18.
3. Rahimpour, M.R., Saidi, M., Baniadam, M. and Parhoudeh, M., "Investigation of natural gas sweetening process in corrugated packed bed column using computational fluid dynamics (CFD) model", ***Journal of Natural Gas Science and Engineering***, Vol. 15, (2013), 127-137. doi: https://doi.org/10.1016/j.jngse.2013.10.003.
4. Al-Sobhi, S.A. and Elkamel, A., "Simulation and optimization of natural gas processing and production network consisting of lng, gtl, and methanol facilities", ***Journal of Natural Gas Science and Engineering***, Vol. 23, (2015), 500-508. doi: https://doi.org/10.1016/j.jngse.2015.02.023.
5. Ahmadi, M., Mostafavi, G. and Bahrami, M., "Natural convection from rectangular interrupted fins", ***International Journal of Thermal Sciences***, Vol. 82, (2014), 62-71. doi: https://doi.org/10.1016/j.ijthermalsci.2014.03.016.
6. Sajedi, R., Taghilou, M. and Jafari, M., "Experimental and numerical study on the optimal fin numbering in an external extended finned tube heat exchanger", ***Applied Thermal Engineering***, Vol. 83, (2015), 139-146. doi: https://doi.org/10.1016/j.applthermaleng.2014.12.040
7. Sebastian, G. and Shine, S.R., "Natural convection from horizontal heated cylinder with and without horizontal confinement", ***International Journal of Heat and Mass Transfer***, Vol. 82, (2015), 325-334. doi:https://doi.org/10.1016/j.ijheatmasstransfer.2014.11.063.
8. Innella, G. and Rodgers, P.A., "The benefits of a convergence between art and engineering", ***HighTech and Innovation Journal***, Vol. 2, No. 1, (2021), 29-37. doi: https://doi.org/10.28991/HIJ-2021-02-01-04.
9. Fazelabdolabadi, B. and Golestan, M.H., "Towards bayesian quantification of permeability in micro-scale porous structures –

the database of micro networks", ***HighTech and Innovation Journal***, Vol. 1, No. 4, (2020), 148-160.doi: https://doi.org/10.28991/HIJ-2020-01-04-02.

10. Bayareh, M., Pordanjani, A.H., Nadooshan, A.A. and Dehkordi, K.S., "Numerical study of the effects of stator boundary conditions and blade geometry on the efficiency of a scraped surface heat exchanger", ***Applied Thermal Engineering***, Vol. 113, (2017), 1426-1436. doi: https://doi.org/10.1016/j.applthermaleng.2016.11.166
11. Matsunaga, T. and Sumitomo, T., "Heat transfer and pressure loss in double-tube type heat exchanger with rotating blades", ***Journal of Research and Applications in Mechanical Engineering***, Vol. 2, No. 1, (2014), 65-73. doi: https://doi.org/10.14456/jrame.2014.7.
12. Shahsavar Goldanlou, A., Sepehrirad, M., Papi, M., Hussein, A.K., Afrand, M. and Rostami, S., "Heat transfer of hybrid nanofluid in a shell and tube heat exchanger equipped with blade-shape turbulators", ***Journal of Thermal Analysis and Calorimetry***, Vol. 143, No. 2, (2021), 1689-1700. doi: https://doi.org/10.1007/s10973-020-09893-4.
13. Zhang, W., Yang, X., Wang, T., Peng, X. and Wang, X., "Experimental study of a gas engine-driven heat pump system for space heating and cooling", ***Civil Engineering Journal***, Vol. 5, No. 10, (2019), 2282-2295. doi: https://doi.org/10.28991/cej-2019-03091411.
14. Kostikov, Y.A. and Romanenkov, A.M., "Approximation of the multidimensional optimal control problem for the heat equation (applicable to computational fluid dynamics (CFD)", ***Civil Engineering Journal***, Vol. 6, No. 4, (2020), 743-768. doi: https://doi.org/10.28991/cej-2020-03091506.
15. Kumar, A., Joshi, J.B., Nayak, A.K. and Vijayan, P.K., "3d cfd simulations of air cooled condenser-ii: Natural draft around a single finned tube kept in a small chimney", ***International Journal of Heat and Mass Transfer***, Vol. 92, (2016), 507-522. doi: doi.org/10.1016/j.ijheatmasstransfer.2015.07.136.
16. Kiatpachai, P., Pikulkajorn, S. and Wongwises, S., "Air-side performance of serrated welded spiral fin-and-tube heat exchangers", ***International Journal of Heat and Mass Transfer***, Vol. 89, (2015), 724-732. doi: doi.org/10.1016/j.ijheatmasstransfer.2015.04.095.
17. Lorenzini, G., Biserni, C., Correa, R.L., dos Santos, E.D., Isoldi, L.A. and Rocha, L.A.O., "Constructal design of t-shaped assemblies of fins cooling a cylindrical solid body", ***International Journal of Thermal Sciences***, Vol. 83, (2014), 96-103. doi: https://doi.org/10.1016/j.ijthermalsci.2014.04.011.
18. Ashouri, E., Veysi, F., Shojaeizadeh, E. and Asadi, M., "The minimum gas temperature at the inlet of regulators in natural gas pressure reduction stations (CGS) for energy saving in water bath heaters", ***Journal of Natural Gas Science and Engineering***, Vol. 21, (2014), 230-240. doi: https://doi.org/10.1016/j.jngse.2014.08.005.
19. Adibi, T., Razavi, S.E., Adibi, O., Vajdi, M. and Moghanlou, F.S., "The response of nano-ceramic doped fluids in heat convection models: A characteristics-based numerical approach", ***Scientia Iranica***, (2021). doi: https://doi.org/10.24200/sci.2021.56574.4794.
20. Adibi, T., Adibi, O. and Razavi, S.E., "A characteristic-based solution of forced and free convection in closed domains with emphasis on various fluids ", ***International Journal of Engineering, Transactions B; Applications***, Vol. 32, No. 10, (2019), 1679-1685. doi: https://doi.org/10.5829/ije.2019.32.11b.20.
21. Razavi, S.E., Adibi, T. and Faramarzi, S., "Impact of inclined and perforated baffles on the laminar thermo-flow behavior in rectangular channels", ***SN Applied Sciences***, Vol. 2, No. 2, (2020), 284.doi: https://doi.org/10.1007/s42452-020-2078-8.
22. Adibi, T. and Razavi, S.E., "A new characteristic approach for incompressible thermo-flow in cartesian and non-cartesian grids", ***International Journal for Numerical Methods in Fluids***, Vol. 79, No. 8, (2015), 371-393.doi: https://doi.org/10.1002/fld.4053.
23. Razavi, S.E. and Adibi, T., "A novel multidimensional characteristic modeling of incompressible convective heat transfer", ***Journal of Applied Fluid Mechanics***, Vol. 9, No. 4, (2016), 1135-1146. doi: https://doi.org/10.18869/acadpub.jafm.68.228.24295.
24. Adibi, T., "Three-dimensional characteristic approach for incompressible thermo-flows and influence of artificial compressibility parameter", ***Journal of Computational & Applied Research in Mechanical Engineering***, Vol. 8, No. 2, (2019), 223-234. doi: https://doi.org/10.22061/jcarme.2018.2032.1178.
25. Tohid Adibi, Omid Adibi and Amrikachi, A., "Investigation on the possibility of substituting compression cooling cycle with a solar absorption cooling cycle in tropical regions of iran", ***European Journal of Electrical Engineering***, Vol. 19, No. 1, (2017), 7-17.doi: 10.3166/EJEE.19.7-17
26. Cesini, G., Paroncini, M., Cortella, G. and Manzan, M., "Natural convection from a horizontal cylinder in a rectangular cavity", ***International Journal of Heat and Mass Transfer***, Vol. 42, No. 10, (1999), 1801-1811. doi: https://doi.org/10.1016/S0017-9310(98)00266-X.
27. Chai, L., Xia, G., Zhou, M., Li, J. and Qi, J., "Optimum thermal design of interrupted microchannel heat sink with rectangular ribs in the transverse microchambers", ***Applied Thermal Engineering***, Vol. 51, No. 1, (2013), 880-889. doi: https://doi.org/10.1016/j.applthermaleng.2012.10.037

Persian Abstract

چکیده

برای جلوگیری از تغییر فاز و تشکیل هیدرات گازی در ایستگاههای کاهش فشار باید گاز طبیعی را از پیش‌گرم کرد. این مقاله با هدف بررسی تأثیر وجود پره روی لوله‌های گاز و پیکربندی آن، چینش و شکل آنها بر انتقال حرارت به گاز و بازده حرارتی انجام می‌گردد. برای آنالیز حساسیت، دو مورد لوله با پره و بدون پره، و برای چینش پره‌ها، دو ترتیب طولی و دایره‌ای، و برای پیکربندی پره‌ها، دو حالت پیوسته و منقطع مورد تحلیل قرار گرفت. همچنین، سه نوع سطح مقطع مستطیلی، سهموی همگرا و سهموی واگرا برای شکل پره‌ها مورد مطالعه قرار گرفته است. برای شبیه سازی، جریان به صورت سه بعدی، تراکم ناپذیر و پایدار در نظر گرفته شد و برای تحلیل عددی و گسسته‌سازی معادلات گرمای همرفت، از روش مشخصه‌محور استفاده شد. برای پیاده‌سازی و حل معادلات با کدنویسی از نرم افزار FORTRAN استفاده شد. نتایج نشان می‌دهند که در حالت پره‌های پیوسته و منقطع، با افزایش تعداد پره‌ها، ضریب انتقال حرارت بی‌بعد افزایش می‌یابد و با افزایش نسبت ارتفاع پره به قطر لوله، ضریب انتقال حرارت کاهش می‌یابد. همچنین، بیشترین بهبود انتقال حرارت مربوط به سطح مقطع پره سهمی واگرا بود.

IJE TRANSACTIONS C: Aspects Vol. 34, No. 6, (June 2021) 1548-1559

International Journal of Engineering

Journal Homepage: www.ije.ir

An Application of Fuzzy-VIKOR Method in Environmental Impact Assessment of the Boog Mine Southeast of Iran

S. Tabasi*, G. H. Kakha

Faculty of Industry & Mining (Khash), University of Sistan and Baluchestan, Zahedan, Iran

P A P E R I N F O

Paper history:
Received 01 March 2021
Received in revised form 03 April 2021
Accepted 19 April 2021

Keywords:
Boog
Environmental Component
Environmental Impact Assessment
Fuzzy Data
Impacting Factor
VIKOR

A B S T R A C T

Mining activities are one of the essential environmental challenges. Rating the environmental components (ECs) that affect by mining activities is a strategic guide for Environmental-Impact-Assessment (EIA). VlseKriterijumska- Optimizacija- I- Kompromisno- Resenje (VIKOR) method is developed as an efficient decision-making method to assess the impacts of the granite quarry Boog (in Southeast of Iran) on the environment. VIKOR method focuses on quantifying the effect of each impacting factor (IF) on each designed EC. This paper represents an evaluation method relying on fuzzy numbers in decision methods to carry out the lack of certainty and ambiguity from experts' subjective knowledge and experience. Shannon entropy theory is used to adjust subjective weights defined by decision makers to objective weights. The results catched through ranking the R, S and Q indices. In this case, the Air quality (R= 0.05, S= 0.16, Q= -0.05) is available as the more important EC that affected by the mining activities contaminations. Compareing the results with standard matrix method confirm that the Air quality has been effected more than the other parameters with 33.63%. Fuzzy-VIKOR is a systematic approach, which can easily extend to deal with quantitative environmental analysis and other mining engineering selection problems.

***doi**: 10.5829/ije.2021.34.06c.19*

NOMENCLATURE

f_i^+	The best rating of all attributes	TFNs	Triangular fuzzy numbers
f_i^-	The worst rating of all attributes	$\tilde{f}_i^*$	Positive triangular ideal solution
S_i	The maximum usefulness of alternatives groups	$\tilde{f}_i^0$	Negative triangular ideal solution
R_i	The minimum individual alternative.	$\tilde{d}_{ij}$	Normalized fuzzy difference
Q_i	VIKOR index	$\tilde{a}_{ij}$	Expert opinions converted to TFNs
A_m	Ranked alternatives	**Greek Symbols**	
e_j	Entropy measure	α_{ij}	Lower bound of expert opinion
div_j	Degree of divergence	δ_{ij}	Geometric mean of expert opinion
w_j	Objective weight	γ_{ij}	Upper bound of expert opinion
IFs	Impacting factors	λ	Numbers of experts
ECs	Environmental components	β_{ijk}	TFNs used for evaluation the effect of each IF on each designed EC

1. INTRODUCTION

Along with world economic growth, sustainable development (SD), has sought to generate a continuous balance through economic, social growth and the environment protection [1, 2]. Over the last decades, there have been remarkable interests in environmental issues. The emphasis of SD is now widely on human activities that cause environmental pollution. Mining activities with the acquisition of various kinds of natural resources, have a number of common stages, each of

*Corresponding Author Institutional Email: somayehtabasi@eng.usb.ac.ir (S. Tabasi)

Please cite this article as: S. Tabasi, G. H. Kakha, An Application of Fuzzy-VIKOR Method in Environmental Impact Assessment of the Boog Mine Southeast of Iran, , International Journal of Engineering, Transactions C: Aspects Vol. 34, No. 6, (2021) 1548-1559

which has potentially adverse impacts on the natural environment [3]. Every mining activity changes and disturbs, more or less, the condition of the natural environment by mainly energy consumption, deformations of the earth, various changes of water relations, emission of gas, dust and noise and the others [4,5]. Hence, it is necessary to use Environmental-Impact-Assessment (EIA) as an ongoing process, identifying the potential impacts of mining activities on the environment and reducing environmental problems for keeping mining activities in line with the principles of SD [6].

A technique and process that collects information about the environmental consequences of a project in advance, is an operational definition of EIA. Understanding these impacts can provide a suitable plan to prevent and reduce the hazardous effects. Since 1970, EIA has been set up as a powerful tool for environmental protection in projects planning process [7]. Today, EIA is essential for identifying all positive and negative impacts of industrial and mining activities on the surrounding environment [1]. Impact prediction's methods vary based on EIA components both qualitatively and quantitatively. Several standard techniques such as checklists, matrices, flowcharts and networks, mathematical/statistical models can be used to assess environmental components (ECs) [8]. In recent years, new tools and techniques such as mapping software and geographical information systems (GIS), remote sensed data were completed and support the EIA process [9].

Leopold et al. [10]. introduced one of the first EIA's evaluation methods Leopold matrix is a simple and efficient method that evaluates the project activities affects on the surrounding environment [11]. Pastakia [12] introduced the Rapid- Impact- Assessment- Matrix (RIAM) technique that alternatives rapidly evaluate without qualitative judgments. Pastakia and Jensen [13] used Rapid- Impact- Assessment- Matrix (RIAM) to provide clear reports that were well-informed. Phillips [14] developed a concept of SD index based on Rapid-Impact- Assessment- Matrix (RIAM) method. Folchi matrix, in contrast to Leopold's matrix, is quantitative and present a numerical judgment [15]. RIAM and Folchi methods did not consider the positive impacts of the project [16]. D-number method developed in order to reduce the uncertainty of the EIA methods and later modified by Wang and Wei [17]. As impacts of the components should take into account simultaneously during EIA, multi-criteria/multi-attribute- decision-analysis (MCDA/MADA) enables an analysis of different aspects of project impacts [18,19]. Decision making is the procedure of detecting the first rated option among the feasible choices; however, if decision-makers refuse to assess some criteria because of their knowledge limitation or because of the uncertainty of information, this assessment information cannot be recorded by the existing methods [1,19]. Therefore, the improved Analytic- Hierarchy- Process (AHP) and fuzzy- AHP, are extended into the MCDM methods to handle EIA problems [20]. Saffari et al. [1] merged ''Fuzzy Delphi'' and ''Folchi'' as an efficient tool in EIA systems with uncertainty.

Recently, some researchers extend the VIKOR (VlseKriterijumska- Optimizacija- I- Kompromisno-Resenje) method either solely or along with other mathematical techniques such as Analytic- Hierarchy-Process (AHP), Analytic- Network- Process (ANP) and Artificial Neural Networks (ANN) to provide decision-making problems with interval data [21].

The main objective of the proposed research is to develop an appropriate EIA method for monitoring the environmental disturbances result from mining activities of the granite quarry Boog. This framework uses fuzzy Logic, VIKOR and Shannon Entropy concept to prevent uncertainties in data and subjectivity in decision-makers opinions. This systematic approach transforms the quantitative and qualitative data into a equivalent scale and improves the ECs prioritizing. EIA's data can use to measure the interrelationships among the SD components and determine the sustainability level of mining activities.

Range from simple to complex, the focus of EIA methods have evolved from generating a list of potential impacts on selected environmental components. The complexity is increased by the diversity of the disciplines. Useful and destructive effective parameters introduced by 0-10 score. The triangular fuzzy numbers (TFNs) were used to describe the opinions of the experts about each IF. A matrix of potential interactions is produced by combining IFs and ECs (placing one on the vertical axis and the other on the horizontal axis). Linguistic values are converted to fuzzy numbers and used as the input for the fuzzy- VIKOR method. In next stage, in order to have comparable criteria, the fuzzy decision matrix is normalized. The Shannon Entropy concept is deploy to derive objective weights. The VIKOR method is used to calculate the positive and negative points of solution and finally the alternatives are ranked by sorting the values R, S and Q in descending order. The alternative with minimum value of Q is the best alternative and the compromise solution could be obtained.

2. MATERIALS AND METHODS

2. 1. VIKOR Method The VIKOR method was extended in 1998 by Opricovic to solve MADM problems with inconsistent and uncertain criteria [22,23]. VIKOR introduces the compromise ranking index based on the closeness rating of all alternatives to

the best ideal alternative using linear normalization to remove units of rule functions [24]. Where the DM at the initial phase of the MCDM process is not able to express his/her preference, the VIKOR method is effective [25]. This multi- attributes measurement use for agreement rating and extend based on the Lp-metric, as a summation function, [26] is shown as follow:

$$L_{p,i}=\left\{\sum_{j=1}^{n}[w_j(f_j^*-f_{ij})/(f^*-f_j^-)]^p\right\}^{1/p} \quad (1)$$
$$1\le p\le\infty;$$
$$i=1,2,....,m$$

where f_{ij} is the evaluation value of attribute j for alternative i; f_j^* and f_j^- are the best and worst value of alternative j, respectively; w_j is attribute weight; m and n are the number of attributes and alternatives respectively; the weight of the maximal deviation from the ideal solution denotes by p.

The VIKOR method deploys $L_{1,i}$ (as S_i in Equation (3) and $L_{\infty,i}$ (as R_i in Equation (4)) in order to formulate the ranking measure. Si is represents the maximum usefulness of alternatives groups, while Ri represents the minimum individual alternative. The main procedure of the VIKOR method comprises of some steps to find a solution of the problem described below [24]:

Step 1: Define Rating

The best f_i^+ and the worst f_i^- rating of all attributes determine using the following formulas:

$$f_i^+=\max_i f_{ij}$$
$$f_i^-=\min_i f_{ij} \quad (2)$$

Step 2: Calculate Si and Ri Values

$$S_i=\sum_{j=1}^{M}w_j([f_j^+-(f_{ij})]/[f_j^+-f_j^-]) \quad (3)$$

$$R_i=\max_j of\,(w_j[f_j^+-(f_{ij})]/[f_j^+-f_j^-])$$
$$|j=1,2,...,M \quad (4)$$

Step 3: Compute Values of Q_i

Values of VIKOR indices (Q_i) calculate as follows:

$$Q_i=v((S_i-S^-)/(S^+-S^-))$$
$$+(1-v)((R_i-R^-)/(R^+-R^-)) \quad (5)$$

where

$$S^+=\max_i S_i$$
$$S^-=\min_i S_i$$
$$R^+=\max_i R_i \quad (6)$$
$$R^-=\min_i R_i$$

v is introduce as the weight of the decision-making of the major criterion, can take any value from 0 to 1. Generally, the quantity of v is 0.5 [27].

Step 4: Rank the Alternatives

The alternatives rank by sorting the S, R and Q quantities in the descending order. For a given value of v, the compromise-ranking list obtaine by Q_i values ranking. In this list, the alternative with the minimum value of Q_i, is the best alternative.

Step 5: Compromise Solution

Propose alternative A_1 which is the first ranked by the Qi values as an agreement solution by fulfilling the two following C1 and C2 states:

C1: "Acceptable Advantage"

Considering A_2 as the second best alternatives based on the Q_i values, the relation $Q(A_2)-Q(A_1)\ge(1/N-1)$ should be established.

C2: "Acceptable Stability in Decision Making"

Established decision- making should be checked. So alternative A_1 must also be the formest rated based on ranking lists of both or at least one of the *S* or/and *R* values. This agreement is stable within a decision-making process and by following intervals of v:

$$\begin{cases}\text{the vote is by } major\ rule & v\succ 0.5\\ \text{the vote is by } consensus & v\approx 0.5\\ \text{the vote is by } veto & v\prec 0.5\end{cases}$$

different perspectives in decision-making can be stimulated.

Two following agreements propose, if one of the C1 and C2 states is not satisfied [28]:

Choose alternatives A_1 and A_2 if only C2 is not satisfied.

Choose alternatives A_1, A_2, ..., Am if C1 is not satisfied, wherein A_m is determined by using equation $Q(A_m)-Q(A_1)\prec(1/N-1)$ for maximum m value that meets the sets of Q_i.

2. 2. Fuzzy Logic Zadeh [29] first introduced fuzzy set theory that trace lingual variables to numerical ones within decision-making processes. Fuzzy Multi-Criteria- Decision-Making (FMCDM) method use to rate alternatives and assigne the weights of criteria in the cases with low precision [30].

A fuzzy set is a category of objects with no boundary between them. Membership function within

the interval [0, 1], states the degree of belonging of each element to the fuzzy set [31].

The fuzzy set

$$M = \{(\chi), \mu_M(\chi), \chi \in R\} \quad (7)$$

describes fuzzy numbers where $\mu_M(\chi)$ is a continued trace from R to closed interval [0,1].

2. 3. Shannon Entropy and Objective Weights Weighting methods categorize into two categories: in subjective methods the preference of decision makers is the basis of assessing weights, in the other side, objective techniques use mathematical models automatically without individuals preference consideration to specify weights [32].

The conception of entropy is a degree of information, disorder, chaos or uncertainty formulized in terms of likelihood theory. The probability of occurrence of an event is a degree of indeterminacy about the occurrence of this event. An event that occurs with high probability needs less information in order to characterize. On the other hand, more data need to describe the events happen with low probability [33]. Since the logarithm of occurrence probability, p (X_i), of an event, X_i, express the information content of this event thus entropy H(X) can define quantitatively as the probability-weighted average of the information content of each event X_i:

$$H_{shannon} = -\sum_i p_i \log(p_i) \quad (8)$$

This concept can deploy as a weighting calculation method through the following steps [32,34]:

Step 1: Normalizing the Evaluation Index

$$P_{ij} = \frac{x_{ij}}{\sum_j x_{ij}} \quad (9)$$

Step 2: Calculating Entropy Measure of Every Index

For every index, entropy measure calculate using the equation

$$e_j = -k\sum_{j=1}^{n} P_{ij} \ln(p_{ij}) \qquad k = (\ln(m))^{-1} \quad (10)$$

where m is the number of alternatives.

Step 3: Defining the Degree of Divergence

$$div_j = 1 - e_j \quad (11)$$

more degree of the div_j indicates the more important of the criterion j^{th}.

Step 4: Obtaining the Normalized Weights of Indexes

The entropy weighting of an attribute compute as following

$$w_j = \frac{div_j}{\sum_j div_j} \quad (12)$$

2. 4. Impacting Factors and Environmental Components Some negative influence of mining activity on the environment include the surface and underground water contamination, air pollution, soil properties changing, ecology changing, noise, waste. In order to investigate the environmental impact of the mining activity through different EIA methods many researches have attempted to describe impacting factors (IFs) and environmental components (ECs) [1].

The activities that have destructive effects on the environment are IFs. Some issues of the surrounding environment that affected by the activities are defined as ECs. Each of the IFs can affect one or several ECs [35,16].

3. CASE STUDY

The granite quarry Boog is one of the well-known quarry mines in the southeast part of Iran, is located 85 km from Zahedan City (Iran). Boog mine has a notable affect on the economy, culture and environment of the region.

4. RESULTS AND DISCUSSION

To study the environmental affect of the Boog granite mine, based on expert's idea, IFs and ECs are listed in Tables 1 and 2, respectively [36,1]. Some IFs like dust diffusion, landscape changing, noise pollution have negative impacts (the smaller factors are the better factors) and the activities like local employment, population control, social and cultural growth and environmental arrangements have positive impacts (the larger factors are the better type). In order to designate the influence of IFs on ECs, the affection of every IF on every EC is represented in Table 3 by the six statements from no (N) to very high influence (VH) and as relative numerical values [35,1].

Technical questionaries sent to the nine mining and environmental specialist experts. The impact of each factors on the ECs scored based on Table 3.

TABLE 1. Impacting factors (IFs)

No.	Impacting factors (IF)
1	Changing the usage of the area
2	Exposition of the area
3	Interference with surface water
4	Interference with ground water
5	Increasing the traffic of the area
6	Dust emission
7	Toxic pollutants and substance emissions to air
8	Noise pollution
9	Land vibration
10	Domestic employment
11	Population control policies
12	Social and cultural development
13	Instability of the established spaces
14	Environmental arrangements
15	Light

Environmental assessments process perform by using the decision matrix. IFs and ECs resulted from experts' scores are decision matrix rows and columns respectively and used as the input for the Fuzzy-VIKOR method.

In present research, in order to approximate the subjective opinions of decision-makers effectively, triangular fuzzy numbers (TFNs) used for the lingual terms. Expert opinions converted to TFNs, $\tilde{a}_{ij}$, which express the optimistic, modest and non-optimistic estimation for evaluating the alternatives in relation to each criterion as follows [37,38]:

TABLE 2. Environmental components (EC)

No.	Environmental components (EC)
1	Human health and immunity
2	Social issues
3	Surface water
4	Ground water
5	Air quality
6	Area usage
7	Ecology
8	Surface constructions 9
9	Area landscape
10	Quietness
11	Economic issues
12	Soil of the are

TABLE 3. Numerical values designed for the answered questionnaires [1, 35]

Expression variable	Associated Numerical values
No influence (N)	0
Very low influence (VL)	1
Low influence (L)	2
Medium influence (M)	3
High influence (H)	4
Very high influence (VH)	5

$$\tilde{a}_{ij} = (\alpha_{ij}, \delta_{ij}, \gamma_{ij}) \tag{13}$$

$$\alpha_{ij} = Min(\beta_{ijk}) \qquad k = 1,2,...,\lambda \tag{14}$$

$$\delta_{ij} = (\prod_{k=1}^{n} \beta_{ijk})^{1/n} \qquad k = 1,...,n \tag{15}$$

$$\gamma_{ij} = Max(\beta_{ijk}) \qquad k = 1,2,...,\lambda \tag{16}$$

where

$$\alpha_{ij} \le \delta_{ij} \le \gamma_{ij}$$

$$\alpha_{ij}, \delta_{ij}, \gamma_{ij} \subseteq [0,5]$$

$\alpha_{ij}, \delta_{ij}, \gamma_{ij}$ are lower bound, geometric mean and the upper bound respectively. The numbers of experts are λ. The relative severity of significance of kth expert opinion express among parameters i and j by β_{ijk}. Table 4 shows the results of this step.

The prime stage of fuzzy- VIKOR method is to draw out the positive triangular perfect resolution ($\tilde{f}_i^*$) correspond to positive ideal factors then the negative triangular perfect resolution ($\tilde{f}_i^0$) correspond to negative ideal factors using Equation (2). The results are presented in Table 5.

The next step normalized fuzzy difference ($\tilde{d}_{ij}, j = 1,...,J, i = 1,...,n$) was calculated using the following equations respectively for positive and negative IFs:

$$\tilde{d}_{ij} = \frac{(\tilde{f}_i^* - \tilde{f}_{ij})}{(r_i^* - l_i^0)} \tag{17}$$

$$\tilde{d}_{ij} = \frac{(\tilde{f}_{ij} - \tilde{f}_j^*)}{(r_j^0 - l_j^*)} \tag{18}$$

Table 6 shows the normalized fuzzy difference values.

The process of weights estimation is derived using the shannon entropy concept. In order to determine the objective weights by entropy measure, the projection value of each IF calculated using Equation (9) at first. Afterward, the entropy value is calculated by using Equation (10). Then, to calculate the degree of divergence of each IF the Equation (11) deployed. The objective weight for each IF is calculated by using Equation (12). Table 7 shows these calculated amounts.

Weighted sum $\tilde{S}$ and operator MAX $\tilde{R}$ calculated in fuzzy form using Equations (3) and (4), respectively. In order to rate ECs, the magnitude of $\tilde{Q}$ computed using Equation (5).

Then the results are defuzzified to detect crisp S, R and Q values of all ECs (Table 8). All ECs prioritized by a descend rule begin from the greatest crisp values of S, R and Q indices. The results are shown in Table 9. As it is obvious in Table 9, Q ranks Air quality, as the most significant component. The condition one (C1) is satisfied. However, Air quality ranked as the second most significant component by R and the condition two (C2) is not satisfied. So Soil of the area is ranked as equal as Air quality.

TABLE 4. Triangular fuzzy numbers (TFN) used for evaluation the effect of each impacting factor on each designed environmental component according to opinions of experts

	Air quality			**Quietness**			**Ecology**			**Surface water**			**Underground water**			**Area usage**		
	l	m	u	l	m	u	l	m	u	l	m	u	l	m	u	l	m	u
Changing the usage of the area	0.00	0.00	4.00	0.00	0.00	3.00	1.00	2.74	5.00	1.00	2.35	5.00	1.00	2.47	4.00	1.00	2.12	4.00
Exposition of the area	0.00	0.00	4.00	1.00	2.12	4.00	1.00	2.74	5.00	2.00	3.09	5.00	1.00	2.12	4.00	1.00	2.39	4.00
Interference with surface water	0.00	0.00	1.00	0.00	0.00	1.00	1.00	2.47	4.00	1.00	2.47	4.00	2.00	3.19	5.00	1.00	2.12	4.00
Interference with ground water	0.00	0.00	2.00	0.00	0.00	1.00	1.00	2.29	4.00	1.00	2.12	4.00	2.00	2.67	4.00	1.00	2.47	4.00
Increasing the traffic of the area	1.00	2.65	5.00	1.00	2.74	5.00	1.00	2.29	4.00	0.00	0.00	3.00	0.00	0.00	4.00	2.00	2.88	4.00
Dust emission	2.00	3.82	6.00	0.00	0.00	4.00	2.00	3.82	6.00	2.00	2.88	4.00	1.00	1.82	3.00	1.00	1.82	3.00
Toxic pollutants and substance emissions to air	1.00	3.03	5.00	0.00	0.00	4.00	2.00	3.30	5.00	1.00	2.47	4.00	1.00	2.47	4.00	1.00	2.47	4.00
Noise pollution	0.00	0.00	3.00	1.00	2.47	4.00	1.00	1.82	3.00	0.00	0.00	1.00	0.00	0.00	1.00	1.00	2.47	4.00
Land vibration	0.00	0.00	1.00	1.00	2.12	4.00	0.00	0.00	1.00	0.00	0.00	1.00	0.00	0.00	1.00	1.00	1.82	3.00
Domestic employment	0.00	0.00	4.00	0.00	0.00	3.00	1.00	2.12	4.00	1.00	1.82	3.00	1.00	1.82	3.00	1.00	1.82	3.00
Population control policies	0.00	0.00	4.00	1.00	2.12	4.00	1.00	2.47	4.00	0.00	0.00	2.00	0.00	0.00	4.00	3.00	3.91	5.00
Social and cultural development	1.00	2.12	4.00	1.00	1.82	3.00	1.00	2.12	4.00	1.00	1.82	3.00	1.00	1.82	3.00	2.00	2.88	4.00
Instability of the established spaces	0.00	0.00	1.00	0.00	0.00	1.00	1.00	2.74	5.00	0.00	0.00	1.00	0.00	0.00	1.00	2.00	2.88	4.00
Environmental arrangements	1.00	2.74	5.00	1.00	2.47	4.00	2.00	3.19	5.00	2.00	3.19	5.00	1.00	2.12	4.00	1.00	2.12	4.00
Light	0.00	0.00	1.00	0.00	0.00	4.00	0.00	0.00	4.00	0.00	0.00	3.00	0.00	0.00	4.00	1.00	1.82	3.00

TABLE 4. Continued

	Surface constructions			Area landscape			Soil of the area			Human health and immunity			Social issues			Economic issues		
	l	m	u	l	m	u	l	m	u	l	m	u	l	m	u	l	m	u
Changing the usage of the area	1.00	1.82	4.00	1.00	2.47	4.00	1.00	2.12	4.00	2.00	3.65	5.00	2.00	3.65	5.00	1.00	2.74	5.00
Exposition of the area	2.00	3.19	4.00	2.00	2.39	4.00	2.00	2.88	4.00	2.00	3.09	5.00	1.00	3.09	5.00	1.00	2.12	4.00
Interference with surface water	1.00	1.82	3.00	1.00	1.74	3.00	1.00	1.82	3.00	1.00	2.47	4.00	1.00	2.47	4.00	0.00	0.00	3.00
Interference with ground water	1.00	1.82	3.00	1.00	1.82	3.00	1.00	1.74	3.00	1.00	2.12	4.00	0.00	2.12	3.00	1.00	1.82	3.00
Increasing the traffic of the area	0.00	0.00	3.00	0.00	1.82	3.00	1.00	1.82	3.00	1.00	2.47	4.00	2.00	2.47	4.00	1.00	2.12	4.00
Dust emission	1.00	2.47	3.00	1.00	1.82	3.00	1.00	1.82	3.00	2.00	3.65	5.00	1.00	3.65	4.00	1.00	2.12	4.00
Toxic pollutants and substance emissions to air	2.00	2.79	4.00	2.00	2.88	4.00	1.00	1.82	3.00	2.00	3.65	5.00	2.00	3.65	4.00	1.00	2.74	5.00
Noise pollution	1.00	2.47	3.00	1.00	1.82	3.00	0.00	0.00	2.00	1.00	1.82	3.00	2.00	1.82	4.00	0.00	0.00	3.00
Land vibration	2.00	3.19	3.00	2.00	1.82	3.00	0.00	0.00	1.00	1.00	1.82	3.00	0.00	1.82	2.00	0.00	0.00	3.00
Domestic employment	2.00	3.19	4.00	2.00	2.88	4.00	1.00	2.47	4.00	1.00	2.42	5.00	2.00	2.42	5.00	2.00	3.54	5.00
Population control policies	1.00	1.82	4.00	1.00	2.88	4.00	1.00	1.82	3.00	2.00	3.19	5.00	2.00	3.19	5.00	2.00	3.74	5.00
Social and cultural development	0.00	0.00	4.00	0.00	2.88	4.00	2.00	2.88	4.00	2.00	3.54	5.00	3.00	3.54	5.00	2.00	3.86	5.00
Instability of the established spaces	1.00	1.82	4.00	1.00	2.88	4.00	1.00	1.82	3.00	2.00	2.88	4.00	1.00	2.88	4.00	1.00	2.74	5.00
Environmental arrangements	1.00	1.82	4.00	1.00	2.88	4.00	2.00	3.19	5.00	1.00	3.31	5.00	2.00	3.31	4.00	2.00	3.19	5.00
Light	2.00	2.67	5.00	2.00	3.54	5.00	0.00	0.00	3.00	2.00	3.74	5.00	2.00	3.74	5.00	0.00	0.00	5.00

TABLE 5. Positive triangular ideal solution ($\tilde{f}_i^*$) and the negative triangular ideal solution ($\tilde{f}_i^0$)

	$\tilde{f}_i^*$			$\tilde{f}_i^0$		
	l^*	m^*	u^*	l^0	m^0	u^0
Changing the usage of the area	0.00	0.00	3.00	2.00	3.65	5.00
Exposition of the area	0.00	0.00	4.00	2.00	3.19	5.00
Interference with surface water	0.00	0.00	1.00	2.00	3.19	5.00
Interference with ground water	0.00	0.00	1.00	2.00	2.67	4.00
Increasing the traffic of the area	0.00	0.00	3.00	2.00	2.88	5.00
Dust emission	0.00	0.00	3.00	2.00	3.82	6.00
Toxic pollutants and substance emissions to air	0.00	0.00	3.00	2.00	3.65	5.00
Noise pollution	0.00	0.00	1.00	2.00	2.47	4.00
Land vibration	0.00	0.00	1.00	2.00	3.19	4.00
Domestic employment	2.00	3.54	5.00	0.00	0.00	3.00
Population control policies	3.00	3.91	5.00	0.00	0.00	2.00
Social and cultural development	3.00	3.86	5.00	0.00	0.00	3.00
Instability of the established spaces	0.00	0.00	1.00	2.00	2.88	5.00
Environmental arrangements	2.00	3.31	5.00	1.00	1.82	4.00
Light	0.00	0.00	1.00	2.00	3.74	5.00

TABLE 6. Normalized decision matrix

	Air quality			Quietness			Ecology			Surface water			Underground water			Area usage		
	l	m	u	l	m	u	l	m	u	l	m	u	l	m	u	l	m	u
Changing the usage of the area	-0.60	0.00	0.80	-0.60	0.00	0.60	-0.40	0.55	1.00	-0.40	0.47	1.00	-0.40	0.49	0.80	-0.40	0.42	0.80
Exposition of the area	-0.80	0.00	0.80	-0.60	0.42	0.80	-0.60	0.55	1.00	-0.40	0.62	1.00	-0.60	0.42	0.80	-0.60	0.48	0.80
Interference with surface water	-0.20	0.00	0.20	-0.20	0.00	0.20	0.00	0.49	0.80	0.00	0.49	0.80	0.20	0.64	1.00	0.00	0.42	0.80
Interference with ground water	-0.25	0.00	0.50	-0.25	0.00	0.25	0.00	0.57	1.00	0.00	0.53	1.00	0.25	0.67	1.00	0.00	0.62	1.00
Increasing the traffic of the area	-0.40	0.53	1.00	-0.40	0.55	1.00	-0.40	0.46	0.80	-0.60	0.00	0.60	-0.60	0.00	0.80	-0.20	0.58	0.80
Dust emission	-0.17	0.64	1.00	-0.50	0.00	0.67	-0.17	0.64	1.00	-0.17	0.48	0.67	-0.33	0.30	0.50	-0.33	0.30	0.50
Toxic pollutants and substance emissions to air	-0.40	0.61	1.00	-0.60	0.00	0.80	-0.20	0.66	1.00	-0.40	0.49	0.80	-0.40	0.49	0.80	-0.40	0.49	0.80
Noise pollution	-0.25	0.00	0.75	0.00	0.62	1.00	0.00	0.45	0.75	-0.25	0.00	0.25	-0.25	0.00	0.25	0.00	0.62	1.00
Land vibration	-0.25	0.00	0.25	0.00	0.53	1.00	-0.25	0.00	0.25	-0.25	0.00	0.25	-0.25	0.00	0.25	0.00	0.45	0.75
Domestic employment	-0.40	0.71	1.00	-0.20	0.71	1.00	-0.40	0.28	0.80	-0.20	0.34	0.80	-0.20	0.34	0.80	-0.20	0.34	0.80
Population control policies	-0.20	0.78	1.00	-0.20	0.36	0.80	-0.20	0.29	0.80	0.20	0.78	1.00	-0.20	0.78	1.00	-0.40	0.00	0.40
Social and cultural development	-0.20	0.35	0.80	0.00	0.41	0.80	-0.20	0.35	0.80	0.00	0.41	0.80	0.00	0.41	0.80	-0.20	0.20	0.60
Instability of the established spaces	-0.20	0.00	0.20	-0.20	0.00	0.20	0.00	0.55	1.00	-0.20	0.00	0.20	-0.20	0.00	0.20	0.20	0.58	0.80
Environmental arrangements	-0.75	0.14	1.00	-0.50	0.21	1.00	-0.75	0.03	0.75	-0.75	0.03	0.75	-0.50	0.30	1.00	-0.50	0.30	1.00
Light	-0.20	0.00	0.20	-0.20	0.00	0.80	-0.20	0.00	0.80	-0.20	0.00	0.60	-0.20	0.00	0.80	0.00	0.36	0.60

TABLE 6. Continued

	Surface constructions			Area landscape			Soil of the area			Human health and immunity			Social issues			Economic issues		
	l	m	u	l	m	u	l	m	u	l	m	u	l	m	u	l	m	u
Changing the usage of the area	-0.40	0.36	0.80	-0.40	0.49	0.80	-0.40	0.42	0.80	-0.20	0.73	1.00	-0.20	0.73	1.00	-0.40	0.55	1.00
Exposition of the area	-0.40	0.64	0.80	-0.40	0.48	0.80	-0.40	0.58	0.80	-0.40	0.62	1.00	-0.60	0.62	1.00	-0.60	0.42	0.80
Interference with surface water	0.00	0.36	0.60	0.00	0.35	0.60	0.00	0.36	0.60	0.00	0.49	0.80	0.00	0.49	0.80	-0.20	0.00	0.60
Interference with ground water	0.00	0.45	0.75	0.00	0.45	0.75	0.00	0.43	0.75	0.00	0.53	1.00	-0.25	0.53	0.75	0.00	0.45	0.75
Increasing the traffic of the area	-0.60	0.00	0.60	-0.60	0.36	0.60	-0.40	0.36	0.60	-0.40	0.49	0.80	-0.20	0.49	0.80	-0.40	0.42	0.80

Dust emission	-0.33	0.41	0.50	-0.33	0.30	0.50	-0.33	0.30	0.50	-0.17	0.61	0.83	-0.33	0.61	0.67	-0.33	0.35	0.67
Toxic pollutants and substance emissions to air	-0.20	0.56	0.80	-0.20	0.58	0.80	-0.40	0.36	0.60	-0.20	0.73	1.00	-0.20	0.73	0.80	-0.40	0.55	1.00
Noise pollution	0.00	0.62	0.75	0.00	0.45	0.75	-0.25	0.00	0.50	0.00	0.45	0.75	0.25	0.45	1.00	-0.25	0.00	0.75
Land vibration	0.25	0.80	0.75	0.25	0.45	0.75	-0.25	0.00	0.25	0.00	0.45	0.75	-0.25	0.45	0.50	-0.25	0.00	0.75
Domestic employment	-0.40	0.07	0.60	-0.40	0.13	0.60	-0.40	0.21	0.80	-0.60	0.22	0.80	-0.60	0.22	0.60	-0.60	0.00	0.60
Population control policies	-0.20	0.42	0.80	-0.20	0.21	0.80	0.00	0.42	0.80	-0.40	0.14	0.60	-0.40	0.14	0.60	-0.40	0.03	0.60
Social and cultural development	-0.20	0.77	1.00	-0.20	0.20	1.00	-0.20	0.20	0.60	-0.40	0.07	0.60	-0.40	0.07	0.40	-0.40	0.00	0.60
Instability of the established spaces	0.00	0.36	0.80	0.00	0.58	0.80	0.00	0.36	0.60	0.20	0.58	0.80	0.00	0.58	0.80	0.00	0.55	1.00
Environmental arrangements	-0.50	0.37	1.00	-0.50	0.11	1.00	-0.75	0.03	0.75	-0.75	0.00	1.00	-0.50	0.00	0.75	-0.75	0.03	0.75
Light	0.20	0.53	1.00	0.20	0.71	1.00	-0.20	0.00	0.60	0.20	0.75	1.00	0.20	0.75	1.00	-0.20	0.00	1.00

TABLE 7. Calculated entropy measure, divergence values and objective weights of IFs

	e_j			div_j			w_j		
	l	**m**	**u**	**l**	**m**	**u**	**l**	**m**	**u**
Changing the usage of the area	0.69	0.75	0.88	0.31	0.25	0.12	0.066	0.054	0.037
Exposition of the area	0.89	0.88	0.88	0.11	0.12	0.12	0.023	0.027	0.036
Interference with surface water	0.60	0.63	0.72	0.40	0.37	0.28	0.085	0.081	0.088
Interference with ground water	0.61	0.67	0.71	0.39	0.33	0.29	0.081	0.073	0.089
Increasing the traffic of the area	0.62	0.68	0.82	0.38	0.32	0.18	0.079	0.07	0.057
Dust emission	0.86	0.87	0.83	0.14	0.13	0.17	0.03	0.028	0.052
Toxic pollutants and substance emissions to air	0.89	0.91	0.87	0.11	0.09	0.13	0.023	0.019	0.04
Noise pollution	0.47	0.46	0.65	0.53	0.54	0.35	0.112	0.119	0.107
Land vibration	0.39	0.39	0.54	0.61	0.61	0.46	0.129	0.134	0.143
Domestic employment	0.75	0.73	0.82	0.25	0.27	0.18	0.052	0.06	0.054
Population control policies	0.71	0.70	0.84	0.29	0.30	0.16	0.06	0.066	0.048
Social and cultural development	0.89	0.90	0.83	0.11	0.10	0.17	0.022	0.022	0.051
Instability of the established spaces	0.53	0.57	0.67	0.47	0.43	0.33	0.099	0.096	0.103
Environmental arrangements	0.98	0.97	0.90	0.02	0.03	0.10	0.004	0.006	0.029
Light	0.39	0.37	0.81	0.61	0.63	0.19	0.128	0.138	0.058

TABEL 8. The values of S, R and Q for all ECs

	S	R	Q
Air quality	0.16	0.05	-0.05
Quietness	0.26	0.07	0.13
Ecology	0.32	0.05	0.18
Surface water	0.21	0.05	0.04
Underground water	0.23	0.05	0.06
Area usage	0.39	0.07	0.31
Surface constructions	0.40	0.09	0.34
Area landscape	0.39	0.08	0.32
Soil of the area	0.21	0.03	0.00
Human health and immunity	0.44	0.09	0.37
Social issues	0.41	0.09	0.36
Economic issues	0.22	0.05	0.01

TABLE 9. The ranking of the ECs by S, R and Q in descending order

	By S	By R	By Q
Air quality	1	2	1
Quietness	6	8	6
Ecology	7	4	7
Surface water	3	3	4
Underground water	5	6	5
Area usage	9	7	8
Surface constructions	10	12	10
Area landscape	8	9	9
Soil of the area	2	1	2
Human health and immunity	12	10	12
Social issues	11	11	11
Economic issues	4	5	3

Based on the results of the last studies the surface infrastructures and economic problems have the least importance in Boog mine environmental effects. The quantitative matrix method was used for the EIA. Air quality, human health and safety and ecology have been effected more than the other parameters with 33.63, 28. 26 and 28.09%, respectively. Considering the accomplished calculations and considering that the environmental parameters is bigger than human parameter, the present project has been evaluated by using Philips mathematical model as a sustainable case; but the sustainability has been located in weak class [39].

5. CONCLUSION

Mining activities are kind of industries with long-term environmental effects. Environmental- impact-assessment (EIA) of mines is important for environmental problems monitoring. Obtaining the optimized alternative with the highest degree of efficiency for all of the relevant attributes is the object of MADM. VIKOR method has been widely used in various domains of decision-making because of its preferences.

The developed Fuzzy- VIKOR method is proposed to study how the mining activities of granite quarry Boog affect the environment. By using the presented method, the uncertainties of decision-makers opinions were expressed numerically. Objective weights are determined based on Shannon entropy for criteria weighting of the impacting factors. The Fuzzy- VIKOR is applied to assess the environmental components priorities. The final response of the Fuzzy- VIKOR method showed that five components of "Air quality" = "Soil of the region" were the most considerable components in the field of interest. The proposed systematic method is very flexible and enables us to assess and rank environmental components (ECs).

6. REFERENCES

1. Saffari, A., Ataei, M., Sereshki, F., Naderi, M. "Environmental impact assessment (EIA) by using the Fuzzy Delphi Folchi (FDF) method (case study: Shahrood cement plant, Iran)" ***Environment, Development and Sustainability*** Vol. 21, (2017), 817-860. DOI: 10.1007/s10668-017-0063-1
2. Kakha, G. H., Tabasi, S., Jami, M., Danesh Narooei, Kh. "Evaluation of the Impacting Factors on Sustainable Mining Development, Using the Grey-Decision Making Trial and Evaluation Laboratory Approach." ***International Journal of Engineering, Transactions A: Basics,*** Vol. 32, No. 10, (2019), 1497-1505. DOI: 10.5829/ije.2019.32.10a.20
3. Owen, J.R., Kemp, D., Extractive Relations: Countervailing Power and the Global Mining Industry. Sheffield, UK. 2017.
4. Dubiński, J. "Sustainable development of mining mineral resources." ***Journal of Sustainable Mining,*** Vol. 12, No. 1, (2013), 1-6. DOI: 10.7424/jsm130102
5. Farjana, S. H., Huda, N., Mahmud, M.A. P., Saidur, R. "A review on the impact of mining and mineral processing industries through life cycle assessment" ***Journal of Cleaner Production*** Vol. 231, (2019), 1200-1217. DOI:10.1016/j.jclepro.2019.05.264
6. Kaya, T., Kahraman C. "An integrated fuzzy AHP-ELECTRE methodology for environmental impact assessment." ***Expert Systems with Applications,*** Vol. 38, No. 7, (2011), 8553-8562, DOI:10.1016/j.eswa.2011.01.057
7. da Silva Dias, A.M., Fonseca, A., Paglia, A.P. "Technical quality of fauna monitoring programs in the environmental impact assessments of large mining projects in southeastern Brazil." ***Science of the Total Environment,*** Vol. 650, (2019), 216-223. DOI:10.1016/j.scitotenv.2018.08.425

8. Glasson, J., Therivel, R., Chadwick, A. Introduction to Environmental Impact Assessment, 3rd Edition, Routledge, London and New York, 2005.
9. Morris, P., Therivel, R. Methods of Environmental Impact Assessment, Taylor & Francis, 2001.
10. Leopold, L.B., Clarke, F.E., Hanshaw, B.B. A Procedure for Evaluating Environmental Impact. United States Department of the Interior, Washington, DC, 1971.
11. Josimovic, B., Petric, J., Milijic, S. "The use of the Leopold matrix in carrying out the EIA for wind farms in Serbia." ***Energy and Environment Research***, Vol. 4, No. 1, (2014), 43. DOI: 10.5539/eer.v4n1p43
12. Pastakia, C. M. R. The rapid impact assessment matrix (RIAM)—a new tool for environmental impact assessment. In Environmental impact assessment using the rapid impact assessment matrix (RIAM), K. Jensen; Fredensborg: Olsen & Olsen, 1998.
13. Pastakia, C. M. R., Jensen, A. "The rapid impact assessment matrix (RIAM) for EIA." ***Environmental Impact Assessment Review***, Vol. 18, (1998), 461-482. DOI: 10.1016/S0195-9255(98)00018-3
14. Phillips, J. "Evaluating the level and nature of sustainable development for a geothermal power plant." ***Renewable and Sustainable Energy Reviews***, Vol. 14, No. 8, (2010), 2414-2425. DOI: 10.1016/j.rser.2010.05.009
15. Folchi, D. I. R. "Environmental impact statement for mining with explosives: A quantitative method", in 29th Annual Conference on Explosives and Blasting Technique, Nashville, Tennessee, USA, (2003).
16. Mohebalia, S., Maghsoudy, S., Doulati Ardejani, F. "Application of data envelopment analysis in environmental impact assessment of a coal washing plant: A new sustainable approach" ***Environmental Impact Assessment Review***, Vol. 83, (2020), 106389. DOI: 10.1016/j.eiar.2020.106389
17. Wang, N., Wei, D. "A modified D numbers methodology for environmental impact assessment" ***Technological and Economic Development of Economy,*** Vol. 24, (2018), 653-669. DOI: 10.3846/20294913.2016.1216018
18. Parkin, J. "A philosophy for multiattribute evaluation in environmental impact assessments" ***Geoforum***, 1992, 23, 467-475. DOI: 10.1016/0016-7185(92)90003-M
19. Zhao, H. X., Zhang, X. Q. "Building index system of tourism environmental impact assessment in the Desert Park based on intuitionistic fuzzy multiple attribute decision making method" ***Issues of Forestry Economics***, Vol. 37, No. 2, (2017), 55-60.
20. Tseng, M. L., Wu, K. J., Lee, C. H., Lim, K. M., Bui, T. D., Chen, C. C. "Assessing sustainable tourism in Vietnam: a hierarchical structure approach" ***Journal of Cleaner Production***, Vol. 195, (2018), 406-417. DOI: 10.1016/j.jclepro.2018.05.198
21. Shemshadi, A., Shirazi, H., Toreihi, M., Tarokh, M.J. "A fuzzy VIKOR method for supplier selection based on entropy measure for objective weighting" ***Expert Systems with Applications***, Vol. 38, (2011), 12160-12167. DOI: 10.1016/j.eswa.2011.03.027
22. Opricovic, S. Multicriteria Optimization of Civil Engineering Systems. Ph.D. Thesis, Faculty of Civil Engineering, Belgrade, Serbia, 1998.
23. Opricovic, S., Tzeng, G. H. "Multicriteria planning of post-earthquake sustainable reconstruction" ***Computer-Aided Civil and Infrastructure Engineering,*** Vol. 17, No. 3, (2002), 211-220. DOI: 10.1111/1467-8667.00269
24. Opricovic, S., Tzeng, G.H. "Compromise solution by MCDM methods: a comparative analysis of VIKOR and TOPSIS" ***European Journal of Operational Research***, Vol. 156, No. 2, (2004), 445-455. DOI: 10.1016/S0377-2217(03)00020-1
25. Tavakkoli-Moghaddam, R., Heydar, M., Mousavi, S.M. "An integrated AHP-VIKOR methodology for plant location selection" ***International Journal of Engineering, Transactions B: Applications***, Vol. 24, No. 2, (2011), 127- 137.
26. Zeleny, M. Multiple criteria decision making. New York: Mc-Graw-Hill, 1982.
27. Zhu, G.-N., Hu, J., Qi, J., Gu, C. C., Peng, Y. H. "An integrated AHP and VIKOR for design concept evaluation based on rough number" ***Advanced Engineering Informatics***, Vol. 29, (2015), 408-418. DOI: 10.1016/j.aei.2015.01.010
28. Tzeng, G. H., Lin, C. W., Opricovic, S. "Multi-criteria analysis of alternative fuel buses for public transportation" ***Energy Policy***, Vol. 33, (2005), 1373-1383. DOI: 10.1016/j.enpol.2003.12.014
29. Zadeh, L. A. "Fuzzy sets" ***Information Control***, Vol. 8, (1965), 338-353. DOI:10.1016/S0019-9958(65)90241-X
30. Bellman, R. E., Zadeh, L. A. "Decision-making in a fuzzy environment" ***Management Science***, Vol. 17, No. 4, (1970), 141-164. DOI:10.1287/mnsc.17.4.B141
31. Bevilacqua, M., Ciarapica, F., Giacchetta, G. "A fuzzy-QFD approach to supplier selection" ***Journal of Purchasing and Supply Management***, Vol. 12, No. 1, (2006), 14-27. DOI:10.1016/j.pursup.2006.02.001
32. Wang, T. C., Lee, H. D. "Developing a fuzzy TOPSIS approach based on subjective weights and objective weights" ***Expert Systems with Applications***, Vol. 36, (2009), 8980-8985. DOI: 10.1016/j.eswa.2008.11.035
33. Mirauda, D., Ostoich, M. "MIMR Criterion Application: Entropy Approach to Select the Optimal Quality Parameter Set Responsible for River Pollution" ***Sustainability***, Vol. 12, (2020), 2078. DOI: 10.3390/su12052078
34. Lihong, M., Yanping, Z., Zhiwei, Z. "Improved VIKOR algorithm based on AHP and Shannon entropy in the selection of thermal power enterprise's coal suppliers", International conference on information management, innovation management and industrial engineering, (2008).
35. Ataei, M., Tajvidi Asr, E., Khalokakaie, R., Ghanbari, K., Tavakoli Mohammadi, M. R. "Semi-quantitative environmental impact assessment and sustainability level determination of coal mining using a mathematical model" ***Journal of Mining and Environment***, Vol. 7, No. 2, (2016), 185-193. DOI: 10.22044/jme.2016.515
36. Mirmohammadi, M., Gholamnejad, J., Fattahpour, V., Seyedsadri P, Ghorbani Y. "Designing of an environmental assessment algorithm for surface mining projects" ***Journal of Environmental Management***, Vol. 90, (2009), 2422-2435. DOI: 10.1016/j.jenvman.2008.12.007
37. Liu, Y. C., Chen, C. S. "A new approach for application of rock mass classification on rock slope stability assessment" ***Engineering Geology***, Vol. 89, (2007a), 129-143. DOI: 10.1016/j.enggeo.2006.09.017
38. Liu, Y. C., Chen, C. S. "A new approach to classification base on association rule mining" ***Decision Support Systems***, Vol. 42, (2007b), 674-689. DOI: 10.1016/j.dss.2005.03.005
39. Kakha, G. H., Tabasi, S., Docheshmeh Gorgij, A., Jami, M. "Environmental impact assessment and sustainability level determination of Boog Granite Mine using Philips model" ***Journal of Natural Environmental Hazards***, Vol.08, No. 22, (2020), 199-212. DOI: 10.22111/JNEH.2019.28328.1488

Persian Abstract

چکیده

یکی از مهم‌ترین چالش‌های زیست محیطی، فعالیت‌های معدنکاری می‌باشد. اخیراً، حل مساله و رده‌بندی مولفه‌های زیست محیطی (ECs) که تحت تاثیر فعالیت‌های معدنکاری قرار می‌گیرند، به یک فاکتور استراتژیک کلیدی در روند ارزیابی آثار زیست محیطی (EIA) تبدیل شده است. روش ویکور به عنوان یک روش تصمیم‌گیری موثر به منظور ارزیابی اثرات زیست محیطی معدن سنگ گرانیت بوگ واقع در جنوب شرق ایران مورد استفاده قرار گرفته است. روش ویکور بر درجه‌بندی میزان تاثیر هر فاکتور موثر (IF) روی مولفه‌های محیط زیستی تعیین شده، تمرکز دارد. در این پژوهش، یک مدل ارزیابی بر مبنای استفاده از اعداد فازی در فرآیندهای تصمیم‌گیری ارائه شده است که مساله عدم قطعیت و ابهام موجود در ادراک ذهنی و تجربه افراد خبره را حل کرده است. آنتروپی شانون به منظور تعدیل اوزان ذهنی افراد تصمیم‌گیرنده به وزن‌های واقعی مورد استفاده قرار گرفته است. نتایج حاصل از رده‌بندی فاکتورهای R، S و Q بدست آمده است. در این مورد، کیفیت هوا (R= 0.05, S= 0.16, Q= -0.05) به عنوان مهم‌ترین مولفه زیست محیطی که تحت تاثیر آلودگی حاصل از فعالیت‌های معدنکاری قرار گرفته است، تعیین شد. مقایسه نتایج با روش ماتریس استاندارد تایید می‌کند که فاکتور کیفیت هوا به میزان ۳۳/۶۳ درصد بیشتر از سایر پارامترها تحت تاثیر فعالیت‌های معدنکاری قرار گرفته است. روش فازی- ویکور، یک روش سیستماتیک است که به راحتی می‌تواند جهت بررسی های کمی زیست محیطی و سایر مسائل گزینشی مهندسی معدن مورد استفاده قرار گیرد.

AIMS AND SCOPE

The objective of the International Journal of Engineering is to provide a forum for communication of information among the world's scientific and technological community and Iranian scientists and engineers. This journal intends to be of interest and utility to researchers and practitioners in the academic, industrial and governmental sectors. All original research contributions of significant value focused on basics, applications and aspects areas of engineering discipline are welcome.

This journal is published in three quarterly transactions: Transactions A (Basics) deal with the engineering fundamentals, Transactions B (Applications) are concerned with the application of the engineering knowledge in the daily life of the human being and Transactions C (Aspects) - starting from January 2012 - emphasize on the main engineering aspects whose elaboration can yield knowledge and expertise that can equally serve all branches of engineering discipline.

This journal will publish authoritative papers on theoretical and experimental researches and advanced applications embodying the results of extensive field, plant, laboratory or theoretical investigation or new interpretations of existing problems. It may also feature - when appropriate - research notes, technical notes, state-of-the-art survey type papers, short communications, letters to the editor, meeting schedules and conference announcements. The language of publication is English. Each paper should contain an abstract both in English and in Persian. However, for the authors who are not familiar with Persian, the publisher will prepare the latter. The abstracts should not exceed 250 words.

All manuscripts will be peer-reviewed by qualified reviewers. The material should be presented clearly and concisely:

- *Full papers* must be based on completed original works of significant novelty. The papers are not strictly limited in length. However, lengthy contributions may be delayed due to limited space. It is advised to keep papers limited to 7500 words.
- *Research* notes are considered as short items that include theoretical or experimental results of immediate current interest.
- *Technical notes* are also considered as short items of enough technical acceptability with more rapid publication appeal. The length of a research or technical note is recommended not to exceed 2500 words or 4 journal pages (including figures and tables).

Review papers are only considered from highly qualified well-known authors generally assigned by the editorial board or editor in chief. Short communications and letters to the editor should contain a text of about 1000 words and whatever figures and tables that may be required to support the text. They include discussion of full papers and short items and should contribute to the original article by providing confirmation or additional interpretation. Discussion of papers will be referred to author(s) for reply and will concurrently be published with reply of author(s).

INSTRUCTIONS FOR AUTHORS

Submission of a manuscript represents that it has neither been published nor submitted for publication elsewhere and is result of research carried out by author(s). Presentation in a conference and appearance in a symposium proceeding is not considered prior publication.

Authors are required to include a list describing all the symbols and abbreviations in the paper. Use of the international system of measurement units is mandatory.

- On-line submission of manuscripts results in faster publication process and is recommended. Instructions are given in the IJE web sites: www.ije.ir-www.ijeir.info
- Hardcopy submissions must include MS Word and jpg files.
- Manuscripts should be typewritten on one side of A4 paper, double-spaced, with adequate margins.
- References should be numbered in brackets and appear in sequence through the text. List of references should be given at the end of the paper.
- Figure captions are to be indicated under the illustrations. They should sufficiently explain the figures.
- Illustrations should appear in their appropriate places in the text.
- Tables and diagrams should be submitted in a form suitable for reproduction.
- Photographs should be of high quality saved as jpg files.
- Tables, Illustrations, Figures and Diagrams will be normally printed in single column width (8cm). Exceptionally large ones may be printed across two columns (17cm).

PAGE CHARGES AND REPRINTS

The papers are strictly limited in length, maximum 6 journal pages (including figures and tables). For the additional to 6 journal pages, there will be page charges. It is advised to keep papers limited to 3500 words.

Page Charges for Papers More Than 6 Pages (Including Abstract)	
For International Author ***	**$55 / per page**
For Local Author	**100,000 Toman / per page**

AUTHOR CHECKLIST

- Author(s), bio-data including affiliation(s) and mail and e-mail addresses).
- Manuscript including abstracts, key words, illustrations, tables, figures with figure captions and list of references.
- MS Word files of the paper.

International **J**ournal of **E**ngineering, P.O. Box 13145-1659, Tehran, I.R. Iran
Materials and Energy Research Center, 5 Ahuramazda St., Alvand Ave., Argentina Sq., Tehran, Islamic Republic of Iran
www.merc.ac.ir - www.emerc.ac.ir

THOMSON REUTERS

WEB OF SCIENCE

Scopus®

CAS®
A DIVISION OF THE
AMERICAN CHEMICAL SOCIETY

Google
Scholar